Sensing the local charge and strain environments surrounding Nitrogen-Vacancy centers in diamond

by

Thomas A. Mittiga

A dissertation submitted in partial satisfaction of the

requirements for the degree of

Doctor of Philosophy

in

Physics

in the

Graduate Division

of the

University of California, Berkeley

Committee in charge:

Assistant Professor Norman Yao, Chair
Professor Dan M. Stamper-Kurn
Associate Professor Naomi Ginsberg

Fall 2020

Sensing the local charge and strain environments surrounding Nitrogen-Vacancy centers in diamond

Copyright 2020
by
Thomas A. Mittiga

Abstract

Sensing the local charge and strain environments surrounding Nitrogen-Vacancy centers in diamond

by

Thomas A. Mittiga

Doctor of Philosophy in Physics

University of California, Berkeley

Assistant Professor Norman Yao, Chair

Nitrogen-Vacancy (NV) centers in diamond have been established as exceptionally versatile probes for quantum technologies from sensing to simulation. Owing to the versatility of diamond fabrication, NVs can be integrated into probes with nanoscale resolution and superb sensitivity. However, because the diamond is host to many other types of defects, the local environment of the NV is unique for each NV, which poses challenges for any devices instrumenting NVs. This thesis contributes to the future of NV technologies along two essential directions. First, we work towards a more complete understanding of the local charge and strain environments of the NV. In addition to permitting the calibration of these effects for NV probes, we suggest potential uses for the local charges and strain that had previously been considered hindrances. Second, we develop new technologies for NV sensing and simulation. Our work integrating NVs into diamond anvil cells opens the door to detecting high pressure phenomena using the NVs as all-in-one sensors. Finally, our study of the coherence regimes of the local defect environment of the NV is a step towards versatile quantum simulation in dimensions lower than three.

To my family
and future Yao lab students

Contents

List of Figures

List of Tables

Acknowledgments

I sincerely hope that I am the worst student to graduate under the tutelage of Prof. Norman Yao. From the start of my PhD., I knew I did not want to continue with research afterwards. This knowledge left me dejected and, coupled to an unhealthy relationship to failure, eventually blossomed into a crippling physics anxiety. Norm guided me through my worst years with the right blend of inspiration, perspiration, and compassion. It is hard to imagine another advisor who would not only provide private "grill sessions," but approach them with extreme patience and honesty as I floundered at the whiteboard for hours. He was stern when he needed to be, yet always friendly and approachable. He supported me when I felt I did not deserve it. He raised me to a scientific standard I did not know I could achieve. There is too much I could say and too much I cannot express. The first acknowledgement must be to you. Thank you, Norm.

My undergraduate career would not have propelled me into a PhD. without the help of some key people. My friends Kevin Sackel, Joe Wysk, and Will London taught me much. Kevin showed me how to accelerate my education, Will was the paragon of a physics student (and a solid commiseration buddy throughout graduate school), and Joe provided much appreciated moral support. Prof. Harold Metcalf's infectious awe encouraged me to ask if I could research with him. His lab storerooms were the fertile playground in which I learned basically all the optics skills I used and taught throughout my PhD. Building a lab from scratch with Prof. Eden Figueroa is what made me worthy of a school like Berkeley. I am forever grateful to have worked one-on-one with him.

My first year and a half at Berkeley was spent with Prof. Dan Stamper-Kurn's lab. His ultracold research got me excited for ambitious projects, and his AMO class was the first class I enjoyed at Berkeley. Most importantly, his students were a welcoming crew that oriented me for the long haul ahead. Thanks especially go to Fang Fang, Justin Gerber, Emma Deist, Zephy Leung, Ryan Olf, Claire Thomas, Sydney Schreppler, and Ed Marti.

When I joined Norm's lab, we had only an optical table and a dream. Fortunately, Norm also had many friends who helped us immensely right from the start and provided wisdom throughout our experiments. For initial diamond sample fabrication: Birgit Haussmann and Kristiaan DeGreve; for the experimental apparatus and measurement protocols: Joonhee Choi, Soonwon Choi, Hengyun Zhou, and Elana Urbach; for help with TMD samples: Chenhai Jin, Jonghwan Kim, and Prof. Feng Wang.

Once the Yao lab was up and running, it burgeoned into a group of friends and colleagues who provided countless physics lessons and endless camaraderie. While I was studying for the qualification exams, I met one-on-one with almost every student in the lab to practice answering questions and toughen me up. Outside of the lab, I enjoyed grabbing dinner, playing games, watching movies, wrestling, enjoying concerts, dancing, or shooting hoops with everyone. Among the theorists, I could always find someone to pester with questions or run through ideas. Innumerable thanks to Francisco Machado, Bingtian Ye, Rahul Sahay, Bryce Kobrin, Thomas Schuster, Greg Meyer, Best Akkaravarawong, Chris Olund, Jack Kemp, Max Block, and (in a new context) Soonwon Choi. Among the experimentalists, I

could always find helping hands and sounding boards. Special thanks to Chong Zu, Satcher Hsieh, Prabudhya Bhattacharyya, Emily Davis, Jordan Hines, and Tim Höhn. I would be remiss not to thank Chong again for being the heart of the lab. I have never met a more jubilant person who could spread so much cheer under any circumstance. In the end, you were all fun bunch to work with and I wish you all the best—Thanks!

A quick thanks goes to Prof. Naomi Ginsberg. You recognized what was troubling me and spoke up. Your action led me to Dr. Robert Epstein, who has helped me develop tools for handling my anxiety and depressive tendencies. At the time of this writing, I have not yet mastered my inner demons, but I am well equipped to progress through the next stages of my life.

So many thanks go to those who were not biologically related to me yet provided family over my years in Berkeley's ivory tower. If I mentioned all my cherished friends, these pages would be far too long, so I will trust you know who you are. I would like to highlight instead those friends who most directly impacted my graduate studies. Eric Copenhaver and Chris $$$, our talks in the gym maintained my sanity as well as my muscles. Eric, you are an Adonis and your marriage is an inspiration. Chris, your crafty approach to life is one I strive to adopt. Marielf Goddu and Tucker Hiatt, communicating science with you has been a delight. Marielf, your empathy taught me how to love again. Tucker, may your wonder never end. Francisco Machado, at the end of the day, you have a much bigger heart than you realize. Thanks for weathering so many physics questions as well as a pandemic with me. Katelin Schutz, Tom Zick, and Cakers, y'all were my good road-trippin' allies. Tea, cooking, baking, pranks, games, and so much more made life a delight.

Penultimate thanks go to Aunt Judy. Your story of perseverance in your own PhD. is incredible. Your advice was invaluable at a crucial time. I recall your strength and wisdom often.

My final thanks must extend to my family. You were with me from the start and you'll be there until the end. Mom and dad, I could always call on you to steady my resolve when I was down. Mom, you always find time to edit my speeches and writing. Dad, the whimsy I got from your side of the family has served me well. Jonathan, your awe for life and audacious endeavors have shaped me much more than you can know. I always appreciate your perspective. Rosalyn, no one has altered the trajectory of my personality more than you. You live as an incredible example. Thank you all.

Citations to Previously Published Work

Aside from changes and additional comments listed below, Chapter 2 has been published as

- "Imaging the Local Charge Environment of Nitrogen-Vacancy Centers in Diamond". T. Mittiga, S. Hsieh, C. Zu, B. Kobrin, F. Machado, P. Bhattacharyya, N. Z. Rui, A. Jarmola, S. Choi, D. Budker, N. Y. Yao *Phys. Rev. Lett.* **121** (24 Dec. 2018), p. 246402. doi: 10.1103/PhysRevLett.121.246402.

Wording was altered and transitions are added in all sections as needed to fit the language of the thesis or to refer to appropriate sections of the thesis or new publications. Completely original content is found in the following sections

- 2.1, 2.7.3, 2.8

Additional technical details and comments are found in the following sections

- 2.3, 2.5.2, 2.5.3, 2.7.2

Most of Chapter 3 has been published with minor changes in

- "Imaging stress and magnetism at high pressures using a nanoscale quantum sensor" S. Hsieh, P. Bhattacharyya, C. Zu, T. Mittiga, T. J. Smart, F. Machado, B. Kobrin, T. O. Höhn, N. Z. Rui, M. Kamrani, S. Chatterjee, S. Choi, M. Zaletel, V. V. Struzhkin, J. E. Moore, V. I. Levitas, R. Jeanloz, N. Y. Yao *Science* 13 Dec 2019: Vol. 366, Issue 6471, pp. 1349-1354 DOI: 10.1126/science.aaw4352

Wording was altered and transitions are added in all sections as needed to fit the language of the thesis or to refer to appropriate sections of the thesis or new publications. Completely original content is found in the following sections

- 3.1, 3.2.3, 3.3, 3.3.1, 3.6

Additional technical details and comments are found in the following section

- 3.2.2

Chapter 1

Introduction to NV Sensing and Simulation

1.1 Motivation

The Platonic form of a diamond is a perfect lattice of identical carbon-12 atoms stretching from one facet of the diamond to the other. A jeweler—indubitably, most of the world—would lament replacing any one of the atoms in that pristine gem with anything else. In the minority as usual are the scientists, who tirelessly struggle against nature to achieve their own notions of perfection. Indeed, the Platonic—and mathematical—form of the Nitrogen-Vacancy (NV) center (Fig. 1.1a) is a single nitrogen atom adjacent to a single vacant lattice site in an otherwise perfect diamond. No such specimen of the NV exists–it is always surrounded by other imperfections that can change the properties of both the NV and the diamond. As testament to the fanatical obsession with which resilient and relentless scientists seek truth, despite lacking such a perfect specimen, The NV's intrinsic properties have been extensively examined regardless, the NV's popularity has exploded, and focus has shifted instead towards employing the NV in quantum tools: sensors, computers, and simulators.

One could argue that the NV's popularity for quantum technology applications stems from the ease with which one can build an apparatus to manipulate and read its spin state. At room-temperature, the NV can be initialized repeatedly and reliably into the same spin state within $\sim 1\mu$s using green light. The coherence of that state lasts for $\sim$10-100 μs on average, which is exceptionally long compared to the $\sim$ 10 ns duration required to perform an operation upon it; the NV can be programmed with thousands of commands each millisecond in principle, though rarely does a protocol require more than ten or a hundred. When desired, the interactions with other NVs or defects in the diamond can be enhanced with proper quantum programming or simply by increasing the density of defects. Because it is hard and inert, a diamond containing NVs can easily be moved around and even swallowed [89], allowing an experiment to reuse NVs that have ideal properties. The diamond can be fabricated for seamless integration into practical devices [83]. Finally, since the technology

of lasers, microwaves, and diamond fabrication is so mature, the instruments involved in using NV spins are relatively cheap, permitting scalable technologies [83, 92, 132, 89, 154, 109, 91, 122, 42, 39, 58] and fundamental physics research [157, 15, 64].

1.1.1 Local Environments

The emphasis on myriad implementations is the correct path forward for science and technology related to the NV. This thesis contributes to the effort in two essential manners: the calibration and understanding of signals intrinsic to NV systems and the creation of new NV-based tools, both of which rely on the study of the surroundings within tens of nanometers of the NV—its "local environment."

The NV's spin is sensitive to a wide range of external signals: from magnetic and electric fields to pressure, temperature and rotation [108, 100, 155, 2, 45, 37, 36, 35, 93, 6]. This sensitivity is both a boon and a burden. Whereas all atoms of the same species are identical, each diamond is not; the crystallographic defects, atomic impurities, and surface chemistry are unique to each diamond. For each new instrumentation, the NV experiences a new local environment of surrounding charges, magnets, crystal strain, and temperature, all of which alter its sensitive properties. Therefore, to use an NV in any application properly, the influence of the local environment must be first calibrated so as not to conflate it with the desired signal to be measured. This calibration could come in the form of detecting how nearby charges and crystallographic strain influence the NV before the it is used to probe another signal (Chapter 2, Chapter 3), or by verifying the geometry of the local environment (Chapter 4, Chapter 5).

Calibrating the NV also entails understanding the physics of the local environment, which contributes to the pursuit of answers to outstanding questions about the NV. For example, this thesis' work on the local charge environment of the NV (Chapter 2) provides some clues into the source of the NV's additional charge (Section 1.2.4). Understanding this source is crucial to the future of creating NV probes. In addition, the techniques developed to study the local charge environment are also applicable to studies of charges on the surface of the diamond that are believed to cause spectral diffusion in NV close to the surface.

The new tools this thesis develops depend on the study of the local environment as well. In creating an NV-based probe that can withstand high pressures, we found that the local stress the NVs experience could potentially reflect the stress experienced by a sample of interest nearby. By fully exploring the local stress environment, the work paved the way to sensing high-pressure phase transitions in exotic materials [136]. Furthermore, the study of local charge as a hindrance to be calibrated away suggests a path towards building nanoscale electric field sensors that can handle a range of extreme environments [16]. The smaller and more robust the sensor, the more versatile the application.

1.1.2 Sensing and Simulation

Simulation is an extension of sensing.

The NV probes in this thesis are used either as quantum sensors or in quantum simulations. In both scenarios, we consider an NV surrounded by an environment that perturbs it. The environment could comprise a single charge, a 'bath' of spins, or a field induced globally upon the diamond by a sample, to name a few examples.

As quantum sensors, NVs reflect changes in their environments as alterations in their magnetic resonance spectra (see 1.5.2 and 1.5.3). As long as the probe's interaction with the environment can be written as a term in the Hamiltonian, this spectroscopy method can be used to calculate information about the source of the environmental changes. These sources could be, for example, the dynamics of electric and magnetic impurities in the diamond, or an exotic sample placed on the diamond's surface which creates a field that the NVs detect.

For use as a sensor, the NV's local environment is often a hindrance to be calibrated, if possible. With enough thought however, otherwise troublesome local spin baths can instead become the expansive playground for quantum simulations and the exploration of exotic phases of matter. As the essential component to quantum simulations, the NV probes its local environment of interacting defects. For our experiments, the NV serves as the probe and a surrounding ensemble bath of strongly-interacting spins perform the simulation. Other experiments instead create a dense ensemble of strongly interacting NVs to both simulate and probe itself [26]. Notably, whether it is the experimentally-designated probe or a designated bath spin, each spin in the system is constantly probing its local environment.

While spectroscopy is generally utilized as a sensing technique, its core notion of isolating individual frequency components is essential to the study of simulations. The quantum simulations in this thesis employ "dynamical decoupling" sequences that selectively filter certain noises in the environment (frequency and/or source) to isolate other noises, which is in essence spectroscopy. The key difference is that the purpose is to isolate the particular aspects of the dynamics being simulated when applying such spectroscopy in simulations, rather than to extract information about a source as occurs in sensing.

1.1.3 Organization of this Thesis

This thesis studies local environments as both burdens and boons. First, the theoretical and experimental considerations of the NV are introduced in detail for the remainder of this chapter. It is intended to serve as a manual for advanced undergraduate or early graduate students starting research. There are many concepts and facts that I felt I learned too slowly or too late in part because they were not in a single location, so I wanted anyone working with NVs to have as much essential information as possible in one place. To that end, I have added in all of the intuition I could think of that made concepts click in my own head, which is missing from the extreme majority of textbooks and papers I have read. I tried to present them in a order such that each concept builds off of the previous ones, so no prior knowledge is necessary if they are read in order.

The remaining chapters review experiments on the discovery of a previously overlooked local charge environment (Chapter 2); the integration of NVs into a hybrid high-pressure sensor, including the calibration and utility of the local stress tensor (Chapter 3); the use

of the NV's local spin bath as a quantum simulator in low dimensions (Chapter 4); and the study of exotic Transition Metal Dichalcogenides (TMDs) by placing them within the local environment of NVs (Chapter 5).

1.2 NV Basics

1.2.1 Diamond Types

Before discussing the NV or any other specific defects in the diamond, we must start with the scientific classification of diamonds by their levels of impurity. There are four main types of diamond: Ia, Ib, IIa, and IIb. For both Type I diamonds, nitrogen is the main impurity. For Type Ia, nitrogen is at levels ¿500 parts per million (ppm). At these levels, the nitrogen are most likely to be clustered into pairs or larger even-numbered groupings. If the the nitrogen groups are predominantly pairs, which does not affect the diamond color, the diamond is categorized as the subtype IaA, and if the nitrogen groups are predominantly large even-numbered groupings, which adds yellow to the color, the diamond is subtyped as IaB. Around 95% of natural diamonds are type Ia. For Type Ib diamonds, the nitrogen content is in the range 1-500 ppm, which is unlikely to produce nitrogen pairs. Most diamonds fabricated by high-pressure high-temperature (HPHT) techniques are type Ib. For both Type II diamonds, the nitrogen content is below 1 ppm. Type IIa is the most pure. Artificial Type IIa are most often produced by chemical vapor deposition (CVD) techniques and come in two subgrades: optical and electronic grades. Both grades have nitrogen content less than or approximately 5 parts per billion (ppb) and grown by CVD. The difference is that electronic grade has additional boron doping, which is usually small enough that it does not bother NV experiments.

In addition to classifying diamonds by type, they can also be classified by single- and poly-crystalline structure. Single crystal diamond have a single periodic carbon lattice (neglecting species impurity) over the diamond sample. Polycrystalline diamonds have only locally periodic carbon lattices, the grain of the diamond changing on occasion. Most CVD diamonds used for NV experiments are single crystal, especially then the experiment focuses on individual NVs.

1.2.2 Generating NVs

The P1 defect center (Fig. 1.1b) is a nitrogen swapped in for a carbon atom–a 'substitutional nitrogen.' The vacancy defect is simply a missing carbon. Vacancies are much less thermally stable than P1s, so when the diamond is annealed (typically 400-1200 C), vacancies hop around, and even out of the diamond if they reach its edge. However, vacancies that meet P1s settle into place, the nitrogen-vacancy pair being much more thermally stable together. One can quickly intuit why by looking at the atomic numbers of carbon and nitrogen. Notably,

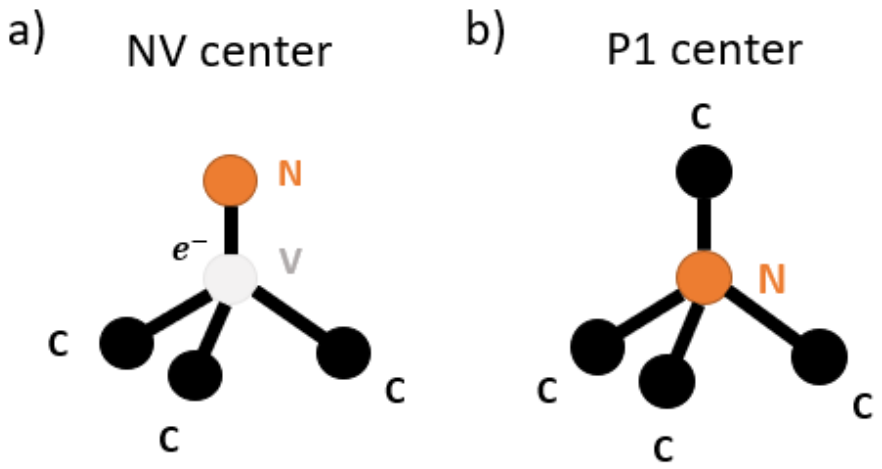

Figure 1.1: a) Molecular diagram of an NV center. b) Molecular diagram of a P1 center

this pairing is not yet the NV used throughout this thesis, it will require an additional charge (Section 1.2.4) from a donor.

The process for generating NVs in general amounts to creating both vacancy and P1 defects in n-doped diamond and then increasing the temperature so that the vacancies eventually collide with the P1s. Most often this is achieved artificially by first implanting the nitrogen to create P1s, then irradiating the diamond with electrons or with ^{12}C to damage the lattice and create vacancies, and finally annealing the sample at temperatures ranging between 200 C and 1200 C [115]. There are many parameters to tune in this method that can control density (gas pressure), depth (implantation energy), and spin and spectral properties (diamond cleanliness). There are also other methods available, most notably introducing nitrogen during the growth process of the diamond, a process called delta-doping [117]. Also, NVs will naturally occur in diamond. If a sample of natural diamond has other defect and crystalline impurity levels that are tolerable, an NV experiment can use a natural NV instead of generating one. For a more complete review of NV generation and a very nice summary of what each technique can accomplish, see [12] and especially their Table IV.

1.2.3 Physical Structure

Since the physical shape of the nitrogen-vacancy pairing impacts the location, dynamics, and energy of its electrons, knowing the structure of the diamond NV is crucial to understanding its electronic and spin properties. The NV structure is constrained by the geometry of the diamond lattice to abide by C_{3v} symmetry (Fig. 1.2). The C_{3v} symmetry group is that of a three-sided pyramid (tetrahedron) with a painted tip or an equilateral triangle in two dimensions: three mirror planes, two rotations, and the identity. As opposed to atoms in

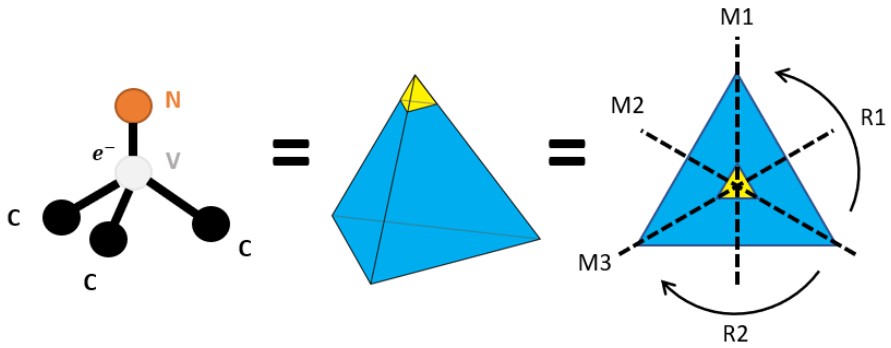

Figure 1.2: The NV has the same symmetries as a tetrahedron with a painted tip, or an equilateral triangle (restricted to 2-dimensional operations): reflections through mirror planes (M1, M2, M3), rotations by $\pm 120^\circ$ (R1, R2), and the identity.

free space, whose electronic states are rotationally invariant, the NV's electronic states are characterized by how they transform under C_{3v} symmetry operations. The fascinating details and intuition of deriving electronic and spin properties are described in (Section 1.3).

The symmetry axis of the C_{3v} point-group is the nitrogen-vacancy bond of the NV. This bond can orient in any one of the four crystallographic directions of the diamond axis, creating four "orientation groups" of NVs with distinct XYZ axes. A typical external field (electric, magnetic, etc.) will have a different projection onto the axes of the NVs of each orientation groups, which changes that group's response to the field.

1.2.4 NV Charge States

Experiments have determined the existence of two NV charge states, the neutral NV^0 and the singly-charged NV^-, distinguished by a zero-phonon line (ZPL) at 575 nm [51] and 637 nm [112, 95], respectively. NV^0 has 5 electrons, 3 associated with the dangling carbon bonds (carbon to vacancy) and 2 valence electrons from the nitrogen. NV^- has one additional electron (6 total), presumably donated by other impurities in the diamond. Due to a lack of useful polarizable spin states, the neutral NV^0 is often neglected or treated as an undesirable byproduct. Experiments and theory almost exclusively focus on the NV^-. The work in this thesis pertains only to the NV^-, hereafter referred to simply as the NV.

1.2.5 Electronic Structure and Levels

To date, there is no perfect derivation of the electronic energy levels of the NV (Fig. 1.3b) from first principles, but between theory and experiments, more than enough has been worked out to provide accurate models of electronic structure and dynamics [95, 103, 101,

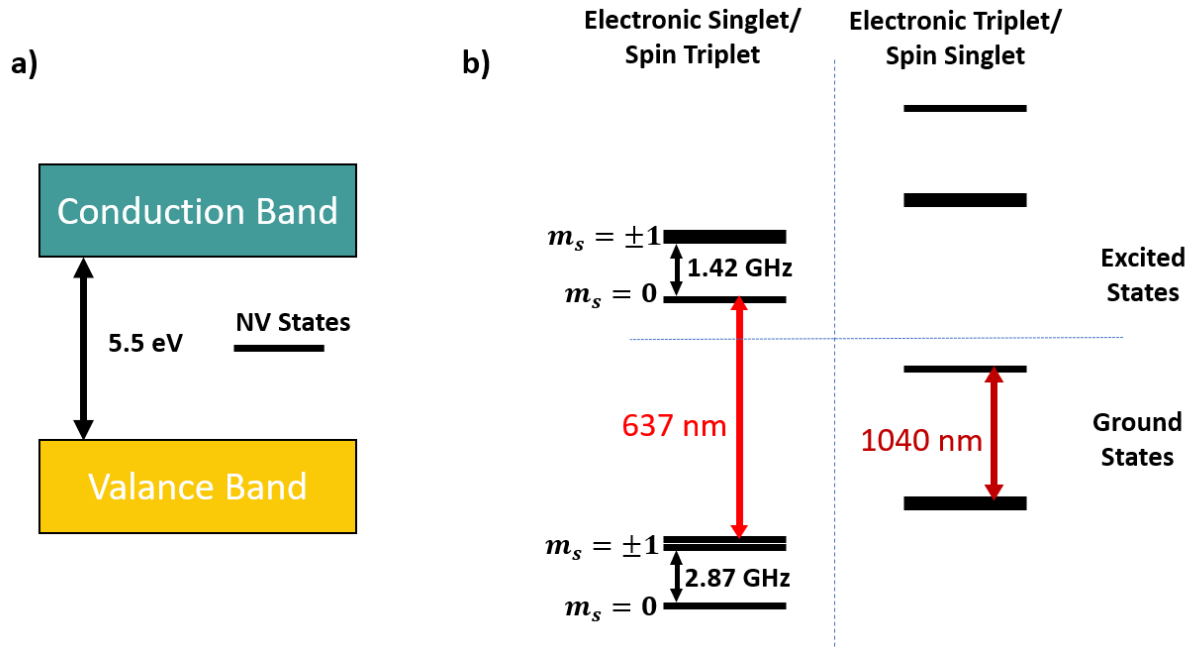

Figure 1.3: a) The NV states exist within the diamond's 5.5 eV bandgap at an unknown location. b) The NV electronic and spin energy levels

107, 150, 128]. Experiments have confirmed the NV's C_{3v} symmetry [31], verifying that the electronic ground and excited states' two electrons can each be in either a anti-symmetric or symmetric spatial configuration, forcing their total electronic spin into a triplet or singlet configuration, respectively. In both the electronic singlet ground and excited states, spin triplets [126, 127, 97, 118, 102] have been well-measured, providing some distinctive and well-established parameters: a 2.87 GHz zero-field splitting in the electronic ground state's spin triplet, a 1.42 GHz splitting in the electronic excited state's spin triplet [150], and a 637 nm electronic dipole transition between the ground and excited states (Fig. 1.3b). As well, the splitting due to the Coulomb interaction for the electronic triplet ground state (spin singlet) has been measured as 1040 nm [129]. The exact location of the ground state electronic-triplet-spin-singlet between the ground and excited electronic-singlet-spin-triplet states is yet unverified (Fig. 1.3a). The electronic triplet excited state is proposed to exist, but relatively few attempts have been made to measure any of its properties. Lastly, all of the NV states exist within the bandgap of diamond, which is crucial because if these states were within the conduction or valence bands they would ionize the NV; however the location within the bandgap is unknown.

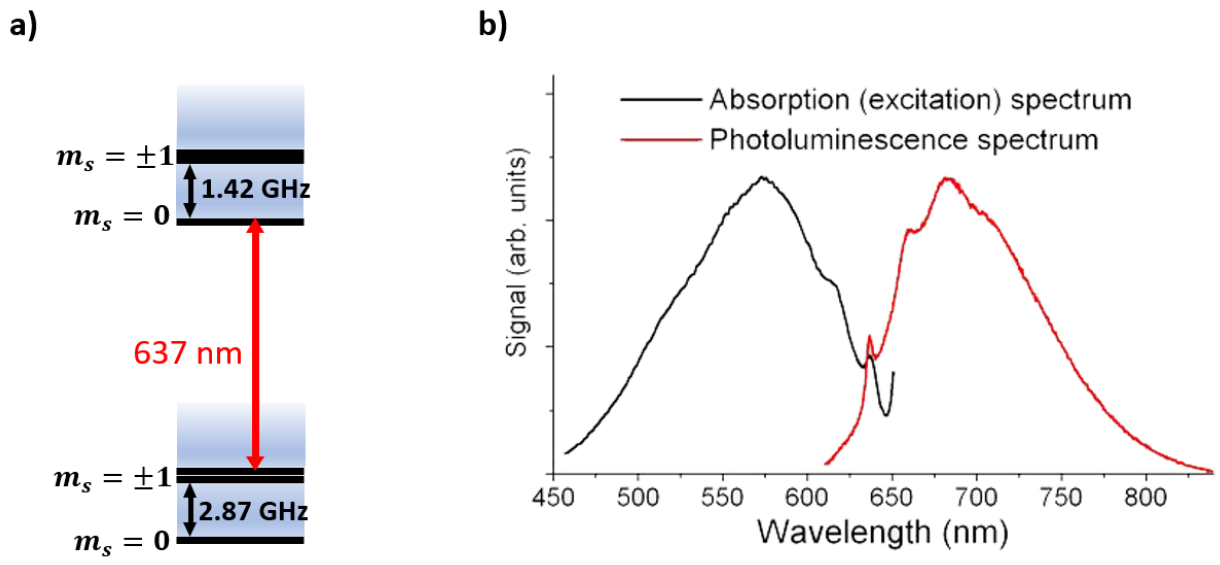

Figure 1.4: a) the NV states are all smeared towards higher energies by phonon excitations of the diamond lattice. This is represented as the gradient shading. b) NV absorption and emission spectra [29]. The central spike is the ZPL.

1.2.6 Phonon Sidebands

The aforementioned values are true of the NV in the absence of any perturbations. The picture of the NV described so far is no different from that of an atom, which suggests that one could use the electronic dipole transition to perform qubit operations. However, the NV lives in a solid-state system that introduces many environmental influences, completely destroying this possibility and adding many complicating factors. The most prominent of these is finite temperature, which adds vibrational excitations in the diamond (phonons) that smear the energy of each electronic state upwards (Fig. 1.4a). In this section, I will cover only the general idea of how vibrational excitations influence the NV. For a more complete understanding, look into the Franck-Condon principle (Wikipedia has a nice diagram showing how the vibrational wavefunction overlap matters).

Because the average thermal energy of a phonon is $\sim 10^{-4}$ eV/K, the smearing completely obfuscates observing the spin resonances optically until the temperature reaches $\lessapprox$10K. The 'Zero-phonon line' (ZPL) specifically refers to the ideal case without any phonons present, whereas the 'phonon sideband' refers to the continuous band of vibronic states (phonon-occupation number states) that smears out the electronic resonance. When a vibronic state is excited, it will on average gain or lose phonons depending on whether it sits below or above the average of the thermal Boltzmann distribution of phonons. This is akin to the everyday intuition that the temperature of an object on average warms up or cools down until it equili-

brates to the temperature of its surrounding. At the usual experimental temperatures, there are more optically accessible states above the average, so it's more common to lose phonons than gain phonons. Consequently, absorption spectra display a sideband with wavelengths mostly below the ZPL, while emission spectra display a sideband with wavelengths mostly above the ZPL (Fig. 1.4b). Note that phonon dispersion turns the coherent electronic transition into an incoherent process, negating the possibility of using it as a cycling transition. This fluorescence process leads to emitting a longer wavelength than what was absorbed. Typically NV fluorescence is spread between 650 nm and 800 nm, with the ZPL accounting for only a few percent of the total photon emission, even at low temperatures.

1.2.7 Polarization/Read-Out Models

Because the phonon sideband smears them out, the spin states are not initially addressable with microwaves. This is annoying since most of the utility of the NV stems from making a qubit out of these states that is highly sensitive to its surroundings. Thankfully, the NV can be easily polarized and read-out even at room-temperature by applying optical radiation, which then permits the states to be addressed with microwaves. The mechanism of initializing the NV population into the $m_s = 0$ state can be described quite accurately by classical rate models; however, a lack of understanding of the ground state spin singlet precludes complete knowledge [150, 128].

In general, the process of polarization is as follows. Assuming a thermally mixed ground state spin triplet, optical light[1] excites the electronic dipole transition, transferring all populations from the ground state (gs) into the excited state (es) spin triplet. Since the operator of the transition is that of an electric dipole, magnetic spin is preserved,[2] that is

$$\begin{aligned} |0_{gs}\rangle &\rightarrow |0_{es}\rangle \\ |-1_{gs}\rangle &\rightarrow |-1_{es}\rangle \\ |+1_{gs}\rangle &\rightarrow |+1_{es}\rangle \end{aligned}$$

Once excited, the lifetime of the excited state is ∼10 ns,[3] after which the NV decays through one of two decay pathways. Either it can decay 1) back through the same spin-preserving dipole transition while emitting an optical photon in the range ∼600-800 nm; or 2) by an effectively non-radiative secondary pathway through the ground state spin singlet (electronic triplet) (Fig. 1.5). The singlet pathway is known

- to happen more than 3x as often for $|\pm 1_{es}\rangle$ than for $|0_{es}\rangle$ [128],

[1] Normally 532 nm is applied at room temperature because it is a cheap wavelength to buy, addresses a large portion of the phonon sideband, and is speculated to pump more charge out of nearby defects to ensure the NV's charge state is negative. At lower temperatures, the optimal wavelength approaches the ZPL.

[2] ...more than 98% of the time [128]

[3] The exact lifetime depends on a few factors: which excited triplet state, whether it is bulk or nanodiamond, the temperature, and the excitation wavelength [128]. It also varies from NV to NV, all other factors being equal.

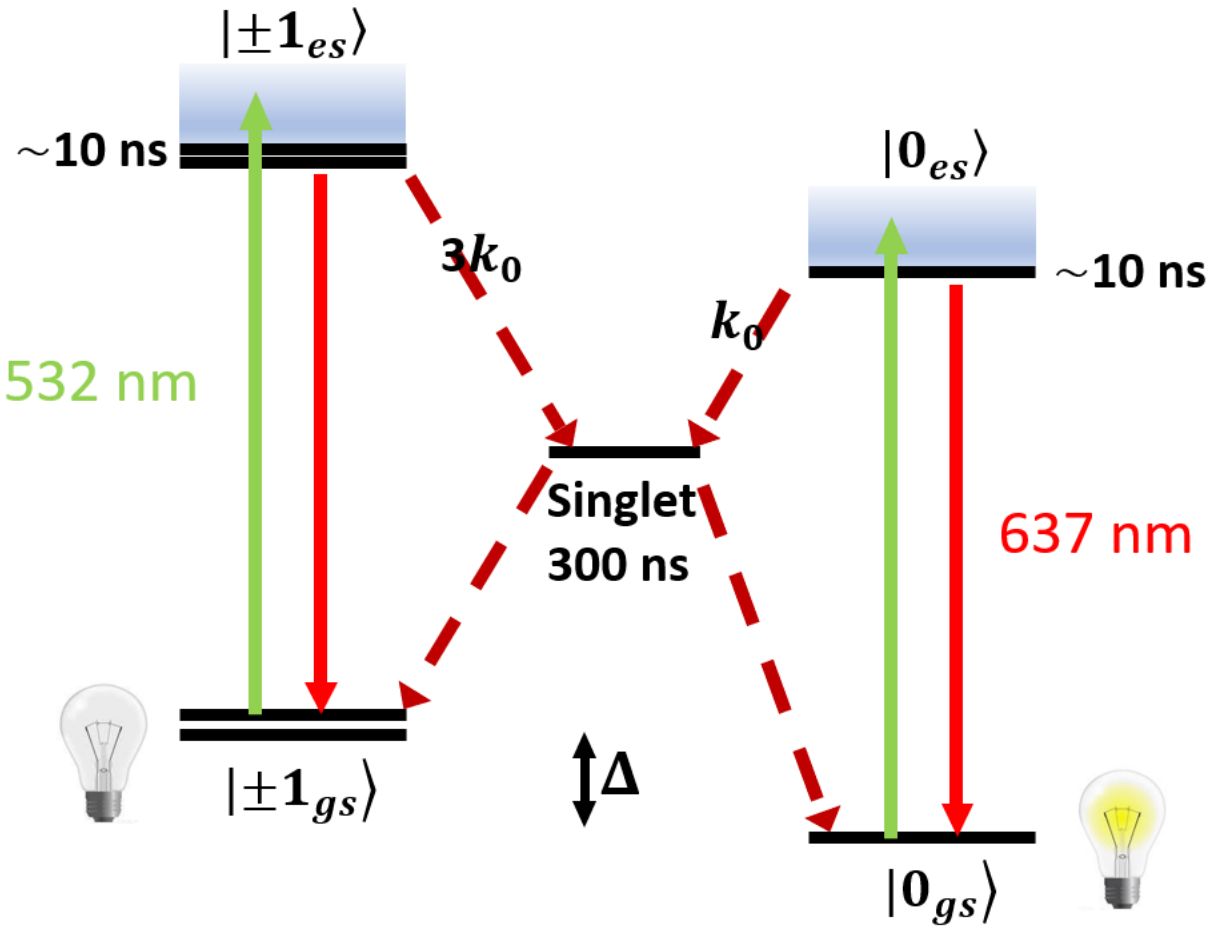

Figure 1.5: Schematic of NV polarization and read-out. $m_2 = \pm 1$ states are drawn on the left $m_s = 0$ states are drawn on the right and the spin singlet states are represented with a single line in the middle. All ground states are excited via 532 nm light through a spin-conserving electric dipole transition to the phonon sideband. After the phonons scatter, they most often decay after ~10 ns by the same electronic transition emitting in the range 600-800 nm. The excited $m_s = 0$ state decays via a non-radiative process at a rate k_0 to the singlet states. The excited $m_s = \pm 1$ states decay to the singlet states at 3 times this rate. The singlet states have a total lifetime ~300 ns before decaying non-radiatively to any ground state. As a results, the ground $m_s = \pm 1$ states are darker than the ground $m_s = 0$ state.

- to decay randomly into *any* spin triplet ground state at roughly the same rate [150],
- to have a lifetime $\sim$ 300 ns [128] (30x longer than the excited triplet lifetime), and
- to emit a 1040 nm infrared (IR) photon while decaying between the electronic triplet states [129],

although notably there is not yet consensus on the matrix elements of this decay. The first two items are primarily what pump population from the ground $m_s = \pm 1$ states to the ground $m_s = 0$ state. Often, polarization between 80-90% of the NV population in $m_s = 0$ at room-temperature are achieved after a few hundred nanoseconds [128], depending on the laser power and wavelength. To complete the polarization procedure, after the laser is turned off, experiments should wait for this metastable spin singlet state to decay back to the ground spin triplet manifold—usually about $\sim 1\mu$s.

The second two items in the above list permit the NV spin state to be read out. The measured fluorescence rate of the NV decreases if it starts in the $m_s = \pm 1$ states, decaying through the spin singlet state more often. Consequently, until the read-out light re-polarizes the NV, it will appear dimmer the larger the $m_s = \pm 1$ components in its spin state.

At this point, take a moment to appreciate how incredibly versatile the NV is to be housed in a durable, inert, readily-and-cheaply-fabricated solid[4], while also being polarizable/readable at room-temperature with coherence times $\sim$100 μs to 1 ms simply by applying a cheap laser. Compare this to other efforts for making qubits, requiring complex vacuum systems, many wavelengths of lasers, dilution fridges, and complex fabrication patterning.

1.3 Representation Theoretic Derivation of NV Properties

Representation theory (RT) came to me too late. I have read and re-read every text on the RT of the NV I could find, but did not feel satisfied with my understanding until I started pestering every theorist I knew with questions on the topic. There are numerous issues I take with the other texts out there, the most important being that they fail to introduce the basic concepts of RT clearly. The abstract nature of RT deters experimentalists a few years distanced from higher mathematics. This is a shame because understanding the RT of the NV provides a wealth of useful intuition best employed early on in one's study of the NV. In fact, the learning curve isn't actually so steep for one merely seeking some deeper understanding of the NV. It just needs to be introduced fully, which is what I attempt in this section.

Starting with the NV's *electronic spatial* symmetries, RT rigorously and elegantly defines the NV's intrinsic *magnetic spin* z-axis and zero-field splitting—reread that and try to reflect

[4]For at home experimenting, you can buy diamond powder for a few cents a gram or nanodiamonds with for a few bucks a gram. You'll find tons of NVs in each.

on how incredible that is. But RT does more. It reveals why the bare ground state spin Hamiltonian is $D_{gs}S_z^2$, what polarization of optical light excites the NV, what electronic energy levels exist and how they reduce to the triplet ground state manifold, and much more. The intuition we gain can immediately be used in back-of-the-envelope estimations or in qualitative predictions of the NV's response to any stimuli.

The following sections assume familiarity with quantum mechanics, linear algebra, and the group axioms (closure, associativity, identity and invertibility), and walk through the fundamental RT derivation of many NV facts from the previous section. Unlike in other representation theoretic derivations of the NV, this section does not assume any knowledge of RT. It starts with the general scheme a representation approach takes to analyzing the NV, which is also the general approach for *any* quantum systems. This section clearly defines what a representation itself actually is as well as the common vocabulary used when discussing it, since these often are points of confusion. Only then does the section derive the NV's properties. If you wish to see the full NV Hamiltonian without going through the derivation, skip to Section 1.3.4. However, I highly recommend reading this section thoroughly at some point.

1.3.1 Intuitive Representation Theory for NVs

Representation theory is essentially a way to study abstract algebraic objects by representing them with matrices and employing the techniques of linear algebra. Quantum mechanics is often performed with representation theory,[5] even if no one tells you; so to ensure you don't go as long as I did without realizing RT's influence, this section walks through the general scheme of deriving the NV properties using RT. By keeping the discussion general, the section introduces the essential concepts of RT that are relevant to the derivation in the following section.

In the case of the NV, RT is effective for enforcing the NV's spatial symmetries and discovering the phenomena derived from them. The approach is as follows. First, the group of NV symmetry operators are rewritten as a group of simplified matrices. In general, this basis of simplified matrices is not the diagonal basis of the Hamiltonian. The matrices are then block-diagonalized, one block for each possible way the NV symmetry operators can transform state vectors. For the NV, after block-diagonalization there are 6 matrices each with 3 blocks representing the 18 possible ways a single-electron orbital could transform under the NV symmetry operators.[6] These transformations constrain all Hamiltonian terms to components that transform according to 18 possibilities. This includes the electrons' Coulomb interaction with the atomic nuclei. We then note that perturbations, by virtue of being small, should not change the way orbitals transform under the symmetry operators.

[5] Any time a matrix is used to perform operations on states, e.g. Bloch sphere operations on a qubit.

[6] The block diagonalization and derivation of representations has been done over many decades by mathematicians. Once a symmetry group is identified, anyone can look up what the representation is, so I will not go over the diagonalization process.

This permits us to add all relevant spin-perturbations to the NV to simplify the derivation of the spin Hamiltonian as well as the general effects of extra perturbations.

Before diving into the derivation, we must note that the literature on representation theory uses somewhat poor language. By definition, a representation is a group homomorphism—a transformation or mapping between groups that preserves algebraic structure. It is not the image (final group) to which the initial group is transformed. However, in both math and physics, the image is commonly called the representation when the homomorphism is clear from context. Often, the phrases "elements of the representation" or "lives in the representation" refer to the elements of the image matrices or of the vector spaces upon which the homomorphism acts. Since the representation is not a group but the mapping between groups, these phrases are absolutely incorrect; however, the meaning is clear once one accepts the conflation and broadens their personal definition of 'representation' to encompass all above-mentioned usages. In this section, I will largely conform to the vernacular, and occasionally offer mathematical precision.

The RT derivation of the NV properties starts with the tight-binding picture of a vacancy in diamond, wherein electrons are bound into pure atomic orbitals of the atoms in the diamond. The vacancy creates broken bonds. The N and three C atoms lack immediate neighbors to form a covalent bond for each of their valance electrons. Each atom's unpaired single-electron orbital (sp3 for both C and N) is called a 'dangling bond,' written as σ_1, σ_2, σ_3, for the carbon and as σ_N for the nitrogen. In general, these dangling bonds are not the single-electron orbitals of the defect, but form a complete basis for them in the tight-binding picture.

Given the symmetry of the diamond lattice, the group of NV spatial symmetries is the C_{3V} point group.[7] With some thought, we can use our knowledge of lattice sites and indistinguishability to determine why the NV symmetries form a point group and find the elements of the point group. Most atoms can only stably inhabit the sites of the diamond lattice. A nitrogen, vacancy, or carbon atom out of place will be restored by strong Coulomb forces into a lattice site, while a silicon atom notably could float between two lattice sites (when forming a Silicon-Vacancy center). For the NV then, symmetry operations must transform atoms from lattice sites into lattice sites; consequently, they are discrete spatial transformations. Next, because quantum particles are indistinguishable, we cannot notice when carbons swap locations, but we can notice a transformation that swaps the locations of distinguishable particles (e.g. the nitrogen, vacancy, and carbon); such a transformation cannot be a symmetry of the NV. Since the N and V can't swap with any other particles, they must remain in their original lattice sites They are fixed points imposed on any operation claiming to be a symmetry of the NV. We can intuit then that all points along a line formed by the N and V are fixed points: the fixed points of the NV point group are the entire NV z-axis (connecting the nitrogen and vacancy). The only six symmetry transformations that

[7] A point group is a group of symmetry operations that all leave at least one point in space fixed. For example, a group of rotation operations that share the same rotation axis do not change any points along their shared axis, so their group is called a point group.

meet the lattice-site and fixed-point criteria in a diamond lattice are the identity, rotations around the z-axis by 120° or by 240°, and reflections through any one of the three vertical planes that each contain the nitrogen and one of the three carbons (Fig. 1.2.

This point group is the absolute symmetry of the bare NV. The way this point group acts upon each dangling bond can be represented using 4x4 matrices in the basis of the 4 dangling bonds (with the mapping from point group operators to matrices being the true representation). Much in the same way linearly-dependent matrices can be reduced to linearly-independent matrices, representations from a basis that fails to diagonalize the Hamiltonian can be decomposed into "irreducible representations," a process which simultaneously block-diagonalizes the unperturbed NV Hamiltonian H_0. Each block is the image from an irreducible representation, but will be referred to as irreducible representations themselves since the homomorphism is clear. The new 4x4 matrices representing the symmetry operators in the irreducible representations are block-diagonalized in the same way as the Hamiltonian. This is directly because the symmetry operators $\{P_R\}$ leave the energy of a state unchanged by definition:

$$\langle\psi|P_R^{-1}H_0P_R|\psi\rangle = \langle\psi|H_0|\psi\rangle \tag{1.1}$$

and consequently satisfy $[H_0, P_R] = 0$.

Group theoreticians have already performed the dirty work of solving for the irreducible representations of the C_{3v} point group and performing the block diagonalizations, so we just have to look up their results. There are three irreducible representations (blocks): A_1, A_2, and E.[8] The first two irreducible representations are each 1x1 blocks, and the E representation is a 2x2 block. Since the new matrices are block diagonalized, we see that neither the point group nor the Hamiltonian can mix basis states living in different irreducible representations—they are closed subspaces under the action of the point group.[9] We can then label the elements of vectors and blocks of matrices by the irreducible representations they live in using superscripts:

$$|\psi\rangle = \begin{pmatrix} \psi^{(A_1)} \\ \psi^{(A_2)} \\ \psi^{(E_x)} \\ \psi^{(E_y)} \end{pmatrix}, P_R = \begin{pmatrix} P_R^{(A_1)} & & & \\ & P_R^{(A_2)} & & \\ & & P_R^{(E)} & \end{pmatrix}, H_0 = \begin{pmatrix} H_0^{(A_1)} & & & \\ & H_0^{(A_2)} & & \\ & & & H_0^{(E)} \end{pmatrix} \tag{1.2}$$

where E_x and E_y are the two degenerate basis states living in the 2x2 E representation. They transform like x and y vectors, but are explicitly *not* x and y vectors.

The specific matrix elements of these blocks for each point group operator are listed in Table 1.1. From the table, we see that states in A_1 have all of the symmetries of the NV, since every operator acts like the identity when applied to such states. States in A_2

[8] In this case, E is not the identity operator. I will use $\mathbb{1}$

[9] However, keep in mind that a basis state in an irreducible representation generally transforms into a new state within the same irreducible representation under these operations. No single vector in an irreducible representation has C_{3v} symmetry—the entire irreducible representation does.

	$P_{\mathbb{1}}$	P_{C_3}	$P_{C_3'}$	$P_{\sigma_v^1}$	$P_{\sigma_v^2}$	$P_{\sigma_v^3}$
A_1	1	1	1	1	1	1
A_2	1	1	1	-1	-1	-1
E	$\begin{pmatrix} 1 & 0 \\ 0 & 1 \end{pmatrix}$	$\begin{pmatrix} -\frac{1}{2} & \frac{\sqrt{3}}{2} \\ -\frac{\sqrt{3}}{2} & -\frac{1}{2} \end{pmatrix}$	$\begin{pmatrix} -\frac{1}{2} & -\frac{\sqrt{3}}{2} \\ \frac{\sqrt{3}}{2} & -\frac{1}{2} \end{pmatrix}$	$\begin{pmatrix} -1 & 0 \\ 0 & 1 \end{pmatrix}$	$\begin{pmatrix} \frac{1}{2} & -\frac{\sqrt{3}}{2} \\ -\frac{\sqrt{3}}{2} & -\frac{1}{2} \end{pmatrix}$	$\begin{pmatrix} \frac{1}{2} & \frac{\sqrt{3}}{2} \\ \frac{\sqrt{3}}{2} & -\frac{1}{2} \end{pmatrix}$

Table 1.1: Matrix elements of the C_{3v} group operators for each irreducible representation. The operators are $P_{\mathbb{1}}$ for identity, P_{C_3} for rotation by $2\pi/3$, $P_{C_3'}$ for rotation by $-2\pi/3$, $P_{\sigma_v^{1,2,3}}$ for reflection through the plane formed by the z-axis and either the first, second, or third carbon.

transform as pseudo-vectors along the z-axis; unchanged by the identity or rotations, but flipped when reflected through the z-$\sigma_v^{1,2,3}$ plane. Already, we can guess that there will not be A_2 components in the bare NV electronic Hamiltonian, since electronic states transform as vectors, not pseudo-vectors. The NV spin Hamiltonian likewise lacks A_2 components, since it originates from a dipole-dipole interaction, which will be discussed later. Finally, we see that the blocks in the E representation are the appropriate 2-dimensional rotation and reflection matrices, one would expect. States in the E representation transform like vectors in the NV's x-y plane.

By multiplying together vector- or operator-elements living in different representations and decomposing their product, we find that there are patterns in the results. Each possible product can be reduced to components that live in a subset of the irreducible representations. The general scheme for products of vector- or operator-elements living in different representations is summarized in Table 1.2. These combinations hold regardless of the specific basis or vector space and also works for a product between an operator and a vector. For example, the state produced by the A_1 component of an operator and the A_2 component of a vector must belong to the $A_1 \otimes A_2 = A_2$ representation.

This table's true predictive power for quantum mechanics stems from an important formulation of the Wigner-Eckhart theorem: since scalars belong to the A_1 representation, and the product of two vectors is a scalar, $\left\langle \psi^{(\Gamma_1)} \right| O^{(\Gamma_2)} \left| \psi^{(\Gamma_3)} \right\rangle$ is non-vanishing only if A_1 is contained in the product $\Gamma_1 \otimes \Gamma_2 \otimes \Gamma_3$, for Γ_i denoting the irreducible representation of each factor. This formulation drastically simplifies derivations and provides useful intuition. For example, we will see later that the Wigner-Eckhart theorem illuminates that the laser polarization must have a linear component in the NV's x-y plane to induce an electronic transition (given the irreducible representations of the ground and excited electronic states).

1.3.2 Derivation of Energy Levels and Ground State

Now that the tools of representation theory have been established, we can derive properties of the NV. We find the linear combinations of dangling bonds $\{\sigma_N, \sigma_1, \sigma_2, \sigma_3\}$ that form the

$\otimes$	A_1	A_2	E
A_1	A_1	A_2	E
A_2	A_2	A_1	E
E	E	E	$A_1 + A_2 + E$

Table 1.2: Direct Product Table. The product between elements of two representations produces a new vector or linear combination of vectors belonging to the representations listed.

single electron orbitals by projecting the bonds on to each irreducible representation [107]

$$\begin{aligned} a_N &= \sigma_N \\ a_C &= \frac{1}{\sqrt{3}}(\sigma_1 + \sigma_2 + \sigma_3) \\ e_x &= \frac{1}{\sqrt{6}}(2\sigma_1 - \sigma_2 - \sigma_3) \\ e_y &= \frac{1}{\sqrt{2}}(\sigma_2 - \sigma_3) \end{aligned}$$

The a_N and a_C orbitals are totally symmetric in C_{3v} and so belong to the A_1 irreducible representation, whereas e_x and e_y are the two basis vectors of the E representation. Since they share the same symmetries, a_N and a_C are degenerate in energy, and likewise for e_x and e_y. Also, notice that there is no single electron wavefunction belonging to the A_2 representation as predicted above.

To find the relative energies of these wavefunction, Maze et. al. introduce the electron-ion interaction between electrons and the nitrogen and carbon ions forming the NV

$$V = v_n \left|\sigma_N\right\rangle\left\langle\sigma_N\right| + \sum_i v_i \left|\sigma_i\right\rangle\left\langle\sigma_i\right| + h_n \left|\sigma_i\right\rangle\left\langle\sigma_N\right| + \sum_{i>j} h_c \left|\sigma_i\right\rangle\left\langle\sigma_j\right| \tag{1.3}$$

where $v_i = v_c < 0$ and $v_n < 0$ are the Coulomb self-energies at the carbon and nitrogen sites and h represent interaction strengths between sites. With a new Hamiltonian term added to the tight-binding model, the previous representations are no longer the irreducible representations. Using the Wigner-Eckhart theorem to impose symmetry constraints, we find that this interaction leads to a new basis that is the same up to mixing of the a_N and a_C orbitals

$$a_1 = \alpha a_N + \beta a_C \tag{1.4}$$

$$a_1' = \beta a_N + \alpha a_C \tag{1.5}$$

$$e_x = \frac{1}{\sqrt{6}}(2\sigma_1 - \sigma_2 - \sigma_3) \tag{1.6}$$

$$e_y = \frac{1}{\sqrt{2}}(\sigma_2 - \sigma_3) \tag{1.7}$$

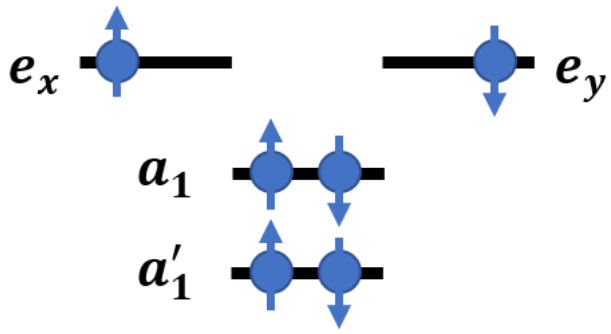

Figure 1.6: NV electronic orbital energy levels with Coulomb potential. For 6 electrons, the lowest two orbital are filled by 2 electrons each (one spin-up and one spin-down). The upper two degenerate levels each contain 1 electron by Hund's rules. The spins of those electrons are form a triplet configuration in the ground state.

for α and β being complex coefficients $\alpha^2 = 1 - \beta^2 = 3h_n^2/\Delta E_{a_1}$, and with energies

$$E_{a_1} = \frac{1}{2}(v_c + 2h_c + v_n) + \frac{1}{2}\Delta \tag{1.8}$$

$$E_{a_1'} = \frac{1}{2}(v_c + 2h_c + v_n) - \frac{1}{2}\Delta \tag{1.9}$$

$$E_{e_x} = v_c - h_c \tag{1.10}$$

$$E_{e_y} = v_c - h_c \tag{1.11}$$

for $\Delta = \sqrt{(v_c + 2h_c - v_n)^2 + 12h_n^2}$ [107]. As usual, mixing states is accompanied by a splitting of their energies. Qualitatively, this procedure finds the correct ordering of the energy levels. The more symmetric the state, the lower its energy in attractive potentials. While the *ab initio* density functional calculations provide more precise numbers [56][53], the RT approach provides exceptionally clear insight for qualitative features by framing them in terms of symmetry constraints.

Although the orbitals are determined, the dynamics of the NV depend on how they are filled. For the negatively-charged NV in our experiments, there are six electrons. Checking atomic numbers on the periodic table, we see that carbon each contributes one electron and nitrogen (as a donor in diamond) contributes two. The origin of the last electron is still unknown, though the work in this thesis contributes to cracking the mystery—it is likely contributed by a proximal ionized nitrogen defect. With six electrons, the two lowest-energy highest-symmetry states a_1 and a_1' are filled completely, and by Hund's rule, the e_x and e_y states will host one electron each.

The electronic dynamics of the NV can be described by either the full six-electron wavefunction, or equivalently by the dynamics of two holes in an otherwise full atomic shell (with some interactions of the opposite polarity). For the sake of simplicity, this thesis will adopt

the hole picture. In either case, we see that the ground state spin Hamiltonian is dominated by the interaction between two spin-$\frac{1}{2}$ particles, which is why it is S_z^2 instead of just S_z. One can also see that in either picture the first electronic excited state of the NV must move an electron from the a_1' state to either the e_x or e_y state. Since there are two choices for where to promote the electron, the excited state is doubly degenerate at this order.

The representation Γ_Ψ of the full wavefunction Ψ, which includes all electrons and their spin, is given by the direct product of the representation of each component $\Gamma_\Psi = \Pi_n(\Gamma_n \otimes \Gamma_{\frac{1}{2}})$, where Γ_n is the representation of each electron and $\Gamma_{\frac{1}{2}}$ is the representation for a spin-$\frac{1}{2}$ particle in C_{3v}. This representation is the representation for the Hamiltonian containing the crystal field potential and any other interactions that are invariant under the elements of the C_{3v} point group; for example, spin-orbit, spin-spin, Coulomb, and any crystal deformations that preserve the NV symmetry axis. Like before, reducing the representation block-diagonalizes the Hamiltonian and determines the new eigenstates.

The full set of eigenstates is calculated in Maze et. al., so we will discuss only the key intuitive results here.

- Not surprisingly, all states are the product of an electronic component and a spin component. Since they represent two fermions, the spin component must be a singlet or triplet state. An electronic (fermionic) wavefunction must be antisymmetric, so the total wavefunction must be a product of the antisymmetric spatial state and the spin triplet state or the symmetric spatial state and the spin singlet state.

- Because the electron-electron Coulomb interaction is repulsive and a much larger energy scale than the spin-spin interaction, the lowest energy state must minimize the energy of the electronic component of the wavefunction by separating the electrons as much as possible. The antisymmetric electron configuration accomplishes this, which is why the ground state spin Hamiltonian is triplet

- The ground state is (up to normalization):

$$|\psi_{GS}\rangle = |e_x e_y - e_y e_x\rangle \otimes \begin{cases} |\uparrow\uparrow\rangle \\ |\uparrow\downarrow + \downarrow\uparrow\rangle \\ |\downarrow\downarrow\rangle \end{cases} \tag{1.12}$$

  It belongs to the A_2 representation, which determines what operators vanish when acting on the state (by Wigner-Eckhart).

- The excited state spin triplets belong to the E representation. Using the direct product table (Table 1.2), we see that the only operators that do not vanish when sandwiched between the ground and excited states contain components belonging to the E representation. This means that the electric dipole transition between ground and excited states must belong to the E representations. Electric dipoles in the E representation are polarization components within the transverse plane.

- The ground state triplet electron configuration is significantly higher energy, so the ground state spin singlet is shown as fractions of eV above the spin triplet states in our NV energy level diagrams. A very common question asked when students first see the NV level diagram is why the ground state spin singlet manifold has three states. Here, we plainly see that it is because the spin singlet manifold contains the electronic triplet states. Incidentally, we expect much larger splitting in the spin singlet manifold compared to the spin triplet manifold because the splitting is electronic in origin for the spin singlet manifold.

- Notice too that the same combination of singlets and triplets exists in the electronic excited state. The key difference is that because of the ambiguity of promoting to e_x or e_y, the excited state spin triplet manifold contains six states and the spin singlet manifold contains two.

- Finally, since the a_1' orbital has much greater overlap with the nitrogen nucleus than the e_x or e_y orbitals, its hyperfine interaction has a significant contact term.[10] Consequently, the electronic excited state has a much stronger hyperfine effect, than the ground state.

1.3.3 Derivation of Ground State Spin Hamiltonian and Zero-Field Splitting

To see how the ground state spin triplet is split by $D_{gs} = 2.87$ GHz, we can look at how RT simplifies the spin Hamiltonian. Since there are two particles of interest, the Hamiltonian is the spin-spin dipole interaction. We can write it in a coupled spin basis

$$H_{ss} = \frac{-\mu_0}{4\pi}\frac{(g\mu_B)^2}{r^3}[3(S\cdot\hat{r})(S\cdot\hat{r}) - S^2] \tag{1.13}$$

where $S = s^{(1)} + s^{(2)}$ is the spin-1 operator acting on the coupled state, composed of the spin-$\frac{1}{2}$ operators $S^{(i)}$. This can be decomposed into parts that act separately on the orbital and spin components of the wavefunction

$$H_{ss} \sim D_{ij}S_iS_j \tag{1.14}$$

where $D_{ij} = \langle\frac{3\hat{r}_i\hat{r}_j-\delta_{ij}}{r^3}\rangle$ is a scalar tensor obtained from the orbital integrals (represented by $\langle\,\rangle$) of the portion of the operator $\hat{D} = \frac{3\hat{r}_i\hat{r}_j-\delta_{ij}}{r^3}$ that acts on the orbital part of the wavefunction. Under Einstein notation, the indices of these operators iterate over the x, y, z basis (i.e. $\{\hat{x}, \hat{y}, \hat{z}\}$, and $\{S_x, S_y, S_z\}$).

In general, D_{ij} is a 3x3 tensor with 9 elements, but it is drastically simplified to 1 element in the following way.[11] By the Wigner-Eckhart theorem, the scalar result of an

[10] Note, that ^{12}C has no nuclear spin, so it is neglected in the NV hyperfine effect.

[11] We could start by recognizing exchange symmetry. Then the tensor must be symmetric, reducing the number of possible unique elements to 6. However, this is an unnecessary step at this order, since the Wigner-Eckhart theorem ensures only the diagonal elements contribute to the bare ground state Hamiltonian.

orbital expectation value must belong to the A_1 representation, $\Gamma_{GS} \otimes \Gamma_{GS} \otimes \Gamma_D \in A_1$, with Γ_i defined as in the previous section as the irreducible representation of the factor in the product. Since the ground state orbitals belong to A_2, and $A_2 \otimes A_2 = A_1$ according to Table 1.2, the only components of $\hat{D}$ that do not vanish after integrating over the orbitals are the components belonging to A_1. To find these components, we consider carefully the components of $\hat{D}$. The $\hat{r}$ operators can be decomposed into $\hat{x}$, $\hat{y}$, and $\hat{z}$ components, so $\hat{r}_i\hat{r}_j$ is decomposed into linear combinations of quadratic products of these operators (e.g. $\hat{x}\hat{y} + \hat{y}\hat{x}$) . Of the possible linear combinations, only $\hat{z}^2$ and $\hat{x}^2 + \hat{y}^2$ belong to the A_1 representation of the C_{3v} point group. Coincidentally, the δ-function portion of the operator is a non-zero scalar that contributes only to these components of $\hat{D}$. This reduces the tensor to only three non-zero elements. Of these three, only two are unique. To see this clearly, consider

$$
\begin{aligned}
D_{zz} &= \langle \hat{D}_{zz} \rangle \\
D_{xx} &= \langle \hat{D}_{xx} \rangle = \left\langle \frac{1}{2}\left(\hat{D}_{xx} + \hat{D}_{yy}\right) + \frac{1}{2}\left(\hat{D}_{xx} - \hat{D}_{yy}\right) \right\rangle = \left\langle \frac{1}{2}\left(\hat{D}_{xx} + \hat{D}_{yy}\right) \right\rangle \\
D_{yy} &= \langle D_{yy} \rangle = \left\langle \frac{1}{2}\left(\hat{D}_{xx} + \hat{D}_{yy}\right) - \frac{1}{2}\left(\hat{D}_{xx} - \hat{D}_{yy}\right) \right\rangle = \left\langle \frac{1}{2}\left(\hat{D}_{xx} + \hat{D}_{yy}\right) \right\rangle
\end{aligned}
$$

where $\left\langle \frac{1}{2}\left(\hat{D}_{xx} - \hat{D}_{yy}\right) \right\rangle = 0$ because it does not belong to A_1. Consequently, there are only two unique non-zero elements, D_{zz} and $D_{xx} = D_{yy}$. We can now write the Hamiltonian as

$$H_{ss} = D_{zz}S_z^2 + D_{xx}(S_x^2 + S_y^2)$$

However, this can be simplified further by considering the basic relation of the spin operator $S_x^2 + S_y^2 = S^2 - S_z^2$. When we make this substitution, we can safely ignore S^2 since it simply contributes a constant energy shift. We finally end up with

$$H_{ss} = D_{gs}S_z^2 \tag{1.15}$$

where $D_{gs} = D_{zz} - D_{xx}$ is the zero-field splitting.

Through this derivation, the origin of D_{gs} is clear: it is the dipole-dipole interaction from the two holes (equivalently, valence electrons), as constrained by C_{3v} symmetry (enforced specifically through the form of the electronic ground state wavefunction and the Wigner-Eckhart theorem). One can see how C_{3v} constrains the electron spins to the z direction by imagining that in the XY plane, the spins are free to rotate, averaging themselves out for lack of a quantization axis in that plane. As well, we can see that regardless of whether both spins have $S_z = +1$ or both have $S_z = -1$, the NV state should have the same energy. Up and down spins are arbitrarily defined in C_{3v} systems since there is no magnetic field or electronic structure to define higher and lower energy along the z-axis. For this reason, it is actually fairly difficult to determine if an NV's carbon bonds point towards or away from an applied magnetic field aligned to the NV axis.

Experimentally, D_{gs} has been measured as 2.87 GHz, but it can be estimated either precisely with density functional methods or roughly with a simple back-of-the-envelope

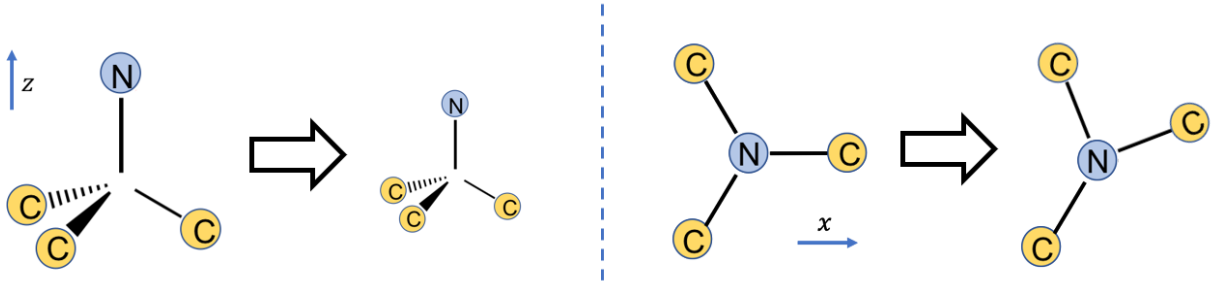

Figure 1.7: Examples of strain perturbations that conserve (left) or break (right) the C_{3v} point group symmetry. Left: the NV was compressed evenly in all directions, effectively shrinking it. Right: One of the nitrogen-carbon bonds was twisted out of place.

calculation using the natural constants in the dipolar interaction and a reasonable guess for the separation of electrons in the NV (the lattice constant).

1.3.4 Perturbations

By the Wigner-Eckhart theorem, perturbations to the NV's spin dipole-dipole Hamiltonian must comply with C_{3v} symmetry. The process of writing down the final form of each perturbation follows a process analogous to what was covered in the previous section. By the indistinguishability of electrons, they also must have exchange symmetry of the two dipoles. While exchange symmetry is absolute, C_{3v} symmetry is only conserved as an approximation. In reality, each perturbation either conserves or breaks the point group symmetry (Fig. 1.7). Regardless, since the NV's geometric symmetry is enforced by the Coulomb interaction, which is much stronger than any other in the system, it is safe to assume the perturbative Hamiltonian terms comply with C_{3v} in practice.

All of the NV ground state spin Hamiltonian terms relevant to this thesis are constrained by these conditions to form the Hamiltonian

$$\begin{aligned} H =& D_{gs}S_z^2 + \gamma_{NV}\vec{B}\cdot\vec{S} + H_{ss'} + \vec{S}\mathrm{A}\vec{I} + P\left(I_z^2 - \frac{1}{3}I^2\right) \\ & \left(\Pi_z + \Delta D(T)\right)S_z^2 + \Pi_x(S_y^2 - S_x^2) + \Pi_y(S_xS_y + S_yS_x) \end{aligned} \tag{1.16}$$

where the first line contains all fundamentally-magnetic interactions, and the second contains all fundamentally-electric interactions. The zero-field splitting $D_{gs}S_z^2$, has already been derived and discussed above. The other terms are derived through an analogous process that will not be covered in this thesis. We will discuss each remaining perturbation in turn.

The second term $\gamma_{NV}\vec{B}\cdot\vec{S}$ expresses the influence of any magnetic field $\vec{B}$ whose source is external to the NV. This can include a magnet placed in the viscinity of the diamond, or a field generated by the environment of paramagnetic impurities in the diamond. The

pre-factor $\gamma_{NV} = g_e\mu_B/h = 2\pi * 2.8$ MHz/G is simply the gyromagnetic ratio for an electron, where g_e is the Landé g-factor for an electron, μ_B is the Bohr magneton, and h is the planck constant. Since perturbative couplings to S_z preserve the goodness of the bare magnetic quantum numbers (m), they are not suppressed by the large ZFS. As a result, γ_{NV} directly sets the Zeeman splitting of both the NV and P1 spin states with axial magnetic fields B_z, as mentioned throughout this thesis. Transverse magnetic fields break the axial magnetic symmetry of the NV, so they do not preserve the m quantum numbers. They mix and split the spin states at first order in perturbation theory, suppressed by D_{gs}, and shift the states at second order.

The third term $H_{ss'}$ is the dipole-dipole interaction with a nearby spin (eq. 1.13. This interaction can be resonant (other NVs or P1s with 510 G applied) or off-resonant and is the main physics underlying the work in Chapter 4. It can break symmetry in the same ways as a generic magnetic field does in the previous paragraph, or it can lead to a coherent transfer of population between the NV and the separate dipole. For electron-electron interactions, all of the pre-factors in this term combine into the handy value 52 MHz/nm^3, which can be used to quickly estimate the NV ZFS (see the end of the previous section) or the effect of temperature discussed below.

The remaining two terms in the first line $\vec{S}\mathrm{A}\vec{I} + P\left(I_z^2 - \frac{1}{3}I^2\right)$ are the hyperfine dipole and quadrupole interactions respectively. A is the hyperfine matrix that encodes both the dipolar and contact interactions with the nucleus, and $\vec{I}$ is the nuclear spin. When the contact term is negligible, the interaction is often written in an expanded form

$$A_\parallel S_z I_z + A_\perp \left(S_x I_x + S_y I_y\right) + P\left(I_z^2 - \frac{1}{3}I^2\right)$$

to emphasize the common distinction between the axial $A_\parallel$ and transverse $A_\perp$ components of the dipolar hyperfine interaction. In general, hyperfine interactions add additional states to the NV's Hilbert space, coming from the tensor product of the NV spin and nuclear spin states. Each NV state is split into the number of nuclear spin states. The two notable hyperfine interactions for an NV are those with its own nitrogen nucleus, and those with nearby ^{13}C nuclei. Since the nitrogen nucleus can be either ^{14}N (spin-1, 99.6% natural abundance) or ^{15}N (spin-1/2, 0.4% natural abundance), there are two sets of values for the hyperfine parameters. For ^{14}N, $A_\parallel = -2.14 \pm 0.07$ MHz, $A_\perp = -2.70 \pm 0.07$ MHz, and the quadrupole factor $P = -5.01 \pm 0.06$ MHz; while for^{15}N, $A_\parallel = 3.03 \pm 0.03$ MHz, $A_\perp = 3.65 \pm 0.03$ MHz, and there is no quadrupole term since its spin is 1/2 [47]. The values of the ^{13}C parameters depend highly on how far away it is from the NV. The additional splitting it induces upon the NV ranges from negligible when it is far away to ~ 1 MHz when it is a few lattice sites away to ~ 100 MHz when it is one of the carbons in the NV's structure, which imparts a significant contact interaction (see [137]).

The second line of this Hamiltonian contains all interactions that are electronic in nature: electric fields, stress, and temperature. Each of these phenomena affect the NV spin by deforming the electron orbital, either directly (electric field) or by deforming the diamond lattice (stress and temperature). The temperature term $\Delta D(T)$ represents thermal expansion

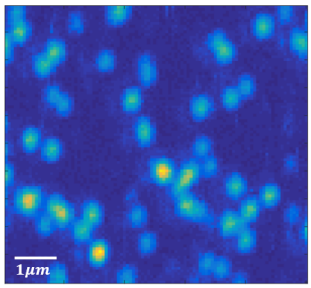

Figure 1.8: Example of a confocal microscope scan. Each pixel in the image represents a spot of the diamond where the laser was focused and photons were counted. In this case, the diamond was full of individual NVs spaced more than 1μm on average.

of the diamond, which preserves the NV's physical symmetry, shifting the energy levels by -14 GHz/K near room-temperature [70]. Since this is the effect of the atoms moving apart, the 52 MHz/nm^3 dipole-dipole interaction can again be used to estimate the effect.

The remaining terms in this line represent the components of stress and electric fields $\Pi_{x,y,z}$ that transform as E_x, E_y, and A_1 (the irreducible representations), respectively. The derivation of these terms is covered in the upcoming publications and theses of Bryce Kobrin and Satcher Hsieh, and so will not be covered here. While the final form of the electric and stress interactions are indistinguishable, there are some key differences. First, as we exploit in Chapter 2, the ratio of the coupling coefficients for the symmetry breaking to symmetry conserving components of strain (i.e x,y to z) is order unity, whereas for the electric field it is about 50. This means a randomly oriented electric field is much more likely to induce splitting of the NV states than shifting, while a random stress is just as likely to split as to shift. The reason for this ratio is covered in the above-mentioned works. Second, since the electric field is a vector, its components that transform as E_x, E_y, and A_1 are actually the x, y, and z components of the electric field. By contrast, stress is not a vector, but a tensor, so interpreting the underlying stress from the splitting and shifting of a single NV spectrum is not straightforward (see Section 3.3.1). An electric field or stress applied at an arbitrary angle breaks the NV's axial symmetry, mixing and splitting the $m_s = \pm 1$ states. It also imparts a phase difference between these new states, which we exploit for our "imbalance" technique in Section 2.4.

1.4 NV Systems

1.4.1 Some Microscopy Methods

In general, there are a number of methods for performing microscopy with NVs, but this thesis will only mention two forms of confocal microscopy. Confocal microscopy is an imaging

technique that increases resolution by focusing the image of the sample through a pinhole before processing the image. Light that does not originate at the image (i.e. not in the image plane) will not be focused through the pinhole and will instead be mostly blocked by it. Confocal microscopy is employed in both scanning and wide-field forms. In scanning microscopy, a diffraction-limited laser spot is rastered across the plane of the diamond (Fig. 1.8), permitting an experimenter to park the laser at a particular spot of interest, and calibrate applied external fields (magnetic, electric, microwave, temperature, strain, etc.) to that specific spatial point. The precision of the calibration enables the application of complicated quantum protocols (e.g. detailed in 1.5), applying sequences of microwave pulses, to measure fast dynamics in the system of interest (diamond environment or external sample). By contrast, wide-field microscopy illuminates the microscope's entire field of view with light, effectively measuring the signal from each pixel in parallel. While this method is in principle much faster at measuring large regions of a diamond than scanning microscopy, the difficulty of applying homogeneous fields to such a large region ($\sim$100x100 μm) prohibits complex quantum protocols. To date, wide-field microscopes are most often used for measuring changes in the NV spectra versus time, pressure, temperature, or other relatively slow environmental effects.

1.4.2 Single vs Ensemble NVs

Optical resolution determines whether one or more NVs are addressed by the applied laser, effectively setting whether the system is measuring in the 'single' or 'ensemble' regime. Barring super-resolution techniques, the resolution is the diffraction limit, for which NVs spaced more than 1 μm apart (<0.01 ppb) on average are individually resolvable (Fig. 1.8).

Single and ensemble measurements have specific advantages and drawbacks. The properties of an isolated single NV can be precisely measured, permitting quantum control with exceptionally low error. In addition, single NVs can be chosen for having innately good properties, such as coherence lifetimes in excess of 1 ms that permit quantum sensing to high precision. Tomography on single NVs can then measure the environment particular to that NV by, for example, localizing all charged/magnetic sources nearby to nanometer precision [98][113]. It is worth noting that such localization uses the NV as the origin, which can only itself be localized to the optical resolution, so the resolution of such localization within the lab frame frame is likely the diffraction limit. Finally, one must take care that when the single NVs are within $\sim$ 10 nm of the surface, prolonged exposure to a laser can cause the NV's excess charge to be trapped by particles bonded to the surface of the diamond. These NVs are permanently 'photobleached' into the undesirable NV^0 charge state. To avoid photobleaching, the laser intensity and the duty-cycle of its application must be reduced. Because of the manifold applications of using shallow NVs, chemically preparing the diamond surface against photobleaching is an active area of research [7, 81, 164].

By contrast, the properties of an NV ensemble are averaged over the ensemble, which reduces both calibration precision and lifetime, so quantum pulse control and sensing cannot be as precise. However, as long as the gradient of local fields (microwave, magnetic, etc.)

are small enough across the diffraction-limited laser spot (i.e. delivering microwave with a stripline instead of a wire), pulse errors $\sim 1\%$ are achievable, permitting the employ of abovementioned quantum measurement protocols. There are in fact a few major advantages ensembles boast over single NVs. First, assuming the signal being sensed by the NVs does not vary considerably over the focused spot of the laser, the sensitivity of the ensemble follows standard quantum limit (SQL) scaling $\sim \sqrt{N}$, for N being the number of NVs in the ensemble. There are currently attempts to entangle the NVs to boost sensitivity beyond SQL scaling by using many-body correlations [158, 135, 80, 19, 25, 13]. Second, NV ensembles with high densities are associated with rich impurity environments, suitable for quantum simulations. Both strongly-interacting ensembles of NVs as well as of P1s have been used for this purpose [141]. Third, because there are so many NVs being addressed simultaneously, all four NV orientation groups are represented at the same time. While this means that there is a shot noise background from 3/4 of the NVs whenever one tries to address a single orientation group, typically, having access to the information from all group within the same spatial location is a boon.

1.4.3 Typical Experimental Apparatus

We conduct NV measurements in a scanning confocal microscope equipped with controllable magnetic field and microwave delivery (Fig. 1.9). A 532 nm laser beam (Coherent Compass 315M) shuttered by an acousto-optic modulator (AOM, Gooch & Housego AOMO 3110-120, rise time $\sim$25 ns) is used for both ground state preparation and spin state detection. An objective lens focuses the beam to a diffraction limited spot size. The lens is designed to use either immersion oil (Nikon Plan Fluor 100x, NA 1.49, diffraction limit $\sim$200-300 nm) or air (Olympus LUCPLFLN, NA 0.6, diffraction limit $\sim$1 μm). The choice of lens depends on the the size of the region of interest.

The combined action of an X-Y galvanometer (Thorlabs GVS212) and a 4F telescope provides the ability to scan the sample at the focal plane of the objective lens. The 4F telescope images the angle of the galvanometer's mirror onto the laser beam's angle of incidence to the objective lens without varying the position of the beam on the input. The objective lens then maps each incidence angle at its input to a position on the focal plane, permitting scanning the plane with minimal alteration of transmission power. Such surface scans are limited by the diameter of the lenses in the 4F telescope to a 200x200 μm region. A closed-loop piezo mount (Physik Instruments) for the objective lens serves to move the scanning plane in the longitudinal direction for depth scans.

The NV fluoresces in a spherical uniform radiation pattern. The objective lens collects and collimates a solid angle of the radiation and sends it counter-propagating along same optical path used by the excitation beam (Fig. 1.9). The fluorescence photons are separated from the excitation beam path by a dichroic mirror (Semrock FF552-Di02), which transmits red, but reflects green light. After passing a series of filters to remove errant excitation photons, the coupling of the fluorescence beam to a single mode fiber serves as an effective pinhole for the confocal microscope. The fiber shuttles the fluorescence photons to a single

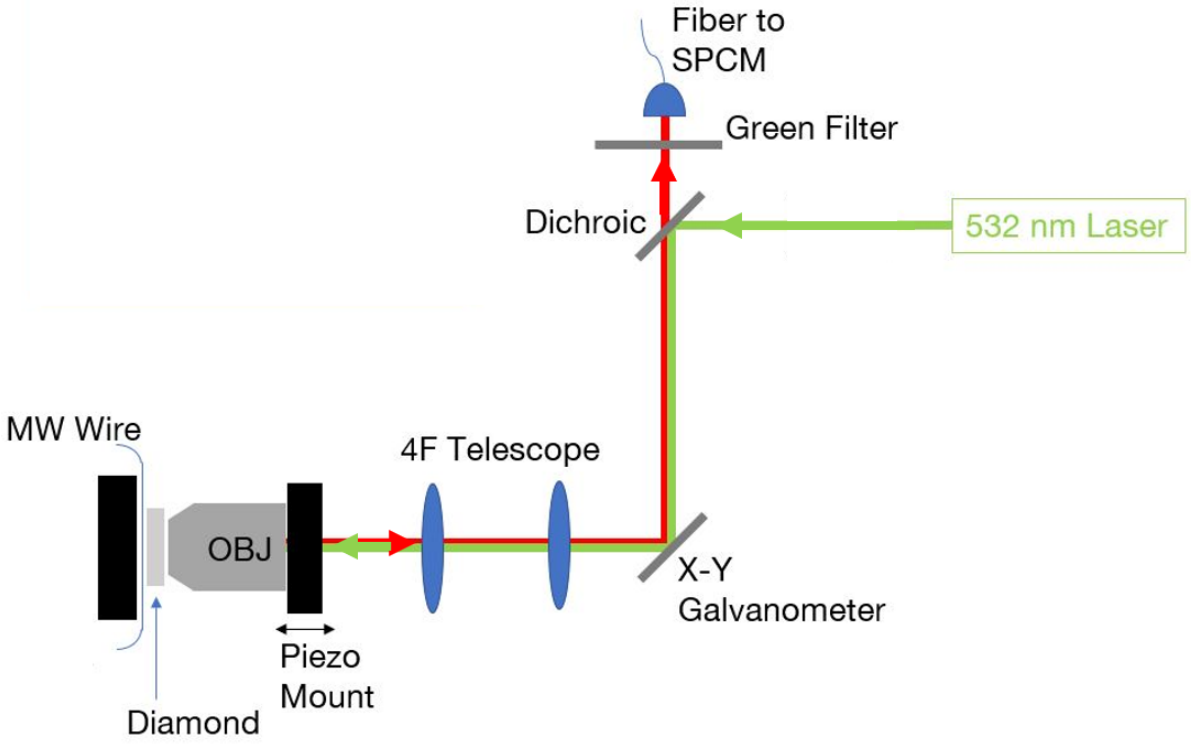

Figure 1.9: Experimental Apparatus: A 532 nm laser shuttered by an AOM light switch excites the NVs, both for state preparation and read-out. A $4f$ telescope permits the galvanometer to scan the surface of the diamond and a piezo-mounted objective controls the depth of the focal plane. The objective lens focuses the excitation beam and collects fluorescence. Microwave fields are delivered by a magnet wire (as pictured) or a coplanar waveguide. Inset: Magnet wire stretched onto an optical rotation mount hovers over the surface of the diamond

photon counting module (SPCM, Excelitas SPCM-AQRH-64-FC) or avalanche photodiode (Thorlabs APD410A). We use a Data Aquisition card (DAQ) for fluorescence measurements and subsequent data processing (National Instruments USB 6343).

A typical NV MW circuit has 4 essential components: a source to generate MW, a shutter to block/pass them, an amplifier to increase the MW power to the desired value, and a delivery line to transmit the magnetic component to the spins (Fig. 1.10).[12] In general, our microwave circuit works by having the source constantly output MW 100 MHz

[12]We cannot call the MW delivery line an antenna. Since our MW are in the GHz range, the wavelength is ∼100 *millimeters*, which is far beyond the size of the ∼1 millimeter diamond, and the ∼10 μm distance between the NVs and the MW delivery line. We are not actually transmitting photons to the spins in our system. Instead we deliver an oscillating magnetic evanescent wave, which drives the NV spin transitions.

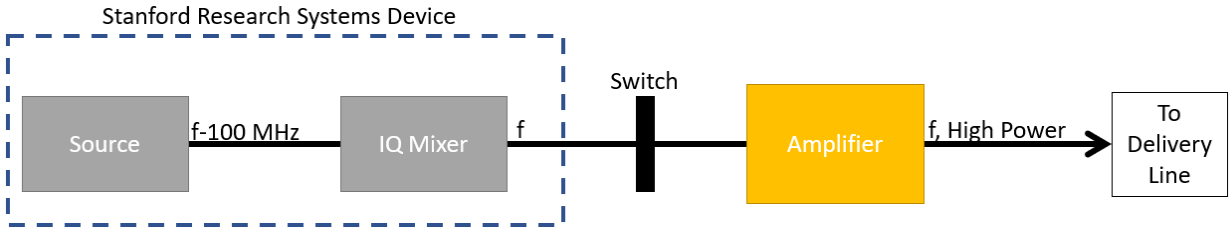

Figure 1.10: A generic MW circuit block diagram. The source, two shutters (IQ mixer and Switch), Amplifier, and delivery line are drawn. In our system, the source and IQ mixer are both contained within the same Stanford Research Systems device. If we plan to apply MW ultimately at a frequency f, we do the following. The source produces MW at $f - 100$ MHz. When the IQ Mixer shutter is open, it shifts the MW frequency up by 100 MHz, to put it back onto resonance. The switch is a simple shutter than only blocks or permits MW to pass. The Amplifier increases the power of the MW before they are appled to the NV via the delivery line.

off-resonance, which are blocked from the remainder of the MW circuit by two shutters with a total extinction greater than 150 dBm. One shutter is a semi-slow MW switch ($>$ 80 dBm): leaking attenuated MW for about 16 ns before rising in about 4 ns when opening, and falling in about 4 ns before leaking for about 16 ns when closing. Its primary use is to prevent the very slow driving of the spins over microsecond to millisecond periods. The other shutter is a fast IQ (70 dBm), with a rise/fall-time of about 1 ns, used for more precise shuttering of the MW pulses. It has the additional task of modulating the source's off-resonant MW by 100 MHz, putting it ultimately on resonance.

As a result of these two shutters, the off-resonant and highly attenuated MW that inevitably leak into the system can be neglected during measurements. For about 15 ns before and after a pulse, less-attenuated off-resonant MW are applied to the spins. Finally, only during the intended pulse period are MW unattenuated and resonant with the spins.

We use a Stanford Research Systems SG384 and/or SG386 as both source and IQ mixer in combination with a Minicircuits ZASWA-2-50DR MW switch as a slow shutter and Mini-Circuits ZHL-16W-43+ and ZHL-10W-2G+ as amplifiers (Fig. 1.10). Together, they generate signals for spin state manipulation. Microwave signals are delivered using a coplanar waveguide (CPW) (or 'stripline') deposited on a coverslip. Each research group has their own designs for the CPW. Figure 1.11 displays two designs our groups have used.

When needed, magnetic fields are applied by either a permanent magnet mounted on adjustable optical posts or by a set of 3 orthogonal magnetic coils. To isolate the system from stray magnetic fields and subsequently improve thermal stability, the sample and magnetic field source are encased in a box of mu metal. To reduce the strength of vibrations due to air currents and to block out additional photons, the entire table is shroud in black plastic curtains.

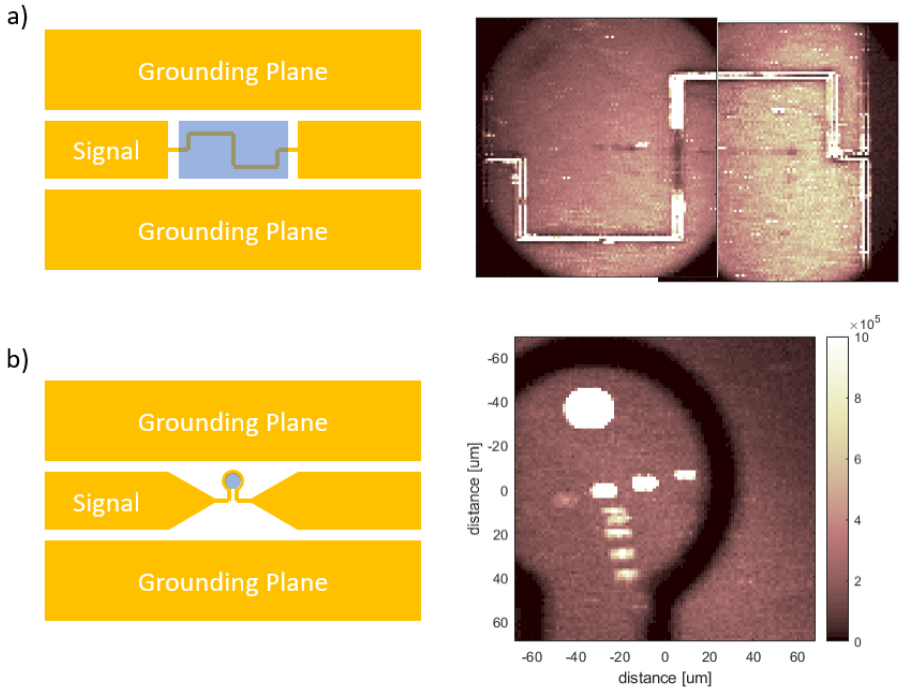

Figure 1.11: Examples of CPW designs used in our lab and confocal images of them. The shaded blue regions mark the locations in which NVs can typically be placed. a) Our lab calls this the "Omega" pattern even though it is barely reminiscent of an omega. b) Watertower pattern. The Watertower pattern is expected to have better impedance matching properties, which should improve MW delivery.

1.4.4 A Quick Word on Immersion Oil

When the objective lens requires immersion oil, moving the objective lens with the piezo mount perturbs the sample stage. As the oil dries out, the mechanical coupling between lens and coverglass/sample increases. If there is too much oil on the lens, it can leak down the sides of the lens and wick the oil out of the space between the lens and coverglass, amplifying the mechanical coupling. It takes some practice and attention to get a sense of how long to pause between piezo adjustments of various sizes, and how often to clean or refresh oil. Usually, I provide a pause around 0.1 s (1 s) after piezo adjustments less than 1 μm, and around 2 s (7 s) after adjustments around 10 μm given fresh (dry) oil. The most common symptom of dry oil is an unstable or a relatively fast drift in z-position after using the piezo to (re)focus on the NV.

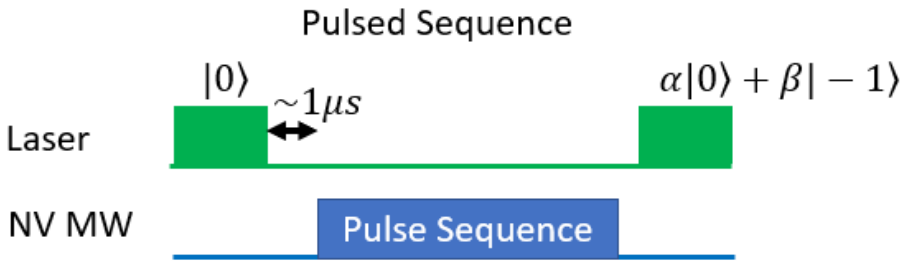

Figure 1.12: Generic Pulsed Sequence: The 532 nm laser polarizes the NV, $\sim$1 μs is waited so spin singlet states can decay, the MW pulse sequence is applied, and the final state of the NV $\alpha\,|0\rangle + \beta\,|-1\rangle$ is read out by applying 532 nm.

1.5 Qubit Probe Measurements

This section describes the protocols and theory underlying the measurements used in this thesis. Some of the physics studied in this thesis is understood by considering both the NV and the P1 centers as qubits that probe their environments. While the descriptions of these measurements often use the lexicon of NVs, they are largely general to all qubits (P1, nuclear spins, atoms, etc.). The organization of the discussion introduces pertinent concepts as they arise. It starts with general notes on implementing these protocols in a lab. It then progresses through the most basic types of measurements that require the least prior understanding as a means to build intuition. By the end of Section 1.5.5, the time is ripe to open the floodgates and dive into the grittier concepts that often confuse people the most, like decay processes and quantum interference. Once those concepts are mastered, the remaining discussion on the quantum interference coherence protocols themselves (Ramsey and the dynamical decoupling sequences) is much easier to grasp.

1.5.1 General Measurement Notes

There are a number of concepts pervading all of the measurements in this section that should be kept in mind.

General Note: Continuous vs. Pulsed Protocols

Regardless of their intended purpose, all NV measurement protocols follow one of two schemes: continuous or pulsed. Continuous measurement protocols simply apply a laser beam and/or microwaves continuously. The scheme for pulsed measurements is always as follows: polarize the NV, perform quantum operations, and read out the NV S_z state (Fig. 1.12). The NV must be polarized into one of its spin states in order to perform quantum

operations, as argued in 1.2.6. To do so, a laser pulse is applied to pump the NV population to $m_s = 0$. After the laser pulse ends, the experiment waits for $\sim 1\mu$s to permit any residual population stuck in the metastable spin singlet state to decay. Once polarized, quantum operations can be performed on the spin states using microwaves. Then the final spin state can be read out by measuring the fluorescence rate and comparing to the fluorescence rate of the $m_s = 0$ state. The polarization and read-out process is described in detail in 1.2.7.

Because a laser or microwave is constantly applied, which alters the spin state, continuous protocols are limited in their ability to probe or manipulate the NV coherence. They are generally useful for quick (in human timescales) measurements of highly-averaged properties, such as fluorescence rate, charge state conversion rate, optical absorption/emission spectra, and rough magnetic spectra. By contrast pulsed measurements are capable of probing faster spin dynamics of the NV, such as coherence times and interactions with other nearby defects.

General Note: Not Single-Shot

The last general note established that the NV's state is determined from its fluorescence rate. Since the NV is a quantum emitter, it can only emit one photon at a time at a maximum rate determined by the inverse of the excited state lifetime $\sim 1/(10$ ns). Since it often repolarizes after a few hundred nanoseconds (Section 1.2.7), even if an experiment could collect 100% of the NV's fluorescence and no background photons, it might barely measure a statistically-significant signal after a single application of a measurement sequence. Moreover, the collection efficiency of the NV's fluorescence is typically about 1% and background photons exist, so only ~ 1 NV photon is collected per NV in a single measurement. Consequently, NV experiments repeat measurements on the NV thousands or even millions of times. Thankfully, each measurement is quick, ranging from $\sim 1\mu$s to ~ 10 ms.

General Note: Differential Measurements

Pulsed measurements that measure the NV's lifetimes (Sections 1.5.8-1.5.11) must be carried out as 'differential measurements.' This entails, performing the measurement protocol once to collect fluorescence counts F_1, then repeating it once more with an additional π-pulse tacked on the end to collect fluorescence counts F_2 (Section 1.2.7, and see 1.5.5). This way, the modified measurement detects the $m_s = -1$ state projection. The final signal S takes the difference between the two measurements up to a normalization

$$S \sim F_1 - F_2 \tag{1.17}$$

Differential measurements keep track of the maximum possible contrast. As well, the fluorescence rate corresponding to complete decoherence is the average of F_1 and F_2 at all iterations of the measurement (Fig. 1.13b). These values can fluctuate given environmental variations over time (e.g. local/global magnetic field variations, laser power fluctuations, etc.).

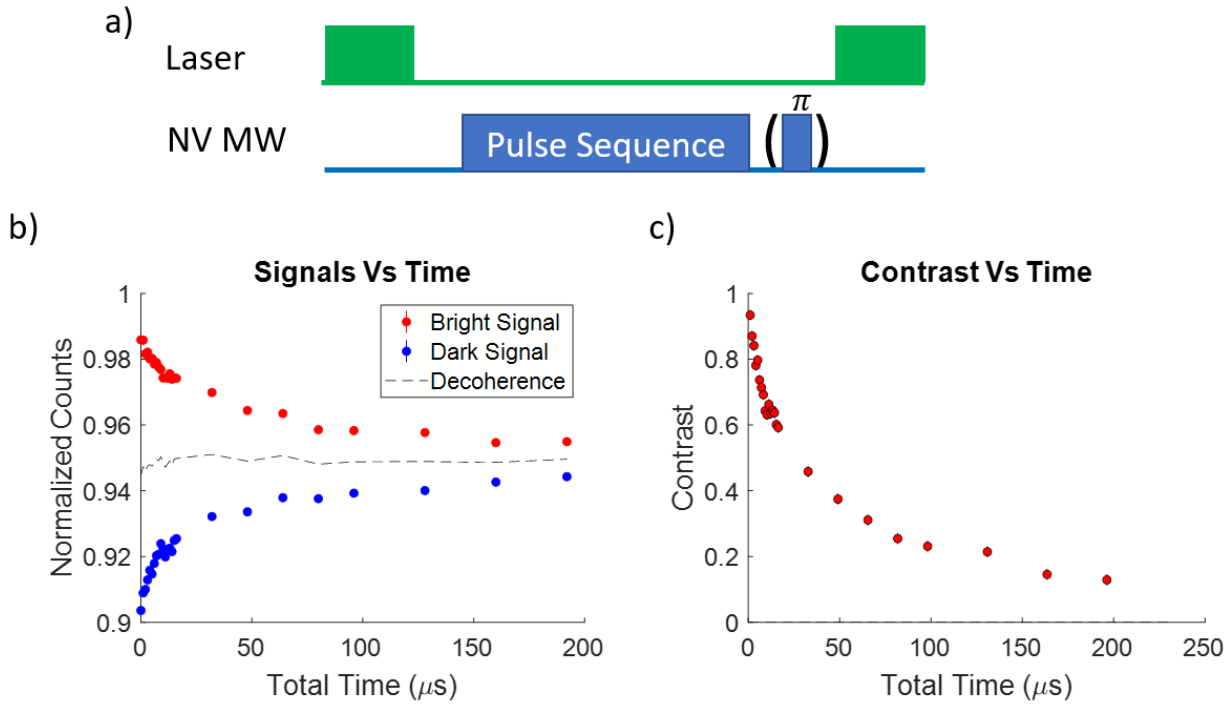

Figure 1.13: a) Differential pulse measurements perform the pulse sequence once (Bright Signal), then once more with an additional π-pulse (Dark Signal). b) Plot of the Bright and Dark Signals normalized by the reference counts. The decoherence fluorescence rate is the average of the Bright and Dark Signals. c) Contrast is the difference between the two normalized signals.

General Note: SNR vs. Acquisition Window

The Signal-to-Noise Ratio (SNR), generally sets how long a measurement will have to average to beat the background noise. The acquisition window is the time window over which the photons are counted. Because the signal being detected is the difference between fluorescence rates of the $m_s = 0$ and $m_s = \pm 1$ states, and the NV re-polarizes to $m_s = 0$ when the read-out laser is applied (Section 1.2.7), there is an ideal acquisition window for optimizing the SNR. Acquire for too long and the NV repolarizes: you count a bunch of photons that contain no information about NV's state at the end of the measurement. These photons only carry shot noise, reducing SNR by increasing noise. Acquire for too short a time and you barely count any photons at all, reducing SNR by reducing signal. The duration and location of the best acquisition window depends on the strength of the laser power and the density of the NVs in the focus spot. To optimize any measurement, you must vary both laser power and the acquisition window to optimize SNR.

1.5.2 Continuous and Pulsed ODMR

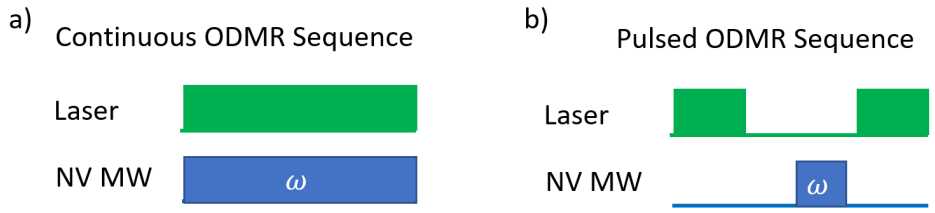

Figure 1.14: Sequences for ODMR measurement. a) Continuous-ODMR applies both laser and MW continuously, varying the MW frequency ω over time. b) Pulsed-ODMR applies a MW pulse of fixed duration and power, but varies ω on each iteration of the measurement.

Optically Detected Magnetic Resonance (ODMR)[13] is the most basic and robust spectroscopy method available. The NV probe is polarized into its initial state, $m_s = 0$. When off-resonant MW are applied, the NV remains in $m_s = 0$, but when the MW is swept onto resonance with one of the spin transitions $m_s = 0 \rightarrow m_s = \pm 1$, they distribute population to the darker $m_s = \pm 1$ states, reducing the fluorescence rate (Fig. 1.14). The difference between continuous-ODMR (cODMR) and pulsed-ODMR (pODMR) is whether the laser and microwave are applied simultaneously and constantly (cODMR) or sequentially (pODMR).

In cODMR, the laser's polarization competes with the MW's redistribution, so to use this measurement, it must be well tuned. There are two parameters to consider when tuning cODMR, SNR and the frequency resolution, which depend respectively on the contrast and linewidth of the resonances. The competition between the laser and MW affects both contrast and linewidth.

The contrast is easily calculated from the fluorescence rate for when the laser is applied alone (or with off-resonant microwaves) R_O, and the fluorescence rate for when the resonant MW are applied R_{MW}

$$C = \frac{R_O - R_{MW}}{R_O} \tag{1.18}$$

Since the fluorescence rates are proportional the the spin population distribution, we infer that the all-optical fluorescence rate is proportional to the rate of optical pumping into $m_s = 0$, $R_O \sim \Gamma$, and likewise that the resonant MW fluorescence rate is proportional to the Rabi frequency $R_{MW} \sim \Omega$. We find then that the contrast depends directly on the competition between laser and MW power.

$$C = \sim \frac{\Omega}{\Gamma} \tag{1.19}$$

While naively, this would suggest that one should simply crank up the MW power and reduce the laser power, there are two physical impediments to doing so. First, the resolution of the

[13] Often called electron spin resonance (ESR), or electron paramagnetic resonance (EPR)

measurement is roughly proportional to the Rabi frequency and laser power[14]. Turning up the MW power increases the Rabi frequency, power-broadening the resonances and reducing resolution. Second, the speed of the measurement depends on SNR $= CR_O t/N$, which relies on the total measurement time t and the noise N. Assuming shot-noise, $N = \delta S \sim \sqrt{(R_O + R_{MW})t}$,[15] we find the SNR is

$$\text{SNR} = C\sqrt{R_O t} \tag{1.20}$$

Consequently, if contrast is maximized by reducing laser power, the SNR also diminishes. Tuning cODMR amounts to finding the right balance between resolution and SNR, depending on one's needs.

cODMR is arguably the most versatile NV measurement. It is fast ($\sim$1 s in some cases), and easy to implement in many highly-constrained scenarios (e.g. inside a diamond-anvil cell or using a widefield microscope). While most often used as a rough calibration of the NV resonance, it is highly effective in sensing measurements.

By contrast, pODMR is usually a slower measurement protocol than its continuous counterpart, but has the advantage that it is much easier to achieve a specific frequency resolution. After polarizing, a single MW pulse is applied with a pre-set power and duration—typically to completely flip the state to $m_s = \pm 1$[16] (see 1.5.5) and with a certain bandwidth when it is on-resonance. By sweeping the pulse frequency, pODMR creates a spectrum with a frequency resolution equal to the bandwidth of the pulse. Since the laser and MW are applied at separate times, there is no competition between Rabi oscillation and re-polarization, drastically increasing the contrast of the resonances over those in cODMR. The ease of determining the frequency resolution and the improved contrast makes pODMR highly desirable and faster in specific scenarios. For example, when the pulse bandwidth is below the natural linewidth of a resonance, the natural linewidth can be measured easily.

Notably, there is a practical limit to the frequency resolution of pODMR. The natural linewidth is determined by the inverse of the 'dephasing' time T_2^* (see Section 1.5.6). As pulse bandwidth decreases below the natural linewidth (equivalently, pulse duration longer than T_2^*), the contrast of the resonance decreases. This can be thought of as the pulse bandwidth failing to address the complete NV population (in frequency space, Fig. 1.15a) or as the NV state decaying before the pulse has fully flipped its state (in time, Fig. 1.15b). As the contrast decreases, the time required to average out the noise increases.

[14]The laser broadens the resonance through a Zeno-type process at higher power, but will narrow the resonance at intermediate regimes. At low laser power, the linewidth is power-broadened by the MW power. At best, the linewidth is set by the dephasing lifetime. See equation 11 in [40] and [79]

[15]Shot-noise is a common assumption for NV experiments. Also, since the NV fluorescence is an incoherent process with a minimum separation between the uncorrelated emission events set by the excited state lifetime, we assume it follows Poissonian statistics. Uncertainty in each parameter is then the square-root of the total counts collected. The noise then can be obtained from error propagation of the signal $S = CR_O t$.

[16]If it is stronger/longer than this, additional oscillations appear in the spectrum. If it is weaker/shorter, the contrast reduces.

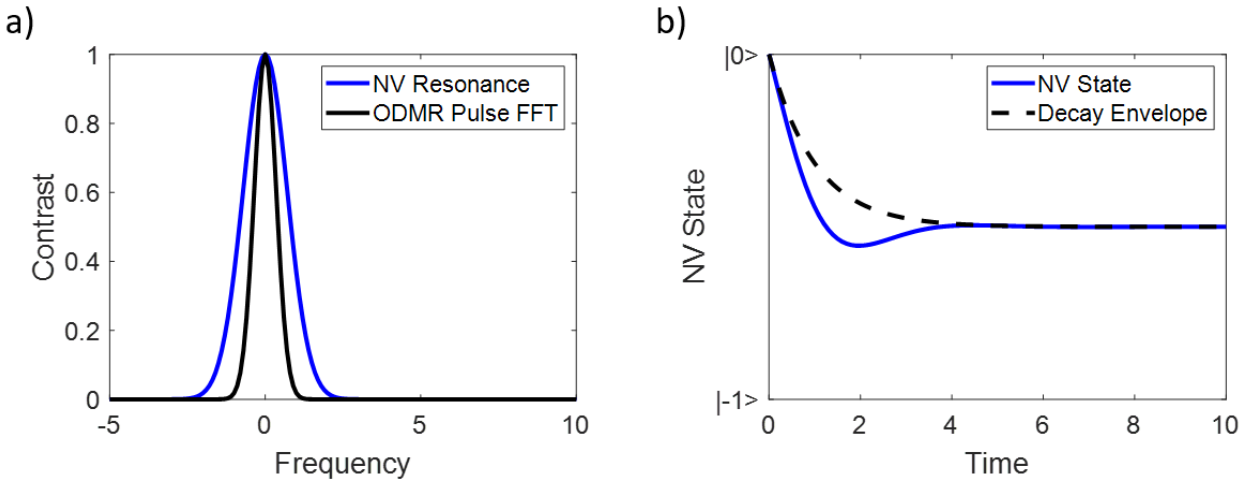

Figure 1.15: Two equivalent pictures for the practical limit to pODMR's frequency resolution. a) The ODMR bandwidth does not encompass all of the NV population. b) The NV state decays before it is fully flipped by the pulse.

1.5.3 Spectroscopy with ODMR

Without any perturbations, the spectra discussed above are simple. The $m_s = \pm 1$ states are degenerate at 2.87 GHz. Perturbations of course change the spectrum dramatically (see Section 1.3.4). In general, symmetry-preserving perturbations shift the $m_s = \pm 1$ states together, whereas symmetry-breaking perturbations split (and possibly mix) them. For example, an external magnetic field aligned along the NV axis splits the states by 2×2.8 MHz/G (each shifted 2.8 MHz/G in opposite directions) to first order. For NV ensembles, the 4 orientation groups will each have a different projection of the applied field onto its axes, and so will exhibit different splittings, resulting in a spectrum with 8 resonances ($m_s = \pm 1$ for each of the 4 groups, Fig. 1.16).[17] Conveniently, three of the four B_z projections are sufficient to calculate the magnitude and orientation of the applied vector field. Generally, this is exactly how NV sensing is performed with cODMR spectroscopy, as in Chapter 3.

1.5.4 T_1 Depolarization

The simplest of the pulsed sequences is the T_1 measurement, which measures how long the NV spin state remains polarized. After the NV is polarized, we wait for a time before reading out (Fig. 1.17a). The duration of the wait-time is swept from short to long times. Any noise that can address the spin transitions, such as resonant phonons or a resonant

[17] If the measurement is performed with enough resolution, the NV's hyperfine structure can be observed. If the NV's nitrogen is ^{15}N, it's nuclear spin is 1/2, whereas it is 1 for ^{14}N. So the hyperfine spectra increases the number of NV resonances to 16 for ^{15}N nuclei and 24 for ^{14}N nuclei.

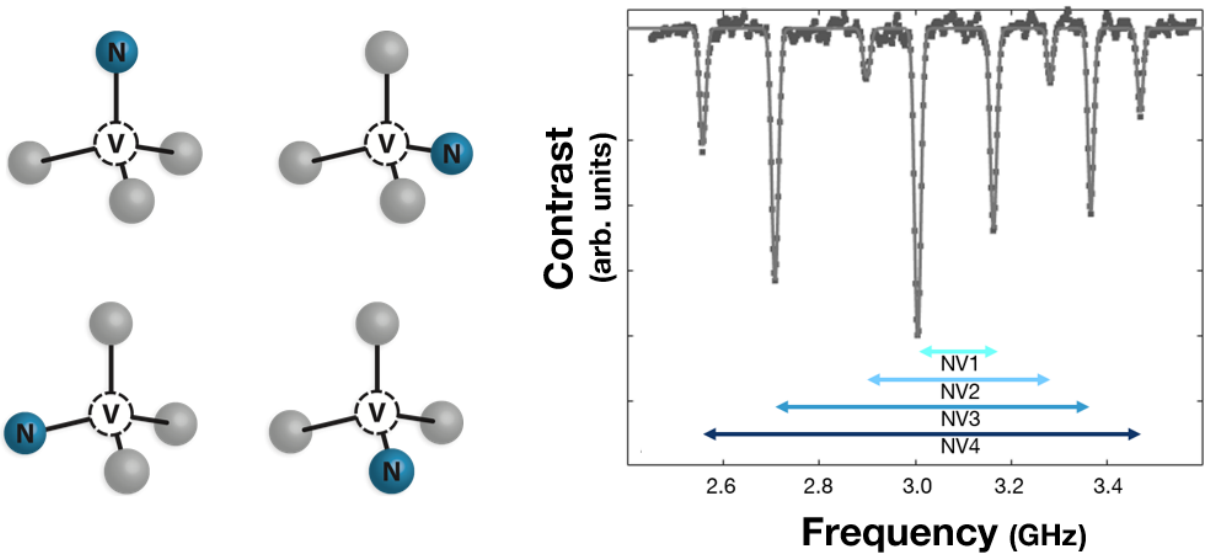

Figure 1.16: When all four crystallographic axes of the NV are included in an ODMR measurement, 4 pairs of resonances appear, each pair corresponding to an orientation group.

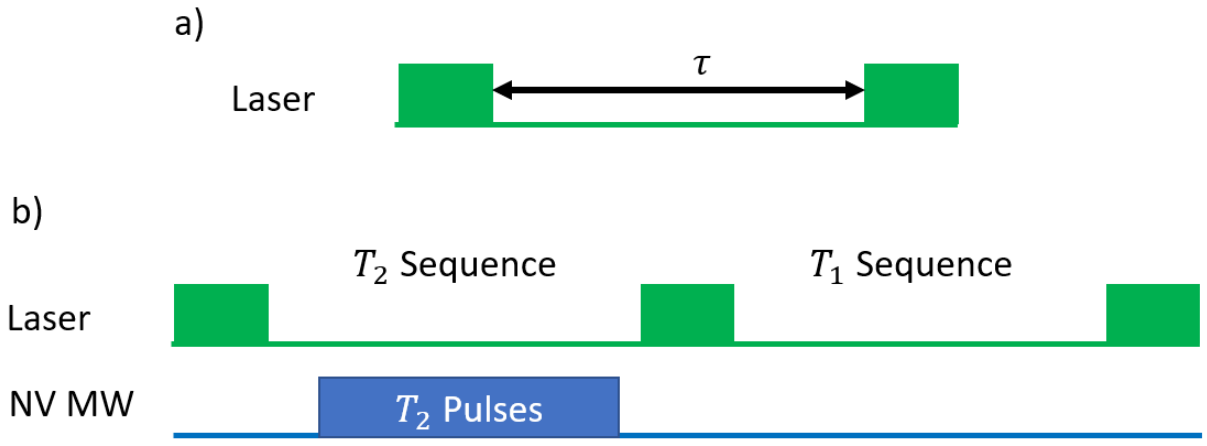

Figure 1.17: a) T_1 measurements sweep the time between the polarization and read-out laser pulses. b) When other measurement sequences (e.g. T_2) get long enough, they must be immediately followed by a T_1 measurement to isolate the effects of T_1 decay.

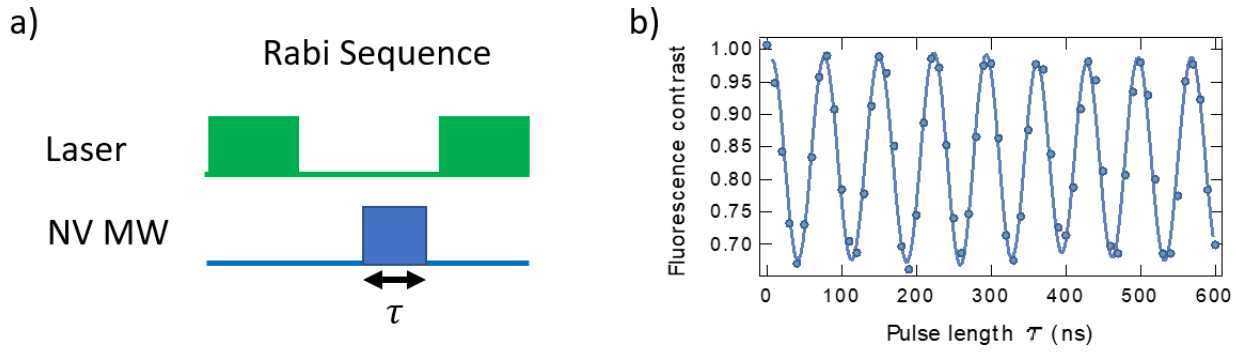

Figure 1.18: a) Rabi pulse sequence b) Rabi Signal

defect environment,[18] will redistribute the NV population, eventually destroying any spin polarization. This is observed as an exponential decay (or stretched exponential decay, see Chapter 4) in the NV contrast. T_1 is defined as the time when the contrast has decayed to $1/e$ of it's original value. Typical T_1 depolarization lifetimes at room-temperature for both single and ensemble NVs are $\sim 1-10$ ms. As the temperature decreases, or the NV's local environment is cleaned, T_1 increases to $\sim 0.1-1$ s and even more than a minute [74].

Since depolarization occurs primarily via local resonant noise, T_1 measurements of the spins can be used as a noise spectroscopy technique (Section 3.5). By sweeping the applied magnetic field B, the NV resonance is swept, altering what depolarizing noise is resonant. Measuring T_1 versus B then provides a noise spectrum in the GHz range.

T_1 measurements are also important in the interpretation of decoherence measurements (T_2 discussions below). When decoherence lifetimes are long enough, the effects of T_1 decay add additional decay to the signal. In order to isolate just the T_2 decay, the T_1 effect must be removed. To do this, a T_1 measurement is concatenated to the end of a T_2 measurement (Fig. 1.17b).

1.5.5 Rabi Oscillations

Rabi oscillations in a two-level system (or qubit) and the Bloch sphere (Appendix A) are crucial atomic physics concepts to understand and have been covered in detail in many textbooks and lectures [133]. As such, I will only briefly cover here the key ideas as they pertain to NV experiments, though they apply equally well to any qubit (including the P1).

When an aligned magnetic field lifts the degeneracy between the $m_s = \pm 1$ states, spin transitions between $m_s = 0$ and either of the other states may constitute an effective two-

[18]Notably, the resonant defect environment must contain many defects. If there is only one other resonant defect in the system, the NV and defect will simply coherently transfer the polarization between themselves, which is observed as an oscillation. If there are many resonant defects in the system, the probability of the NV polarization returning to the NV is diminishingly small

level system. For most purposes, experiments choose the $m_s = 0 \rightarrow m_s = -1$ transition for the two-level system, since it is by definition a lower frequency transition, although the decision is often arbitrary. A magnetic field projected into the XY plane of the NV (i.e. with S_x and S_y components) that oscillates at or near the NV's resonance frequency will transfer the population from one of the eigenstates to the other and back (Fig. 1.18).[19] The way this is performed in the lab is to polarize the NV, drive the transition for a variable duration with resonant MW (oscillating magnetic field), and read out the $m_s = 0$ population.

The angular frequency Ω of the population oscillations, called the 'Rabi Frequency,' is related to the applied MW power P_{MW} as $\Omega \propto \sqrt{P_{MW}}$. The MW pulse duration for which the population has transferred completely from $m_s = 0$ to $m_s = -1$ is known as the π-pulse, since it the halfway point of the oscillation period. Likewise, pulses of any angle can be defined, most notably the $\pi/2$-pulse, which transforms the $m_s = 0$ eigenstate $|0\rangle$ into an equal superposition $(|0\rangle - i\,|-1\rangle)/\sqrt{2}$, where $|-1\rangle$ is the $m_s = -1$ eigenstate. Pulses of arbitrary lengths vary the distribution of the population between the two states in the superposition.

The Rabi frequency of the pulses sets the bandwidth of the pulses, meaning that for MW of an angular frequency ω any transitions within a frequency range of $\omega - \Omega/2 < \omega < \omega + \Omega/2$, are considered on-resonance. Bandwidth is an important consideration when NV (or other defect) resonances become close to each other (e.g. for NV hyperfine resonances, or for off-axis magnetic field ensemble measurements). Transitions outside of the bandwidth of the pulse are driven with an effective Rabi frequency $\Omega' = \sqrt{\Omega^2 + \delta^2}$, where the 'detuning' δ is the difference between the MW center frequency ω and the off-resonant transition frequency. Off-resonant Rabi oscillations do not perfectly transfer population. The amount of population transferred is limited to $(\Omega/\delta)^2)$ in the perturbative limit (δ large, Ω small). Due to the variation in Rabi contrast and frequency, undesirable beating patterns can emerge in measurements that drive multiple nearby off-resonant transitions.

Rabi measurements are usually the primary method of calibrating the pulses used in all other measurement protocols, but they are quite useful beyond calibration. The decay of the contrast throughout Rabi oscillations can indicate the pulse error or dephasing lifetime (discussed in 1.5.6). Additionally, fast Rabi oscillations are the primary component of the useful technique "Spin Locking."

1.5.6 Lifetime Limits to Measurements: Dephasing T_2^* and Decoherence T_2

With Rabi and the Bloch sphere in hand, we can now clearly discuss the phenomena of dephasing T_2^* and decoherence T_2 lifetimes, which despite comprising quite distinct under-

[19] Note that because the NV is a spin-1 system, S_x and S_y matrices have a $1/\sqrt{2}$ pre-factor. So for the same applied MW power, NVs oscillate $\sqrt{2}$ faster than their spin-1/2 P1 counterparts. It is important to remember that the dipole moments of systems with different spins are still different, even when you reduce them both to two-level systems. Also note that if the the population in each state is equal, no population oscillation is observed in general.

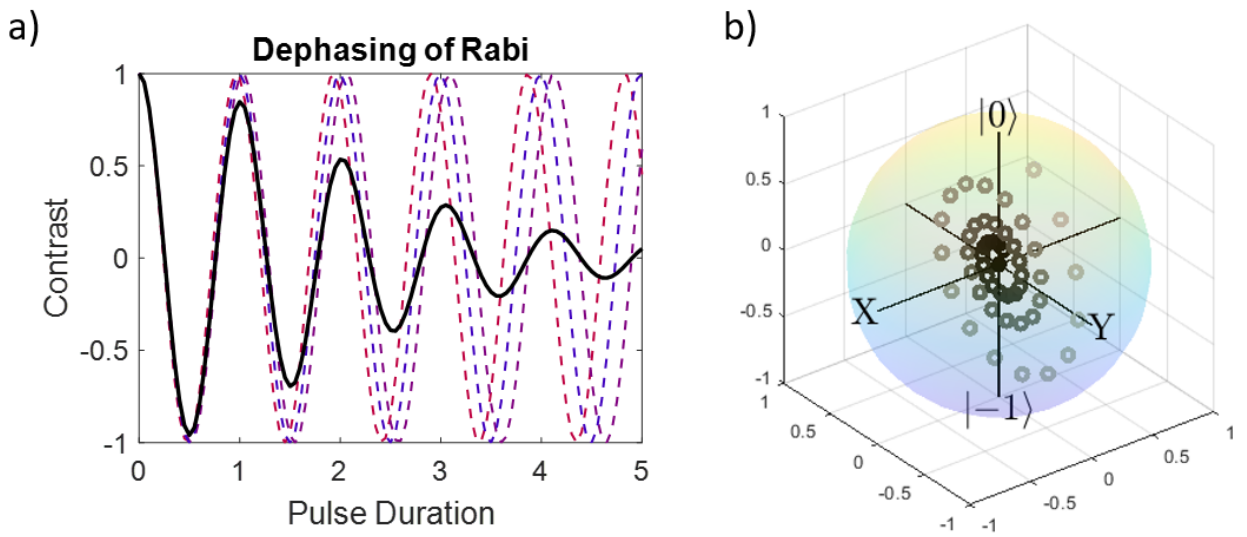

Figure 1.19: a) Dephasing of a Rabi measurement. Each individual NV in the Rabi measurement (dashed) would oscillate at a slightly different frequency. The averaged signal (solid black) exhibits oscillation at the average frequency with an exponential decay envelope. b) Decoherence in a Rabi measurement. For clarity, only the tip of the Bloch vector is plotted. As the oscillations progress, the Bloch vector shortens, tracing a spiral into the center of the sphere.

lying physics, are often confused with each other. Both should be considered whenever the NV's (or any qubit's) state is transformed into a superposition containing both $|0\rangle$ and $|-1\rangle$ (or whatever the qubit's levels are). That is, for any measurement besides T_1, their effects are relevant. In fact, these two decay lifetimes are what the remaining measurement protocols often seek to measure: they rotate the NV state onto the equator of the Bloch sphere ($|0\rangle \rightarrow \frac{1}{\sqrt{2}}(|0\rangle - i\,|-1\rangle)$), accumulate the effects of dephasing and/or decoherence, and attempt to rotate the state back to $|0\rangle$ before read-out. In all of these measurements, T_2^* and T_2 are the times at which dephasing and decoherence, respectively, have reduced the contrast to $1/e$ of it's original value. Notably, the shape of the exponential decay profile is generally stretched (see Section 4.4).

Dephasing

Dephasing is a decay of signal contrast that appears *only when all repetitions of a measurement are averaged together*. It is a phenomenon that emerges from the lack of single-shot non-demolition read-out for each NV (see Section 1.5.1). Within each measurement, the final state of the NV oscillates between $|0\rangle$ and $|-1\rangle$ perfectly until some other effect arises (i.e. the T_1 or T_2 limit). However, the final state of each measurement accumulates a ran-

dom phase relative to the final state of each other measurement in the set. Since the sum of oscillations with random phases and/or frequencies tends to zero, the average over all measurements displays a decay of the contrast.

We can see this effect clearly by taking as an example the decay of Rabi oscillations of an NV ensemble (also see Ramsey in Section 1.5.8 for a different incarnation of dephasing). Usually, the limit to Rabi oscillations in an ensemble originates from the gradient of the MW field applied.[20] Each NV in the ensemble sees a slightly different MW power and so oscillates with a slightly different Rabi frequency. The total signal is the sum of the cosines with a distribution of frequencies set by the gradient of the MW power. As time progresses, the Rabi oscillations go out of phase with each other. The average signal is consequently a single oscillation with an exponential decay envelope with T_2^* lifetime (Fig. 1.19a).

As mentioned in Section 1.5.2, $1/T_2^*$ sets the natural linewidth of the NV resonance. The uncertainty principle provides the hand-waving intuition for why lifetime generally sets linewidth. Time t and energy E are canonically conjugate variables, so $\sigma_E \sim \hbar/\sigma_t$. The uncertainty in the energy σ_E is directly the linewidth of the resonance. The natural linewidth depends on all noise intrinsic to the environment, which contribute to the decay of the NV with a T_2^* lifetime. In the example above, the decay was dominated by an effective MW noise environment. In the Ramsey section below, we will explore a noise environment internal to the diamond.

Decoherence

By contrast, decoherence is an *absolute limit to the signal of each specific measurement protocol*.[21] Specifically, it arises from the decay of the off-diagonal matrix elements of the NV's density matrix (also known as the 'coherence'), which is responsible for the transfer of population between the qubit levels. More intuitively, it is contrast decay from either or both of the following: 1) the entangling of the NV's state with the environment (e.g. the NV spin superposition being shared with other spin defects);[22] or 2) the altering of the environment during a single measurement (e.g. rearrangment of environmental spins imparting a changing magnetic field on the NV).[23] In both cases, since measurements can only detect the NV's

[20] A 1% variation in MW power across the diffraction-limited spot is considered good for a stripline.

[21] Each measurement protocol either isolates the NV from its environment or enhances its susceptibility to the environment. These effects are inherent to the measurement protocol and lead to a different T_2 decoherence lifetime for each. This is why T_2 often comes with an additional superscript or subscript labeling the measurement it applies to (e.g. T_2^{Rabi}, T_2^{Echo}, etc.)

[22] This may sound similar to T_1 depolarization, but it is distinct. In T_1 polarization (often called longitudinal relaxation), the qubit state $|0\rangle$ or $|-1\rangle$ (the longitudinal poles of the Bloch sphere) is flipped by the transfer of population and energy to another defect through a resonant process. In T_2 decoherence (often called transverse relaxation), the superposition of the qubit states is entangled with the environment without a flipping of the state, and need not be resonant.

[23] This could be conflated with the dephasing discussed in Section 1.5.8, but it should not be. In dephasing, the environment's state does not change, so it can be traced out of the NV-environment density matrix without altering the NV's reduced density matrix. In decoherence, because the environment's state changes,

S_z projection—tracing out the environment from the NV-environment density matrix—the NV's superposition changes from a pure state to a classical statistically mixed state.

As an example of the first type of decoherence effect, we consider now the decay of fast Rabi oscillations of a single NV. See Section 1.5.9 on Spin Echo for an example of the second type of decoherence, and for the reason why fast Rabi oscillations suppress both dephasing and the second decoherence effect. Since we are focusing on a single NV, MW gradients can be neglected. In this situation, each repetition of the Rabi measurement looks exactly the same. The decay stems from the NV's superposition becoming entangled with more and more of the environment. The coherence between $|0\rangle$ and $|-1\rangle$ is drawn out of the NV as the NV becomes more coherent with its surroundings. One can think that the environment is constantly and slowly measuring the state of the NV through its interaction, which effectively collapses the NV wavefunction from the experiment's perspective. On the Bloch sphere, we would see the length of the Bloch vector decreasing over time as it rotates perfectly around the x-axis at a constant rate (Fig. 1.19b).

In the above situation, the T_2 coherence time is limited to the rate of spread of the NV coherence with the environment; however, that is not the theoretical limit. At room-temperature, the rate of this decay is theoretically limited to the rate of T_1 depolarization, which has yet to to be achieved in experiments. In this limit, the two effects are indistinguishable in an experiment, but that does not mean they are the same effect. When there are few resonant phonons to drive depolarizing transitions between $|0\rangle$ and $|-1\rangle$ at low temperatures, $T_2 \leqslant 2T_1$ [114], clearly indicating a difference between the effects.

1.5.7 How All Coherence Decay Interference Measurements Work

In short technical terms, the way coherence decay measurements (Ramsey and the dynamical decoupling sequences) work is by encoding information in the phase of the NV's coherence, and then transferring that information into the population difference between $|0\rangle$ and $|-1\rangle$ (i.e. the contrast). Let's unpack that slowly.

At any given time, $|0\rangle$ and $|-1\rangle$ separately gain phase from almost any perturbation. As long as the two eigenstates are separate, the phase difference between them doesn't matter, amounting to global phases. We can see this on the Bloch sphere easily. If a vector points towards one of the poles, azimuthal angles are inconsequential.

When the eigenstates are made coherent with each other via a MW pulse that puts them into a superposition, the phase difference between them gains a real meaning, but until one studies and internalizes some of the more fundamental aspects of quantum mechanics, they will often struggle to glean what that meaning is. Certainly, we can see that azimuthal

when it is traced out it removes some of the NV's information with it, even if the NV is otherwise undisturbed. Because the NV and environment are coupled by their interaction, a change to either of them is a change to both of them. As we will see in Section 1.5.9, this change in the environment directly alters the phase accumulation of the NV state.

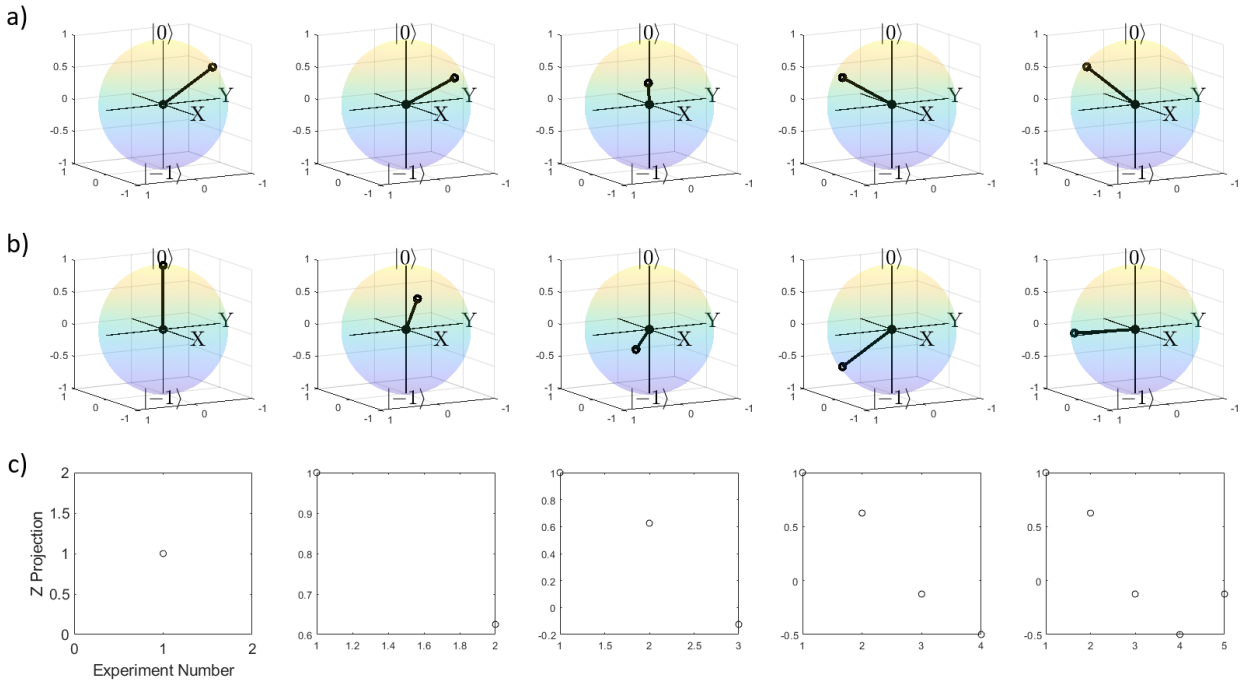

Figure 1.20: a) The precession of a classical gyroscope after an initial tilt θ_x, drawing the spin axis of the gyroscope. The gyroscope is allowed to precess for a longer time on each iteration of the experiment. b) The gyroscope spin axis at the end of each iteration after the $-\theta_x$ tilt is applied. c) Plotting the z-projection of the gyroscope as the iterations progress. Eventually, a full cosine curve will be plotted.

angles actually affect a vector on the Bloch sphere's equator. Certainly, we can calculate the phase gained by the coherence term in the density matrix. But what does this mean for a qubit's spin and why do these measurements actually work?

First, let's start with the classical analog of spin: the gyroscope.[24] When the gyroscope is perfectly balanced, its axle points straight up, precisely parallel to the downward pull of gravity along the z-axis. If one were to tilt the axle of the gyroscope away from the z-axis by an angle θ_x around the x axis, it would precess around the z-axis. For us humans watching a gyroscope precess, we can clearly see the entire gyroscope at all times. We see that it isn't changing size or shape, it is just spinning and precessing.

Now imagine that instead of being able to watch the entire gyroscope as we could normally, we are constrained only to observe the projection of the gyroscope's axle onto the

[24]Remember, spin and gyroscopes are described by the same physics of angular momentum, but that does NOT mean that spin represents the spinning of a quantum particle. As has been shown many times, an electron is not a ball of charge with finite radius that spins like a top. The universe would've imploded by now if that was the case. Still, I will speak of spin as if it is a top or a gyroscope throughout this thesis.

z-axis. When the gyroscope is untilted, we see 100% projection of the axle along z (Fig. 1.20a b column 1). When the gyroscope is tilted and precessing, we can see that the z-projection has reduced, but we can't see the precession (Fig. 1.20a). At first, we seem to have lost the ability to observe precession, but in fact, there is still a way to track it. When the gryoscope is first tilted, we can record the angle θ_x by which we tilted it. Simultaneously, we call the axis towards which we tilted, the y-axis, even though we may not know what direction that is relative to the rest of the world. If we immediately reverse that tilt, rotating by $-\theta_x$ before the gyroscope has the chance to precess, we will measure 100% projection along z (Fig. 1.20b c column 1). This becomes our reference point: the initial state right after tilting by θ_x but right before precession. Next, we let the gyroscope precess for a time we record, and then rotate it by $-\theta_x$. Because the gyroscope is at a new azimuthal angle, this rotation fails to return it to the z-axis (Fig. 1.20b). We no longer measure 100% projection. However, if we repeat our experiment, varying the time we permit the gyroscope to precess, we will plot out an oscillation in the z-projection (Fig. 1.20c). The rate and phase of this oscillation is precisely the rate and phase of the precession! With this, we have extracted a complete observation of the precession process.

The constraint and solution in our classical gyroscope are precisely those of our quantum spin. One needs to remember that a quantization axis, along which we define our basis $\{|0, \pm 1\rangle\}$, creates a constrained coordinate system that we humans use to comprehend and work with quantum states. It is a limitation on our part. The NV's spin is actually tilting by θ_x when we apply MW pulses. It is actually precessing. When we say there is a relative phase accumulated between $|0\rangle$ and $|-1\rangle$ (or alternatively in the coherence), that is our human way of expressing the precession using the coordinate system to which we are constrained.

No, we cannot observe precession directly. If we only look at the projection onto the z-axis of the Bloch sphere after tilting the spin (i.e. apply a MW pulse, wait, then read-out with the laser), we still cannot see it. Thankfully, we can detect precession by determining a way to measure this phase. Applying a final MW rotation of $-\theta_x$,[25], we are no longer blindly projecting onto the z-axis; we are transferring the relative phase to a measurable population difference first. See Section 1.5.8 for a calculation explicitly showing phase imprinted upon population. In fact, we can go further and declare that we actually interfere—homodyne—the initial state before precession $|\psi_i\rangle$ with the final state after precession $|\psi_f\rangle$, which we explicitly see in the math as $|\langle\psi_i|\psi_f\rangle|^2$. This is how coherence interference works. This interference of phase and amplitude between the two state is why these types of measurements are especially effective for measuring the dephasing and decoherence decay lifetimes.

As a bonus note on this matter, sometimes it is experimentally possible (e.g. Spin Locking) for us humans to chose a new quantization axis parallel to the tilted spin, call that the z axis of a new tilted Bloch sphere, and watch the dynamics of precession from this new perspective.

[25]The final rotation does not have to be around the same axis as the initial rotation, but it does make the interpretation easier. There are many scenarios beyond the scope of this discussion when the final pulse should be around other axes.

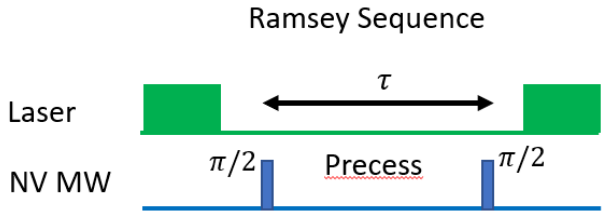

Figure 1.21: The Ramsey pulse sequence

1.5.8 Ramsey

At first blush, Ramsey's method[26] seems to be the simplest of the coherence decay measurements. A $\pi/2$ - pulse around the x-axis rotates the NV to the equator of the Bloch sphere $|\psi_i\rangle = \frac{1}{\sqrt{2}}(|0\rangle - i\,|-1\rangle)$, it is allowed to evolve freely for a variable wait-time τ, and a final $-\pi/2$ around x attempts to rotate the NV back to $|0\rangle$ (Fig. 1.21. However, we will see in the following sections and Chapter 4 that this 'simple' measurement is almost insidiously pervasive.

On the equator of the Bloch sphere, the NV superposition is susceptible to gaining phase from almost any perturbation. First and foremost, a magnetic field along the NV/Bloch sphere z-axis induces precession in the spin moment. Take as an example the unitary evolution for a duration τ due to a static B_z field

$$\begin{aligned} U(\tau) &= \mathrm{Exp}\left[-i\hbar\int_0^\tau \gamma_{NV} B_z\,|-1\rangle\langle -1|\,\sigma_z dt\right] \\ U(\tau) &= \mathrm{Exp}\left[-i\hbar\gamma_{NV} B_z \tau\right]\sigma_z + |0\rangle\langle 0| \\ U(\tau) &= \mathrm{Exp}\left[-i\phi(\tau)\right]\sigma_z + |0\rangle\langle 0| \end{aligned} \tag{1.21}$$

where we have absorbed the prefactors of the spin-1 $\hat{S}_z$ operator into B_z and σ_z is the pauli spin-1 z-matrix. We have reduced and redefined σ_z as

$$\sigma_z = \begin{pmatrix} 0 & 0 \\ 0 & 1 \end{pmatrix} = |-1\rangle\langle -1|$$

where the top left element is 0 because $|0\rangle$ lacks a spin moment and so is unaffected by B_z, and the direction of the phase gained by the $|-1\rangle$ state is arbitrary (coefficient $-1 \rightarrow 1$). Applying eq. 1.21 to our Bloch vector,

$$|\psi_f\rangle = U(\tau)\,|\psi_i\rangle = U(\tau)\frac{1}{\sqrt{2}}(|0\rangle - i\,|-1\rangle) = \frac{1}{\sqrt{2}}\left(|0\rangle - ie^{-i\phi(\tau)}\,|-1\rangle\right) \tag{1.22}$$

[26] While Ramsey is a person, we usually call the method itself simply "Ramsey" in daily work. I will do this for the rest of this thesis.

we see that only the $|-1\rangle$ state gains a phase amounting to rotation around the Bloch sphere's z-axis by an angle $\phi(\tau) = \gamma_{NV} B_z t$, which is precisely Larmor precession. By finishing the Ramsey measurement with a rotation of $-\pi/2$ around x, we transfer the phase into the NV population. There are two equivalent ways of seeing this in the calculation. Either we can perform the final $-\pi/2$ pulse and ask what the S_z projection is, or we can simply project the final evolved state onto the initial state. I will do the latter to emphasize how this is an interference measurement. The probability of being in $|0\rangle$ is

$$P_0(\tau) = |\langle\psi_i|\psi_f\rangle|^2 = \frac{1}{2}\left(1 + \cos\phi(\tau)\right) \tag{1.23}$$

Note $P_0(\tau) = 1$ only if the Bloch vector returned to its initial position (i.e. the relative phase between $|0\rangle$ and $|-1\rangle$ returns to its initial value up to factors of 2π).

Any perturbation that changes the splitting between $|0\rangle$ and $|-1\rangle$, imparts a phase difference between them: oscillating magnetic fields, electric fields, stress, temperature, etc. Because the initial and final $\pi/2$ pulses are around the same axis, Ramsey and the dynamical decoupling measurements turn this phase difference into population by interfering the final state with the initial state, as described in the previous section.

In the case of Ramsey, all perturbations influence the phase,[27] generating precession around the z-axis. The strength and the frequency of these perturbations each impart a particular rate and pattern of rotation along the Bloch sphere equator. Integrating the phase $\phi(\tau)$ over different frequencies and patterns of precession creates a beating pattern in the final signal, called "Ramsey Fringes." The Fourier transform of this signal teases out the individual perturbative frequency components, permitting Ramsey to extract information about the noise environment of the NV.

Ramsey measurements on NVs tend to be dominated by random relatively-slow magnetic noise through the dephasing process (see Section 1.5.6). On each run of Ramsey, there is a strong possibility that the spins in the diamond reorient themselves due to thermal fluctuations. Each unique configuration of spin baths imparts a different static magnetic field on the NV, inducing a different precession rate. As discussed in Section 1.5.6, summing over a distribution of frequencies leads to an exponential decay envelope. In actuality, the decay envelope for Ramsey is in general a stretched exponential decay that depends on a few factors (see Section 4.4).

The remaining dynamical decoupling measurements in this chapter are designed to extract information on particular types of noise. All perturbations also impart phase throughout these measurements, but in contrast to Ramsey, dynamical decoupling selectively filters phase accumulation from particular perturbations by performing additional operations between the two $\pi/2$ pulses. The process of selective filtering is called "dynamical decoupling."

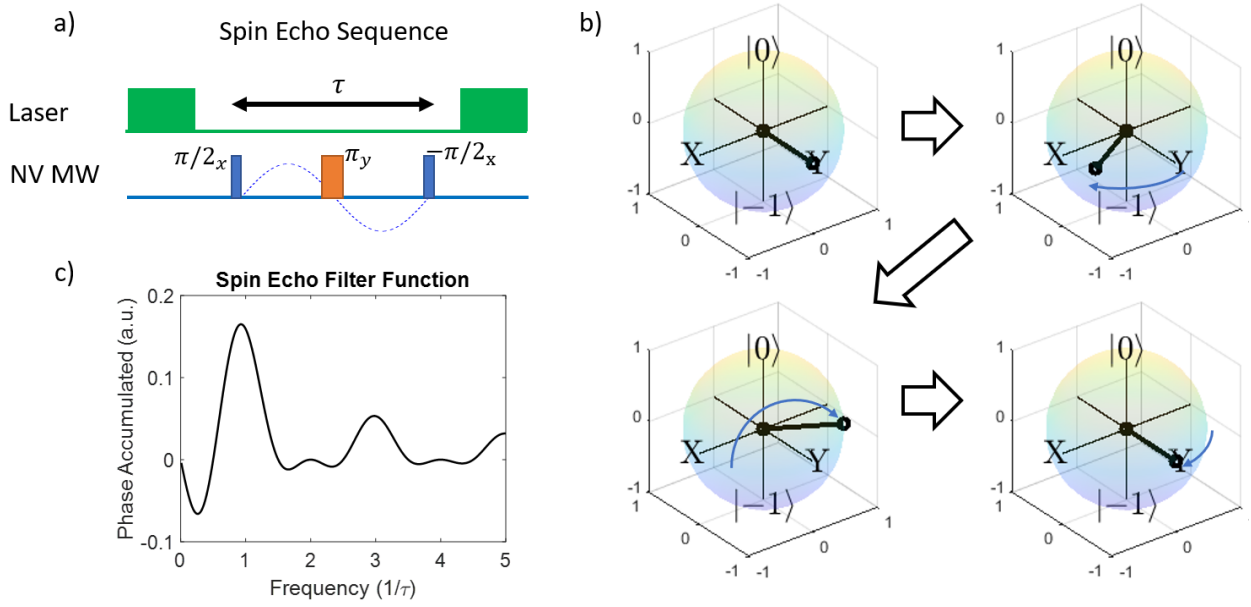

Figure 1.22: a) The Spin Echo pulse sequence. The initial and final $\pi/2$-pulses are around the x-axis and the refocusing pulse is around the y-axis. The phase accumulation of noise on resonance with the filter function (blue dashed) is not suppressed. b) Spin Echo on the Bloch sphere. After the $\pi/2$-pulse the spin is initially on the y-axis (top left). It then precesses by some angle over time $\tau/2$ (top right), is flipped by π around y (bottom left), and is permitted to precess for the same duration $\tau/2$ (bottom right).

1.5.9 Spin Echo

Often the first dynamical decoupling sequence students learn, there are many explanations and gorgeous Bloch sphere animations to be found online for the spin echo method [28]. Its pulse protocol looks like Ramsey's except for the single π-pulse in the middle, sometimes called the "refocusing pulse" (Fig. 1.22a). This pulse reflects the spin across the pulse axis, geometrically yielding the negation of the phase angle $\phi_1(\tau/2) \rightarrow -\phi_1(\tau/2)$ accumulated over the first evolution time $\tau/2$ (Fig. 1.22b). If the spin is permitted to continue evolving for the same amount of time $\tau/2$ and accrues the same phase angle $\phi_2(\tau/2) = \phi_1(\tau/2)$, the total phase of the final state is $\Phi(\tau) = \phi_2(\tau/2) - \phi_1(\tau/2) = 0$ and the final S_z projection is perfect. This state with a refocused phase is called an 'Echo.'[29] Immediately, we see that Spin Echo filters the effects of dephasing due to DC/slow noise, and of most correlated AC

[27] This is why Ramsey is also called "Free Induction Decay."

[28] To comply with the vernacular of the lab, I will call it simple "Spin Echo" for the remainder of the thesis.

[29] There are actually multiple echos after the first one, if the second evolution time is permitted to increase. Each subsequent echo is less refocused than the first.

noise. The only way to acquire a nonzero final phase is for the two evolution periods to impart different phases $\phi_1(\tau/2) \neq \phi_2(\tau/2)$. Decay in Spin Echo most often originates then from the second type of decoherence (Section 1.5.6): from correlated AC noise that meets a resonance condition intrinsic to the measurement's filter and from the decorrelation of the environment. The uncorrelated alterations of the environment trivially imply that $\phi_1(\tau/2) \neq \phi_2(\tau/2)$, but understanding the intrinsic resonance condition benefits from further attention.

AC noise whose period is an nearly an odd integer multiple of the total evolution time τ resonates with the Spin Echo filter and passes through. We can see this diagrammatically in Fig. 1.22a, or mathematically in the following example of unitary evolution due to a B_z field oscillating with frequency ν. Over the first evolution period the evolution operator is

$$\begin{aligned} U_1(\tau/2) &= \text{Exp}\left[-i\hbar \int_0^{\tau/2} \gamma_{NV} B_z \left|-1\right\rangle\!\left\langle -1\right| \sigma_z \sin(2\pi\nu t + \phi_0) dt\right] \\ &= \text{Exp}\left[-i\frac{\hbar\gamma_{NV} B_z}{2\pi\nu}\left(\cos(2\pi\nu\tau/2 + \phi_0) - \cos(\phi_0)\right)\right]\sigma_z + \left|0\right\rangle\!\left\langle 0\right| \\ &= \text{Exp}\left[-i\phi_1(\tau/2)\right]\sigma_z + \left|0\right\rangle\!\left\langle 0\right| \end{aligned} \tag{1.24}$$

where σ_z is defined as in the previous section. Over the second evolution period we see similarly

$$\begin{aligned} U_2(\tau) &= \text{Exp}\left[-i\frac{\hbar\gamma_{NV} B_z}{2\pi\nu}\left(\cos(2\pi\nu\tau + \phi_0) - \cos(2\pi\nu\tau/2 + \phi_0)\right)\right]\sigma_z + \left|0\right\rangle\!\left\langle 0\right| \\ &= \text{Exp}\left[-i\phi_2(\tau)\right]\sigma_z + \left|0\right\rangle\!\left\langle 0\right| \end{aligned} \tag{1.25}$$

Since the full calculation is a good exercise for the reader and does not add much more to the current discussion of the resonance condition, we will trust that the π-pulse ensures the final phase is the difference between these phases

$$\begin{aligned} \Phi(\tau) &= \phi_2(\tau/2) - \phi_1(\tau) \\ &= -\frac{\hbar\gamma_{NV} B_z}{2\pi\nu}\left[\cos(2\pi\nu\tau/2 + \phi_0) - \cos(2\pi\nu\tau + \phi_0) - \cos(\phi_0) + \cos(2\pi\nu\tau/2 + \phi_0)\right] \\ &= -\frac{\hbar\gamma_{NV} B_z}{2\pi\nu}\sin^2\left(\frac{\pi\nu\tau}{2}\right)\cos(\pi\nu\tau + \phi_0) \end{aligned} \tag{1.26}$$

We see that the final phase is has maxima near $\nu = n/\tau$ for n being odd integers.

Since eqn. 1.26 is the phase due to a single frequency environment, by plotting it as a function of frequency (and setting $\phi_0 = 0$), we obtain the Spin Echo's response to each frequency component of the environment given a fixed evolution time τ (Fig. 1.22c). Such functions are called the filter function of the sequence. The Spin Echo filter function is peaked at the resonance $\nu = 1/\tau$, with the higher/lower harmonics falling off in amplitude. The width of the resonance is about $0.5/\tau$. The total phase accumulated during a measurement is a convolution between the filter function and the noise spectrum of the environment.

Typically, to measure the lifetime, τ is swept, which sweeps the location of the filter function resonance as well. Sometimes, this makes interpreting the underlying physics of the environment more difficult, as different aspects of the environment are probed at each time-step of the measurement. Other times, this sweeping is useful for performing spectroscopy on the noise environment: the signal decays sharply at some τ corresponding to a large noise at $\nu = 1/\tau$ and revives at other τ where there are no noise sources at a corresponding frequency. For this reason, Spin Echo has immense popularity in multiple scientific fields.

A few remarks are in order. First, since the actual phase accumulated is the convolution of the filter function and the noise spectrum of the environment, if off-resonant noise is much stronger than resonant noise, the signal can still decay significantly. Second, Spin Echo is a particular form of the more general suite of measurement protocols called Hahn Echo. These sequences vary the pulse angles as well as the timing between pulses to alter the filter function. They have been developed by the NMR community since Hahn's original paper in 1950 [62], and should be kept in mind as a worthwhile literature review. Finally, the concept of the filter function only works for correlated noise. If the noise is truly uncorrelated and random, there is no reason applying a π-pulse should cancel any phase accumulation. We can see that the phase integrals usually average out to zero, but the variance of the integrals becomes nonzero. The variance autocorrelation of the noise becomes the source of decay (first type of decoherence), and the sequence effectively reduces to a Ramsey sequence, incapable of filtering any noise (Section 4.4).

1.5.10 DEER

The double electron-electron resonance (DEER) sequence is the same as Spin Echo, except that during the refocusing π-pulse, an additional pulse is applied to the environment bath (Fig. 1.23a). Assuming the additional pulse is a resonant π-pulse, the bath will reorient in time with the probe and pass completely through the Spin Echo filter. For this reason, DEER is effectively a Ramsey sequence performed on a select portion of the environment. The selectivity grants DEER exceptional versatility as a spectroscopic tool. Holding evolution times τ fixed, one could sweep the frequency of the bath pulse to perform an effective ODMR on the bath (Fig. 1.23b). Sweeping the duration or power of the bath pulse (the pulse angle) performs an effective Rabi measurement on a particular portion of the bath (Fig. 1.23c). Finally, sweeping the evolution time, the decay profile is a direct measurement of the probe's interaction strength J with the selected bath $T_2^{DEER} \sim 1/J$. The resultant interaction-induced decay can be either a dephasing or decoherence process, depending on what the bath is and whether its interaction with the NV is coherent or incoherent (Fig. 1.23c).

1.5.11 CPMG and XY8

The Carr-Purcell-Meiboom-Gill (CPMG) and XY8 dynamical decoupling pulse sequences (Figure 1.24) both accomplish the same goals: reduce the width of the filter function resonance, ensure the location of the resonance does not move, and suppress all off-resonant

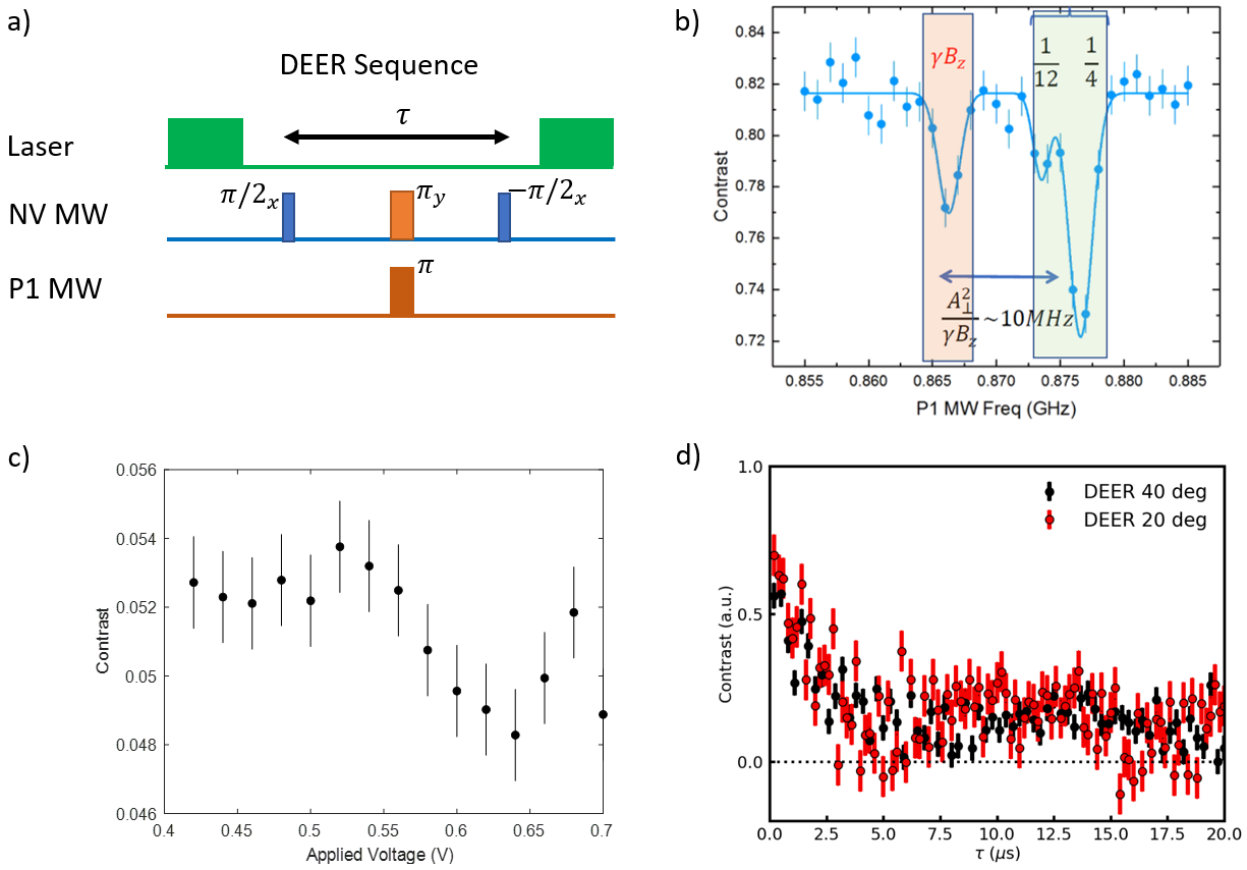

Figure 1.23: a) The DEER pulse sequence. b) As zoomed in portion of the spectrum of P1 centers (around 875 MHz) and a free electron (around 865 MHz) at 309 G. c) P1 Rabi oscillation vs the microwave pulse's applied voltage. Because at sufficiently lower voltages, the P1s are not driven, the curve should initially be flat before the oscillations begin. d) DEER coherence decay measurement on P1 centers for variable external magnetic field angle applied.

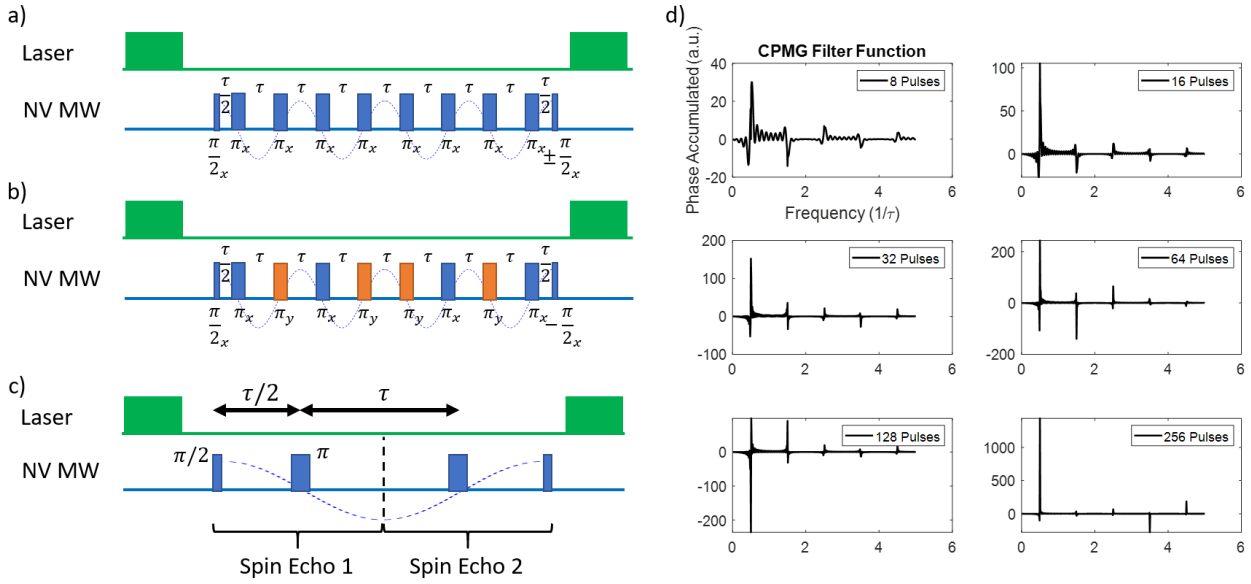

Figure 1.24: a) The CPMG pulse sequence. The phase accumulation of noise on resonance with the filter function (blue dashed) is not suppressed. The polarity of the final $\pi/2$-pulse depends on the number of pulses in the sequence. b) The XY8 pulse sequence with unfiltered phase accumulation (blue dashed) c) Zoom in on a two-pulse CPMG sequence to emphasize how it can be decomposed into two concatenated Spin Echo sequences with unfiltered phase accumulation (blue dashed). d) Filter function of CPMG vs pulse number for a sinusoidal magnetic field with initial phase $\pi/4$. With increasing pulse number, the resonances in the filter function sharpen and harmonics usually become suppressed. The shape of the filter function is highly sensitive to the initial phase.

noise to a greater extent than Spin Echo. First, by extending the Spin Echo protocol with more π-pulses; with ever more pulses, fewer frequencies are close enough to meeting the resonance condition to contribute significant phase, reducing the filter function width. Second, by keeping the inter-pulse time τ_p fixed and adding more pulses on each iteration, the total evolution time of the measurement can be swept without sweeping the resonance condition. Finally, by applying π-pulses more often with small τ_p evolution time, the small phase accumulation during each τ_p is quickly cancelled, minimizing the effects of dephasing and decoherence from environmental changes.[30] This last feature drastically facilitates the interpretation of CPMG and XY8 data, since it must be dominated by environmental interactions on resonance with the protocol. In this case, the $T_2^{CPMG/XY8}$ decay time is usually

[30]In the extreme case of our dense NV ensemble (Chapter 4), Spin Echo, CPMG, and XY8 filter enough of the environmental interactions such that the dominant interaction became the unfiltered NV-NV interaction. These measurements became NV-NV Ramsey measurements, proving once again, that Ramsey is not so simple as it seems.

due to the variance in the autocorrelation of the noise environment, as discussed in Section 1.5.9 and especially in Section 4.4. If desired, the number of pulses can be held fixed and the evolution time swept instead for noise spectroscopy with an improved filter (see Section 5.3.2); though the interpretation of the decay is again more difficult (Section 1.5.9).

The difference between CPMG and XY8 is the degree to which they suppress certain types of pulse error. In theory, XY8 should reduce the effects of pulse error more than CPMG. By alternating π-pulses around the X and Y axes, the XY8 pulses repeatedly perform Spin Echo sequences on their own pulse error. In practice, it does not always perform better [8]. There are also other pulse sequences (XY4, KDD, etc.) that also address pulse error, with varying degrees of success. For all of these pulse error-correcting sequences, the entire sequence must be applied to suppress the error. Performing only a portion of the pulses in these sequences could actually magnify the pulse error. For this reason, CPMG is more advantageous to perform when early-time resolution is necessary, since it can be performed with only 2 π-pulses.

Note, the evolution time $\tau/2$ between the $\pi/2$-pulses and their adjacent π-pulse is half of the time τ between adjacent π-pulses. The intuition for this is that at a time $\tau/2$ halfway between the π-pulses, the Bloch vector should refocus into an Echo. Clearly, these protocols are simply repeating Spin Echo multiple times over. However, despite concatenating Spin Echo, the filter function resonance frequency of CPMG and XY8 is half that of Spin Echo. Comparing the diagrams for each sequence closely (Figures 1.22 and 1.24), we see that to resonate with CPMG and XY8, the noise must progress through only a quarter of a cycle for each $\tau/2$, whereas it must progress a half-cycle in the same time for Spin Echo.

Lastly, like Spin Echo, CPMG and XY8 both lend themselves to a DEER/Ramsey modification simply by applying bath pulses concurrently with the probe pulses. One caveat to note is that because the sequences suppress noise, they also suppress DC disordered fields for both the probe and the bath spins.[31] Less disorder means that the probe is more likely to be on resonance with the bath spins, and the bath spins more on resonance with each other, boosting each interaction.

1.5.12 Correlation Spectroscopy

While we ultimately did not use any of the data, we did perform some measurements with the correlation spectroscopy technique and discussed its viability many times. For completion, I think it is worth mentioning broadly. Since it comes in many forms, I will stick only to the form used in NV experiments for measuring properties of a bath. In this case, what seems to confuse the most people is that correlation spectroscopy is *not* a coherence interference measurement even though it looks like one. It works by first creating a correlation function between two measurements of NV phase, rather than interfering the two phases (adding

[31] Each bath spin also accumulates phase due to random DC fields. By applying pulses to the bath, its phase is also cancelled out.

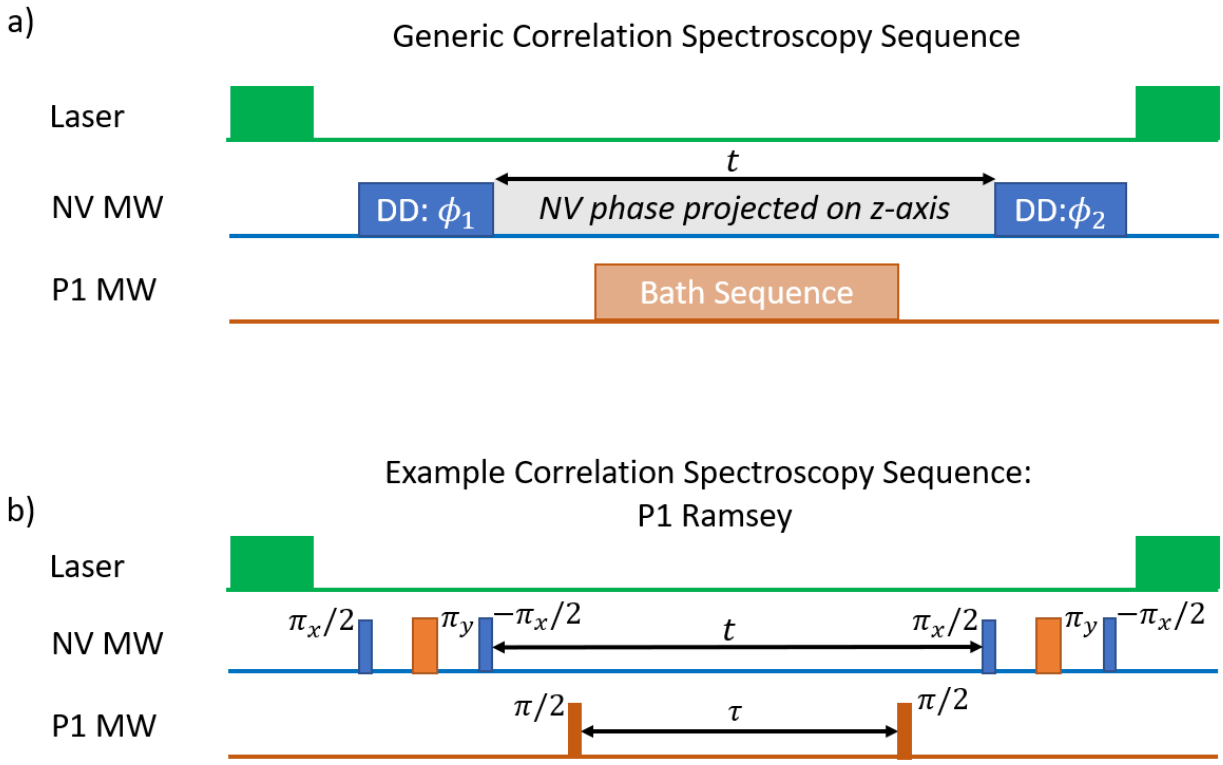

Figure 1.25: a) A block diagram of the correlation spectroscopy sequence as used for measurements on a bath. Two identical dynamical decoupling (DD) sequences are applied to the NV, with a fixed wait time $t \gg T_2$ separating them. At the end of the first dynamical decoupling sequence, the NV has accumulated ϕ_1 phase from the environment and its Bloch vector has been projected onto the z-axis of the Bloch sphere. The magnitude of this projection is determined by ϕ_1. The second NV dynamical decoupling imparts ϕ_2 phase onto the NV and creates a correlation function relating the two phases. The value of this correlation function changes as the bath measurement sequence changes. b) An example of a correlation spectroscopy sequence that measures P1 Ramsey. The two NV dynamical decoupling sequences are Spin Echo sequences. The Bath sequence is the P1 Ramsey sequence. The value of the correlation function changes with the free induction decay time τ, reflecting the Ramsey measurement.

or subtracting them). Then, changes in the phase correlations reflect the result of the measurement performed on the bath.

A generic correlation spectroscopy sequence is shown in the block diagram of Figure 1.25a and one particular example, of the many possibilities, is shown in Figure 1.25b. The sequence is composed of three essential parts: 1) an initial dynamical decoupling sequence on the NV; 2) a wait period during which a measurement sequence is applied to the bath; and 3) a final dynamical decoupling sequence on the NV.

First, a dynamical decoupling sequence is applied to the NV, so it gains some phase ϕ_1. By the end of this step, the NV has been projected back onto S_z, the z-axis of the Bloch sphere.[32] The phase ϕ_1 determines the magnitude of the this projection. For this particular run of the measurement, the NV signal S_1 at the end of this step is

$$S_1 \sim F(\phi_1)$$

where F is some function determined by the particular dynamical decoupling sequence applied. Second, a fixed wait period $t \gg T_2$ is applied to the NV, and a measurement sequence is applied to the bath. It is crucial that the wait period is much longer than the NV's decoherence time. This ensures any S_x or S_y components of the NV's Bloch vector are decohered and may be safely ignored. Finally, a second dynamical decoupling sequence is applied to the NV. This sequence is identical to the first and imparts a phase ϕ_2 on the NV. If it were the only measurement performed on the NV, the signal would be $S_2 \sim F(\phi_2)$, but because the first two parts of correlation spectroscopy reduced the length of the NV's Bloch vector to S_1, the final signal for one run of the measurement is the product of the two

$$S \sim S_1 S_2 \sim F(\phi_1)F(\phi_2)$$

By repeating the measurement sequence many times, we take the average of the final signal

$$\langle S \rangle \sim \langle F(\phi_1)F(\phi_2) \rangle \tag{1.27}$$

This result is a correlation function that relates the two phases accumulated by the NV.

The value of each phase changes on each run of the measurement, but the correlation between them is constant for constant NV and bath measurement sequences. Varying the bath measurement sequence will change the correlation between the two phases.[33] Tracking these changes in the correlation with respect to the bath measurement then extracts the desired information about the bath.

[32] I use the word "projected" here instead of the usual word "stored." When people say the phase or magnetization is stored on the z-axis, it sounds like the all of the information of the Bloch vector is saved for later. This is absolutely false. By saying "projected" I hope it is a bit clearer that information about S_x and S_y will be thrown out during the wait period.

[33] We assume we keep t and the NV sequence fixed, so it is strictly a bath measurement. If we allow these to vary, they will also affect the correlation.

As an example, Figure 1.25b shows what the sequence looks like when the two dynamical decoupling sequences are Spin Echo sequences, and the bath sequence is a Ramsey measurement on the P1s. The final signal in this case should be

$$\langle S \rangle \sim \langle \sin(\phi_1)\sin(\phi_2) \rangle \tag{1.28}$$

since the final S_z projection from a Spin Echo sequence is a trigonometric function of the phase accumulated. By sweeping the free induction decay time τ of the P1s and holding the wait time of the NV, this correlation function reflects the results of the P1 Ramsey measurement.

1.5.13 Other Dynamical Decoupling Sequences

While the dynamical decoupling sequences outlined above are excellent at decoupling off-resonant on-site disorder (S_z-dominated noise), they do nothing to filter out transverse interactions (S_x-dominated). Typically, the large ZFS or the application of an external aligned magnetic field suppress transverse noise without the need for a pulse sequence, but when that noise is on resonance (e.g. resonant flip-flop dipolar interaction), they become significant hindrances and sometimes desirable targets of study. Thankfully, there are many other dynamical decoupling sequences in existence, some with names like WAHUHA and DROID [24, 169] and some unnamed, that can accomplish this. As a general principle, sequences can only cancel interactions along the axis for which they consider phase accumulation. The measurements described above only consider phase rotations around the z-axis, limiting them to S_z noise. By contrast, WAHUHA and DROID rotate the Bloch vector sequentially to each of the x, y, and z axes to collect phase along all of them. New pulse sequences are crafted all the time for the unique purposes of the immediate experiment—one should not hesitate to seek them out or invent for something new.

As an aid to compare common NV measurement protocols, Tables 1.3, 1.4, and 1.5 compile all of the spectroscopic techniques mentioned in this chapter as well as a few others. This is by no means an exhaustive list.

Name & Description	Measures	Pros	Cons
Continuous ODMR Laser/MW always applied	T_2^*, NV Resonance	• Easiest implementation; no need for pulsed controls • Very fast for low frequency resolution	• Difficult to set resolution due to competition between laser and MW power • Contrast drastically reduces with increased resolution
Pulsed ODMR One MW pulse	T_2^*, NV Resonance	• Frequency resolution equals the Rabi frequency Ω	• Slower than cODMR at low resolution

Table 1.3: Summary of spectroscopic measurement protocols for NV resonances. MW frequencies are swept.

Name & Description	Measures	Pros	Cons
T_1 Polarize-τ-Readout	T_1, Resonant Noise	• Easy implementation	• Must sweep B-field strength for full noise spectrum
Ramsey $\pi/2$-τ-$\pi/2$	T_2^*	• Easy implementation • Dominated by DC noise	• Difficult when $T_2^* \sim \Omega$ • Hard interpretation in the presence of many noise sources
Spin Echo $\pi/2$-$\tau/2$-π-$\tau/2$-$\pi/2$	T_2^{Echo}	• Easy implementation • Widely used (many references) • Filters DC noise	• τ-sweep changes location of filter function, changing susceptibility to noise sources
Hahn Echo (Instantaneous Diffusion) $\pi/2$-$\tau/2$-θ-$\tau/2$-$\pi/2$	Intragroup interaction (at high density)	• Widely used in NMR • Provides a continuous probe parameter θ	• No clear quantum coherent intuition (classical picture as a probabilistic flipping of spins) • Susceptible to undesired noises • Need to apply 4 times in a row with "phase-cycling" technique
CPMG $\pi/2$-$(\tau/2$-π-$\tau/2)^N$-$\pi/2$	T_2^{CPMG}, Intragroup interaction (at high density), an AC signal synchronized to pulse timing	• Isolates AC signal • Strongly suppress off-resonant noise • Sweeping N fixes filter function location • Better time resolution than XY	• For sensing: limited by intragroup interaction for high density samples • Sometimes worse pulse error than XY
XY-[4,8,16, ...] Similar to CPMG, but phase of π-pulse alternates	T_2^{XY}, Intragroup interaction (at high density), an AC signal synchronized to pulse timing	• Isolates AC signal • Strongly suppress off-resonant noise • Sweeping N fixes filter function location • Sometimes better pulse error than CPMG	• For sensing: limited by intragroup interaction for high density samples • Worse time resolution than CPMG

Table 1.4: Summary of spectroscopic measurement protocols using NVs. Sweep evolution time τ for first four, and the number of pulses for the last two. Ω is Rabi frequency.

Name & Description	Measures	Pros	Cons
DEER (aka SEDOR) Similar to Spin Echo, but during π-pulse there is an additional pulse on the target spin	Intra- and Inter-group interaction, Resonance spectrum of target spin	• Applies to any MW-addressable spin • Can perform ODMR / Rabi on target spin. • Corresponds to NV-Ramsey, isolating target spin contribution • Basic idea extends to other sequences	• Intragroup interactions may dominate (high density)
WAHUHA $\{\frac{\pi_x}{2}$-2τ-$\frac{-\pi_x}{2}$-τ-$\frac{\pi_y}{2}$-2τ-$\frac{-\pi_y}{2}$-$\tau\}^N$	T_2^{WAHUHA}	• Cancels interactions between spin-1/2 (e.g. P1s) • Can apply in parallel to NV sequence • Can be applied to NVs to turn dipolar into Heisenberg interaction	• (High density) limited by higher-order interaction terms
Correlation Spectroscopy Two DD sandwiching bath sequence DD spacing $\gg T_2$	Bath's T_1, T_2^*, T_2, τ_c	• Uses NV to measure defects that can't be read directly	• Low contrast/long integration
Stimulated Echo In general: any 3 pulses with spacing $\ll T_2$ In particular: Correlation spectroscopy with DD spacing $\ll T_2$	Combination of T_1, T_2^*, T_2, τ_c	• Widely used in NMR	• Signal includes contributions from T_1, T_2^*, T_2, τ_c • Often an unwanted byproduct • Not clearly useful to NV community
Advanced DD Specified by designer	Specified by designer	• Can design pulse sequences to suppress interactions, on-site fields, pulse errors... [24]	• May be difficult to realize in a lab (e.g. limited power and inhomogeneity of MW driving)

Table 1.5: Summary of spectroscopic measurement protocols on: P1, ^{13}C, other NV groups, any MW-addressable spin. DD is dynamical decoupling and τ_c is the correlation time of the bath.

Chapter 2

Imaging the Local Charge Environment

2.1 Introduction

In the previous chapter, we motivated and outlined the use of NV centers [34, 132] as sensors, establishing that its electronic spin is sensitive to a wide range of external signals [108, 100, 155, 2, 45, 37, 36, 35, 93, 6]. While the language employed was specific to the NV, the ideas are general to many nano-scale solid-state defects, which has generated great intrigue [5, 132]. In this chapter, we explore one of the primary obstacles to using any solid-state defect. The sensitivity of these defects is a double-edged sword: at once suggesting their use as nanoscale quantum probes of *external* signals, but muddling the desirable signal with a turbulent *internal* local environment. To successfully utilize these defects in a tool, one must accurately calibrate the tool itself first.

Pre-calibration is especially germane to probes composed of spin defect ensembles. As a means to enhance the probe's sensitivity, many efforts have focused on exploiting the power of many-body correlations available in interacting ensembles [158, 135, 80, 19, 25]. In NV systems, numerous studies have striven toward this goal by leveraging the properties of high-density NV systems [3, 144, 99, 2, 140, 123, 74, 11, 75]. However, the local environment of dense ensembles is far more complex than that of single defects, owing to the fact that with high NV densities come high densities of other defects. As a result, multiple effects contribute to the local noise: lattice strain, paramagnetic impurities, charge dynamics, and NV-NV dipolar interactions. Depending on the diamond sample, some or all of these effects strongly influence the NV's magnetic spectrum. Most often though, an external magnetic field is applied to suppress undesirable effects, but doing so constrains the scope of sensing applications to those that can tolerate the extra field. Other applications would remain inaccessible, such as zero-field nuclear magnetic resonance spectroscopy [159, 151], or strain-sensing [136] (see also Chapter 3). Thus, studying the zero-field spectral properties of NV ensembles is a crucial step towards expanding the versatility of defect-based quantum sensors.

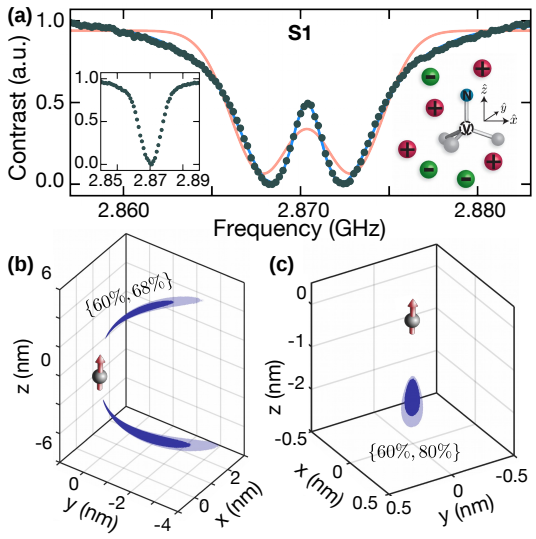

Figure 2.1: Typical optically-detected magnetic resonance (ODMR) spectrum of an electron-irradiated and annealed Type-Ib diamond sample (S1) at zero magnetic field. The spectrum exhibits heavy tails which cannot be reproduced by either a double Lorentzian or Gaussian (orange fit) profile. The blue theory curve is obtained via our microscopic charge model. (Left inset) A typical zero-field spectrum for a single NV center shows only a single resonance. (Right inset) Schematic depicting an equal density of positive (e.g. N^+) and negative (e.g. NV) charges, which together, create a random local electric field at each NV center's position. (b) Nanoscale localization (∼5 nm) of a single positive charge via dark-state spectroscopy of an isolated NV center. The shaded regions indicate the probable location of the charge with darker indicating a higher likelihood. Percentages shown correspond to the confidence intervals of the dark/light region, respectively. (c) Analogous localization of a more proximal charge defect (∼2 nm) for a different NV center.

In this chapter, we present three main results. First, we demonstrate that the characteristic splitting of the NV's magnetic resonance spectrum (Fig. 2.1a), observed in ensemble NV experiments [59, 89, 14, 37, 68, 49, 171, 134, 4, 86, 90, 17, 130, 73, 134, 104, 22, 96, 142], originates from its local electric environment; this contrasts with the conventional picture that strain dominates the zero-field properties of these systems (Section 2.2). Second, we introduce a charge-based model (Fig. 2.1a, right inset) that quantitatively reproduces the observed ODMR spectra for samples spanning two orders of magnitude in NV density (Section 2.3). Third, our model suggests the ability to directly *image* the position of individual charges inside the diamond lattice (Section 2.4. To this end, we propose and implement a novel method that localizes such charges to nanometer-size volumes (Fig. 2.1b,c). The essence of our approach is to leverage the interplay between the polarization of the applied microwave field and the orientation of the local electric field. After discussing the results,

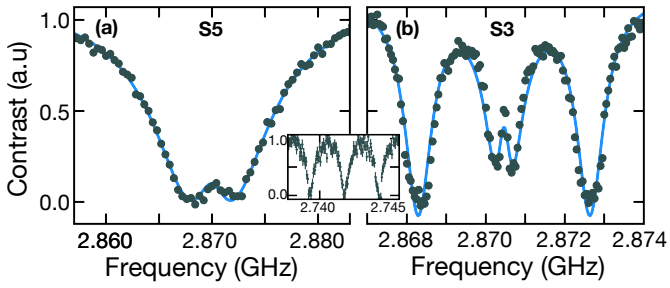

Figure 2.2: Pulsed ODMR spectra at zero magnetic field for (a) a Type-Ib untreated diamond sample (S5) and (b) a Type-IIa electron-irradiated and annealed sample (S3). The spectra portray the two qualitative regimes one expects based upon the average electric field strength as shown schematically in the right panel of Fig. 2.3d. The blue theory curve is obtained via our microscopic charge model. (inset) The spectrum for S3 at a magnetic field ≈ 45 G exhibits three identical hyperfine resonances.

we provide more details into the methods involved in this work.

2.2 Magnetic spectra of NV ensembles

As discussed in Chapter 1, the NV center has a spin triplet ground state ($|m_s = \pm 1, 0\rangle$), which can be initialized and read out via optical excitation and coherently manipulated using microwave fields [107]. In the absence of any external perturbations, the $|m_s = \pm 1\rangle$ states are degenerate and separated from $|m_s = 0\rangle$ by $D_{\rm gs} = (2\pi) \times 2.87$ GHz (Fig. 2.3a).

This leads to the usual expectation of a single resonance peak at $D_{\rm gs}$, consistent with experimental observations of isolated NVs (Fig. 2.1a, inset). However, for high-density NV ensembles, one observes a qualitatively distinct spectrum, consisting of a pair of resonances centered at $D_{\rm gs}$ (Fig. 2.1a, sample S1). This spectrum poses a number of puzzles: First, the line-shape of each resonance is asymmetric and cannot be captured by either a Gaussian or Lorentzian profile. Second, the central feature between the resonances is sharper than the inhomogenous linewidth. Third, despite the presence of a strong *splitting*, there exists almost no *shift* of the NV's overall spectrum.

These generic features are present in diamond samples with NV and P1 (nitrogen impurity) densities spanning over two orders of magnitude. Fig. 2.2 demonstrates this ubiquity. In particular, it depicts the spectrum for two other samples: one with a significantly lower NV concentration (Fig. 2.2a, sample S5) and a second with significantly lower concentrations for both NVs and P1s (Fig. 2.2b, sample S3). In this latter case, the P1 density is low enough that the hyperfine interaction between the NV's electronic spin and its host ^{14}N nuclear spin can be resolved. Normally, this hyperfine splitting would simply result in three identical resonances split from one another by $A_{zz} = (2\pi) \times 2.16$ MHz [137] (Fig. 2.2, inset).

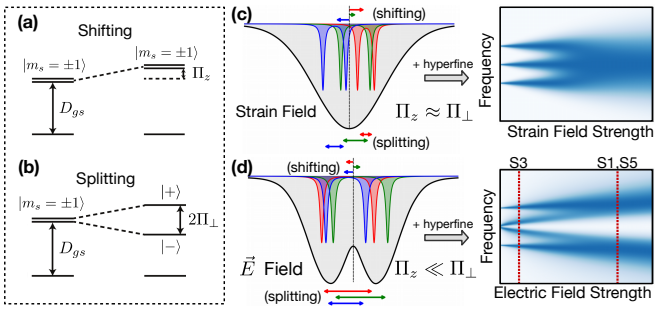

Figure 2.3: Both strain and electric fields lead to (a) shifting Π_z and (b) splitting $2\Pi_\perp$ of the $|m_s = \pm 1\rangle$ manifold. (c) When averaged over an ensemble of NV centers, random local strain fields lead to a single broad spectral feature (at large strain). (d) In contrast, random local electric fields lead to two distinct spectral regimes: at small electric fields, the center hyperfine resonance splits, leading to a total of four resolvable features (S3); at large electric field, one obtains the characteristic split resonance seen in typical high density NV ensembles (S1, S5).

However, as shown in Fig. 2.2b, one finds that the central hyperfine resonance is split in direct analogy to the prior spectra.

The most distinct of the aforementioned features – a split central resonance – has typically been attributed to the presence of lattice strain [14, 37, 68, 49, 171, 134, 4, 86, 90, 17, 130, 73, 134, 104, 22, 96, 142]. Such strain can indeed lead to a coupling between the $|m_s = \pm 1\rangle$ states, and thus split their energy levels. However, a more careful analysis reveals an important inconsistency. In particular, given the measured strain susceptibility parameters [14], for each individual NV, any strain-induced splitting should be accompanied by a comparable shift of the overall spectrum (Fig. 2.3). When shifting is comparable to splitting, each NV typically leaves a resonance at the central frequency value. Ensemble averaging then naturally leads to a spectrum that exhibits *only* a single broadened resonance (Fig. 2.3c).

2.3 Microscopic charge model

In contrast, we demonstrate that all of the observed features can be quantitatively explained via a microscopic model based upon randomly positioned charges inside the diamond lattice. The physical intuition underlying this model is simple: each (negatively charged) NV center plays the role of an electron acceptor, and charge neutrality implies that there must be a corresponding positively charged electron donor (typically thought to be N^+, a positively charged P1 center).

Such charges produce an electric field that also (like strain) couples the $|m_s = \pm 1\rangle$ states, leading to the splitting of the resulting eigenstates. Crucially, however, the NV's susceptibility to transverse electric fields (which cause splitting) is ∼50 times larger than its suscep-

Sample	ρ_c (ppm)	ρ_{NV} (ppm)	ρ_s (ppm)	Γ (MHz)
Ib treated (S1)	1.35(5)	1-10	70(5)	1.16(2)
Ib treated (S2)	1.7(1)	1-10	100(5)	0.78(3)
IIa treated (S3)	0.06(2)	0.01-0.1	12(3)	0.26(2)
Ib untreated (S4)	3.6(4)	0.001-0.01	90(20)	1.0(1)
Ib untreated (S5)	0.9(2)	0.001-0.01	130(30)	3.3(1)
IIa untreated (S6)	0.05(1)	0.001-0.01	16(2)	0.08(3)

Table 2.1: Summary of the measured and extracted parameters for each diamond sample. ρ_c and Γ are directly extracted from our microscopic model, while ρ_s is independently measured at high magnetic fields and ρ_{NV} is estimated from fluorescence counts.

tibility to axial electric fields (which cause shifting) [119, 1]. This implies that even upon ensemble averaging, the electric-field-induced splitting remains prominent (Fig. 2.3d).

Qualitative picture in hand, let us now introduce the details of our microscopic model. In particular, we consider each NV to be surrounded by an equal density, ρ_c, of positive and negative charges[1]. These charges generate a local electric field at the position of the NV center and couple to its spin via the Hamiltonian:

$$\begin{aligned} H = &\left(D_{gs} + \Pi_z\right) S_z^2 + (\delta B_z + A_{zz} I_z) S_z + \\ &\Pi_x (S_y^2 - S_x^2) + \Pi_y (S_x S_y + S_y S_x). \end{aligned} \tag{2.1}$$

Here, $\hat{z}$ is the NV-axis, $\hat{x}$ is defined such that one of the carbon-vacancy bonds lies in the x-z plane (Fig. 2.1a, right inset), $\vec{S}$ are the electronic spin-1 operators of the NV, $\vec{I}$ are the nuclear spin-1 operators of the host ^{14}N [2], and δB_z represents a random local magnetic field (for example, generated by nearby paramagnetic impurities). Note that we absorb the gyromagnetic ratio into δB_z. The two terms $\Pi_{\{x,y\}} = d_\perp E_{\{x,y\}}$ and $\Pi_z = d_\parallel E_z$ characterize the NV's coupling to the electric field, $\vec{E}$, with susceptibilities $\left\{d_\parallel, d_\perp\right\} = \{0.35, 17\}$ Hz cm/V [119].

In order to obtain the spectra for a single NV, we sample $\vec{E}$ and δB_z from their random distributions and then diagonalize the Hamiltonian. Moreover, to account for the natural linewidth of each resonance, we include an additional Lorentzian broadening with full-width-half-maximum, Γ (Section 2.6.3). Averaging over this procedure yields the ensemble spectrum. The distribution of $\vec{E}$ is determined by the random positioning of the aforementioned charges. The distribution of δB_z is determined by the local magnetic environment, which depends sensitively on the concentration of spin defects (Table 2.1).

[1] We assume that the charges are independently positioned in three dimensions

[2] We note that the the hyperfine interaction in the Hamiltonian is obtained under the secular approximation.

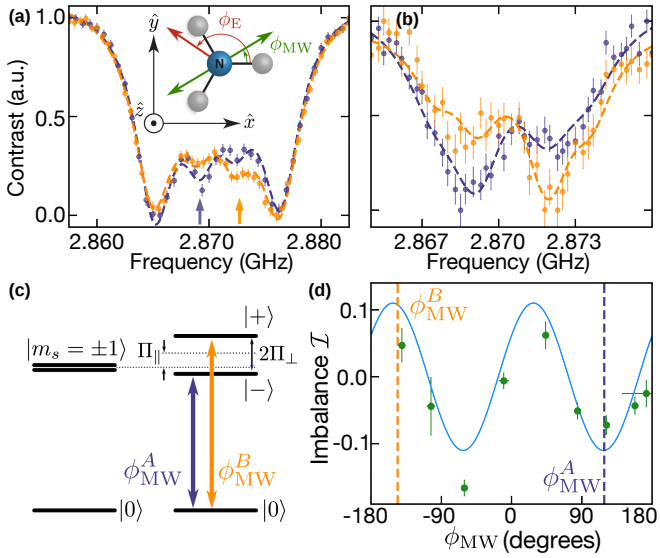

Figure 2.4: Charge localization via dark-state spectroscopy. (a) Single NV ODMR spectra (untreated Type-Ib diamond) for two different microwave polarizations, ϕ_{MW}, depicting the reversal of the split-peak imbalance. The data correspond to the localized charge shown in Fig. 2.1b. (inset) Top view through the NV-axis ($\hat{z}$), where ϕ_E and ϕ_{MW} are defined with respect to $\hat{x}$ (along a carbon-vacancy bond). (b) Analogous split-peak imbalance data corresponding to the localized charge shown in Fig. 1c. (c) By changing the microwave polarization, ϕ_{MW}, one can directly control the coupling strength between the $|0\rangle$ and $|\pm\rangle$ states. (d) Measuring the change in the imbalance as a function of ϕ_{MW} allows one to extract the orientation of the electric field. Dashed lines indicate the polarizations plotted in (a).

In samples S1 and S5 (Type-Ib diamond), δB_z is dominated by the dipolar interaction with a high-density P1 spin bath, whose concentration, ρ_{s}, is independently characterized. Meanwhile, in sample S3 (Type-IIa diamond), the P1 density is over two orders of magnitude smaller, leading to a δB_z that is dominated by interactions with ^{13}C nuclei (with a natural abundance of 1.1%); despite this difference in microscopic origin, one can also characterize the effect of this nuclear spin bath using an effective density, ρ_s. For each sample, using this independently characterized ρ_{s}, we then fit the experimental spectrum by varying ρ_{c} and Γ . We find excellent agreement for all three samples (Fig. 2.1, 2.2) despite their vastly different defect concentrations (Table 2.1).

A few remarks are in order. First, the presence of local electric fields suppresses the effect of magnetic noise when $\delta B_z \ll \Pi_\perp = \sqrt{\Pi_x^2 + \Pi_y^2}$. This is precisely the origin for both the sharpness of the inner central feature seen in Fig. 2.1a, as well as the narrowness of the inner hyperfine resonances seen in Fig. 2.2b. In the absence of electric field, the magnetic noise B_z leads to a *symmetric* lineshape arising from the symmetric distribution of B_z. However, in the presence of an electric field, the energy splitting is given by $2\sqrt{(gB_z)^2 + \Pi_\perp^2}$, where

g is the Landé g-factor of NV^- electron. As a result, for the local charge configuration of each NV^-, there is a minimum splitting of $2\Pi_\perp$ and the presence of B_z can only increase it, leading to an *asymmetric lineshape*. These results then also suggest that the density of the charge defects is similar to the density of NV^-; because most configurations have a non-zero minimum splitting $2\Pi_\perp$, the ensemble averaging largely preserves this sharp inner feature. Second, in samples where the electric field dominates, the long-range, power-law nature of the electric field leads to a particularly heavy tailed spectrum. Third, the extracted charge density, ρ_c, is consistent with the estimated NV density, ρ_{NV}, for all "treated" (electron-irradiated and annealed) samples (S1-S3). This agrees with our previous physical intuition: NVs behave as electron acceptors while P1s behave as electron donors. Interestingly, this simple picture does not directly translate to "untreated" samples (S4-S6) where the observed charge density is significantly larger than ρ_{NV} (Table 2.1); one possible explanation is that such samples harbor a higher density of non-NV charged defects (e.g. vacancy complexes [32]).

2.4 Nanoscale imaging of a single charge

Our microscopic model suggests that in samples where one can resolve single NV centers, it should be possible to directly probe the *local* charge environment. However, one expects a key difference in contrast to ensemble measurements: for a single NV, the electric field has a definite orientation with respect to the NV axes (Fig. 2.4a diagram).

Crucially, this orientation (namely, the angle, ϕ_E, in the NV's transverse plane) dictates the way in which the electric field mixes the original $|m_s = \pm 1\rangle$ states into bright and dark states:[3]

$$|\pm\rangle = \frac{1}{\sqrt{2}}\left(|m_s = +1\rangle \mp e^{-i\phi_E}|m_s = -1\rangle\right). \tag{2.2}$$

Applying a linearly polarized microwave field will then drive transitions between the $|m_s = 0\rangle$ state and the $|\pm\rangle$ states. However, the relative strength of the two transitions depends on both ϕ_E and the polarization of the microwave field, ϕ_{MW} (Fig. 2.4c). Thus, one generally expects the measured amplitudes of the corresponding resonances to be different. These expectations are indeed borne out by the data (Fig. 2.4a,b) [4]. We note that this observed imbalance in the inner hyperfine resonances for a *single* NV is naturally averaged out in an ensemble measurement.

Our detailed understanding of this spectroscopy for a single NV suggests a novel method to extract the full vector electric field and to localize the position of the corresponding charge. In particular, by measuring the imbalance as a function of ϕ_{MW}, one can extract the electric

[3] So called because for an single NV the bright state can be addressed with microwaves while the dark state theoretically cannot. This leads to the "imbalance" discussed in this section. Albeit, we do not observe perfect bright or dark states. While we did not study deeper as to why, see Section 2.7.4 for our guesses.

[4] We measure the ODMR spectra of 68 single NV centers in an untreated Type-Ib sample, and find four that exhibit a significant electric-field-induced splitting with amplitude difference at zero magnetic field.

Sample name	Synthesis	[N] (ppm)	Electron irradiation dose	Energy (MeV)	Anneal temperature (°C)	Spectrum
Ib treated (S1)	HPHT	$\lesssim$200	2×10^{18} cm^{-2}	2	800	Fig. 2.7a, main text Fig. 1a
Ib treated (S2)	HPHT	$\lesssim$200	1×10^{17} cm^{-2}	14	400; 800; 1200	Fig 2.7b
IIa treated (S3)	CVD	$\lesssim 1$	1×10^{17} cm^{-2}	2	700; 875	Fig. 2.7c, main text Fig. 2a
Ib untreated (S4)	HPHT	$\lesssim$200	n/a	n/a	n/a	Fig. 2.8a
Ib untreated (S5)	HPHT	$\lesssim$200	n/a	n/a	n/a	Fig. 2.8b, main text Fig. 2b
IIa untreated (S6)	CVD	$\lesssim$1	n/a	n/a	n/a	Fig. 2.8c

Table 2.2: Details of all samples shown in main and supplementary text. All samples are sourced from Element Six. [N] is specified by the manufacturer.

field orientation, ϕ_E. More specifically, we define the imbalance, $\mathcal{I} \equiv \frac{A_+ - A_-}{A_+ + A_-}$, where $A_\pm$ are the amplitudes of the $|m_s = 0\rangle \leftrightarrow |\pm\rangle$ resonances and derive:

$$\mathcal{I} \sim -\cos(2\phi_{MW} + \phi_E). \tag{2.3}$$

Thus, $\phi_E = 124(5)^\circ$ can be extracted as the phase offset in Fig. 4d. In combination with the observed splitting and shifting of the inner resonances, $\Pi_z = 30(50)$ kHz, $\Pi_\perp = 650(10)$ kHz, one can fully reconstruct the local electric field vector. We do not observe any changes to this field over the course of the experiment (months) and find that it varies for different NV centers. This suggests that it originates from a stationary local charge environment. Moreover, charge neutrality and a low defect density suggest that the electric field is generated by a single positive charge, which we can then localize to within a nanoscale volume (Fig. 2.1b,c).

2.5 Apparatus and Samples

2.5.1 Sample details

The six diamond samples used in this work are all sourced from Element Six. Three of them have been treated (electron irradiation at Prism Gem and vacuum annealing) to increase NV density. The details are listed in Table 2.2.

2.5.2 Experimental apparatus

The experimental apparatus is as described in Section 1.4.3, with some modifications. Foremost, to rotate the MW polarization, we deliver microwaves via a 46 AWG magnet wire. The wire is mounted on a lens rotation mount (Thorlabs RSP05)), and is long enough to prevent major stress on the wire during rotation. By rotating the wire using the mount, we effectively change the polarization of the microwaves at the site of the single NV center of interest. The calculation of the polarization angle in the NV center frame is discussed later in the Section Microwave Angle Projection.

Using a translation stage the height and XY position of the wire is set so the wire hovers a few microns above the back surface of the diamond, and approximately 550 um above the focal plane containing our single NVs. This configuration was designed for simplicity, rather than efficiency. While approximating the microwave linear polarization angle at the location of the NV is simplified, the power delivery to the NV is severely limited, as will be more explicitly addressed in the discussion of Rabi frequency calibration. The wire heats due to poor transmission, but since it is not in thermal contact with the diamond, positional drift of single NVs is undetectable.

When needed, magnetic fields are set by a permanent magnet mounted on adjustable posts. Since only rough alignment to the NV z-axis is required for our purposes, the magnetic fields are aligned by hand. The posts can be moved to different locations on the optical table for alignment to each of the four possible NV orientations.

2.5.3 Isolating single NVs

The diamond sample used for single NV experiments is sample S4 (untreated type Ib). We found a region of the sample where we could isolate single NVs as confirmed by a $g^{(2)}$ measurement (Fig. 2.5).

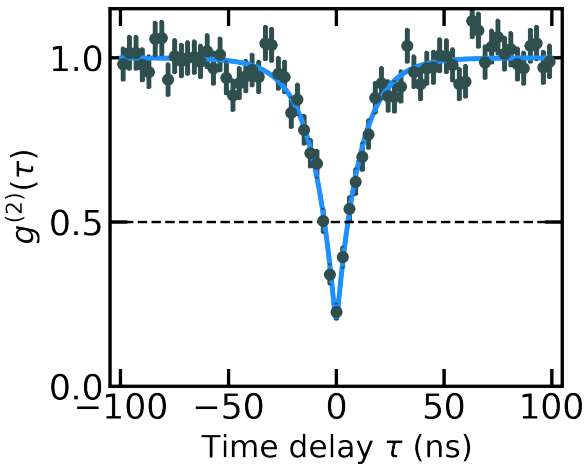

Figure 2.5: $g^2(\tau)$ measurement on NV1: the extracted $g^2(0) = 0.17^{+0.05}_{-0.03} < 0.5$ definitively confirms it is a single NV center.

We chose this type for the high charge density that ensemble measurements on similar samples suggested. High charge density should increase the chance that any given NV would exhibit a signature of local charge in its spectrum.

Whereas the expected NV density of Type Ib diamond precludes addressing single NVs with a diffraction-limited optical resolution, in our sample, the observed NV density varies

over orders of magnitudes between distinct regions. Within one confocal scan, four regions are easily distinguished. In the darkest of these regions, isolated single NVs are spaced roughly 2 μm apart. We do not know the origins of these regions, but suppose they are related to the growth process.

The charge source in regions is highly correlated to the NV density, so we should not expect to find many isolated single NVs exhibiting a charge signature. Indeed, we searched through 68 isolated single NVs in this dark region and found only 4 single isolated NVs exhibiting a charge signature, much lower than the NV density. Evidently, in the low density region, where the NVs are too far apart for their charges to contribute much to each other, charge interaction likely arises due to a mechanism distinct from that of the high density region. Further study is required to understand the origin of charges for individual NVs and whether the charge density can be accurately estimated by the number of spectra exhibiting charge influence.

2.6 Charge model and ensemble spectrum: details

In this section, we provide additional details regarding our charge model. This includes an analysis of the electric and magnetic field distributions, as well as an explanation of the fitting procedure of the ensemble spectra and the estimation of error bars.

2.6.1 Electric field distribution

In our model, we consider each NV to be surrounded by an equal density, ρ_c of positive and negative point-like charges. We simulate the positions of these charges by randomly placing a large number ($N_{\text{charge}} \sim 100$) of points within a spherical volume. The radius of the sphere, R, is determined such that the average density of the charges matches ρ_{c}; in particular, this implies

$$R = \left(\frac{3}{4\pi} \frac{N_{\text{charge}}}{n_0 \rho_{\text{c}}} \right)^{\frac{1}{3}} \tag{2.4}$$

where $n_0 = 1.76 \times 10^{-4}$ (ppm·nm^3)$^{-1}$ is the factor relating the number density (in ppm) to the volume density. Based on the positions of the charges $\{\vec{r}_i\}$, we calculate the electric field at the center of the sphere (the NV's location):

$$\vec{E} = \sum_i \frac{e}{4\pi\epsilon_0\epsilon_r} \frac{\hat{r}_i}{r_i^2} \tag{2.5}$$

where $\epsilon_r = 5.7$ is the relative permittivity of diamond[160].

Sampling over $\{\vec{r}_i\}$ yields a distribution for $\vec{E}$. We are particularly interested in the transverse component, $E_\perp$, which couples ~ 50 times stronger to the NV, i.e. $\Pi_\perp = d_\perp E_\perp$. The distribution $P(\Pi_\perp)$ for various densities are shown in Fig. 2.6. We note that these distributions are related to each other by a simple rescaling, $\Pi_\perp \to \rho_{\text{c}}^{2/3}\Pi_\perp$, though we do not incorporate this rescaling explicitly in our sampling procedure.

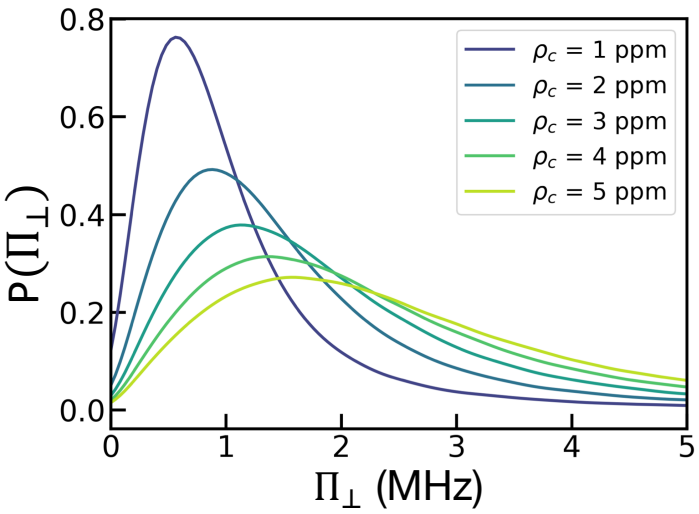

Figure 2.6: Distributions for the transverse electric field component, $\Pi_\perp = d_\perp E_\perp$, at various charge densities. The distributions were generated by the charge sampling procedure described in the text.

2.6.2 Magnetic field distribution

We assume that the local magnetic environment arises from interactions with other magnetic impurities. For Type-Ib diamond, the dominant impurities are the electronic spins associated with P1 centers. For Type-IIa diamond, the leading contribution comes from the nuclear spins associated with ^{13}C (1.1% natural abundance).

In both cases, we model the effect of the magnetic impurities as a dipolar interaction between the NV and a bath of electronic spins $\left(s = \frac{1}{2}\right)$ at density ρ_s:

$$H_{\text{dipolar}} = \sum_i -\frac{J_0}{r_i^3}\left(3(\hat{S}\cdot\hat{r}_i)(\hat{P}_i\cdot\hat{r}_i) - \hat{S}\cdot\hat{P}_i\right). \tag{2.6}$$

Here $\{\vec{r}_i\}$ are the positions of the magnetic impurities, $\hat{S}$, $\hat{P}_i$ are the spin operators for the NV and impurities, respectively, and $J_0 = (2\pi)52$ MHz·nm^3. Under the secular approximation, this interaction further simplifies to:

$$H_{\text{dipolar}} = \delta B_z\ S_z \quad , \quad \delta B_z = \sum_i -\frac{J_0}{r_i^3}\left(3\hat{n}_i^z - 1\right) p_i \ , \tag{2.7}$$

where $\hat{n}_i^z = \hat{z}\cdot\hat{r}_i$, and $p_i = \pm 1/2$ are the spins of the magnetic impurities at the mean-field level.

A few remarks are in order. First, the coupling strength for nuclear spins is ~ 2600 times weaker. This can be effectively modeled by an electronic spin bath, whose the density is

reduced by the same factor. All samples are then characterized with a single parameter ρ_s. Second, the ^{13}C nuclear spins give rise to an additional interaction via the Fermi contact term [137]. Because directly accounting for this is difficult, we approximate its effect as an extra contribution to ρ_s. The resulting spectra are in quantitative agreement with the experimental data at high field (Fig. 2.7,2.8), validating this approximation.

Similar to the electric field distribution, we sample $\{\vec{r}_i\}$ for $N_{spin} \sim 100$ from a sphere whose radius is chosen to be consistent with ρ_s (Eq. 2.4). In this case, we also sample a configuration of spins $\{p_i\}$ from a uniform distribution. Inserting $\{\vec{r}_i\}$ and ρ_s into Eq. 2.7 allows us to calculate δB_z for each realization.

2.6.3 Fitting procedure and error estimation

Our fitting procedure for each ensemble sample consists of two steps. First, we fit a spectrum taken at high magnetic field, where the effects of electric fields are highly suppressed and the dominant broadening is due to magnetic impurities (Figs. 2.7 and 2.8, left column). This allows us to characterize ρ_s independently. Second, we fit a spectrum at zero applied field using the previously determined magnetic noise and an additional contribution due to electric fields (Figs. 2.7 and 2.8, right column). This determines the charge density ρ_c, as well the the natural linewidth Γ.

For the high-field spectra, we sample over the magnetic impurities configurations following the procedure outlined in the previous section. For each configuration, we calculate the NV's resonance frequencies using the full Hamiltonian of the system, Eq. (1) of the main text. Repeating this procedure for ~ 5000 realizations, we obtain a histogram of resonance energies that is proportional to the experimentally observed spectra. We generate such spectra for a range of ρ_s and fit each individually to the high-field measurement, optimizing with respect to the center frequency, vertical offset, and overall amplitude. We characterize ρ_s by calculating the least-square residuals between our simulated spectra and the experimental data (Figs. 2.7 and 2.8, left column). In particular, we identify ρ_s that minimizes the residual as the best-fit parameter and estimate its error from the range of values whose residuals lie within 10% of the minimum.

The fitting procedure for the zero-field spectra follows in close analogy, except we now average over both the charge distribution and the magnetic impurity distribution. Specifically, we first sample the positions of the charges and calculate the electric field at the NV center (~ 5000 realizations). For each charge realization, we then sample over many configurations of magnetic impurities to simulate the magnetic noise (additional ~ 5000 realizations). Another important difference from before is that we now incorporate a natural linewidth for each resonance. To do so, we convolve the distribution of resonance frequencies with a Lorentzian profile characterized by a full-width-half-maximum Γ. This linewidth accounts for broadening that is independent from the charge environment or static magnetic fields. For example, it would include contributions from power broadening, fluctuating fields in the environment (i.e. $T_{2,\mathrm{echo}}$), and strain-induced broadening.

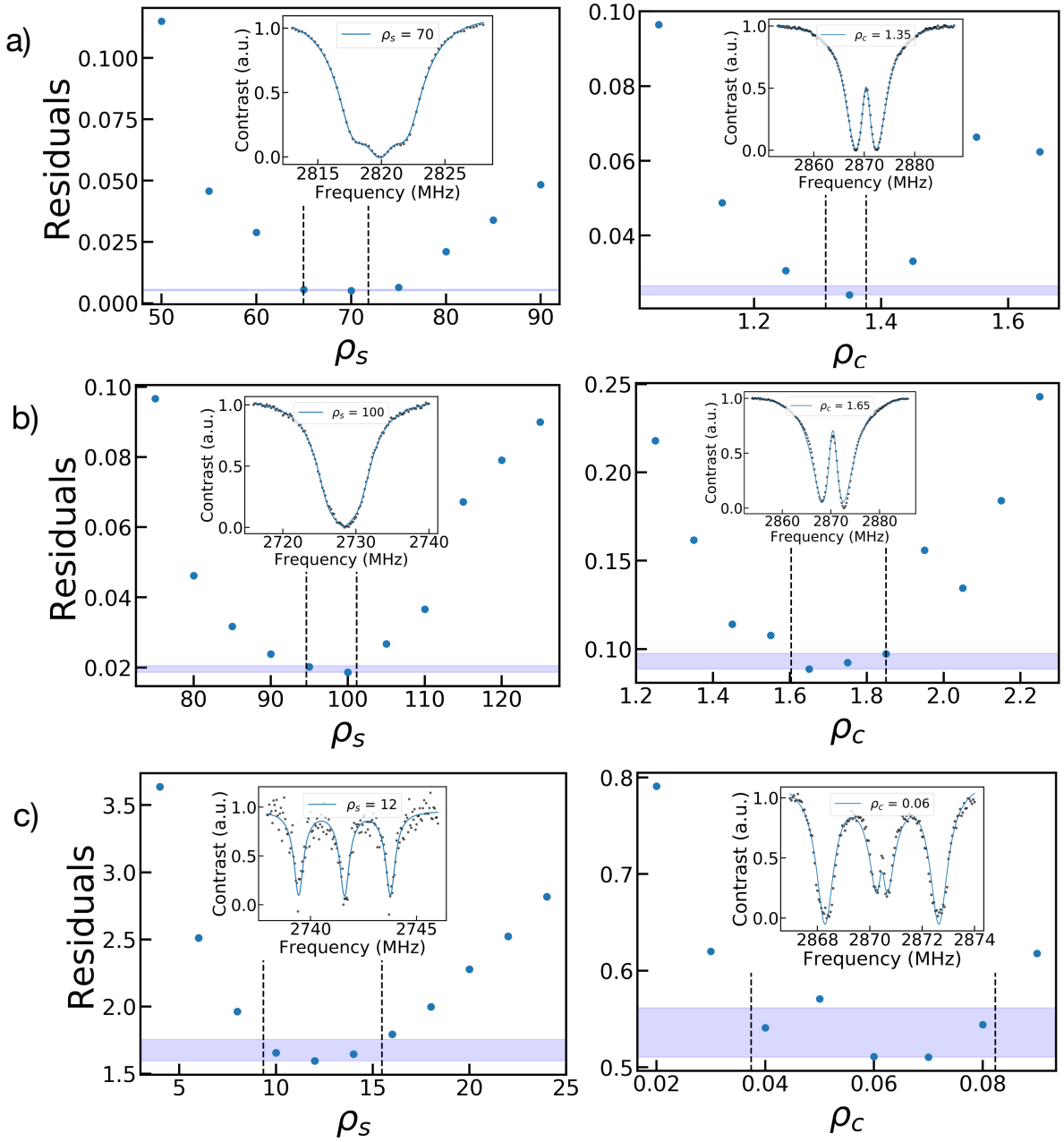

Figure 2.7: Ensemble fitting procedure applied to the treated samples: (a) Ib treated (S1), (b) Ib treated (S2), and (c) IIa treated (S3). The main plots show the least-square residuals as a function of ρ_s (left) and ρ_c (right) under large ($\sim$ 25-50 G) and zero applied field, respectively. We identify the best-fit values for ρ_s, ρ_c based on the minimum residual, and we estimate their error from the range values whose residuals lie within 10% of the minimum (blue shaded regions). The insets depict the best-fit spectra (blue curve), along with the experimental data (black points).

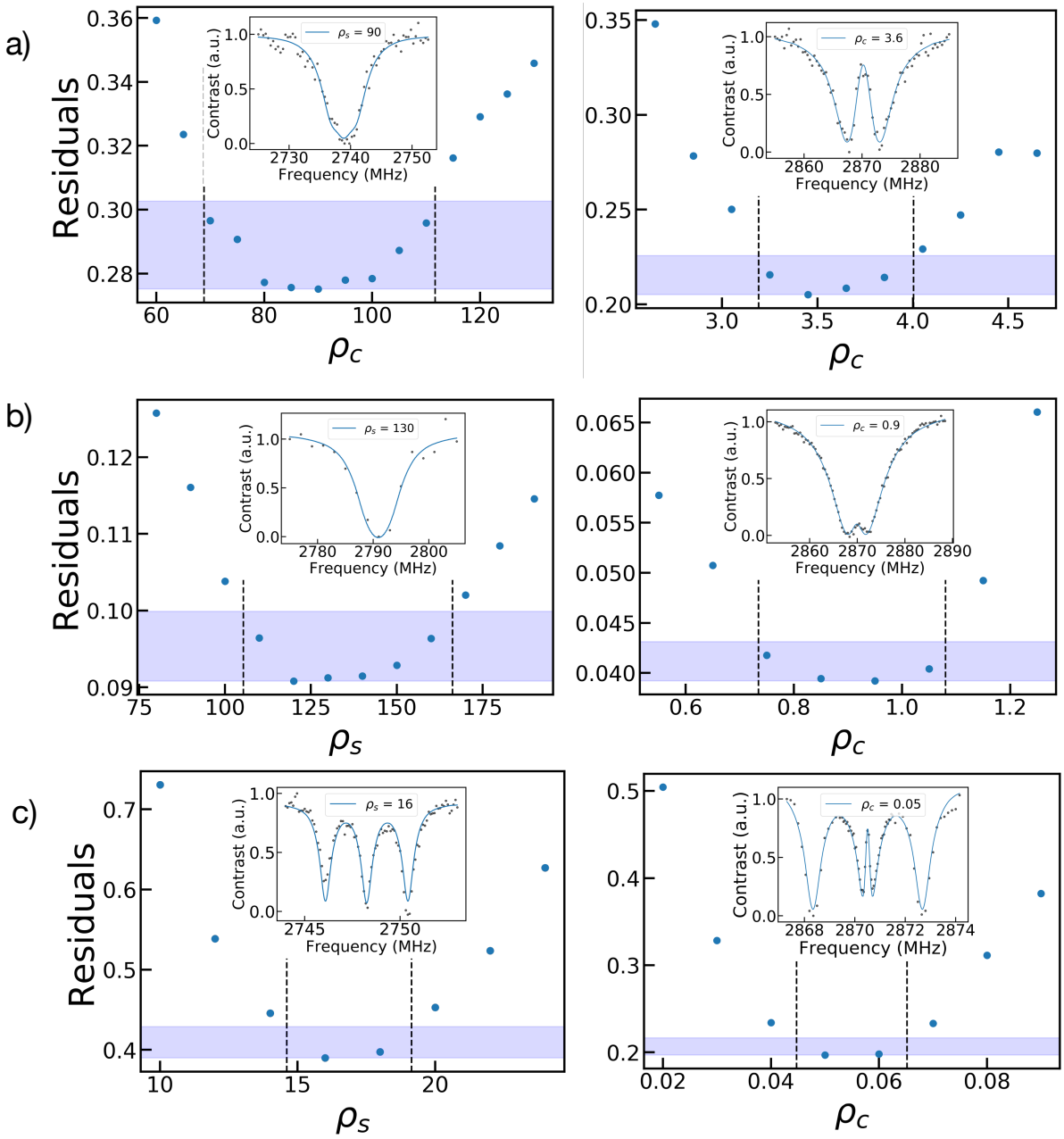

Figure 2.8: Fitting procedure applied to the untreated samples: (a) Ib untreated (S4), (b) Ib untreated (S5), and (c) IIa treated (S6). See caption of Fig. 2.7 for description.

To isolate the effects due to the charge environment, we fit the zero-field spectra as a function of ρ_c while fixing the magnetic noise (ρ_s) based on the previous step. For each value

of ρ_c, we optimize with respect to the natural linewidth Γ, the center frequency, overall amplitude, and vertical offset. These results are shown in the right column of Figs. 2.7 and 2.8. As before, we estimate the error on ρ_c from the 10% interval of the residuals, while for Γ we take the standard error estimated by the fitting routine.

All simulated spectra agree quantitatively with the experimental data, and the extracted ρ_s, ρ_c and Γ are listed in Table I in the main text. We note that for one of the six samples (S5), the linewidth contribution from δB_z is on the same order as Γ. Since we assume δB_z is the dominant source of noise in the high field spectra when extracting ρ_s, the magnetic impurity density for this sample may not be precise.

2.7 Charge localization using single NVs: details

In this section, we discuss the details associated with the charge localization based on a single NV. We consider the derivation of the imbalance and relate it to the electric field orientation and the microwave polarization. We note that the imbalance of the resonances is strong evidence for the presence of a nearby charge, as most other interactions would not modify the transition amplitudes differentially with respect to linearly polarized microwave fields.

To extract the position of the charge, we first calculate the polarization of the microwave field in the reference frame of the NV, ϕ_{MW} (Fig. 2.6a inset of the main text). By varying ϕ_{MW}, and measuring the imbalance one can directly extract the transverse orientation of the electric field ϕ_E. Combined with the observed splitting $2\Pi_\perp$ and shifting Π_z we can fully determine the local electric field vector and localize the corresponding charge. These procedures are detailed below.

2.7.1 Derivation of the Imbalance

In order to quantitatively extract the orientation of the electric field ϕ_E, we introduce the notion of imbalance as the difference in the weights of the resonances in the observed spectra. This imbalance $\mathcal{I}$ is directly related to ϕ_{MW} and the transverse orientation of the electric field ϕ_E.

We begin by focusing our attention to the states with ^{14}N nuclear spin $m_I = 0$ (two inner resonances). In the presence of an electric field, these states are described by the Hamiltonian:

$$H = (D_{gs} + \Pi_z)S_z^2 + \Pi_x(S_y^2 - S_x^2) + \Pi_y(S_xS_y + S_yS_x). \tag{2.8}$$

One finds that the electric field couples only the $|m_s = \pm 1\rangle$ states, leading to the new eigen-

states:

$$|+\rangle = \frac{1}{\sqrt{2}}\left(|m_s = +1\rangle - e^{-i\phi_E}|m_s = -1\rangle\right) \tag{2.9}$$

$$|-\rangle = \frac{1}{\sqrt{2}}\left(e^{i\phi_E}|m_s = +1\rangle + |m_s = -1\rangle\right) \tag{2.10}$$

with energy splitting $2\Pi_\perp = 2\sqrt{\Pi_x^2 + \Pi_y^2}$.

The magnetic resonance spectrum is obtained by driving transitions from the $|m_s = 0\rangle$ state to the $|\pm\rangle$ states using a linearly polarized microwave field. The matrix elements associated with these transitions are

$$\mathcal{M}_\pm = \langle 0|\, S_x \cos\phi_{\mathrm{MW}} + S_y \sin\phi_{\mathrm{MW}}\,|\pm\rangle \tag{2.11}$$

$$= \frac{1}{2}\left[e^{-i\phi_{\mathrm{MW}}} \mp e^{i(\phi_E+\phi_{\mathrm{MW}})}\right] \tag{2.12}$$

where ϕ_{MW} is the direction of microwave polarization. This results in two resonances with amplitudes, $A_\pm \equiv |\mathcal{M}_\pm|^2$:

$$A_\pm = \frac{1}{2} \mp \frac{1}{2}\cos(2\phi_{\mathrm{MW}} + \phi_E). \tag{2.13}$$

By defining the imbalance $\mathcal{I} \equiv \frac{A_+ - A_-}{A_+ + A_-}$, we recover Eq. (2) in the main text:

$$\mathcal{I} = -\cos(2\phi_{\mathrm{MW}} + \phi_E). \tag{2.14}$$

We note that the imbalance reverses direction for $\phi_{\mathrm{MW}} \to \phi_{\mathrm{MW}} + 90^\circ$ and that, for certain microwave angles, the amplitude of one resonance can fully vanish.

For completeness, we also derive the imbalance of the outer ^{14}N hyperfine states, which correspond to $m_I = \pm 1$. The derivation follows the same logic as above, except the Hamiltonian is now

$$H = (D_{gs} + \Pi_z)S_z^2 + \Pi_x(S_y^2 - S_x^2) + \Pi_y(S_xS_y + S_yS_x) \pm 2A_{zz}S_z. \tag{2.15}$$

The eigenstates $|\pm\rangle$ are split by $2\sqrt{A_{zz}^2 + \Pi_\perp^2}$. For $m_I = 1$, one finds

$$|+\rangle = \frac{1}{\sqrt{1+\xi^2}}\left(|+1\rangle - \xi e^{-i\phi_E}|-1\rangle\right) \tag{2.16}$$

$$|-\rangle = \frac{1}{\sqrt{1+\xi^2}}\left(\xi e^{i\phi_E}|+1\rangle + |-1\rangle\right) \tag{2.17}$$

where

$$\xi = \frac{A_{zz}}{\Pi_\perp}\left(\sqrt{1 + \left(\frac{\Pi_\perp}{A_{zz}}\right)^2} - 1\right) \tag{2.18}$$

An analogous expression holds for $m_I = -1$. In both cases, the amplitudes of the $|m_s = 0\rangle \leftrightarrow |\pm\rangle$ resonances are

$$A_\pm = \frac{1}{\sqrt{1+\xi^2}}\left(1 + \xi^2 \mp 2\xi\cos(2\phi_{\rm MW} + \phi_E)\right). \tag{2.19}$$

This leads to an imbalance:

$$\mathcal{I} = \frac{-2\xi\cos(2\phi_{\rm MW} + \phi_E)}{1+\xi^2}. \tag{2.20}$$

Thus, the imbalance of the outer resonances follows the same phase dependence as the inner resonances, but the maximum imbalance depends on the ratio $\Pi_\perp/A_{zz}$. In particular, in the limit $\Pi_\perp \gg A_{zz}$, $\xi \approx 1$ and a fully dark state is still possible; whereas, for $\Pi_\perp \ll A_{zz}$, the maximum imbalance is reduced to $\mathcal{I}_{\rm max} \approx \Pi_\perp/A_{zz}$.

The resulting dependence on ϕ_{MW} and ϕ_E does not change if we include the interaction with a nearby ^{13}C (within the secular approximation), since it interacts with the NV in a similar fashion to ^{14}N hyperfine.

2.7.2 Microwave Angle Projection

We define $(\hat{X}, \hat{Y}, \hat{Z})$ as our lab frame shown in Fig. 2.9a and the NV frame $(\hat{x}, \hat{y}, \hat{z})$ as shown in Fig. 2.1a left inset in Section 2.4. These two frames are related by the crystallographic axes of the sample, and can be easily related once the angle of the NV axis is determined by an external magnetic field. The translation to the origin of the NV frame from the origin of the lab frame is known to within a few tens of um by a series of overlapping confocal image scans.

Because the magnet wire is so long and placed so far away from the target NVs, we approximate the microwave delivery wire to be infinitely long, with an angle $\phi_{\rm Wire}$ with respect to $\hat{X}$, and an in-plane distance r away from the NV. We extract $\phi_{\rm Wire}$ and r from an image of the sample geometry (Fig. 1.9 inset). The height h of the wire's plane above the NV is assumed to be 550 $\pm$ 100 μm given the thickness of the diamond 500 μm, the wire diameter 40 μm, and an intentional air gap to avoid contact to the sample ($\sim$ 30 μm). The wire carries a current which generates a linearly polarized microwave field at the location of the NV (Fig. 2.9) whose transverse projection $\phi_{\rm MW}$ drives the $|m_s = 0\rangle \leftrightarrow |\pm\rangle$ transition. $\phi_{\rm MW}$ is fully determined by the values $\{\phi_{\rm Wire}, h, r\}$.

To estimate error in each realization of $\phi_{\rm Wire}$, we use a Monte Carlo method. We account for the existence of an immeasurable tilt of the wire. This tilt is imperceptible because the wire is so close to the diamond surface that the rotation mount obscures viewing the tilt. As well, the immersion oil distorts the image of any tilt. Consequently, we assume the tilt has an upper bound of $\pm 10^\circ$ out of the plane. We sample $\phi_{\rm MW}$ across the random variables 4000 times to obtain a distribution for the $\phi_{\rm MW}$.

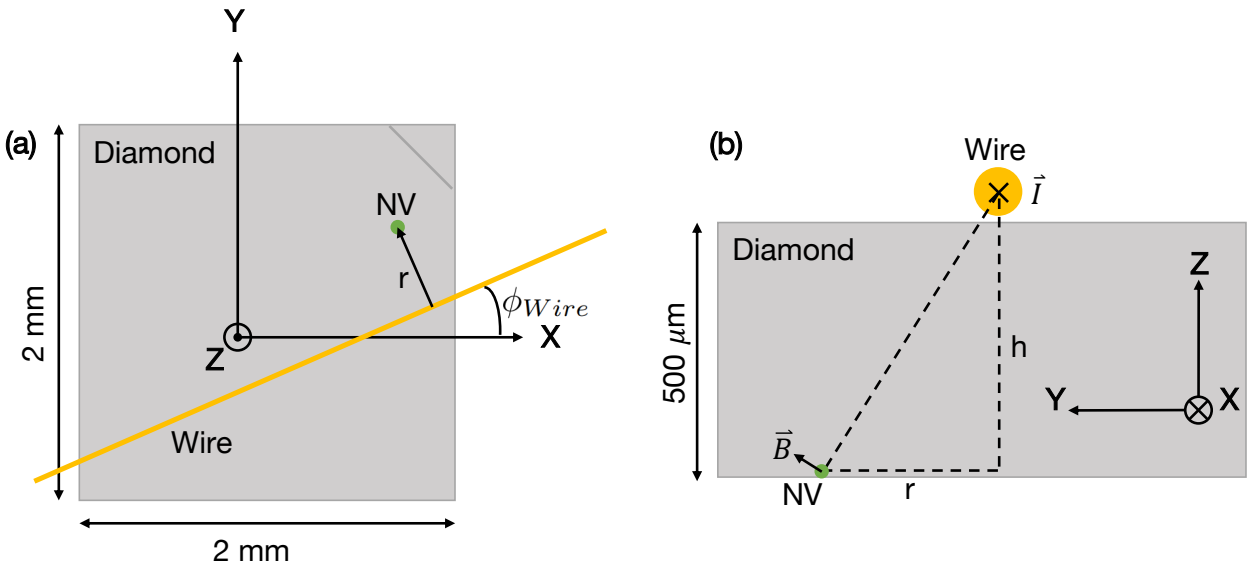

Figure 2.9: a) Top view of lab frame, $\hat{X}$, $\hat{Y}$, and $\hat{Z}$ axes are defined as shown. Wire is displayed at an angle ϕ_{Wire} relative to X, and r is the distance between the wire and the NV. The top-right corner of the diamond has been marked as a fiducial. b) Side view of lab frame. With $\phi_{\text{Wire}} = 0$, when the oscillating current $\vec{I}$ flows in the direction shown, we calculate the direction of the magnetic field vector $\vec{B}$ at a height h below the wire as shown.

2.7.3 Experimental Hindrances to Localization

There are some limitations to this set up. First, there are some angles for which the projection of the microwave magnetic field onto the NV transverse plane is much lower than the projection onto the NV z-axis. At these angles, the maximum Rabi frequency is much lower, reducing contrast in our measurements, as explained in Section 1.5.2. Often, the Rabi frequency is slower than the decoherence rate, such that no Rabi oscillations can be observed at all. In these cases, we assume the decoherence rate to be an the upper bound on the Rabi frequency and the actual frequency resolution.

Second, since our frequency resolution is slower than the decoherence rate, the contrast of these spectra is very small. Consequently, the measurement takes ∼week to complete. Since a single high-quality ODMR spectrum captures the shifting and splitting necessary to extract the magnitudes of the axial and transverse electric fields, we only took one complete ODMR spectrum with high resolution. For the polarization rotation angles, we either reduced the frequency resolution, or measured at only 6 specific frequencies as detailed in the following section.

Third, since the ultimate MW polarization the NV receives is $\phi_{\text{MW}} = \arctan(B_{y,NV}/B_{x,NV})$, there are potentially a large range of polarization angles that are highly sensitive to small changes in the wire geometry due to the large slope in the arctangent function. Particularly,

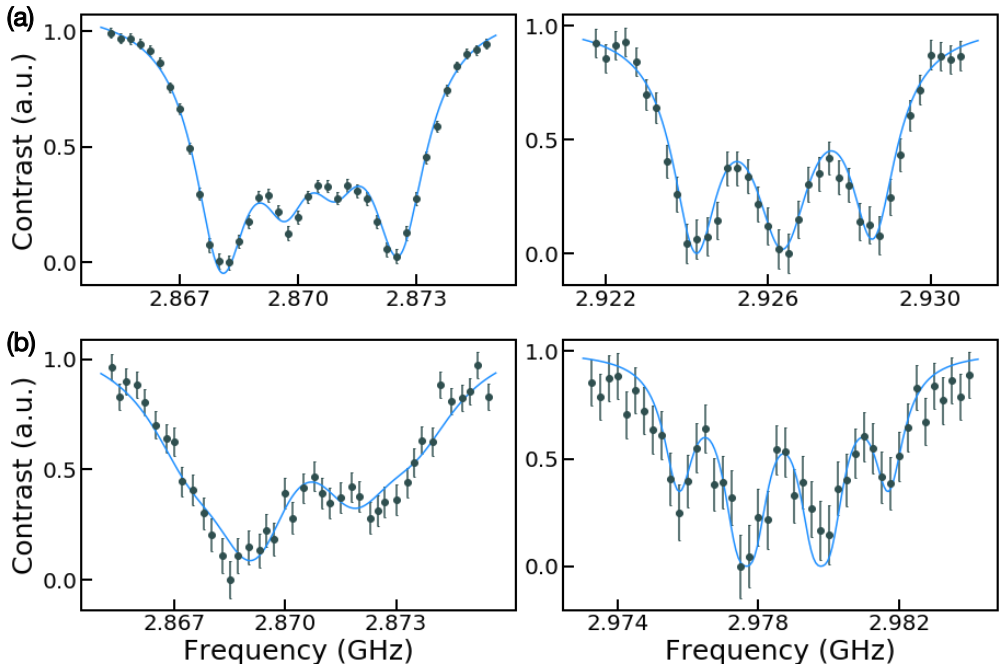

Figure 2.10: Spectra taken with and without a magnetic field applied along the NV z-axis. a) Left: zero-field spectrum for NV1 with microscopic model fit; Right: spectrum with an applied magnetic field and a fit to 3 Lorentzians. b) Left: zero-field spectrum for NV2 with microscopic model fit; Right: spectrum with an applied magnetic field. The fit function is two sets of three Lorentzians. The Lorentzians in each set are separated by the ^{14}N hyperfine splitting. The sets are split from each other by a fit parameter for the ^{13}C hyperfine interaction.

if the over displacements in the XY plane between the NV and the wire is small, minor changes to the displacement transform to large polarization rotations in the NV transverse plane. To combat this, we displace the wire by $r = 100\mu m \pm 30\mu m$ from the NV, which effectively reduces the sensitively.

2.7.4 Single Charge Localization

We search through 68 single NVs and find four exhibiting a significant imbalance in the zero-field spectrum consistent with a nearby charge, from which we analyze two in this work (referred to as NV1 and NV2). Because these spectra can also be affected by the presence of a nearby strongly-coupled ^{13}C, we apply a bias B_z field, which suppresses the effect of the electric field and reveals such a presence. The zero- and high-field spectra for these two NVs are shown in Fig. 2.10. For NV1, we find three resonances spaced ~2.16 MHz apart, a signal associated exclusively with ^{14}N hyperfine. In contrast, for NV2 we observe four resonances,

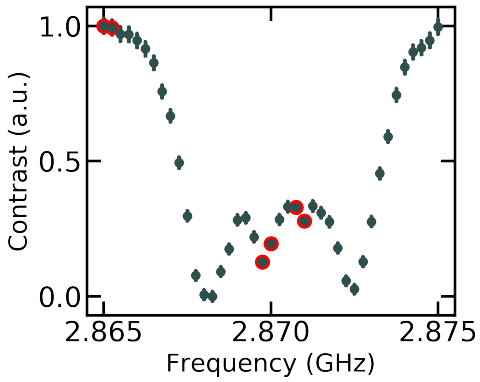

Figure 2.11: Position of the six frequencies (red) considered when computing the imbalance. Instead of measuring full-spectra, we take data points closely spaced at the location of each of the two inner resonances and two data points far from the resonances, so as to measure the baseline signal.

indicating the additional presence of a strongly-coupled ^{13}C. We fit the spectrum of NV2 to extract the ^{13}C hyperfine coupling strength $\approx$ 1.65(7) MHz. To confirm the charge origin, we then measure the full imbalance curve using dark-state spectroscopy.

For NV1, we can clearly resolve the four resonances. The information about the imbalance is encoded into the amplitude of the inner two resonances. To estimate these amplitudes we measure only six spectral data points for each ϕ_{MW} (Fig. 2.11): two data points closely spaced at the location of each of the two inner resonances and two data points far from the resonances (measurement of the baseline contrast) . The imbalance extracted with this method is shown in the main text Fig. 4d, from which we extract $\phi_E = 124(5)^\circ$.

For NV2, since we cannot clearly resolve the four resonances due to the presence of the nearby ^{13}C, we estimate imbalance by integrating the area on either side of the fit center frequency (Fig. 2.12 a). For these set of spectra, the frequency resolution can be reduced, which increases the speed of the measurements. The imbalance curve is shown in Fig. 2.12b, from which we extract $\phi_E = 236(15)^\circ$.

We note that the amplitudes of these curves are much smaller than unity. This discrepancy from our simple theoretical model can also be explained by a few possibilities. First, our methods do not directly probe the weight of the transitions. Second, due to the intrinsic linewidth and power broadening, the inner and outer resonances overlap, which precludes isolating any single transition. Third, a dynamic charge bath may generate a background spectrum that is not included in our model.

In order to localize the charge, we also need to extract the charge-induced splitting $\Pi_\perp$ and shifting Π_z. In direct analogy to the treatment of ensembles, we fit the full zero-field single NV spectra using our microscopic model to extract these parameters as follows:

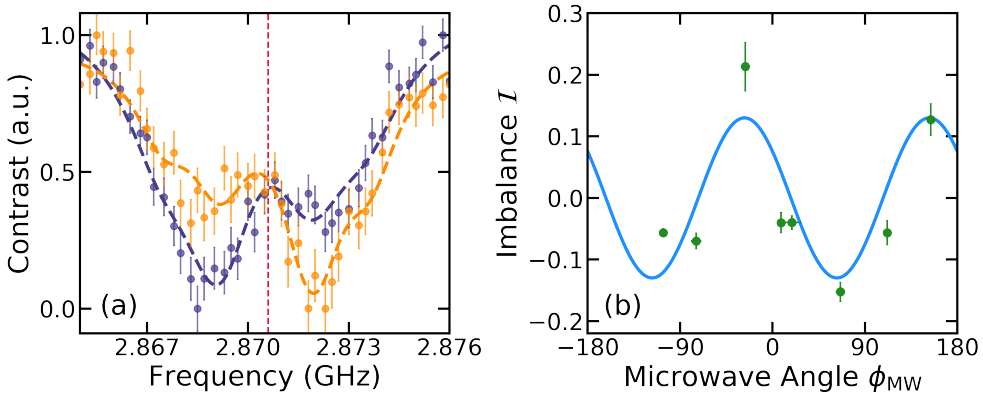

Figure 2.12: a) Two spectra from NV2 with fit from the microscopic model at different values of ϕ_{MW}. The dashed vertical line indicates the fit center frequency (2.8706 GHz). We estimate the imbalance by compare the integral on either side of the center frequency. b) Resultant imbalance sinusoid, from where we extract $\phi_E = 236(15)^\circ$.

1. The spectra depend on five physical parameters: the three components of the electric field $\vec{E}$, the density of magnetic defects ρ_{s}, and the natural linewidth Γ. We also include a global amplitude scaling factor and background offset.

2. To account for the magnetic noise distribution, we follow a prescription similar to the previous magnetic field distribution section. We begin by considering the distribution of magnetic field for ρ_{s} which yields a probability distribution for measuring a particular value of δB_z. We then discretize over δB_z and for each possible value, perform steps 3-5. Each of the resulting spectra is weighted by the probability of measuring δB_z.

3. We solve the full Hamiltonian of the system (including ^{13}C and ^{14}N hyperfine interactions where applicable) to find the positions of the resonances.

4. We generate a spectrum by weighting each resonance by its transition amplitude with the $|m_s = 0\rangle$ state. We compute the weight by fixing the microwave direction in the $\hat{x}$ axis and computing $|\langle 0| S_x |\pm\rangle|^2$.

5. We broaden each resonance by a Lorentzian distribution with full-width-half-maximum of Γ.

6. We use a least-squares regression method on steps 1-5 over the seven fitting parameters, reproducing the experimental spectra.

Note, in order to determine Π_z, we use the ensemble-averaged $D_{\mathrm{gs}} = 2870.25(5)$ MHz from the adjacent region of the same diamond containing a high density of NVs as a reference value (Figure 2.8a).

From the fits (see Figure 2.4a,b) we extract the shifting and splitting due to the electric field:

$$\text{NV1:} \quad \Pi_z = (30 \pm 50) \text{ kHz} \quad , \quad \Pi_\perp = (650 \pm 10) \text{ kHz} \tag{2.21}$$

$$\text{NV2:} \quad \Pi_z = (270 \pm 70) \text{ kHz} \quad , \quad \Pi_\perp = (850 \pm 80) \text{ kHz} \, . \tag{2.22}$$

Using the susceptibilities [119], we extract the electric field vectors at the position of the single NVs:

$$\text{NV1:} \quad (E_x, E_y, E_z) = (-2.1 \pm 0.2, \ \ 3.2 \pm 0.2, \ \ 9 \pm 14) \text{ MV/m} \tag{2.23}$$

$$\text{NV2:} \quad (E_x, E_y, E_z) = (-2.8 \pm 1.1, \ \ -4.1 \pm 0.8, \ \ 77 \pm 20) \text{ MV/m} \, . \tag{2.24}$$

The parameters of the electric field uniquely determine the position of the positive single fundamental charge (main text Fig. 1b and 1c). The confidence intervals can be estimated using a Monte Carlo method.

2.8 Summary and outlook

This chapter demonstrates that the zero-field spectral features of NV ensembles are in fact dominated by the influence of local electric fields, an explanation that stands in stark contrast to the notion that is originates from lattice strain as is asserted abundantly in literature. Our microscopic charge model quantitatively captures the magnetic resonance spectra for NV ensembles spanning two orders of magnitude in defect density. It also suggests a method to locate the position of individual charges near a single NV center. We then employed this method to image a single charge to within a nanoscale volume of an NV.

Our work encouraged a path for a number of follow-up studies and applications. First, while we consistently correlated charge density and NV density in all of the treated samples we measured (simultaneously consistent with the expectation of charge neutrality), all of the untreated samples exhibited spectral features indicative of an anomalously large charge density. The origin of these additional charges remains an open question as of the time of this writing. Second, the picture our results provides for NV ensembles at low magnetic fields lays the groundwork for precise sensing of electric fields, lattice strain [66, 136], gyroscopic precession, and magnetically-sensitive quantum materials. Third, by using the charge-induced suppression of δB_z, one could conceive of a method to enhance the NV's resilience to magnetic noise. Fourth, to date, the charge model has been expanded to provide explanations for exotic optical phenomena in the NV, and is the central foundation for an enhanced electric field sensing technique [16]. Finally, given the previous success with understanding optical phenomena, there is hope that further understanding the local charge environment of single NVs could reveal the physics of optical spectral diffusion at low temperatures [28, 78].

Chapter 3

NVs Under Pressure

3.1 Introduction

In the pursuit of understanding materials on a fundamental level, one of the generic techniques is to tune the strengths of the interactions intrinsic to the object of study. In physics, the material is often cooled, which brings its particles closer together, strengthening their interactions. However, few table-top experimental physicists have paid much attention to a technique common to the realm of geo- and planetary-sciences: increasing pressure. While the effects of temperature have a hard cut-off of 0 K and the coldest achievable temperatures are currently limited to Bose-Einstein condensed gases, in principle pressure can increase interactions far beyond the limits of temperature—just look at white dwarfs and neutron stars—and do so for almost any material. Using pressure, the physical, chemical and electronic properties of matter are all highly tunable. This knowledge compelled the geo- and planetary -sciences to develop the diamond anvil cell (DAC), enabling tabletop experiments to investigate a diverse landscape of high-pressure phenomena ranging from the properties of planetary interiors to transitions between quantum mechanical phases.

In this chapter, we demonstrate the versatility of a novel platform based upon NV spin defects combined with the common DAC [76, 61]. In particular, we instrument DACs with a layer of NV centers directly at the tip (culet) of the diamond anvils, enabling the pursuit of two complementary objectives in high pressure science: first, to understand the strength and failure of materials under pressure (e.g. the brittle-ductile transition) and second, to discover and characterize new phases of matter (e.g. high temperature superconductors) [161, 65, 54, 41, 138]. Achieving both goals hinges upon the sensitive *in situ* imaging of signals within the high pressure chamber of the DAC. For the first goal, measuring the *local* stress environment permits the direct observation of inhomogeneities in plastic flow and the formation of line defects. For the second goal, the ability to spatially resolve field distributions can provide a direct image of complex order parameters and textured phenomena such as magnetic domains. Unfortunately, the utility of most conventional tabletop spectroscopy techniques is limited from achieving either goal due to enormous stress gradients generated near the sam-

ple, which stem from the high pressure inside the chamber and ambient pressure outside. As a result, conventional techniques are often restricted to measuring bulk properties averaged over the entire DAC geometry via a probe external to the device.

Our approach to these challenges is to utilize an ensemble of NV centers (∼1 ppm density) implanted ∼50 nm from the surface of the diamond anvil culet (Fig. 3.1, A and B). Crucially, both the nature and energy of these spin states are sensitive to local changes in stress, temperature, magnetic and electric fields (Fig. 3.1C) [**Barson:2017a**, 4, 108, 37, 121, 35, 143]. Their energy levels are probed by performing ODMR spectroscopy (Fig. 3.1D). [87, 20, 113].Measuring the local stress environment intrinsic to the DAC serves as a calibration for using the NVs subsequently as probes of a multitude of extrinsic signals (akin to the previous chapter) over the wide range of environmental conditions and DAC can produce.

3.2 Experimental Apparatus Particulars

3.2.1 Diamond Anvil Cells

In our experiments, we utilize a miniature DAC (Fig. 3.1, A and B) consisting of two opposing anvils compressing either a beryllium copper or rhenium gasket [145]. The sample chamber defined by the gasket and diamond-anvil culets is filled with a pressure-transmitting medium (either a 16:3:1 methanol/ethanol/water solution or cesium iodide) to provide a quasi-hydrostatic environment. The miniature diamond anvil cell body is made of nonmagnetic steel with cubic boron nitride backing plates (Technodiamant). Microwave excitation is applied via a 4 μm thick platinum foil compressed between the gasket and anvil pavilion facets [146], while scanning confocal microscopy (with a transverse diffraction-limited spot size ∼600 nm, containing $\sim 10^3$ NVs) allows us to obtain two-dimensional ODMR maps across the culet.

All diamond anvils used in this work are synthetic type-Ib ([N] $\lesssim$ 200 ppm) single crystal diamonds cut into a 16-sided standard design with dimensions 0.2 mm diameter culet, 2.75 mm diameter girdle, and 2 mm height (Almax-easyLab and Syntek Co., Ltd.). For stress measurement, both anvils with (111)-cut-culet and (110)-cut-culet are used, while for magnetic measurements on iron and gadolinium, (110)-cut-culet anvil is used. We perform $^{12}C^+$ ion implantation (CuttingEdge Ions, 30 keV energy, 5×10^{12} cm^{-2}) to generate a ∼50 nm layer of vacancies near the culet surface. After implantation, the diamonds are annealed in vacuum ($< 10^{-6}$ Torr) using a home-built furnace with the following recipe: 12 hours ramp to 400°C, dwell for 8 hours, 12 hours ramp to 800°C, dwell for 8 hours, 12 hours ramp to 1200°C, dwell for 2 hours. During annealing, the vacancies become mobile, and probabilistically form NV centers with intrinsic nitrogen defects. After annealing, the NV concentration is estimated to be around 1 ppm as measured by fluorescence intensity. The NV centers remain photostable after several iterations of compression and decompression up to 48 GPa, with spin-echo coherence time $T_2 \approx 1$ μs, mainly limited by the nitrogen electronic spin bath.

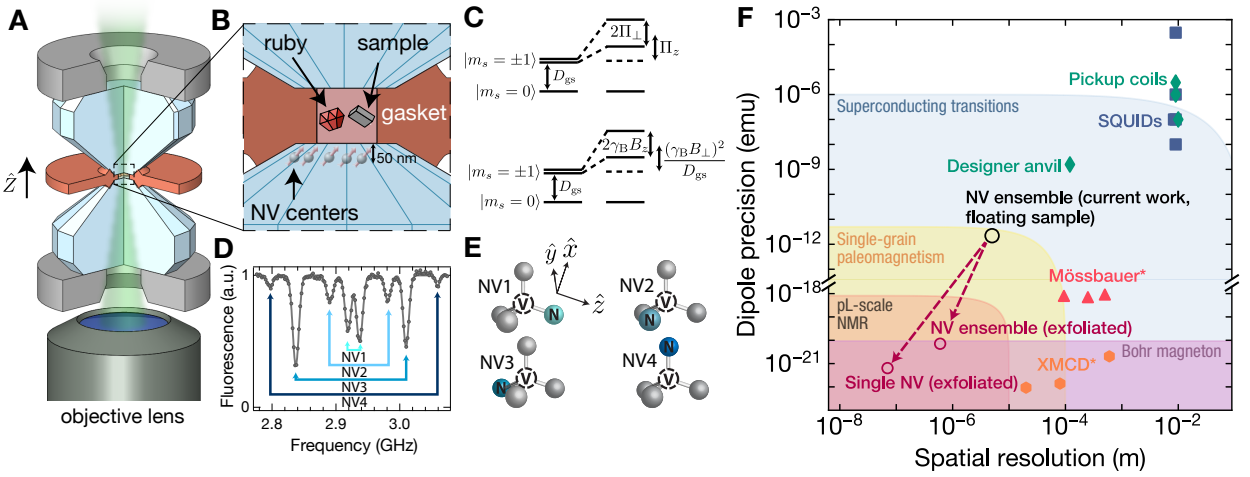

Figure 3.1: NV centers integrated into a diamond anvil cell. (a) Schematic of the DAC geometry. Two opposing anvils are compressed by a nonmagnetic steel cell and cubic boron nitride backing plates (gray). NV centers are initialized and read out using a 532 nm laser focused to a diffraction-limited spot (∼600 nm) which is scanned across the culet surface. (b) The DAC sample chamber is defined by the gasket-anvil assembly (diagram not to scale); it is loaded with the sample of interest, a pressure-transmitting medium, and a single ruby microsphere (pressure calibration). A ∼50 nm layer of NV centers is embedded into the diamond anvil directly below the sample chamber. (c) Stress (top) both shifts and splits the $|m_s = \pm 1\rangle$ sublevels at first order; in particular, the shifting is characterized by $\Pi_z = \alpha_1(\sigma_{xx}+\sigma_{yy})+\beta_1\sigma_{zz}$, and the splitting is characterized by $\Pi_\perp^2 = [\alpha_2(\sigma_{yy} - \sigma_{xx}) + \beta_2(2\sigma_{xz})]^2 + [\alpha_2(2\sigma_{xy}) + \beta_2(2\sigma_{yz})]^2$. An axial magnetic field (bottom) splits the $|m_s = \pm 1\rangle$ sublevels at first order, but a transverse magnetic field leads to shifts only at second order. (d) ODMR spectrum from an NV center ensemble under an applied magnetic field. (e) Each pair of resonances in (D) corresponds to one of the four NV crystallographic orientations. (f) Comparison of high pressure magnetometry techniques. We define the spatial resolution as a characteristic sensor length scale over which the sample magnetism is *integrated*. Estimates for our current work are shown assuming a sample suspended in a pressure medium 5 μm away from the culet (black open circle). We project that by exfoliating a sample directly onto the culet surface and using 5 nm implanted NV centers, the distance from the sample can be significantly reduced, thus improving both dipole precision and spatial resolution (open red circles). Inductive methods (pickup coils [green diamonds] and SQUIDs [blue squares]) integrate the magnetization of a sample over the coil's area [146]; to this end, the diameter associated with the coil is taken as the "spatial resolution" although in principle, the sample inside the chamber can be significantly smaller. In contrast, high energy photon scattering techniques (x-ray magnetic circular dichroism [orange hexagons], and Mössbauer spectroscopy [pink triangles]) probe atomic scale magnetism [146]; the length scale for these methods is shown here as the spot size of the excitation beam.

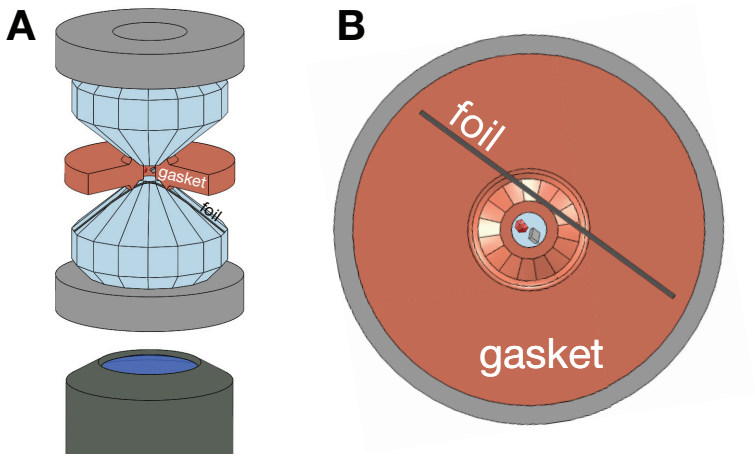

Figure 3.2: (**A**) Schematic of the setup explicitly depicting the platinum foil used for microwave excitation. The gasket has been cross sectioned for visual clarity. (**B**) Schematic from the perspective of the objective lens. The anvil has been omitted for visual clarity. Diagrams are not to scale.

3.2.2 Cryostat

To create the gadolinium P-T phase diagram (Section), we put the DAC into a closed-cycle cryostat (attocube attoDRY800). The DAC is placed on the sample mount of the cryostat, which is incorporated with a heater and a temperature sensor for temperature control and readout from 35 - 320 K. The AOM and the SPCM are gated by a programmable multi-channel pulse generator (SpinCore PulseBlasterESR-PRO 500) with 2 ns temporal resolution. A microwave source (Stanford Research Systems SG384) in combination with a 16W amplifier (Mini-Circuits ZHL-16W-43+) serves to generate signals for NV spin state manipulation. The microwave field is delivered to the DAC through a 4 μm thick platinum foil compressed between the gasket and anvil pavilion facets (Fig. 3.2), followed by a 40 dB attenuator and a 50 Ω termination. Electrical contact between the conducting gasket and platinum foil reduces the microwave transmission efficiency and was chosen out of technical simplicity.

For this experiment, we use beryllium copper gaskets in the DAC. The Gd sample is cut from a 25 μ m thick Gd foil (Alfa Aesar Stock No. 12397-FF) to a size of $\sim$ 30 μm $\times$ 30 μm and loaded with cesium iodide (CsI) as the pressure-transmitting medium. A single ruby microsphere loaded into the chamber is used as a pressure scale.

For each experimental run, we start with an initial pressure (applied at room temperature 300 K) and cool the cell in the cryostat. Due to contraction of the DAC components with decreasing temperature, each run of the experiment traverses a non-isobaric path in P-T phase space, Fig. S16A. Using fiducial markers in the confocal scans of the sample chamber, we track points near and far from the Gd sample throughout the measurement. By performing ODMR spectroscopy at these points for each temperature, we monitor the

magnetic behavior of the sample. More specifically, comparing the spectra between the close point (probe) against the far away one (control), Fig. 3.10, enables us to isolate the induced field from the Gd sample.

3.2.3 Noise Spectroscopy Humidity Control

The T_1 measurements in Section 3.5 were performed by placing the sample on a Peltier module to reduce temperature. We these measurements did not require cooling to freezing temperatures, they still needed temperatures below the dew point of the lab. Out of expediency, we decided to forgo a vacuum chamber and directly reduce the dew point around the sample to prevent condensation. We used a normal dehumidifier to reduce moisture in the room, and placed as many silicone desiccants (both tubs and packets) around the sample and mount as we could fit. Finally, we covered the sample region of the table with plastic cloth to minimize moist airflow

3.3 Stress Sensing

Stress imaging in a DAC permits the study of pressure-related phenomena to a level of detail that was previously impossible. For example, access to the fine details of the stress in a material reveals specific modes of failure, the precise nature of plastic flow, and the particularities of defect formation. In addition, stress imaging is a prerequisite for the imaging of magnetic, electric, and thermal textures in a DAC, for in order to isolate their effects, the effects of the pressure-induced stress must first be calibrated.

3.3.1 Stress and Strain

Stress and strain provide complementary perspectives on the phenomena of deformation. Strain is a measure of the displacement between a particle's position in a deformed material relative to its position in that material before it was deformed. Stress is a measure of the internal forces that neighboring particles in a continuous material exert on each other[1]. The transformation between the two is akin to the transformation between a magnetic field and the displacement of a magnetic particle: it is direct, but relies on particular susceptibilities the particle has to being moved. Given the meanings of each quantity, it is clear why stress (akin to magnetic fields: maps of the force a magnetic particle would feel at any given location) appears in the Hamiltonian.

Both quantities are 3-dimensional rank-2 tensors (i.e. 3x3 matrices) describing the state of an infinitesimal volume. The specific quantities of the tensor elements depends on the choice of coordinate system. Their diagonal elements represent forces and displacements in the X, Y, and Z directions, while their off-diagonal elements represent torque and rotational

[1]Technically, stress expresses the derivative of the force with respect to an infinitesimal surface area. The study of continuous materials relies on differential geometry.

displacements around the X, Y, and Z axes. As long as the material has finished deforming, it is in static equilibrium, so all forces and torque must be balanced, implying straightforwardly that the tensors must be symmetric. As an example, consider the off-diagonal stress element σ_{xy} which represents a force in the y-direction applied to a surface facing the x-direction in a Cartesian coordinate system. It is a torque on the XY corner of an infinitesimal cube. There is only one other torque on this corner coming from the σ_{yx} element, representing a force in the x-direction applied to a surface facing the y-direction. Since in static equilibrium there can be no net torque, the two components must be equal and opposite torques.

As described in Section 1.3.4, any Hamiltonian perturbing the NV must abide by C_{3v} symmetry, which reduces any perturbation to components that transform like A_1, e_x, and e_y. Rotations and torques independently do not transform this way, but their linear combinations may, as presented in the following section. Since each independent NV can only provide two parameters (splitting and shifting)[2], extracting the entire stress tensor requires more careful planning than a vector electric field, even though their perturbations ultimately look the same. A symmetric 3x3 matrix only has 6 distinct elements, which at first glance suggests a mere 3 of the 4 NV orientation groups within a diffraction-limited spot are sufficient to reconstruct the stress tensor; however, given the geometry of the DAC and the cut of the diamond culet, many NV orientation groups experience identical stress (see the works and theses of Satcher Hsieh and Bryce Kobrin for details). The solution then is to use a different cut of diamond for the other anvil and ensure the pressure medium is hydrostatic.

3.3.2 Stress Hamiltonian

Here, we focus on the sensing of stress and magnetic fields, wherein the NV is governed by the Hamiltonian [14, 156], $H = H_0 + H_\mathrm{B} + H_\mathrm{S}$, with $H_0 = D_\mathrm{gs} S_z^2$ (zero-field splitting), $H_\mathrm{B} = \gamma_\mathrm{B} \vec{B} \cdot \vec{S}$ (Zeeman splitting), and $H_\mathrm{S} = \left[\alpha_1(\sigma_{xx} + \sigma_{yy}) + \beta_1 \sigma_{zz}\right] S_z^2 + \left[\alpha_2(\sigma_{yy} - \sigma_{xx}) + \beta_2(2\sigma_{xz})\right](S_y^2 - S_x^2) + \left[\alpha_2(2\sigma_{xy}) + \beta_2(2\sigma_{yz})\right](S_x S_y + S_y S_x)$ capturing the NV's response to the local diamond stress tensor, σ (Fig. 3.1C). Note that in the above, $\gamma_\mathrm{B} \approx (2\pi) \times 2.8$ MHz/G is the gyromagnetic ratio, $\{\alpha_{1,2}, \beta_{1,2}\}$ are the stress susceptibility coefficients [35, 14, 143, 146], $\hat{z}$ is the NV orientation axis, and $\hat{x}$ is defined such that the xz-plane contains one of the carbon-vacancy bonds (Fig. 3.1E). In general, the resulting ODMR spectra exhibit eight resonances arising from the four possible crystallographic orientations of the NV (Fig. 3.1D). By extracting the energy shifting and splitting of the spin sublevels for each NV orientation group, one obtains an overconstrained set of equations enabling the reconstruction of either the (six component) local stress tensor or the (three component) vector magnetic field [146].

[2]Actually, individually-resolvable NVs can provide up to three parameters for Stress and Electric fields by using Dark State Tomography (Section 2.7).

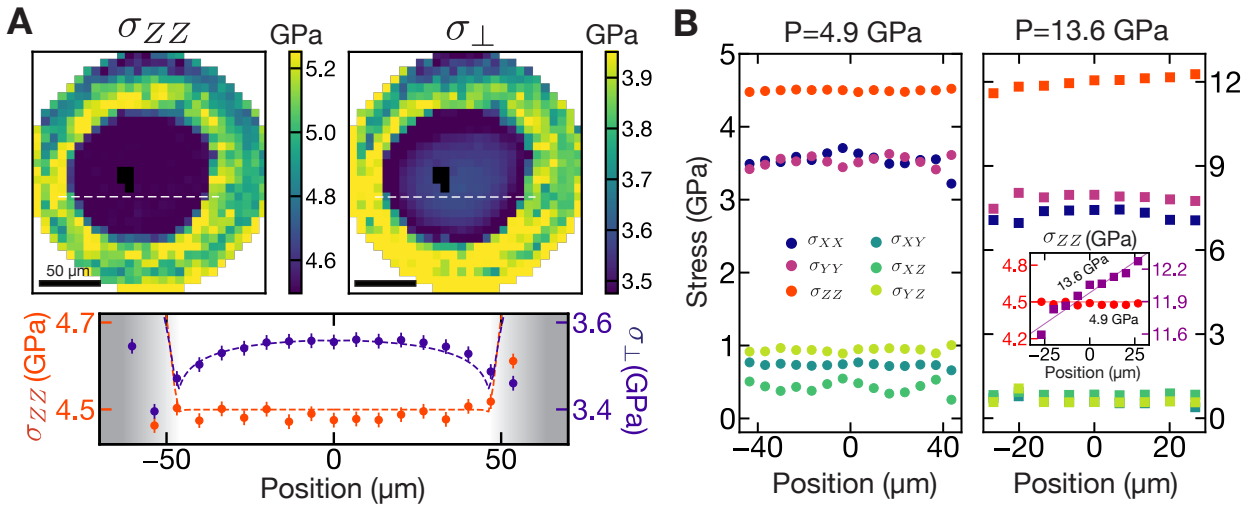

Figure 3.3: Full tensorial reconstruction of the stresses in a (111)-cut diamond anvil. (**A**) Spatially resolved maps of the loading stress (left) and mean lateral stress (right), $\sigma_\perp = \frac{1}{2}(\sigma_{XX} + \sigma_{YY})$, across the culet surface. In the inner region, where the culet surface contacts the pressure-transmitting medium (16:3:1 methanol/ethanol/water), the loading stress is spatially uniform, while the lateral stress is concentrated towards the center; this qualitative difference is highlighted by a linecut of the two stresses (below), and reconstructed by finite element analysis (orange and purple dashed lines). The black pixels indicate where the NV spectrum was obfuscated by the ruby microsphere. (**B**) Comparison of all stress tensor components in the fluid-contact region at $P = 4.9$ GPa and $P = 13.6$ GPa. At $P = 13.6$ GPa, the pressure-transmitting medium has entered its glassy phase and we observe a spatial gradient in the loading stress σ_{ZZ} (inset).

3.3.3 Stress Imaging

We begin by probing the stress tensor across the culet surface using two different cuts of diamond (i.e. (111)-cut and (110)-cut culet). For a generic stress environment, the intrinsic degeneracy associated with the four NV orientations is not sufficiently lifted, implying that individual resonances cannot be resolved. In order to resolve these resonances while preserving the stress contribution, we sequentially tune a well-controlled external magnetic field to be perpendicular to each of the different NV orientations [146]. For each perpendicular field choice, three of the four NV orientations exhibit a strong Zeeman splitting proportional to the projection of the external magnetic field along their symmetry axes. Crucially, this enables one to resolve the stress information encoded in the remaining NV orientation, while the other three groups of NVs are spectroscopically split away. Using this method, we obtain sufficient information to extract the full stress tensor, as depicted in Fig. 3.3. A number of intriguing features are observed at the interface between the culet and the sample chamber,

which provide insight into both elastic (reversible) and plastic (irreversible) deformations.

At low pressures ($P = 4.9$ GPa), the normal stress along the loading axis, σ_{ZZ}, is spatially uniform (Fig. 3.3A), while all shear stresses, $\{\sigma_{XY}, \sigma_{XZ}, \sigma_{YZ}\}$, are minimal (Fig. 3.3B). These observations are in agreement with conventional stress continuity predictions for the interface between a solid and an ideal fluid [46]. Moreover, σ_{ZZ} is consistent with the independently measured pressure inside the sample chamber (via ruby fluorescence), demonstrating the NV's potential as a built-in pressure scale [33]. In contrast to the uniformity of σ_{ZZ}, the field profile for the mean lateral stress, $\sigma_\perp \equiv \frac{1}{2}(\sigma_{XX} + \sigma_{YY})$, exhibits a concentration of forces toward the center of the culet (Fig. 3.3A). Using the measured σ_{ZZ} as a boundary condition, we perform finite element simulations to reproduce this spatial pattern[146].

Upon increasing pressure ($P = 13.6$ GPa), a pronounced spatial gradient in σ_{ZZ} emerges (Fig. 3.3B, inset). This qualitatively distinct feature is consistent with the solidification of the pressure-transmitting medium into its glassy phase above $P_g \approx 10.5$ GPa [84]. Crucially, this demonstrates our ability to characterize the effective viscosity of solids and liquids under pressure. To characterize the sensitivity of our system, we perform ODMR spectroscopy with a static applied magnetic field and pressure under varying integration times and extract the frequency uncertainty from a Gaussian fit. We observe a stress sensitivity of $\{0.023, 0.030, 0.027\}$ GPa/$\sqrt{\text{Hz}}$ for hydrostatic, average normal, and average shear stresses, respectively. This is consistent with the theoretically derived stress sensitivity, $\eta_S \sim \frac{\Delta\nu}{\xi C\sqrt{Nt}} = \{0.017, 0.022, 0.020\}$ GPa/$\sqrt{\text{Hz}}$, respectively, where N is the number of NV centers, $\Delta\nu$ is the linewidth, ξ is the relevant stress susceptibility, t is the integration time, and C is an overall factor accounting for measurement infidelity [146]. In combination with diffraction-limited imaging resolution, this sensitivity opens the door to measuring and ultimately controlling the full stress tensor distribution across a sample.

3.3.4 Extracting splitting and shifting information

Having developed a technique above to spectrally resolve the resonances, we extract the above-mentioned splitting and shifting by fiting the resulting spectra to four pairs of Lorentzian lineshapes. Each pair of Lorentzians is defined by a center frequency, a splitting, and a common amplitude and width. To sweep across the two-dimensional layer of implanted NV centers, we sequentially fit the spectrum at each point by seeding with the best-fit parameters of nearby points. We ensure the accuracy of the fits by inspecting the frequencies of each resonance across linecuts of the 2D data (Fig. S3B).

Converting the fitted energies to shifting ($\Pi_{z,i}$) and splitting parameters ($\Pi_{\perp,i}$) requires us to take into account two additional effects. First, in the case of the shifting parameter, we subtract off the second-order shifting induced by transverse magnetic fields. In particular, the effective shifting is given by $\Pi_{z,B} \approx (\gamma_B B_\perp)^2/D_{gs}$, which, under our experimental conditions, corresponds to $\Pi_{z,B} \approx 5$ - 10 MHz. To characterize this shift, one can measure each of the NV orientations with a magnetic field aligned parallel to its principal axis, such that the transverse magnetic shift vanishes. In practice, we obtain the zero-field shifting for each of the NV orientations without the need for additional measurements, as part of our electromagnet

calibration scheme. We perform this calibration at a single point in the two-dimensional map and use this point to characterize and subtract off the magnetic-induced shift in subsequent measurements with arbitrary applied field. Second, in the case of the splitting parameter, we correct for an effect arising from the NV's charge environment. We discuss this effect in the following section. The final results for the shifting ($\Pi_{z,i}$) and splitting ($\Pi_{\perp,i}$) parameters for the (111)-cut diamond at 4.9 GPa are shown in Fig. 3.6C.

3.3.5 Effect of local charge environment

As discussed in Section 1.3.4, B_z will suppress both stress and electric fields, so extracting stress components requires no external B_z. However, as described in Chapter 2, in the absence of magnetic fields, charged defects dominate the spectra of NV ensembles (splitting 5-10 MHz) for Type Ib diamonds). This effect should be subtracted from the total splitting to determine the stress-induced splitting at zero axial magnetic field.

To this end, let us first recall the NV interaction with transverse electric fields:

$$H_E = d_\perp \left[\mathcal{E}_x(S_y^2 - S_x^2) + \mathcal{E}_x(S_xS_y + S_yS_x)\right] \tag{3.1}$$

where $d_\perp = 17$ Hz cm/V. We can define

$$\tilde{\Pi}_x = \Pi_{\mathrm{s},x} + \Pi_{\mathrm{E},x} \tag{3.2}$$

$$\tilde{\Pi}_y = \Pi_{\mathrm{s},y} + \Pi_{\mathrm{E},y} \tag{3.3}$$

where

$$\Pi_{z,i} = \alpha_1 \left(\sigma_{xx}^{(i)} + \sigma_{yy}^{(i)}\right) + \beta_1 \sigma_{zz}^{(i)} \tag{3.4}$$

$$\Pi_{x,i} = \alpha_2 \left(\sigma_{yy}^{(i)} - \sigma_{xx}^{(i)}\right) + \beta_2 \left(2\sigma_{xz}^{(i)}\right) \tag{3.5}$$

$$\Pi_{y,i} = \alpha_2 \left(2\sigma_{xy}^{(i)}\right) + \beta_2 \left(2\sigma_{yz}^{(i)}\right) \tag{3.6}$$

$$\Pi_{\mathrm{E},\{x,y\}} = d_\perp \mathrm{E}_{\{x,y\}} \tag{3.7}$$

$\sigma^{(i)}$ is the stress tensor in the local frame of each of NV orientations labeled by $\{i = 1, 2, 3, 4\}$, and $\{\alpha_{1,2}, \beta_{1,2}\}$ are stress susceptibility parameters. The combined splitting for electric fields and stress is then given by

$$2\tilde{\Pi}_\perp = 2\left((\Pi_{\mathrm{s},x} + \Pi_{\mathrm{E},x})^2 + (\Pi_{\mathrm{s},y} + \Pi_{\mathrm{E},y})^2\right)^{1/2} . \tag{3.8}$$

We note that the NV center also couples to longitudinal fields, but its susceptibility is ~ 50 times weaker and is thus negligible in the present context.

To model the charge environment, we consider a distribution of transverse electric fields. For simplicity, we assume that the electric field strength is given by a single value $\mathcal{E}_0$, and

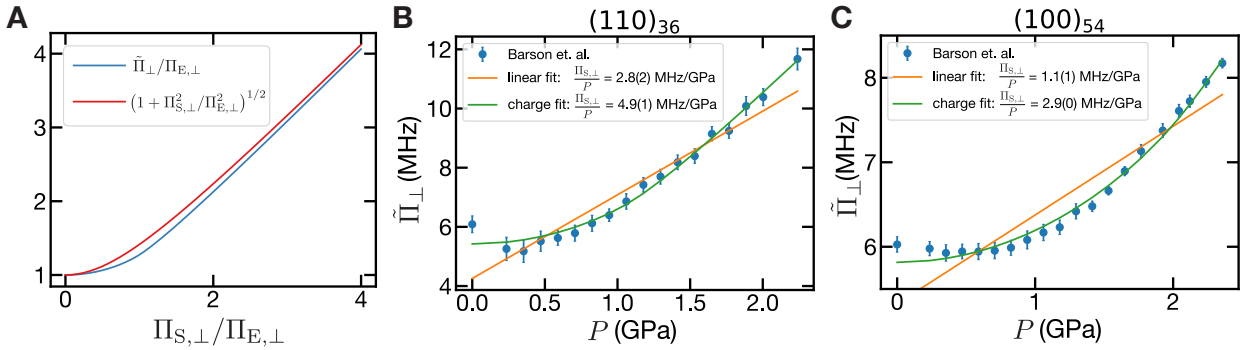

Figure 3.4: Interplay between stress and random electric fields. (**A**) Theoretical curve (blue) for the total splitting in the presence of stress and electric fields, Eq. (3.9). We compare this to a quadratic sum (red). (**B-C**) Measured splitting parameter (blue) for uniaxial pressure applied to a (110)-cut and (100)-cut diamond, reprinted with permission from [14]. We fit the data using (a) a linear function (orange), $\tilde{\Pi}_\perp = \Pi_{E,\perp} + \Pi_{S,\perp}$, and (b) the aforementioned theoretical curve, Eq. (3.9) (green). Both fits include two free parameters: $\Pi_{E,\perp}$ and $a = \Pi_{S,\perp}/P$. We report the best-fit value for the latter parameter in the inset.

its angle is randomly sampled in the perpendicular plane. Adding the contributions from stress and electric fields and averaging over angles, the total splitting becomes

$$\begin{aligned}\tilde{\Pi}_{\perp,\text{avg}} &= \int d\theta (\Pi^2_{S,\perp} + \Pi^2_{E,\perp} + 2\Pi_{S,\perp}\Pi_{E,\perp}\cos\theta)^{1/2} \\ &= \frac{1}{\pi}\left[\sqrt{\Pi^2_{s,\perp} - \Pi^2_{E,\perp}}\,\text{EllipticE}\left(-\frac{4\Pi_{S,\perp}\Pi_{E,\perp}}{\sqrt{\Pi^2_{S,\perp} - \Pi^2_{E,\perp}}}\right)\right. \\ &\quad \left. + \sqrt{\Pi^2_{S,\perp} + \Pi^2_{E,\perp}}\,\text{EllipticE}\left(-\frac{4\Pi_{s,\perp}\Pi_{E,\perp}}{\sqrt{\Pi^2_{S,\perp} + \Pi^2_{E,\perp}}}\right)\right] \end{aligned} \tag{3.9}$$

where $\text{EllipticE}(z)$ is the elliptic integral of the second kind. This function is plotted in Fig. 3.4A, and we note its qualitative similarity to a quadrature sum.

To characterize the intrinsic charge splitting ($\Pi_{E,\perp}$), we first acquire an ODMR spectrum for each diamond sample under ambient conditions. For example, for the (111)-cut diamond, we measured $\Pi_{E,\perp} \approx 4.5$ MHz. For subsequent measures under pressure, we then subtract off the charge contribution from the observed splitting by numerically from inverting Eq. (3.9) and solving for $\Pi_{s,\perp}$.

3.4 Magnetometry in a DAC

3.4.1 Magnetic Imaging at Room Temperature

Having characterized the stress environment, we can safely remove its effect while utilizing the NV centers as an *in situ* magnetometer to detect phase transitions inside the high-pressure chamber. Analogous to the case of stress, we observe a magnetic sensitivity of 12 $\mu\mathrm{T}/\sqrt{\mathrm{Hz}}$, in agreement with the theoretically estimated value, $\eta_B \sim \frac{\delta\nu}{C\gamma_\mathrm{B}\sqrt{Nt}} = 8.8\ \mu\mathrm{T}/\sqrt{\mathrm{Hz}}$. Assuming a point dipole located a distance $d \sim 5\ \mu$m from the NV layer, this corresponds to an experimentally measured magnetic moment sensitivity: $7.5\times10^{-12}\ \mathrm{emu}/\sqrt{\mathrm{Hz}}$ (Fig. 3.1F).

Sensitivity in hand, we begin by directly measuring the magnetization of iron as it undergoes the pressure-driven $\alpha \leftrightarrow \epsilon$ phase transition from body-centered cubic (bcc) to hexagonal close-packed (hcp) crystal structures [149]; crucially, this structural phase transition is accompanied by the depletion of the magnetic moment, and it is this change in the iron's magnetic behavior that we image. Our sample chamber is loaded with a $\sim$10 μm polycrystalline iron pellet as well as a ruby microsphere (pressure scale), and we apply an external magnetic field $B_\mathrm{ext}\sim$180 G. As before, by performing a confocal scan across the culet, we acquire a two-dimensional magnetic resonance map (Fig. 3). At low pressures (Fig. 3A), near the iron pellet, we observe significant shifts in the eight NV resonances, owing to the presence of a ferromagnetic field from the iron pellet. As one increases pressure (Fig. 3B), these shifts begin to diminish, signaling a reduction in the magnetic susceptibility. Finally, at the highest pressures ($P \sim 22$ GPa, Fig. 3C), the magnetic field from the pellet has reduced by over two orders of magnitude.

To quantify this phase transition, we reconstruct the full vector magnetic field produced by the iron sample from the aforementioned two-dimensional NV magnetic resonance maps (Fig. 3.5, D-F). We then compare this information with the expected field distribution at the NV layer inside the culet, assuming the iron pellet generates a dipole field [146]. This enables us to extract an effective dipole moment as a function of applied pressure (Fig. 3.5G). In order to identify the critical pressure, we fit the transition using a logistic function [146]. This procedure yields the transition at $P = 16.7 \pm 0.7$ GPa (Fig. 3.5J).

In addition to changes in the magnetic behavior, another key signature of this first order transition is the presence of hysteresis. We investigate this by slowly decompressing the diamond anvil cell and monitoring the dipole moment; the decompression transition occurs at $P = 10.5 \pm 0.7$ GPa (Fig. 3.5J), suggesting a hysteresis width of approximately $\sim$6 GPa, consistent with a combination of intrinsic hysteresis and finite shear stresses in the methanol/ethanol/water pressure-transmitting medium [149]. Taking the average of the forward and backward hysteresis pressures, we find a critical pressure of $P_\mathrm{c} = 13.6 \pm 3.6$ GPa, in excellent agreement with independent measurements by Mössbauer spectroscopy, where $P_\mathrm{c} \approx 12$ GPa (Fig. 3J) [149].

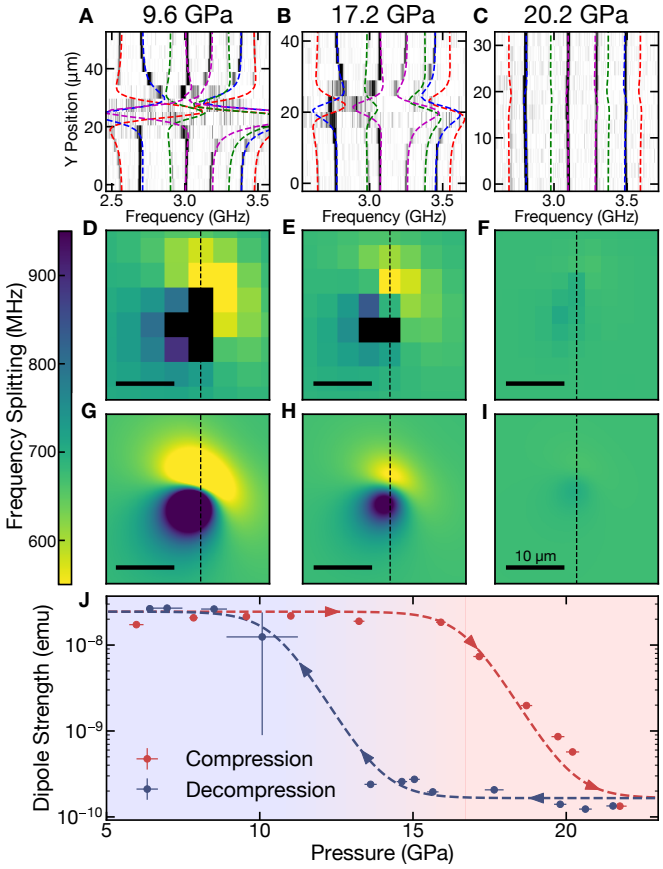

Figure 3.5: Imaging iron's $\alpha \leftrightarrow \epsilon$ phase transition. Applying an external magnetic field ($\mathbf{B}_{\text{ext}} \sim 180$ G) induces a dipole moment in the polycrystalline iron pellet which generates a spatially varying magnetic field across the culet of the diamond anvil. By mapping the ODMR spectra across the culet surface, we reconstruct the local magnetic field which characterizes the iron pellet's magnetization. (**A**-**C**) Comparison between the measured ODMR spectra (dark regions correspond to resonances) and the theoretical resonance positions (different colors correspond to different NV crystallographic orientations) across vertical spatial cuts at pressures 9.6 GPa, 17.2 GPa and 20.2 GPa, respectively (16:3:1 methanol/ethanol/water solution). (**D**-**F**) Map of the measured energy difference of a particular NV crystallographic orientation (blue lines in (A-C)). Black pixels correspond to ODMR spectra where the splitting could not be accurately extracted owing to large magnetic field gradients [146]. (**G**-**I**) Theoretical reconstruction of the energy differences shown in (D-F). Data depicted in (A-C) are taken along the thin black dashed lines. (**J**) Measured dipole moment of the iron pellet as a function of applied pressure at room temperature, for both compression (red) and decompression (blue). Based on the hysteresis observed ($\sim$ 6 GPa), we find the critical pressure $P_c = 13.6 \pm 3.6$ GPa, in excellent agreement with previous studies [149].

Iron Dipole Reconstruction

In this section, we discuss the study of the pressure-induced $\alpha \leftrightarrow \epsilon$ transition in iron. In particular, we provide the experimental details, describe the model used for fitting the data, and outline the procedure to ascertain the transition pressure.

For this experiment, the DAC is prepared with a rhenium gasket preindented to 60 μm thickness and laser drilled with a 100 μm diameter hole. We load a $\sim$ 10 μm iron pellet, extracted from a powder (Alfa Aesar Stock No. 00737-30), and a ruby microsphere for pressure calibration. A solution of methanol, ethanol and water (16:3:1 by volume) is used as the pressure-transmitting medium.

The focused laser is sequentially scanned across a 10×10 grid corresponding to a $\sim$ 30 $\times$ 30 μm area of the NV layer in the vicinity of the iron pellet, taking an ODMR spectrum at each point. Each pixel in the grid is integrated for $\sim$3 minutes. As discussed previously, the energy levels of the NV are determined by both the magnetic field and the stress in the diamond. Owing to their different crystallographic orientations, the four NV orientations in general respond differently to these two local parameters. As a result, for each location in the scan, eight resonances are observed.

A large bias magnetic field ($\sim$ 180 G), not perpendicular to any of the axes, is used to suppress the effect of the transverse stress in the splitting for each NV orientation. However, the longitudinal stress still induces an orientation-dependent shift of the resonances which is nearly constant across the imaging area, as measured independently (Fig 3.6C).

By analyzing the splittings of the NV resonances across the culet, we can determine the local magnetic field and thereby reconstruct the dipole moment of the iron pellet.

To estimate the error in pressure, a ruby fluorescence spectrum was measured before and after the ODMR mapping, from which the pressure could be obtained [33]. The pressure was taken to be the mean value, while the error was estimated using both the pressure range and the uncertainty associated with each pressure point.

Extracting Splitting Information

The eight resonances in a typical ODMR spectrum are fit to Gaussian lineshapes to extract the resonance frequency (Fig 3.7A). Resonances are paired as in Fig. 1D of the main text: from outermost resonances to innermost, corresponding to NV orientations with the strongest magnetic field projection to the weakest, respectively. Once identified, we calculate the splitting and magnetic field projection for each NV orientation.

We note that there are two regimes where our spectra cannot confidently resolve and identify all the eight resonances. First, at high pressure, the resonance contrast for some NV orientations is diminished, possibly due to a modification of the frequency response of the microwave delivery system. Second, close to or on top of the iron pellet, the resonances are broadened; we attribute this to the large magnetic field gradients (relative to the imaging resolution) caused by the sample. The resulting overlap in spectral features obfuscates the

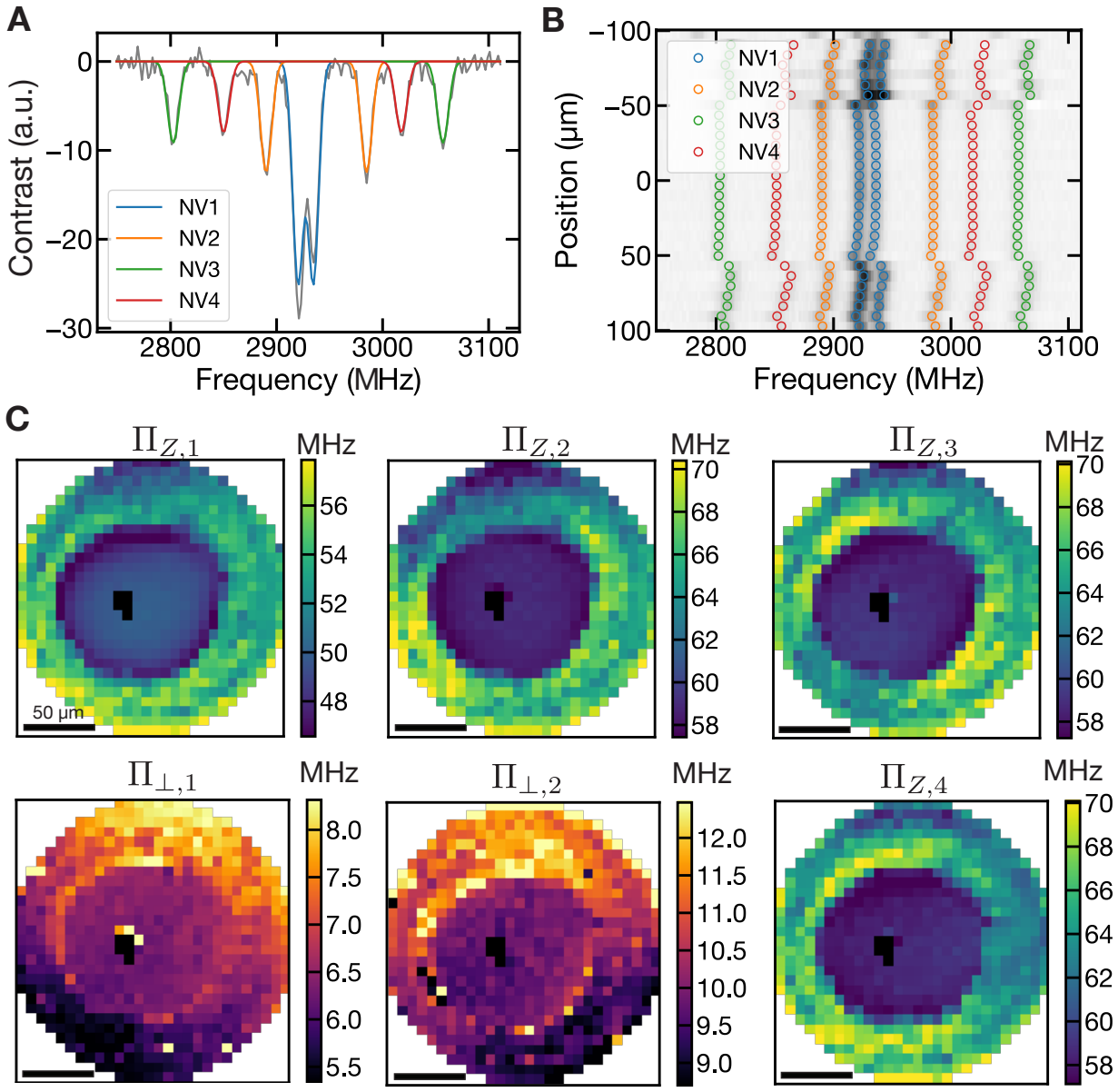

Figure 3.6: Stress reconstruction procedure applied to the (111)-cut diamond at 4.9 GPa. (**A**) A typical ODMR spectrum under an applied magnetic field. The resonances correspond to each NV crystallographic orientation fit to a pair of Lorentzian lineshapes. (**B**) A line-cut indicating the fitted resonance energies (colored points) superimposed on the measured spectra (grey colormap). (**C**) 2D maps of the shifting ($\Pi_{z,i}$) and splitting parameters ($\Pi_{\perp,i}$) for each NV orientation across the entire culet.

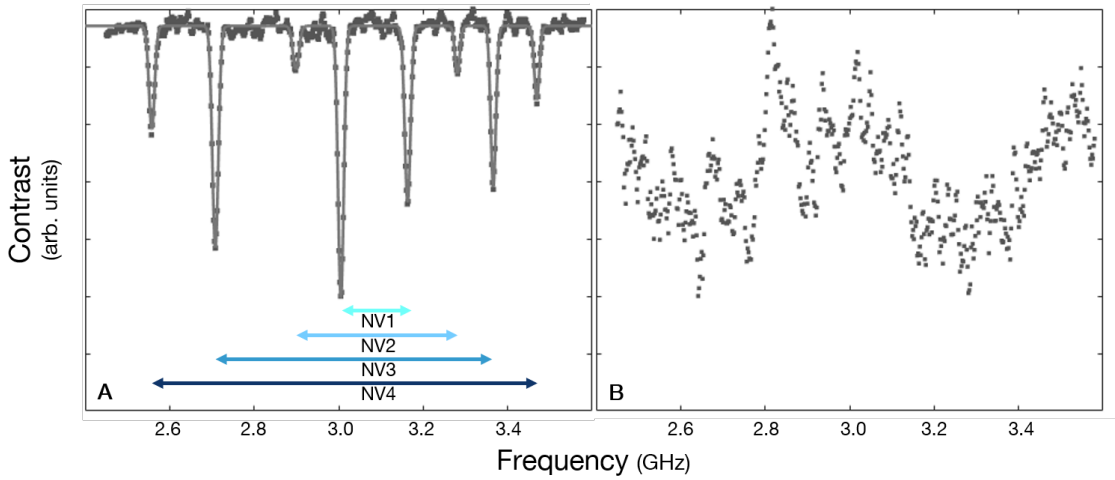

Figure 3.7: **(A)** Example of a typical spectrum with a fit to eight free Gaussians. Resonance pairs are identified as in Fig. 1D of the main text: NV4 has the strongest magnetic field projection and NV1 has the weakest. **(B)** Example spectrum for which resonances are broadened and shifted. In this case we cannot correlate any resonances in the spectrum to specific NV orientations.

identity of each resonance (Fig. 3.7B). In both cases, we fit and extract splittings only for the orientations we could identify with certainty.

Point Dipole Model

We model the magnetization of our pellet sample as a point dipole at some location within the sample chamber. The total magnetic field is then characterized by the external applied field, B_0, the dipole of the sample, d, and the position of the dipole, r. Because of the presence of a large applied field, we observe that the magnetization of the sample aligns with B_0, and thus, we require only the strength of the dipole to characterize its moment, $d = D\hat{B}_0$. We expect the external magnetic field and the depth of the particle to remain nearly constant at different pressures. This is indeed borne out by the data. As a result, we consider the external magnetic field B_0 = (-23(7), -160(1), 92(2)) G and depth of the iron pellet $r_Z = 5(1)$ μm to be fixed.

Due to the dipole of the iron pellet, the magnetic field across the NV layer at position x is given by:

$$B(x) = B_0 + \frac{\mu_0}{4\pi}\frac{1}{|x|^3}(3\hat{x}(d\cdot\hat{x}) - d) \tag{3.10}$$

where hats represent unit vectors. At each point, the local field induces a different splitting, $\Delta^{(i)}$, to the 4 NV crystallographic orientations $i \in 1, 2, 3, 4$, measured by diagonalizing the

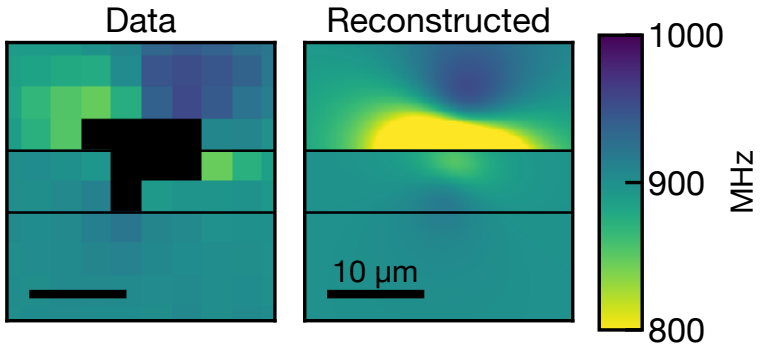

Figure 3.8: Measured map of the splittings of one of the NV orientations (left). Near the top of the plot we observe a much stronger splitting compared to the bottom of the plot. Throughout the measurement, the shift in the pressure induced a shift in the dipole moment of the sample. We consider 3 different regions (seperated by horizontal lines) corresponding to 3 different dipole strengths. The reconstructed map of the splittings is shown on the right in agreement with the data. From the center and the spread of dipole strengths, we extract the dipole moment and its error. Black bar corresponds to 10 μm.

Hamiltonian $H = D_{gs}S_z^2 + B_z^{(i)}S_z + B_\perp^{(i)}S_x$, where $B_z = |B \cdot \hat{z}^{(i)}|$ is the projection of B onto the axis of the NV, and $B_\perp^{(i)} = \sqrt{|B|^2 - (B_z^{(i)})^2)}$ its transverse component. D_{gs} is the zero field splitting of the NV. For each choice of D, r_X and r_Y , we obtain a two dimensional map of $\{\Delta^{(i)}\}$. Performing a least squares fit of this map against the experimental splittings determines the best parameters for each pressure point. The error in the fitting procedure is taken as the error in the dipole strength D.

Large error bar in the 11 GPa decompression point

During the decompression, around 11 GPa, we observed a significant drift of the pressure during measurement of the ODMR spectra. Unfortunately, the starting pressure was close to the transition pressure, and the drift in pressure led to a very large change in the pellet's dipole moment throughout the scanning measurement. This is clear in the measured data, Fig. 3.8, with the top-half of the map displaying a significantly larger shift with respect to the bottom-half.

To extract the drift in the dipole moment, we divide the two-dimensional map into three different regions, each assumed to arise from a constant value of the dipole moment of the pellet. By fitting to three different dipole moments (given a fixed position, r_X and r_Y) we obtain an estimate of the drift of the dipole moment that allows us to compute an errorbar of that measurement. The estimated dipole moment at this pressure point is taken as the midpoint of the three extracted values, $\frac{D_{max} + D_{min}}{2}$, while the error is estimated by the

range, $\frac{D_{max} - D_{min}}{2}$.

3.4.2 *In Situ* Magnetometry at Extreme Temperature and Pressure

We demonstrate the integration of our platform into a cryogenic system, enabling us to make spatially resolved *in situ* measurements across the pressure-temperature (P-T) phase diagram of materials. Specifically, we investigate the magnetic P-T phase diagram of the rare-earth element gadolinium (Gd) up to pressures $P \approx 8$ GPa and between temperatures $T = 25 - 340$ K. Owing to an interplay between localized 4f electrons and mobile conduction electrons, Gd represents an interesting playground for studying metallic magnetism; in particular, the itinerant electrons mediate RKKY-type interactions between the local moments, which in turn induce spin-polarization of the itinerant electrons [120]. Moreover, much like its other rare-earth cousins, Gd exhibits a series of pressure-driven structural phase transitions from hexagonal close-packed (hcp) to samarium-type (Sm-type) to double hexagonal close-packed (dhcp) (Fig. 3.9)[77]. The interplay between these different structural phases, various types of magnetic ordering, and metastable transition dynamics leads to a complex magnetic P-T phase diagram that remains the object of study to this day [77, 131, 120].

In analogy to our measurements of iron, we monitor the magnetic ordering of a Gd flake via the NV's ODMR spectra at two different locations inside the culet: close to and far away from the sample (the latter to be used as a control) [146]. Due to thermal contraction of the DAC (which induces a change in pressure), each experimental run traces a distinct non-isobaric path through the P-T phase diagram (Fig. 4C, blue curves). In addition to these DC magnetometry measurements, we also operate the NV sensors in a complementary mode, i.e. as a noise spectrometer.

We begin by characterizing Gd's well-known ferromagnetic Curie transition at ambient pressure, which induces a sharp jump in the splitting of the NV resonances at $T_{\mathrm{C}} = 292.2 \pm 0.1$ K (Fig. 4D). As depicted in Fig. 4A, upon increasing pressure, this transition shifts to lower temperatures, and consonant with its second order nature [63], we observe no hysteresis; this motivates us to fit the data and extract T_{C} by solving a regularized Landau free-energy equation [146]. Combining all of the low pressure data (Fig. 4C, red squares), we find a linear decrease in the Curie temperature at a rate: $dT_{\mathrm{C}}/dP = -18.7 \pm 0.2$ K/GPa, consistent with prior studies via both DC conductivity and AC-magnetic susceptibility [77]. Surprisingly, this linear decrease extends well into the Sm-type phase. Upon increasing pressure above ~ 6 GPa (path [b] in Fig. 4C), we observe the loss of ferromagnetic (FM) signal (Fig. 4B), indicating a first order structural transition into the paramagnetic (PM) dhcp phase [77]. In stark contrast to the previous Curie transition, there is no revival of a ferromagnetic signal even after heating up ($\sim$315 K) and significantly reducing the pressure (< 0.1 GPa).

A few remarks are in order. The linear decrease of T_{C} well beyond the $\sim$2 GPa structural transition between hcp and Sm-type is consistent with the "sluggish" equilibration between these two phases at low temperatures [77]. The metastable dynamics of this transition are

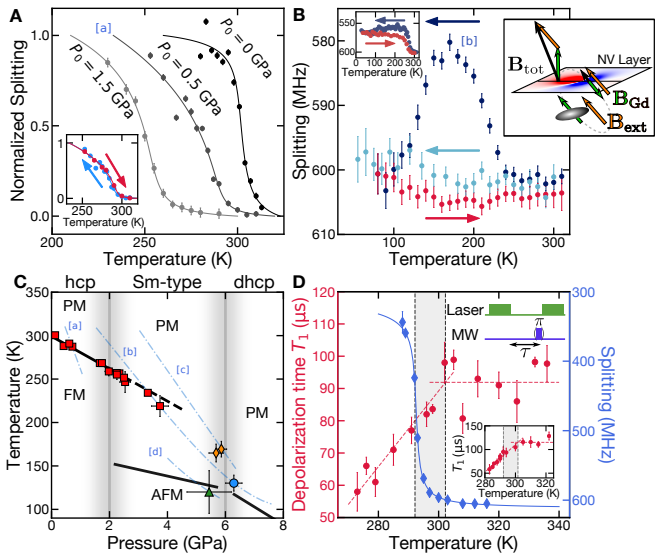

Figure 3.9: **F**ig. 4. Magnetic P-T phase diagram of gadolinium. A $\sim 30\ \mu\text{m} \times 30\ \mu\text{m} \times 25\ \mu\text{m}$ polycrystalline Gd foil is loaded into a beryllium copper gasket with a cesium iodide pressure medium. An external magnetic field, $\mathbf{B}_{\text{ext}} \sim 120$ G, induces a dipole field, $\mathbf{B}_{\text{Gd}}$, detected by the splitting of the NVs (right inset, (B)). (**A**) The FM Curie temperature T_{C} decreases with increasing pressure up to $\sim$4 GPa. NV splittings for three P-T paths, labeled by their initial pressure P_0, are shown. The P-T path for run [a] ($P_0 = 0.5$ GPa) is shown in (C). The cool-down (blue) and heat-up (red) of a single P-T cycle shows negligible hysteresis (inset). (**B**) If a P-T path starting in hcp is taken into the dhcp phase (at pressures $\gtrsim 6$ GPa) [77], the FM signal is lost and not reversible, as shown in (C) (path [b]). Upon cool-down (dark blue), we observe the aforementioned Curie transition, followed by the loss of FM signal at 6.3 GPa, 130 K. But upon heat-up (red) and second cool-down (light blue), the FM signal is not recovered. When the pressure does not go beyond $\sim$ 6 GPa, the FM signal is recoverable (left inset) [146]. (**C**) Magnetic P-T phase diagram of Gd. At low pressures, we observe the linear decrease of T_{C} (black line) with slope -18.7 ± 0.2 K/GPa, in agreement with previous measurements [77]. This linear regime extends into the Sm-type phase (black dashed line) due to the slow dynamics of the hcp $\rightarrow$ Sm-type transition [77]. When starting in the Sm-type phase, we no longer observe a FM signal, but rather a small change in the magnetic field at either the transition from Sm-type to dhcp (orange diamonds) or from PM to AFM (green triangle), depending on the P-T path. The bottom two phase boundaries (black lines) are taken from Ref. [131]. (**D**) At ambient pressure, we observe a Curie temperature, $T_{\text{C}} = 292.2 \pm 0.1$ K, via DC magnetometry (blue data). Using nanodiamonds drop-cast onto a Gd foil (and no applied external magnetic field), we find that the depolarization time (T_1) of the NVs is qualitatively different in the two phases (red data). T_1 is measured using the pulse sequence shown in the top right inset. The T_1 measurement on another nanodiamond exhibits nearly identical behavior (bottom inset).

strongly pressure and temperature dependent, suggesting that different starting points (in the P-T phase diagram) can exhibit dramatically different behaviors [77]. To highlight this, we probe two *different* transitions out of the paramagnetic Sm-type phase by tailoring specific paths in the P-T phase diagram. By taking a shallow path in P-T space, we observe a small change in the local magnetic field across the *structural* transition into the PM dhcp phase at ∼6 GPa (Fig. 4C, path [c], orange diamonds). By taking a steeper path in P-T space, one can also investigate the *magnetic* transition into the antiferromagnetic (AFM) Sm-type phase at ∼ 150 K (Fig. 4C, path [d], green triangle). In general, these two transitions are extremely challenging to probe via DC magnetometry since their signals arise only from small differences in the susceptibilities between the various phases [146]. To improve upon this weak signature, complementary schemes are required that depend on more relevant quantities (see Section 3.5).

Additional Data

In this section we present all of the data for the different paths taken in P-T phase and the resulting fits. Table 3.1 summarizes the observations for all experimental runs. Figure 3.10 contains the data used in determining the linear pressure dependence of the hcp phase. Figure 3.11 comprises the data used in determining the transition to the dhcp phase, either via the FM hcp to PM dhcp transition, Figure 3.11B, or via the difference in susceptibilities between PM Sm-type and PM dhcp of Gd, Figure 3.11C and D. We emphasize that in the blue path, we begin the experiment below 2 GPa and thus in the hcp structure, while for the orange and green, we begin above 2 GPa, so we expect the system to be in Sm-type. Finally, Figure 3.12 contains the data where we observe a change in the susceptibility of Gd that occurs at the purported Sm-type PM to AFM transition.

Fitting the phase transition of Gd

There are three different transitions we attempt to identify in Gd's P-T phase diagram: a magnetic transition from PM dhcp to FM dchp; structural phase transitions, either hcp → dhcp or Sm-type ↔ dhcp; and a magnetic phase transition from PM Sm-type to AFM Sm-type.

In order to extract the transition temperature of the paramagnet to ferromagnet transition from our data, we model the magnetization of our sample near the magnetic phase transition using a regularized mean field theory.

The magnetism of gadolinium is well-described by a three dimensional Heisenberg magnet of core electrons [120]. In the presence of an external magnetic field, the free energy near the critical point is expanded in even powers of the magnetization with a linear term that couples to the external magnetic field:

$$f = -Bm + \frac{\alpha}{2}(T - T_{\mathrm{C}})m^2 + \frac{\beta}{4}m^4, \tag{3.11}$$

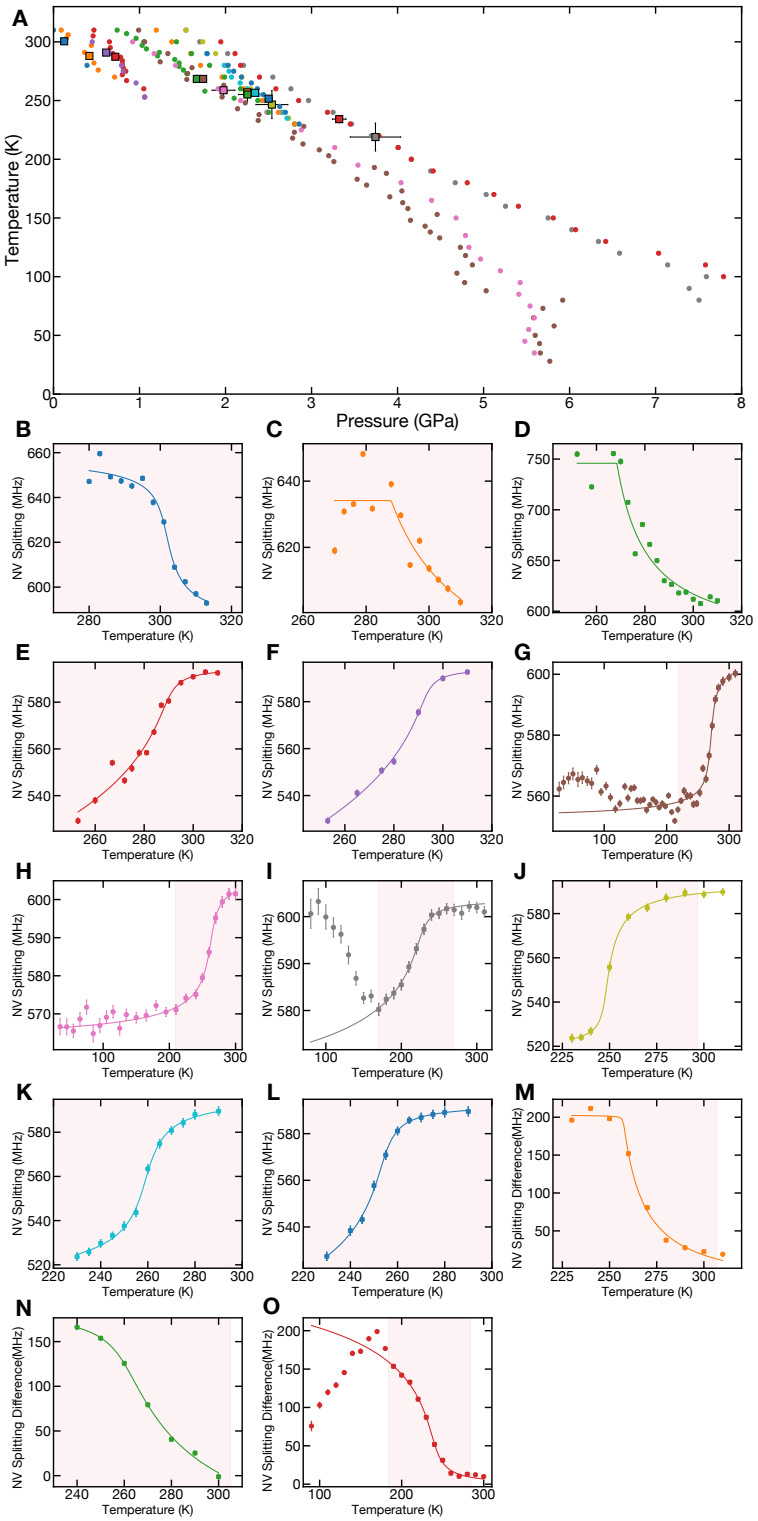

Figure 3.10: (A) Paths in the P-T phase space that inform about the hcp PM phase to the hcp FM phase. (B-O) Measured NV splitting and corresponding fit. The resulting transition temperatures are highlighted in (A) with squares. Shaded region corresponds to the part of the spectrum fitted.

Run	Direction	Phase transition	Remarks, visible in Fig.
1	Heat-up	hcp (FM) $\longrightarrow$ hcp (PM)	New sample, Fig. 3.10B
2	Cool-down	hcp (PM) $\longrightarrow$ hcp (FM)	Fig. 3.10C
3	Cool-down	hcp (PM) $\longrightarrow$ hcp (FM)	Fig. 3.10D
4	Cool-down	No observation	Probably starting in Sm due to large initial pressure
5	Cool-down	hcp (PM) $\longrightarrow$ hcp (FM)	New sample, Fig. 3.10E
6	Heat-up	hcp (FM) $\longrightarrow$ hcp (PM)	Fig. 3.10F
7	Cool-down	hcp (PM) $\longrightarrow$ hcp (FM)	Fig. 3.10G
8	Heat-up	hcp (FM) $\longrightarrow$ hcp (PM)	Fig. 3.10H
9	Cool-down	hcp (PM) $\longrightarrow$ hcp (FM) $\longrightarrow$ dhcp (PM)	Fig. 3.10I, 3.11B
10	Cool-down	Weak evidence for Sm (PM) $\longrightarrow$ Sm (AFM)	Probably starting in Sm due to metastability, Fig. 3.12B
11	Cool-down	hcp (PM) $\longrightarrow$ hcp (FM)	New sample, Fig. 3.10J
12	Heat-up	hcp (FM) $\longrightarrow$ hcp (PM)	Fig. 3.10K
13	Cool-down	hcp (PM) $\longrightarrow$ hcp (FM)	Fig. 3.10L
14	Cool-down	Weak evidence for Sm (PM) $\longrightarrow$ dhcp (PM)	Probably starting in Sm due to large initial pressure
15	Cool-down	Weak evidence for Sm (PM) $\longrightarrow$ dhcp (PM)	Probably starting in Sm due to metastability, Fig. 3.11C
16	Heat-up	Weak evidence for dhcp (PM) $\longrightarrow$ Sm (PM)	Fig. 3.11D
17	Cool-down	hcp (PM) $\longrightarrow$ hcp (FM)	New sample, Fig. 3.10M
18	Heat-up	hcp (FM) $\longrightarrow$ hcp (PM)	Fig. 3.10N
19	Cool-down	hcp (PM) $\longrightarrow$ hcp (FM) and start of transition to dhcp (PM)	Fig. 3.10O

Table 3.1: Summary of all experimental runs in the P-T phase diagram, indexing either a decrease or increase in temperature during this path, and the observed phase transitions. Each group of runs, between double lines in the table, corresponds to a different sample.

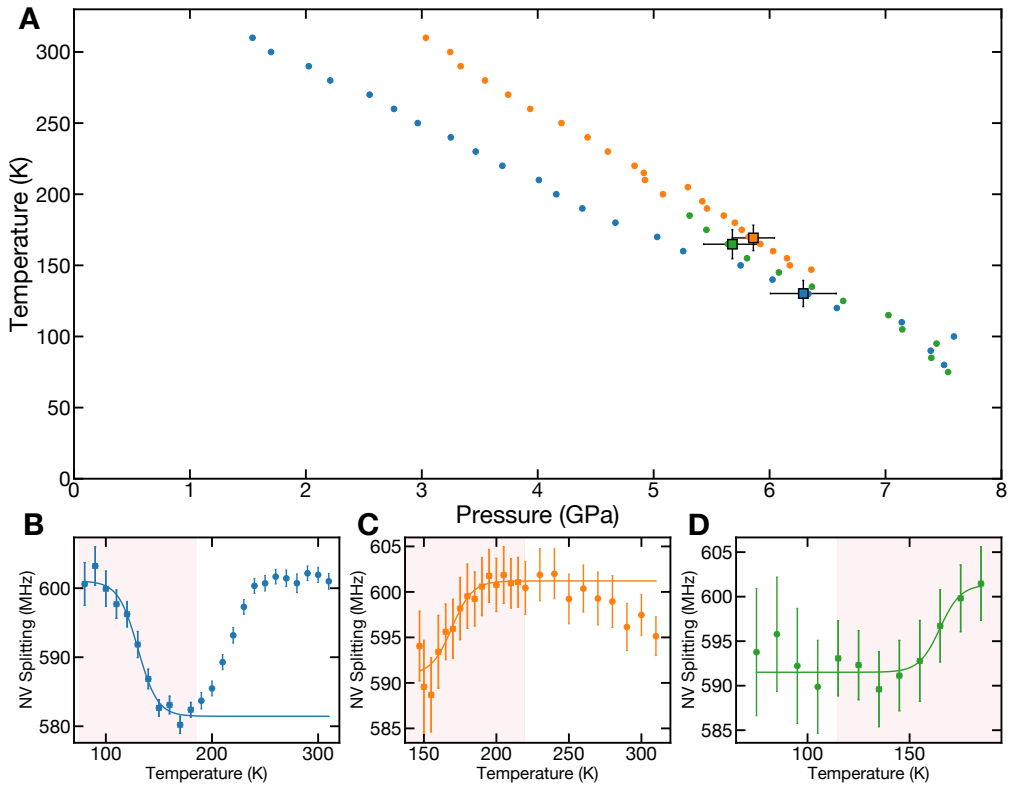

Figure 3.11: (A) Paths in the P-T phase space that inform about the transition to the PM dhcp phase. (B-D) Measured NV splitting and corresponding fit. The resulting transition temperatures are highlighted in (A) with squares. We interpret (B) as a transition from FM hcp to PM dhcp, while (C),(D) as a transition from PM Sm-type to PM dhcp. Shaded region corresponds to the part of the spectrum fitted.

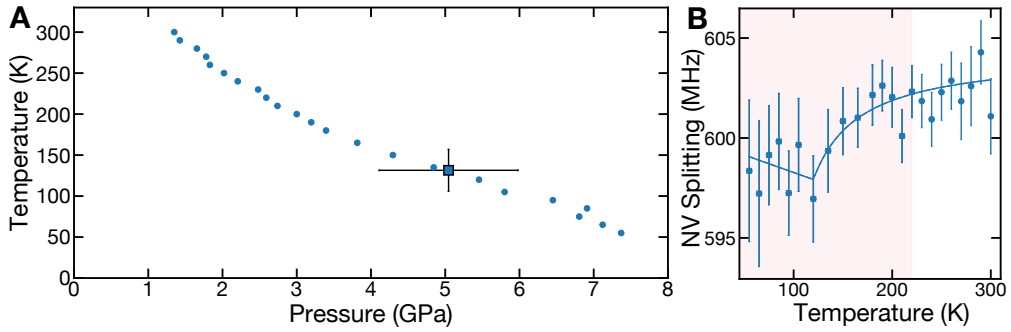

Figure 3.12: (A) Path in the P-T phase space where a signal consistent with the purported AFM transition in Sm-type Gd is seen (B). Shaded region corresponds to the part of the spectrum fitted.

where m is the magnetization, B is the external magnetic field, α and β the expansion coefficients, T the temperature, and T_{C} the transition temperature. In this treatment, we implicitly assume that α and β do not vary significantly with pressure and thus can be taken to be constant across paths in P-T phase space. The magnetization $m_{\min}$ is then obtained by minimizing the free energy.

Because our observation region extends far away from the transition, we observe a plateauing of the splittings that emerges from the microscopics of Gd. Using R as the regularization scale and $\tilde{A}$ as the maximum magnetization of the sample we propose the simple regularization scheme:

$$m(T,P) = \tilde{A}\frac{m_{\min}}{m_{\min}+R}. \tag{3.12}$$

The splitting of the NV group, up to some offset, is proportional to the magnetization of the sample. This proportionality constant, A, captures he relation between magnetization and induced magnetic field, the geometry of sample relative to the measurement spot, as well as the susceptibility of the NV to the magnetic field. The splitting of the NV is then given by:

$$\Delta = A\frac{m_{\min}}{m_{\min}+R} + c \tag{3.13}$$

where we incorporated $\tilde{A}$ into A as well. Normalizing α and β with respect to B, we obtain six parameters that describe the magnetization profile, directly extracting T_{C}.

In the case of the first order structural phase transitions, similar to that of iron, we take the susceptibility to follow a logistic distribution. We model the observed splitting as:

$$\Delta = \frac{A}{e^{B(T-T_{\mathrm{C}})}+1} + c \tag{3.14}$$

Fitting to the functional form provides the transition temperature T_{C}. Error bar is taken as largest between $1/B$ and the fitting error.

In the case of the paramagnetic to antiferromagnetic transition, we use the mean field susceptibility across the phase transition of the system. The susceptibility across such transition is peaked at the transition temperature:

$$\chi(T) \propto \begin{cases} \dfrac{1}{T-\theta_p} & T > T_c \\ \\ C\dfrac{3L'(H/T)}{T-\theta_p 3L'(H/T)} & T < T_c \end{cases} \tag{3.15}$$

where C is chosen to ensure continuity of χ, $L'(x)$ is the derivative of the Langevin function $L(x)$, H is a measure of the applied field, and θ_p is the asymptotic Curie point. Finally, we fit the observed splitting to:

$$\Delta = A\chi(T; T_c, H, \theta_p) + c \tag{3.16}$$

where, as before, A captures both the geometric effects, as well as the response of the chosen NV group to the magnetic field.

Recreating the P-T phase diagram of Gd

The rich magnetic behavior of Gd is partially dependent on its structural phases, captured in the sequence: hexagonal closed packed (hcp) to Samarium (Sm) type at $\sim$ 2 GPa, and then to double hexagonal closed packed (dhcp) at $\sim$ 6 GPa. In particular, while the paramagnetic (PM) phase of hcp orders to a ferromagnet (FM), the PM phase of Sm-type orders to an antiferromagnet (AFM) [77]. Similarly, dhcp undergoes a PM to magnetically ordered phase transition.

For experimental runs with initial pressures $<$ 2 GPa (runs 1-3, 5-9, 11-13, 17-19), we observe a PM $\leftrightarrow$ FM phase transition in hcp Gd. In agreement with previous studies, we see a linear decrease of the Curie temperature with increasing pressure up to $\sim$ 4 GPa [30]. Notably, prior studies have shown a structural transition from hcp to Sm-type at 2 GPa [30, 131, 71], which is believed to be "sluggish" [77, 30]. This is indeed consistent with our observation that the linear dependence of the Curie temperature persists well into the Sm-type region, suggesting the existence of both structural phases over our experimental timescales.

Furthermore, in run 9 (Table 3.1 and Fig. 3.11A,B), we observe a complete loss of FM signal when pressures exceed $\sim$ 6 GPa at $\sim$ 150 K, in good agreement with the previously reported phase transition from hcp (FM) to dhcp (PM) structure [131, 30]. Upon performing a similar path in P-T space (run 19), we observe the same behavior. In contrast to the previous slow hcp to Sm-type transition, we believe that the equilibrium timescale for the hcp (FM) to dhcp (PM) transition is much faster at this temperature.

After entering the dhcp structure (run 9), we no longer observe a clear FM signal from the sample even after heating to 315 K and depressurizing $<$ 0.1 GPa. This can be explained by the retention of dhcp or Sm-type structure in the sample. Previous studies, suggesting that the Sm-type phase in Gd is metastable up to ambient pressure and temperature [77], corroborate that our sample is likely still in the Sm-type structural phase. It is not too surprising, that by continuing to cool down and walking along a slightly different P-T path, we observe only a small change in the NV splitting at $\sim$ 150 K and $\sim$ 5 GPa as we cross the purported Sm-type PM to AFM phase boundary (run 10 in Table 3.1)[131, 77, 30].

Moreover, the metastable dynamics of hcp to Sm-type transitions are strongly pressure and temperature dependent, suggesting that different starting points (in the P-T phase diagram) can lead to dramatically different behaviors. Indeed, by preparing the sample above 2 GPa at room temperature (run 4), we no longer detect evidence for a ferromagnetic Curie transition, hinting the transition to the Sm-type structure. Instead, we only observe a small change in the NV splitting at $\sim$ 6 GPa and $\sim$ 170 K, which could be related to the presence of different paramagnetic susceptibilities of the Sm-type and dhcp structural phases. Interestingly, by cycling temperature across the transition (run 14-16 in Table 3.1), we observe negligible hysteresis, suggesting fast equilibration of this structural transition.

3.5 Noise Spectroscopy

Motivated by the limitations to DC magnetometry we encountered above, we demonstrate a complementary NV sensing modality based upon noise spectroscopy, which can probe phase transitions even in the absence of a direct magnetic signal. [21]. Thanks to the simplicity of the measurement, the technique is easy to implement in a DAC. Specifically, returning to Gd's ferromagnetic Curie transition, we use nanodiamonds at ambient pressure to monitor the NV's depolarization time, T_1, as one crosses the phase transition (Fig. 3.9D). Normally, the NV's T_1 time is limited by spin-phonon interactions and *increases* dramatically as one decreases temperature. Here, we observe a strikingly disparate behavior. In particular, using nanodiamonds drop-cast on a Gd foil at ambient pressure, we find that the NV T_1 is nearly temperature independent in the paramagnetic phase, before exhibiting a kink and subsequent *decrease* as one enters the ferromagnetic phase (Fig. 3.9D). We note two intriguing observations: first, one possible microscopic explanation for this behavior is that T_1 is dominated by Johnson-Nyquist noise from the thermal fluctuations of charge carriers inside Gd [85].[3] Gapless critical spin fluctuations or magnons in the ordered phase, while expected, are less likely to cause this signal [146]. Second, we observe that the Curie temperature, as identified via T_1-noise spectroscopy, is ~ 10 K higher than that observed via DC magnetometry (Fig. 3.9D). Similar behavior has previously been reported for the surface of Gd [120, 148], suggesting that our noise spectroscopy could be more sensitive to surface physics.

3.5.1 Specifics

In order to perform magnetic noise spectroscopy of Gd at temperatures ranging from 273 K to 340 K, we attach a small chunk of Gd foil (100 μm $\times$ 100 μm $\times$ 25 μm) close to a microwave wire on a Peltier element with which we tune the temperature. Instead of millimeter-scale diamonds as before, we use nano-diamonds (Adámas Nanotechnologies, $\sim$ 140 nm average diameter). The nano-diamonds are prepared in solution and allowed to evaporate onto the Gd foil to minimize the distance to the surface of our sample.

With no external field applied, all eight resonances of the NVs inside the nano-diamonds are found within our resolution to be at the zero-field splitting D_{gs} for either para- and ferromagnetic phase of Gd, leading to a larger resonance contrast since we can drive all NVs with the same microwave frequency. Measuring the NV's spin relaxation time T1 under these circumstances is equivalent to ascertaining the AC magnetic noise at ~ 2.87 GHz.

For this purpose, we utilize the following pulse sequence to measure T1. First, we apply a 10 μs laser pulse to intialize the spin into the $|m_s = 0\rangle$ state. After laser pumping, we let the spin state relax for a variable time before turning on a second laser pulse to detect the spin state (signal bright). We repeat the exact same sequence once more, but right before spin detection, an additional NV π-pulse is applied to swap the $|ms = 0\rangle$ and $|ms = \pm 1\rangle$ populations (signal dark). The difference between signal bright and dark gives us a reliable

[3] As opposed to isolated NV samples, where T_1 is limited by spin-phonon interactions.

measurement of the NV polarization (Fig. 4D top inset) after time . The resulting T1 curve exhibits a stretched exponential decay $\propto e^{-(\tau/T_1)^\alpha}$ with $\alpha \sim 0.65$ (Fig. S19).

By sweeping the Peltier current over a range of ~ 3.5 A, we adjust the temperature of the sample from 273 K to 340 K, therefore determining the temperature dependence of T_1.

This procedure is performed on two different nano-diamonds on top of the Gd flake to confirm that the signal is not an artifact. Furthermore, this is contrasted with an additional measurement at a nano-diamond far away from the Gd foil, exhibiting no temperature dependence of T_1.

3.6 Conclusions and Outlook

In this chapter, we discussed the development of a hybrid platform integrating quantum sensors into DACs. This work succeeded in creating the first image of the complete local stress tensor across the sample and gasket as a function of pressure. Primarily, calibrating the local stress environment of the NVs inside the culet permits their use in probing further phenomena unique to DACs. By studying the stress of other fluids and solids, we may discover new insights into viscous flow, plastic deformation, pressure-dependent yield strength, and other mechanical phenomena. The NV-DAC platform is then a clear advancement beyond the CPU limitations of numerical finite-element simulations or the practical hurdles of more conventional experimental methods. Furthermore, it may eventually enable control over deviatoric- and normal-stress conditions in a high pressure apparatus [48].

The technique developed in this chapter can be expanded to employ other atomic defects instead of or in addition to the NV center. The increasingly-popular silicon-vacancy centers in diamond could be a natural candidate due to their all-optical control schemes that may supplant the need for pesky microwave delivery wires [10]. As well, there are DAC applications that benefit from anvils made of materials other than diamond. Recent studies find that moissanite anvils (6H silicon carbide) host optically-active defects one may also use as local sensors [10]. One distinct advantage of moissanite anvils is that they can be manufactured with centimeter-scale or larger culets, in contrast the the millimeter-scale or smaller culets of diamond anvils. Defect sensors in these larger DACs could potentially release the constraints on experiments by increasing the sample volumes.

We found that the proximity with which we can place our highly-sensitive NV probes near a sample under extreme pressure provides many capabilities beyond previous techniques (Fig. 1F); including for example, measuring nuclear magnetic resonance (NMR) at picoliter volumes [82] and single grain remnant magnetism [55], in addition to imaging phenomena that exhibit spatial textures such as magnetic skyrmions [38] and superconducting vortices [152]. We expect that the manifold sensing capabilities that have been extensively-developed for NV centers (i.e. electric, thermal, gryroscopic precession etc.) may now be implemented in high pressure environments. This work reveals the potential for a vast range of new experiments that quantitatively characterize materials under extreme temperature and pressure, finally complementing the work of first-principles theory.

Chapter 4

Quasi-2D Defect Dynamics

4.1 Introduction

Dimensionality has emerged as a promising tuning-knob in the enduring pursuit of improved sensors and exotic many-body phases of matter. Sensors comprising spin systems benefit from lower dimensions. Reducing the spread of spins reduces signal broadening and the gradient of MW pulses across the probes, both of which are sources of error in the measurement. Decreasing the thickness of the NV layer has also been found to extend the coherence time [117, 43]. Delta-doped layers of spin ensembles with thickness much less than the diffraction limit holds much promise for sensing applications. In the realm of simulation, spin systems in three dimensions are subject to a fast thermalization that precludes the observation of exotic driven phases of matter (owing to the long-range nature of the dipolar interaction) [88], but lowering the dimensions of the spin system abates the issue by extending the prethermal lifetime of the desired phase.

While three-dimensional spin systems of NVs have been used extensively for research and technological applications as seen throughout this thesis, the advent of the delta-doping technique has kindled anticipation for two-dimensional NV spin platforms [117, 110]. The technique permits nanometer-precision depth control of nitrogen-doping near the surface of synthetic diamond. Irradiation then generates NV and substitutional nitrogen (P1) spin defects in layers of nanometer-scale thickness. Even in samples with high NV and P1 densities, long NV coherence times are expected for clean enough diamonds [43, 72]. In principle, delta-doping can create quasi-two-dimensional (q2D) defect environments, in which the average defect spacing is larger than the layer thickness, yet no conventional sample characterization methods have proven the growth of q2D NV systems.

In this Chapter, we present theoretical developments and on-going research that exploit the local dynamics of the NV to verify the q2D nature of a platform for subsequent studies of exotic may-body phenomena in lower dimensions. First, we discuss a proposal and its challenges for verifying the dimensionality of a q2D NV-P1 spin defect sample grown via delta-doping. This procedure entails the observation of non-monotonic variations in the coherence

lifetimes of the NV ensemble over a sweep of the angle of an externally-applied magnetic field. These variations in lifetime are a distinctly two-dimensional signature. Second, we provide an analytical understanding of the coherence decay dynamics for any dimension. In our Ising-dominated regime, the ensemble average of the coherence decay has a parametric dependence on dimension and the interaction exponent. Consequently, we observe stretched exponential decay profiles, with a stretched power depending on the convolution of the measurement protocol's filter function and the autocorrelation of the bath. Finally, we discuss on-going research utilizing the change in the stretched exponential decay profile as the NVs enter different regimes of interaction. For any ensemble of interacting spins in a quasi-2D environment, there is an interaction-regime crossover between the ensemble exhibiting correlated dynamics and uncorrelated dynamics. In our NV-P1 environment, both the NVs and the P1s are interacting ensembles of spins, presenting the possibility of up to two crossovers in any coherence decay measurement.

4.2 Experimental Apparatus and Sample

The experimental apparatus used for the work presented in this chapter is indistinct from those described in Section 1.4.3: a confocal microscope with 3D magnetic coils and mu-metal shielding that delivers MW using a stripline. However, since measurement sequences in this chapter aimed to use 100s or 1000s of MW pulses, the pulse error had to be more carefully analyzed and minimized. To this end, we create and test the pulse error properties of a few different stripline designs. The only other distinguishing feature of this apparatus from those in previous chapters is the diamond sample itself.

4.2.1 Microwave Pulse Error in Striplines

Our stripline MW delivery design is as described in Section 1.4.3. It was used in all experiments that do not use a magnet wire. The coverslip was hosted on a printed circuit board (PCB), which the conducted the MW from the SMA connectors that served as the ports for the MW cables. Both the coverslip and SMA connectors were soldered to the PCB. Since we used XY8 sequences with hundreds or thousands of pulses in the process of this research, small pulse error could accumulate into large effects. More than ever, we needed to characterize and minimize pulse error.

Using a 13 GHz bandwidth oscilloscope, we could resolve the details of the shape of our MW pulses (Fig. 4.2a). By varying where in our circuit we diverted MW to the scope, we could identify impurities in the pulse shape. We tested both the amplifier output and stripline output. Taking the Fourier transform of specific regions of the traces, we found resonant noise following the end of each pulse (Fig. 4.2b). By adding a circulator either after the amplifier or after the stripline, we found that the resonant noise output from the stripline was only partially suppressed (beyond the insertion loss of the circulator), suggesting the noise is resonant reflections occurring within the stripline PCB board itself.

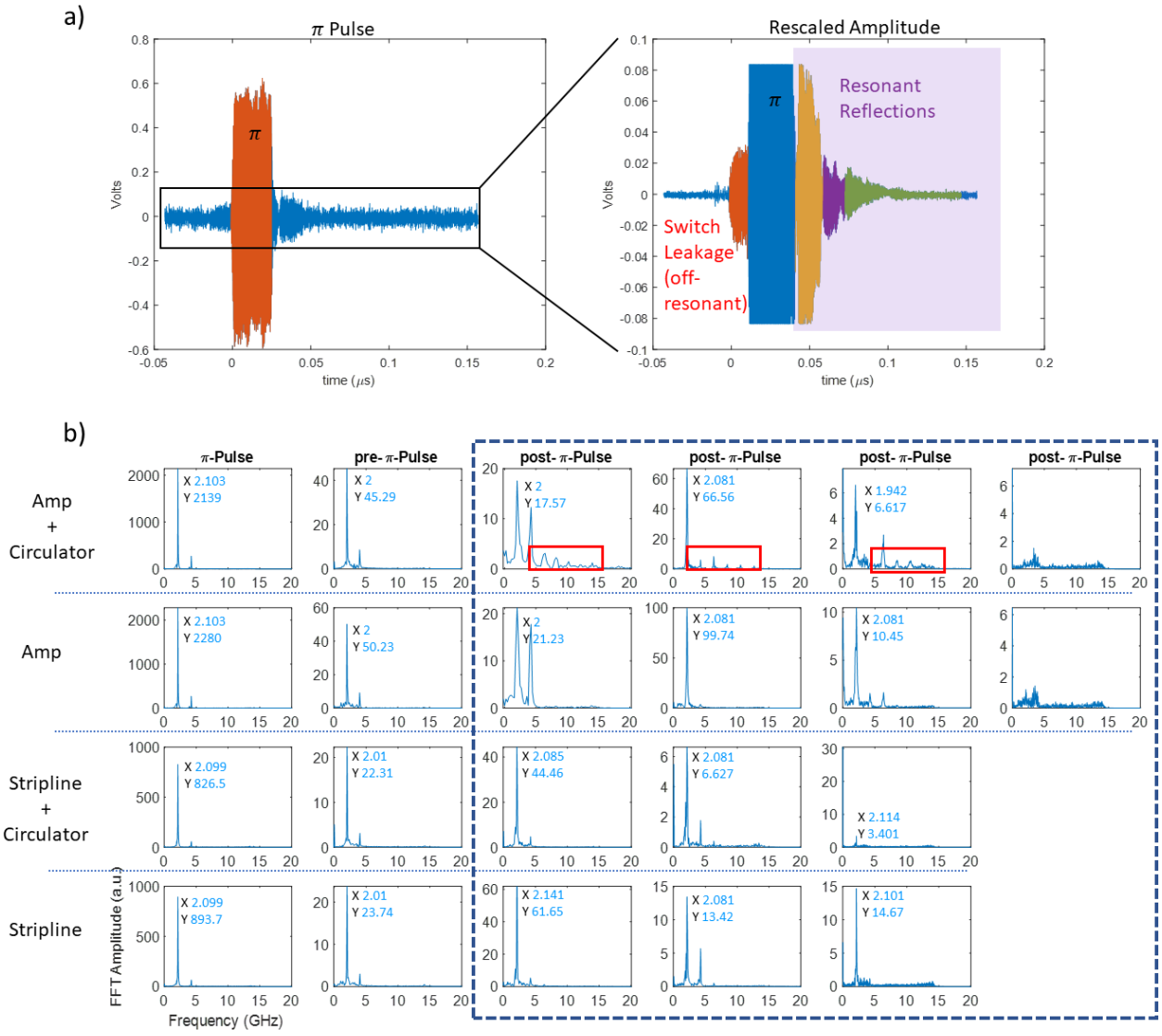

Figure 4.1: a) A π-pulse output from the stripline observed on a 13 GHz bandwidth oscilloscope. Since the MW are $\sim$2 GHz and the pulses $\sim$ 20 MHz, the MW oscillate too fast to resolve individual oscillations at the given time resolution, instead appearing as a solid block of color. Left: Entire pulse on the scope (red). Right: Zoom in on the black boxed area of the left plot, which enhances the voltage resolution of the scope. Individual sections that are analyzed in b) are colored non-blue: MW switch turns on pre-π-pulse (red), three of four possible post-π-pulse ringdown regimes that were observed (orange, purple, green). The time preceding the pulse is found to contain only off-resonant noise, whereas the time following the pulse is found to contain some resonant noise. b) Fourier transforms of the time windows colored non-blue for either amplifier output or stripline output with or without a circulator in place to suppress reflections. The circulator suppressed resonant noise (blue dashed box), but also added new resonances to the amplifier output (red boxes).

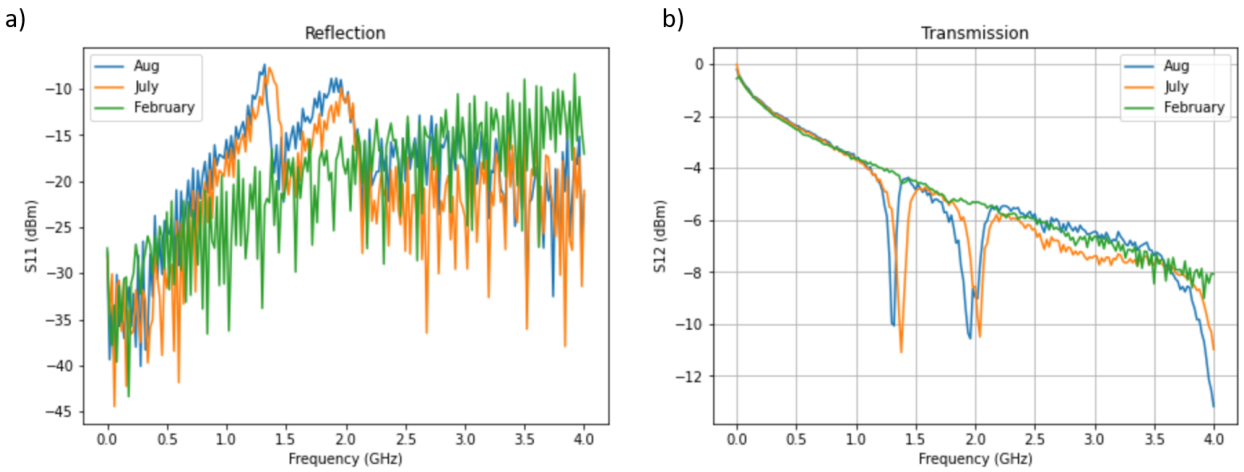

Figure 4.2: Deterioration of stripline properties with time. a) Reflection spectrum of stripline. b) Transmission spectrum of stripline. Both reflection and transmission spectra developed resonances with time. Poking the SMA connectors on the PCB could move these around.

We can directly measure transmission and reflection properties of the stripline and its PCB mount. Using a vector network analyzer, we observed the emergence of transmission dips after using the stripline for about 5 months. We found we could move the location of the dip by pressing on the SMA connectors. In addition, pressing the connectors too much created a second transmission dip, that moved and permanently combined with the first. After discussing these as well as the FFT tests above with other NV research groups, we concluded that the PCB solder connections were wearing out. In addition, the slope of the initial transmission spectrum is worse than observed in some other research groups, suggesting the need to improve impedance mismatch in our PCB design.

The second design we implemented replaced solder with silver epoxy paste. It also bypassed the PCB by connecting the SMA to the coverslip directly to reduce the number of connections. As of the time of this writing, the new design is awaiting testing and implementation for final measurements of the sample.

4.2.2 Quasi-2D Sample

Our gracious collaborators in Prof. Ania Jayich's research lab grew the q2D sample used throughout this chapter. We aimed to grow an isotopically-purified ^{12}C diamond sample containing a thin layer of NV and P1 centers such that each spin-1 NV center is surrounded by an ensemble of spin-1/2 P1 centers (Fig. 4.3a) with no significant interactions between the NVs. In such a sample, the NV center serves as a probe of the local P1 environment because its electronic spin triplet ground state ($|m_s = \pm 1, 0\rangle$) can be initialized and read out

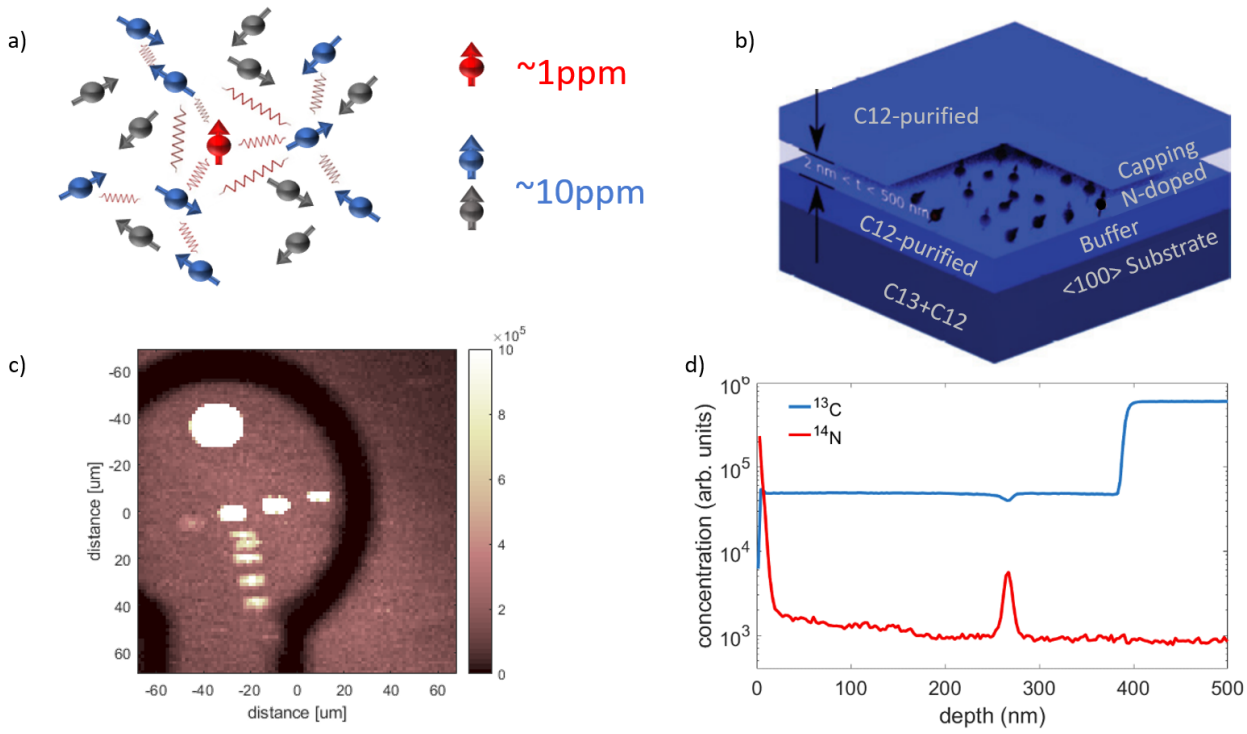

Figure 4.3: a) An NV surrounded by a thermal spin bath of P1 centers. When DEER is performed, we can select a portion of the P1 population to interact with the NV. b) The delta-doping scheme. Starting with ⟨100⟩ cut diamond, a buffer layer of isotopically-purified ^{12}C diamond is grown. During the growth process nitrogen is introduced and incorporated. Finally, a capping layer of purified diamond protects the delta-doped layer. c) Secondary Ion Mass Spectroscopy (SIMS) reveals the relative densities of ^{13}C and nitrogen vs depth below the diamond surface. The resolution of the device is 8 nm, suggesting the width of the delta-doped layer may be less.

via optical excitation and can be coherently controlled with microwave fields [107], whereas the P1 centers' electrons are unpolarized and cannot be read out. Instead, the P1 centers form a thermal spin bath whose dipolar field dominates the NV decoherence.

To shield the q2D layer from extraneous influences, a buffer layer of purified diamond attenuates interactions between the delta-doped layer and spins from the diamond bulk; as well a capping layer of purified diamond is grown on top of delta-doped layer to protect the it from the effects of surface chemistry (Fig. 4.3b). The sample was created from a Type Ib diamond, cleaned and etched to 10 pm flatness. The growth procedure was as follows: a 10 minute hydrogen etch at 400 sccm, a 3.5 hour growth of 99.999% 12C enriched diamond buffer layer using an isotopically purified methane at 0.2 sccm; a 10 minute growth of 98% ^{14}N enriched nitrogen doped layer at 5 sccm; and a 4.5 hour capping layer growth with

the same purified methane. Throughout growth, the pressure was held at 25 Torr and the temperature at 800°C.

A transmission electron microscope beam of 145 keV generated vacancies at specific locations in the diamond. The exposure time at each selected location was varied, creating a range of total electron fluence from approximately 7×10^{20} e^-/m^2 to 7×10^{25} e^-/m^2 (Fig. 4.3c). The irradiation spot we use throughout this work had a total fluence of 7×10^{24} e^-/m^2 The diamond was annealed at 800°C to generate NVs. Secondary Ion Mass Spectroscopy (SIMS) reveals a high nitrogen concentration in a layer at most 8 nm thick, the resolution of the device, and buffer/capping layers ∼100-200 nm thick (Fig. 4.3d). Comparing the SIMS results to those of previous recipes, the P1 density is estimated at ∼10 ppm. NV density is estimated at ∼1 ppm using optical brightness. Since the average spacing between defects is on the order of or larger than the thickness of the defect layer, the sample is expected to be q2D; however, proof requires the observation of a signature specific to two dimensions.

4.2.3 3D Delta-Doped Sample

In Section 4.4.2, we analyze a 3D sample grown for us by collaborators by Prof. Ronald Walsworth research group. The sample started as an Element-6 electronic-grade diamond. The company delta-doped a $\sim 1\mu$m thick layer with ^{15}N, then irradiated and annealed it. Within the layer, they quote an NV density ∼1 ppm and a P1 density ∼3 ppm with an isotopically-purification of ^{12}C∼99.995%.

4.3 Proposals: Dimensionality via Density Scaling and Magnetic Tomography

We can observe distinctly 2D signatures using the NV coherence decay. The NV coherence times T_2^{SE} and T_2^D, undergoing respectively Spin Echo (SE) or Double Electron-Electron Resonance (DEER) measurement protocols, are inversely-proportional to the interaction strengths in the system. All interactions in our system are dipolar, whose average strength J depends on the average spin spacing $\bar{r}$ as well as on the relative angle between spins. As a result, we expect T_2 to scale with both density ρ and field angle in distinct manners for each dimension.

If one could increase the density of the P1s in the sample, they naively should expect T_2 to scale nonlinearly in 2D and linearly in 3D.[1] We can see this by comparing the dipolar interactions and $\bar{r}$ in each dimension. In any dimension, the average dipolar interaction depends on the average spin spacing as $J \sim 1/\bar{r}^3$. The relationship between ρ and $\bar{r}$, is unique to each dimension, since density is volume is dependent in 3D $\rho \sim 1/\bar{r}^3$ and and area dependent in 2D $\rho \sim 1/\bar{r}^2$. Swapping spacing for density results in a $J \sim \rho^{3/2}$ scaling in 2D and linear scaling in 3D.

[1] This naive calculation is well-founded, as we will see in Section 4.4.

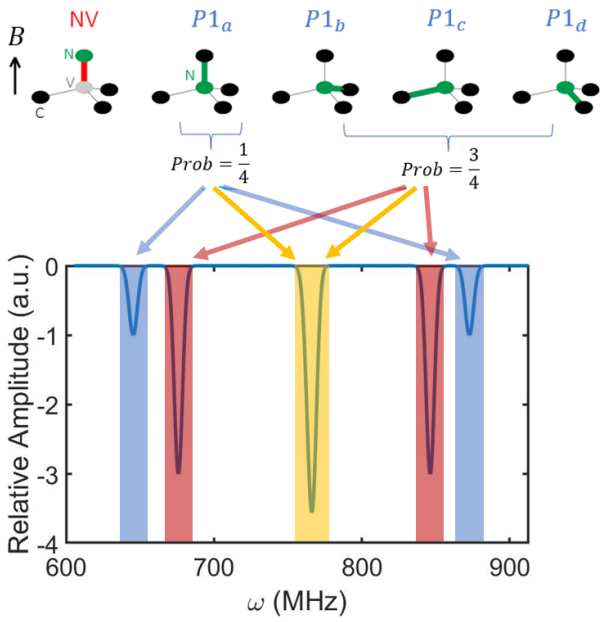

Figure 4.4: When the applied magnetic field is aligned with the NV, one P1 orientation group is also aligned, and the other three are misaligned by the same angle. The aligned P1 group exhibits larger hyperfine splitting than the unaligned groups, resulting in 5 P1 resonances, each representing a fraction of the total P1 population.

To perform this measurement, we could find samples with the same thickness and different P1 density, and measure Spin Echo on them, but ensuring the same nano-scale thickness is beyond current practical technology. Instead, we can use a method demonstrated in another work by the Yao group.[2] The effective density of the P1 bath can be tuned between 1/12, 1/4, and 1/3 of its total population by addressing the associated hyperfine resonances during DEER measurements. A large applied magnetic field sets the P1 electronic spin quantization axis, but the hyperfine interaction's quantization axis is set to any of the 4 crystallographic orientations via the Jahn-Teller effect. If we apply a B field aligned along one diamond axis, it sets all of the electron spin axes, but does not alter the hyperfine axes. When the P1 spin and hyperfine axes are aligned, the P1 will exhibit stronger hyperfine splitting than when unaligned. Given that the Jahn-Teller-induced hyperfine axis is randomly distributed and that the axis flips to another crystallographic axis on roughly second timescales, at any given time an NV's hyperfine axis has a 1/4 chance to be each crystallographic axis. As a result, 1/4 of the P1 population will split more than the remaining 3/4 of the population.[3] As a

[2]In review at the time of this writing.

[3]In truth, the spectra will not actually be symmetric. The hyperfine interactions of the aligned vs unaligned groups have different projections onto the electronic spin S_xI_x and S_yI_y that will also shift the spectra (even when I_z=0). The shift is stronger for the more aligned electron and nucleus. Consequently, the

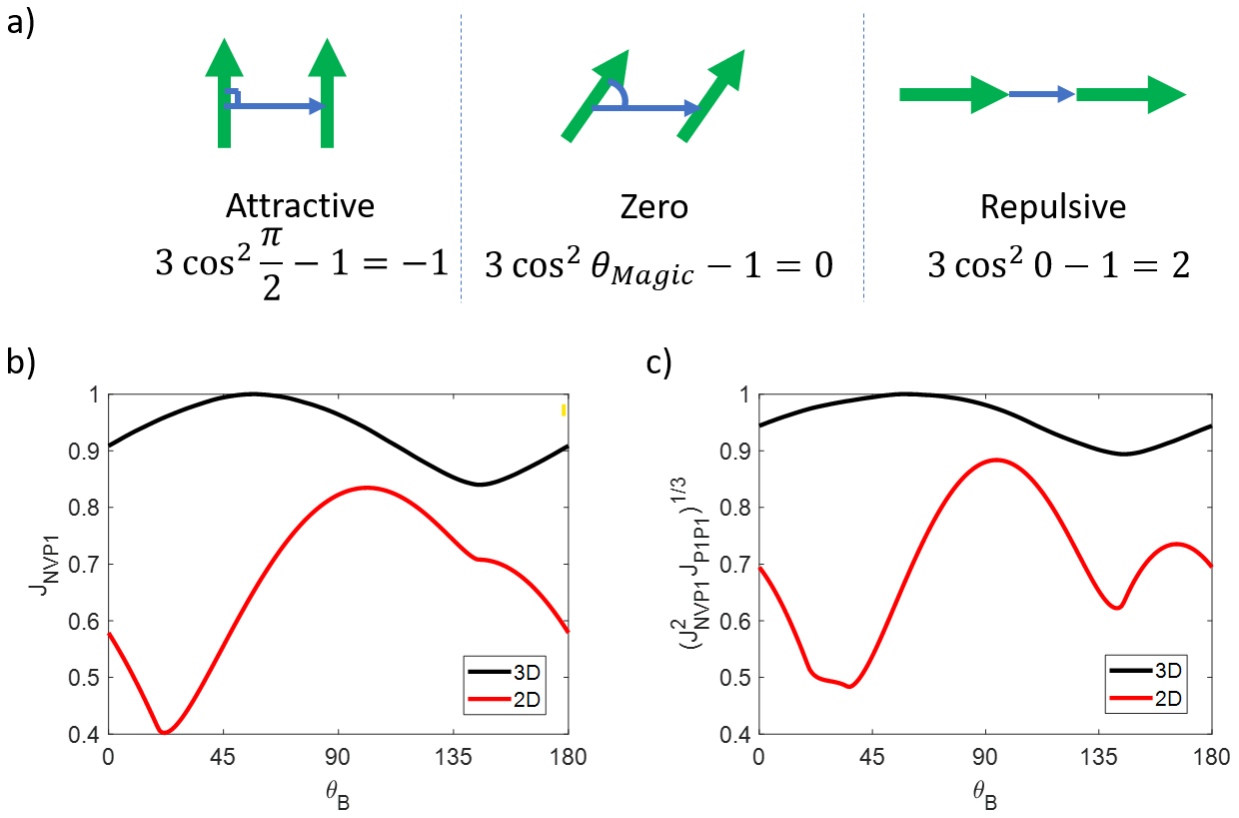

Figure 4.5: a) Two dipoles can switch their interaction from attractive to zero to repulsive, depending on their relative angle. b) Simulated polar-angular dependence of the NV-P1 interaction that dominates DEER measurements. c) Spin Echo dependence on field polar-angle. For both b) and c) the azimuthal angle is assumed to be the NV's azimuthal angle.

result, there are 5 distinct P1 resonances, each with a fraction of the total P1 population $\{1/12, 1/4, 1/3, 1/4, 1/2\}$ (Fig. 4.4). Since the resonances are separated by $\sim 10 - 100$ MHz, a DEER measurement can easily address a subset of them, effectively choosing and tuning a P1 density.

As an alternative to the previous proposal, one can exploit the angle of the applied field to switch the NV-P1 interaction from attractive to repulsive by rotating the P1 spin axis (Fig. 4.5a). Whereas the NV spin quantization axis is set parallel to one of the diamond crystallographic axes by its large zero-field splitting, the P1 spin axis is set by the external magnetic field. When considering the possible geometric configurations of NV-P1 systems,

splitting between the lowest two frequency resonances is less than that between the highest two frequency resonances. Also, the resonance corresponding to 1/3 of the P1 population has has a small splitting between the 1/12 and 1/4 resonances comprising it. Most often, the bandwidth of the P1 drive pulses are much larger than this splitting.

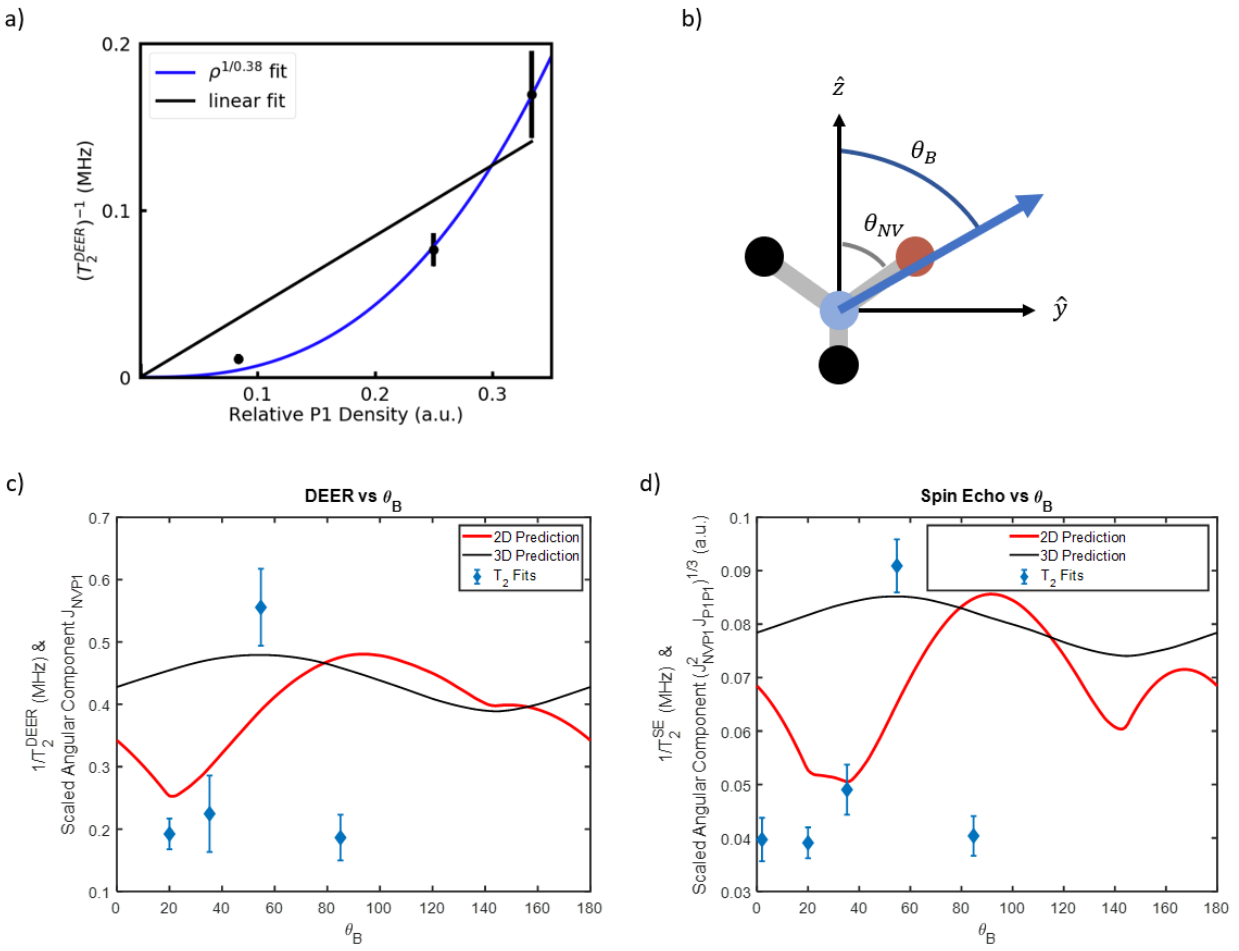

Figure 4.6: a) DEER interaction scaling with P1 density for a 330 G field. b) Side view of NV indicating the definition of the polar angle θ_B c) DEER interaction scaling with 270 G magnetic field polar angle. c) Spin Echo interaction scaling with 270 G magnetic field angle. The measured data in b) and d) does not match any predicted simulations.

we can see that an NV surrounded by a P1 spin bath has an *average* angular dependence that is entirely distinct to the number of dimensions of the spin bath's geometry. Sweeping the angle of an externally applied field causes the NV coherence times to fluctuate through patterns that are qualitatively unique to the number of dimensions of the system. Not only is the numerically-predicted 3D pattern smaller in magnitude, but it also fluctuates completely out of phase with the 2D pattern.

We chose one NV orientation group at a particular spot on our diamond and attempted these measurements. We measured T_2^D with varying effective P1 density (Figure 2a), as well as T_2^{SE} and T_2^D while deviating the polar angle of an applied magnetic field from the NV

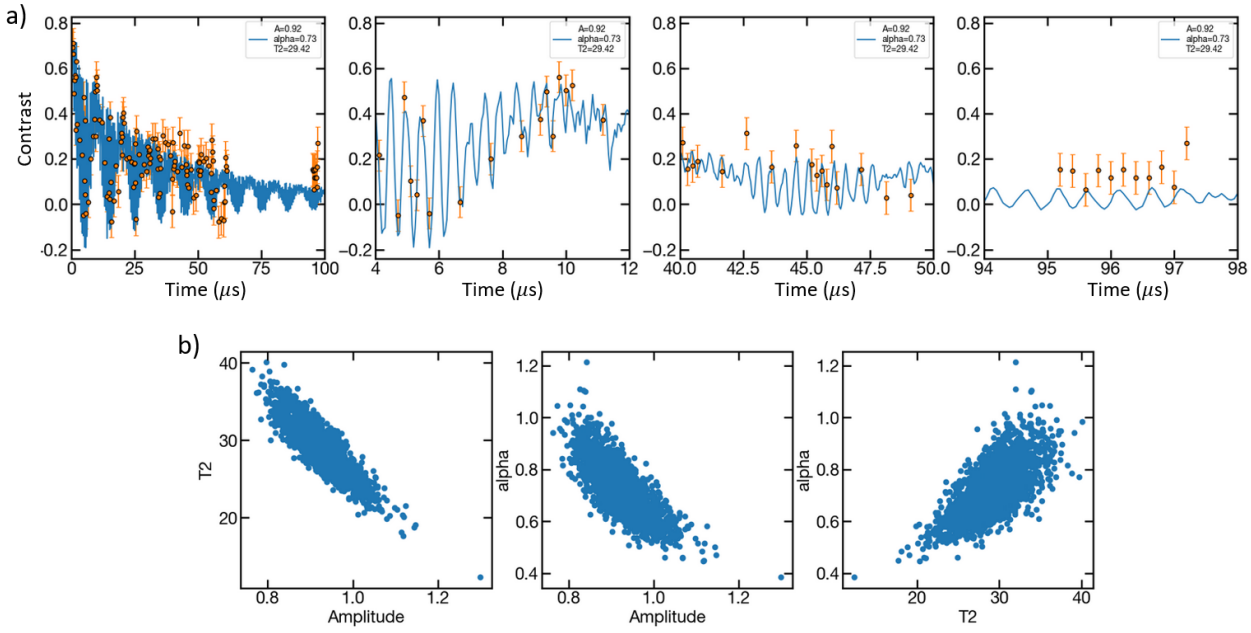

Figure 4.7: a) Example of hyperfine beating observed in Spin Echo signal for a 270 G field at the polar angles $\theta_B = 88°$. THe solution to the hyperfine Hamiltonian fits well at early times, but not at late times. Of the free fit parameters, A corresponds to the exponential decay amplitude, alpha to the stretched power of the decay, and T2 to the T_2 decay time. b) The free fit parameters are highly correlated, stifling the extraction of T_2.

axis (Fig. 4.6a). In all measurements, we find that the decay envelope of the data fits to a stretched exponential with stretched power $\beta_{SE} = 0.5 \pm 0.05$ and $\beta_{DEER} = 0.39 \pm 0.05$ for Spin Echo and DEER, respectively. However, the results of extracting timescales over density and angle are disappointing. Instead of 3/2, we find $J \sim \rho^{1/\beta_{DEER}}$. As well, through both SE and DEER we measure no significant variations in the dipolar interaction strength that match any patterns we predicted (Fig. 4.6b & c).

4.3.1 Challenges

There were a few impediments hindering a successful experiment. The first two largely affected only the angular sweep measurements, but the last one affects both. We must surmount all three to successfully implement the proposed experiments in the lab.

^{14}N Hyperfine Oscillations

Foremost, at many steps of the field sweep, there is a large angle between the applied magnetic field and the NV axis, creating a significant transverse field in the coordinate

system of the chosen NV orientation group. We observe a beating pattern in both SE and DEER measurements at these angles (Fig. 4.7a). The beating is produced by a strong back-action of the hyperfine interaction on the ^{14}N nuclear spin states. Specifically, the $S_x I_x$ hyperfine term induces a onsite disorder on the NV's electronic spin equal to the hyperfine splitting ($\approx$ 2 MHz) at first order. This explains why there should be fast oscillations. At second order, the term mixes the $|m_I = \pm 1\rangle$ nuclear spin states. These states have slightly different hyperfine splittings due to their I_z interactions, so coupling their slightly different hyperfine oscillations leads fast oscillations with a beat envelope. Under a large transverse field this term becomes strong even to second order, generating coherent oscillations with the nucleus that can completely flip the S_z projection throughout our measurement.

For a known NV-magnetic field angle and field strength, we can solve the NV hyperfine Hamiltonian to obtain beating oscillations. We can then multiply the fixed solution by a decaying exponential with two free parameters to fit the model to the data (Fig. 4.7a). However, while the fit is fantastic at fitting early-time data, it clearly fails to do so at later times. We could not tell if we simply could not find the correct beat frequency or if the beating suffered from nuclear dephasing, adding more frequency components to the beat. Worse still, fitting to the hyperfine oscillations removes the envelope's weight from the fit, which led to large correlations between the free fit parameters. As a result, we could not fit consistent decay amplitudes A or stretch powers α across our data sets, so the fit decay times T_2 could not be compared. We tried a few other fitting methods, including Fourier transforms and fits by eye, but could not extract a reliable T_2 scaling pattern. The T_2 fits presented in Figure 4.6c & d are for free envelope fit parameters.

Dependence on Thickness

A more careful look at our numerical predictions of DEER reveals that adding even a small finite width to a 2D layer drastically alters the pattern of interaction strength versus magnetic field angle (Fig. 4.8). Increasing the thickness to 4 nm, the predicted pattern is highly deviated from that of a pure 2D system. When the thickness is 8 nm (the resolution of SIMS), the system is nearly indistinguishable from 3D. The T_2 predicted by these simulations is on the same order of magnitude as what is measured in our experiments, indicating that there are few experimental imperfections to deviate the measured signals from these predictions. Even if we could see an fluctuation in the T_2 with magnetic field angle, this effect then precludes a guarantee that we would be able to distinguish q2D from 3D.

Stretched Exponential Factor

We find that regardless of how we fit, the envelope of the decay clearly does not follow a single exponential, but rather a stretched exponential with power $\beta < 1$ (Fig. 4.9). Stretched exponential decay has been observed and numerically predicted in the SE signal of a three-dimensional NV-bath system, but to date has lacked an analytical explanation [141]. A deviation from exponential decay suggests more complicated physics underlying our

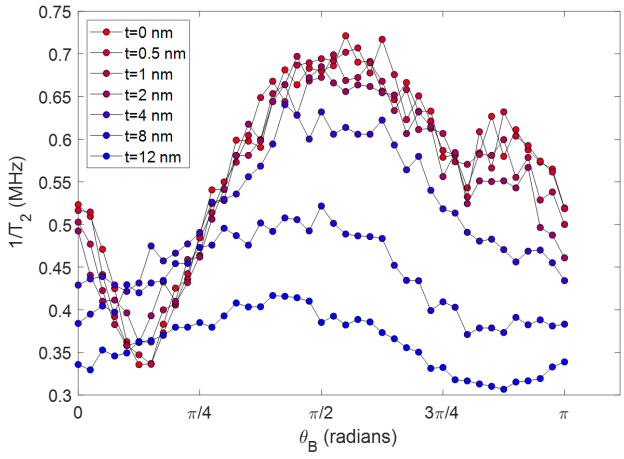

Figure 4.8: Numerical simulations of the dependence of DEER $1/T_2$ on the polar angle θ_B of an applied 270 G field, varying over the thickness of the delta-doped layer. The azimuthal angle is assumed to aligned with the NV axis. The DEER measurement is assumed to be performed on the 1/3 group, so the P1 density is taken as 10/3 ppm.

data. Without a definitive understanding of and predictive power over the stretch, we will have a hard time convincing ourselves that any trends in T_2 are entirely due to q2D nature phenomena. So even the pleasant result that the interaction strength scales as $J \sim \rho^{1/\beta_{DEER}}$, seemingly depending on the decay exponent, cannot be proven to be more than coincidence. Furthermore, the ultimate purpose of growing a this sample is to study exotic driven phases of matter, once its q2D nature has been verified. For such research, any underlying physics that could produce a stretch factor could muddle our interpretation of the exotic phase.

4.3.2 Proposed Solutions

There are a few possibilities for overcoming the challenges to magnetic tomography. For those issues arising out of the hyperfine backaction, we could first try to reduce the magnetic field strength while rotating the field to diminish the effect. Unfortunately, we found that at fields < 200 G, we could observe ^{13}C hyperfine oscillations in our data. We would need to regrow a more isotopically pure sample to work at lower fields, which is difficult in its own right. A better solution for this diamond is to increase the field. At high enough fields, the ^{14}N nuclear spin's population polarizes into one of its three states. By polarizing the nucleus into one of its states, there is little population to beat, so the contrast of the hyperfine oscillations should drastically reduce.

Another consideration is to perform a measurement that is insensitive to hyperfine effects. By increasing the magnetic field to $\sim$510 G, the NV and P1 become resonant with each other (neglecting hyperfine interactions). Much as we addressed different P1 populations

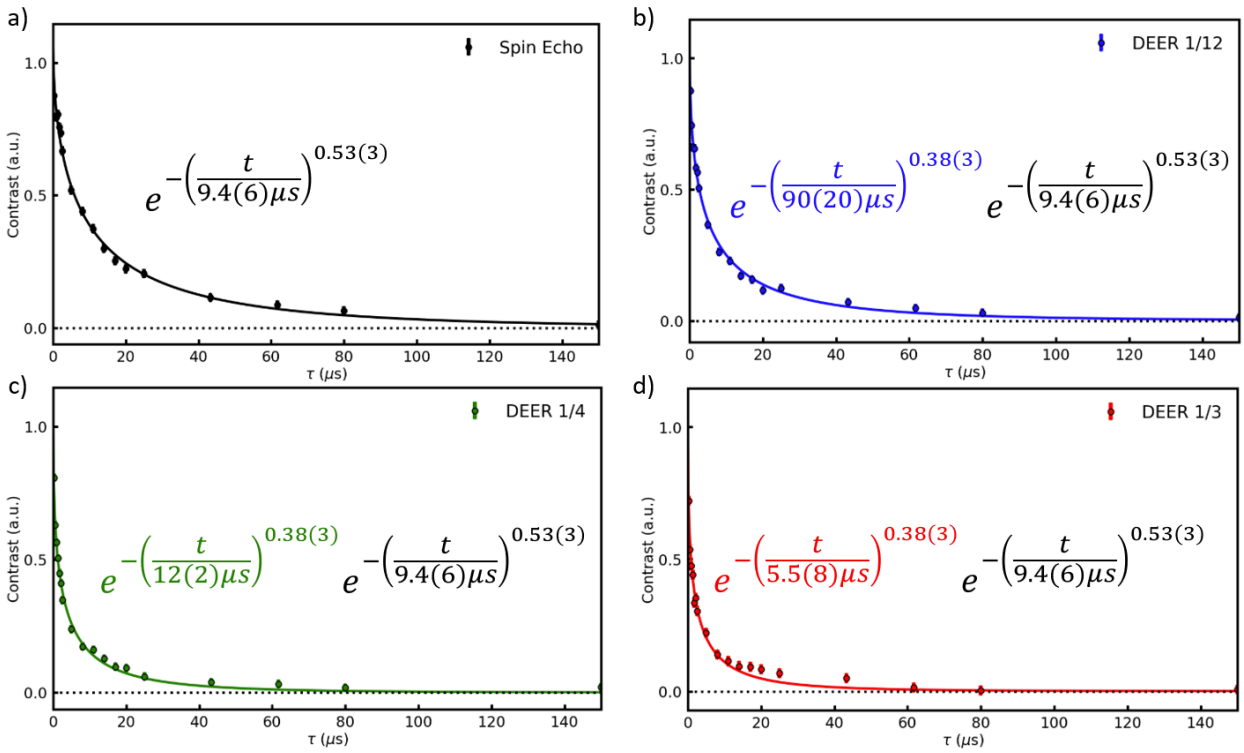

Figure 4.9: Spin Echo and DEER measurements used to create the interaction scaling in Figure 4.6a. a) Spin Echo b-d) DEER for the indicated P1 density fraction.

by varying the MW frequency, varying the field around this value can shift the different hyperfine-split densities of P1s on to resonance with the NV [**RT3**]. In this regime, we could look at T_1 scaling against density. Scaling with density should be non-linear in dimensions less than three, as discussed previously in this section. We also avoid rotating the field for this series of measurements. This experiment also circumvents the possibility of the layer being too thick, as scaling is distinct for each thickness.

However, none of these solutions fix the problems stretched exponential decay poses to a complete interpretation of the data. The best option we have to address this issue is to study it deeply, which is exactly what we do in the remaining sections of this chapter.

4.4 Coherence Decay Dynamics

4.4.1 General Form of Coherence Decay for Ising Qubit-Bath Interactions

To better understand the source of the stretch, we provide a well-motivated and general analytical derivation. We assume that the central NV spin shares an Ising interaction $J_0/r^\alpha S^z_{NV} S^z_j$ with each P1 bath spin and that P1-P1 interactions are fully dipolar. For a single realization of the positional disorder of the P1 bath, the time average of the single central NV coherence is

$$\langle S^x_{NV}(t)\rangle = \frac{1}{2}\mathrm{Re}\left\{\left\langle \mathrm{Exp}\left[i\Sigma_j \frac{J}{r^\alpha_j}\int_0^t S^z_j(\tau)\eta(\tau)d\tau\right]\right\rangle\right\} \tag{4.1}$$

where $\eta(\tau)$ is the filter function of Spin Echo or DEER in the time domain. For a thermal P1 bath, we take the natural assumption that the accumulated phase is a Gaussian variable, which permits us to exploit the relationship $\mathrm{Re}\langle e^{iX}\rangle = e^{\langle X^2\rangle}$, for Gaussian variable X. This average of the square of the Gaussian variable provides us with an autocorrelator of the bath's spin configuration $\langle S^z_j(t')S^z_j(t'')\rangle$. We now see the phase as a convolution $\chi(t)$ between the autocorrelation of the bath and the filter function of the measurement with some coefficients in front representing the squared interaction strength:

$$\langle S^x_{NV}(t)\rangle = \frac{1}{2}\Pi_j \mathrm{Exp}\left\{-\frac{1}{2}\left[\frac{J}{r^\alpha_j}\chi(t)^{\frac{1}{2}}\right]^2\right\} \tag{4.2}$$

where

$$\chi(t) = \langle(\int_0^t S^z_j(\tau)\eta(\tau)d\tau)^2\rangle \approx \int_0^t dt' \int_0^t dt'' \eta(t')\eta(t'')e^{-\frac{|t'-t''|}{\tau_c}} \tag{4.3}$$

for $\langle S^z(t')S^z(t'')\rangle = e^{-\frac{|t'-t''|}{\tau_c}}$, and τ_c being the spin correlation time of the bath. The exponential form of the autocorrelator is one way of expressing the assumption that it peaks when $t' \approx t''$. It is motivated by the decay profile of depolarization in single-NV experiments.

All of this solved for a single positional realization. Now we must average over positional disorder—the entire NV ensemble. To do so, we pull the parametric time dependence out of the positional integral to find a general form of the coherence decay

$$\langle \overline{S^x(t)}\rangle = \mathrm{Exp}[-(J^2\chi)^{\frac{D}{2\alpha}}] \tag{4.4}$$

This general solution does not assume anything about the timescales in the problem, permitting decay by both types of decoherence as discussed in Section 1.5.6. In this case, the filter-autocorrelator convolution χ is solved for analytically (Table 4.1). With the analytical solution in hand, we can isolate the effects of the two types of decoherence by taking

Measurement	$\chi(t)$	$\chi(t \ll \tau_c)$	$\chi(t \gg \tau_c)$
Ramsey-type	$2\tau_c t - 2\tau_c(1 - e^{-\frac{t}{\tau_c}})$	$t^2 - \frac{t^3}{3\tau_c}$	$2\tau_c t - 2\tau_c^2$
Spin Echo-type	$2\tau_c t - 2\tau_c(3 + e^{-\frac{t}{\tau_c}} - 4e^{-\frac{t}{2\tau_c}})$	$\frac{t^3}{6\tau_c}$	$2\tau_c t - 6\tau_c^2$
XY8	$\frac{\tau_p^2}{12\tau_c}t$	$\frac{\tau_p^2}{12\tau_c}t$	$\frac{\tau_p^2}{12\tau_c}t$

Table 4.1: The general analytical solution of the phase convolutions for different measurement sequences, as well as the limits for large and small evolution time with respect to bath dynamics.

the limits $t \ll \tau_c$ (coherence spreading) and $t \gg \tau_c$ (environment changing). Notably, the Ramsey- and Spin Echo-type measurements exhibit drastically different behaviors in the two regimes because they are initially influenced by coherent interactions between the probe spin and the bath (coherence spreading) until the incoherent interaction with the decorrelated bath dominates (dephasing and decoherence from environment changing). By contrast, the behavior of an ideal XY8 does not change between the two regimes because it perfectly suppresses coherent interactions between the probe and the bath at all times, implying that the decay can only be from decoherence due to decorrelation in the bath. Crucially, while the stretched power of the decay in the uncorrelated regime is the same for all measurements for each dimension, the T_2 measured in those regimes is different for each measurement due to the degree to which each protocol filters the interaction with the bath. Take for example, Spin Echo and XY8. Both are capable of suppressing the probe's interaction with the correlated bath and its interaction with the decorrelation dynamics in the bath. The difference is that Spin Echo's suppression of correlated dynamics is imperfect, whereas XY8's is perfect, so Spin Echo's T_2 should be smaller in principle. Furthermore, XY8 can also improve its suppression of the uncorrelated bath dynamics by decreasing the inter-pulse time τ_p and increasing the number of pulses, in which case it still decays with a stretched power of 1/3, but $T_2 \to \infty$.

A few remarks are in order. First, ensemble-averaging $\langle\overline{S^x(t)}\rangle$ ensures both the exponential form and the parametric dependence $D/2\alpha$. The exponential form arises from a geometric identity associated with multiplying the outcomes from every possible location of bath spins. Specifically, we integrate over spherical shells, with each shell having a probability of containing a P1 that can cause the NV to decay.

$$\begin{aligned}\langle\overline{S^x(t)}\rangle &\sim \prod_{\text{Shells}} (\text{Probability of no particle})(\text{No Decay}) + (\text{Probability of a particle})(\text{Decay}) \\ &= \prod_{r_i}(1 - \rho 4\pi r_i^{D-1} dr)(1) + (\rho 4\pi r_i^{D-1} dr)(e^{-\gamma_i t}) \\ &= \prod_{r_i} \text{Exp}\left[-\rho 4\pi r_i^{D-1} dr(1 - e^{-\gamma_i t})\right] \end{aligned} \tag{4.5}$$

where ρ is the bath spin density, r_i is the radius of the spherical shell being integrated over,

and γ_i is the associated NV decay rate for a bath spin located on the corresponding spherical shell. The parametric dependence extracted from

$$\langle \overline{S^x(t)} \rangle \sim \text{Exp}\left[-\int_0^\infty e^{-\frac{J}{r^\alpha}t} \rho 4\pi r^{D-1} dr \right] \tag{4.6}$$

is necessary from dimensional analysis. The $D/2\alpha$ comes from reconciling the power-law α scaling of the dipolar interaction and the D-dimensional Jacobian of the spatial integral; the 2 comes from the assuming Gaussian variables, transforming $r^\alpha \rightarrow r^{2\alpha}$. Second, the assumption that the central spin shares an Ising interaction with the bath is a good approximation for our system since the NV and P1 are far off-resonance with each other, suppressing flip-flops. Third, the stretch power derivation can be generalized beyond a Gaussian distribution of phase accumulation. At least for a binary distribution of phases, the same parametric dependence will be isolated (eq. 4.4 due to the geometric nature of the ensemble average. The only difference is the addition of a coefficient inside the exponent of order 1.

Finally, one might reasonably assume that $\tau_c >> T_2$, so $\tau_c >> t$ in most experiments. Ising and flip-flop terms in the bath dipolar interaction share the same coefficient for any pair of bath spins. Notably, the Ising contribution to disorder is cumulative with the number of neighboring bath spins whereas the flip-flop contribution to decorrelation in the bath is not. Consequently, for any given flip-flop rate, disorder is likely to be a stronger interaction, scaling with both the number of spins and the volume of the d-dimensional geometry. However, this assumption must be checked self-consistently in the experiment, and in our case, it is not true. We believe this is the reason the predicted stretch powers are a bit larger than what was measured. While there are a number of experimental reasons for this—local density fluctuations, the existance of more flip-flop than predicted, one-dimensional contributions, etc.—we find that it arises out of the fact that we are measuring evolution times both before and after τ_c, so we probe both correlated and uncorrelated bath dynamics. When there are two distinct and subsequent stretched exponential decays, fitting a single stretched exponential is inappropriate. In the next section, we will explore the ongoing efforts to observe the crossover between these different interaction regimes of our model stemming from this fact.

4.4.2 Interaction Crossovers

Given our strongly-interacting system, one could reason that the correlation time τ_c of the bath might be small enough to observe. If so, we qualitatively expect stretch exponential decay with stretched powers as presented in Table 4.2 for each measurement protocol. To verify the crossover from correlated bath dynamics to uncorrelated bath dynamics, we measure Spin Echo, DEER, XY8, and XY8-DEER for our ostensibly 2D sample as well as a 3D sample with NV density $\sim$ 1 ppm and P1 density $\sim$ 4 ppm (Section 4.2.3). Since these are qualitative theoretical predictions of power-law decays, we plot the results in log-log space with fits by eye to two stretched exponential decays fixed at the predicted stretched powers (Fig. 4.10 & Fig. 4.11). On the whole, the data exhibits the qualitative behavior of Ramsey decay in 2D ($2/3 \rightarrow 1/3$) for the 2D sample and in 3D ($1 \rightarrow 1/2$) for the 3D sample.

	2D		3D	
Measurement	$\chi(t \ll \tau_c)$	$\chi(t \gg \tau_c)$	$\chi(t \ll \tau_c)$	$\chi(t \gg \tau_c)$
Ramsey-type	2/3	1/3	1	1/2
Spin Echo-type	1	1/3	3/2	1/2
XY8	1/3	1/3	1/2	1/2

Table 4.2: The general analytical solution of the phase convolutions for different measurement sequences, as well as the limits for large and small evolution time with respect to bath dynamics.

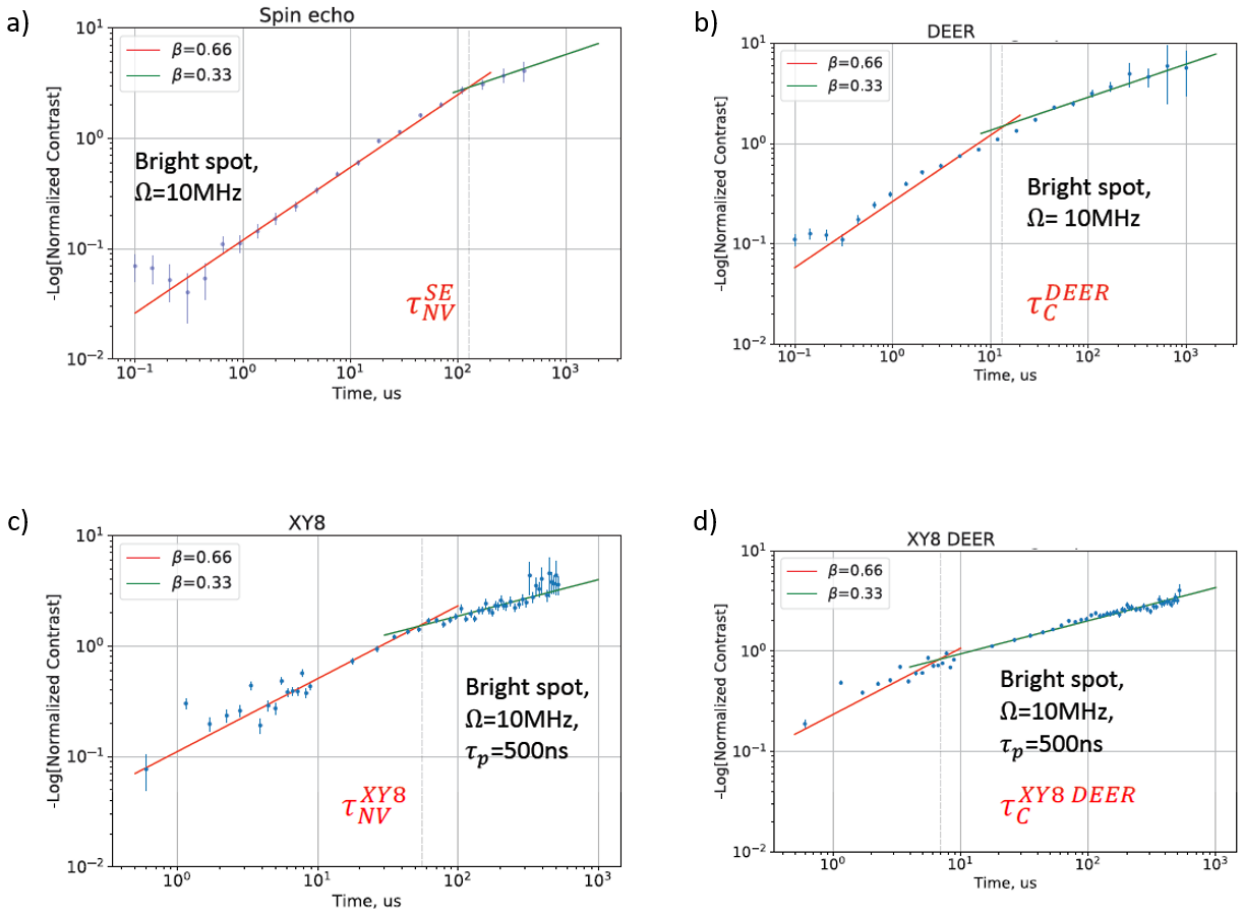

Figure 4.10: Crossovers verified in 2D sample for different measurements. a) Spin Echo b) DEER c) XY8 d) XY8-DEER

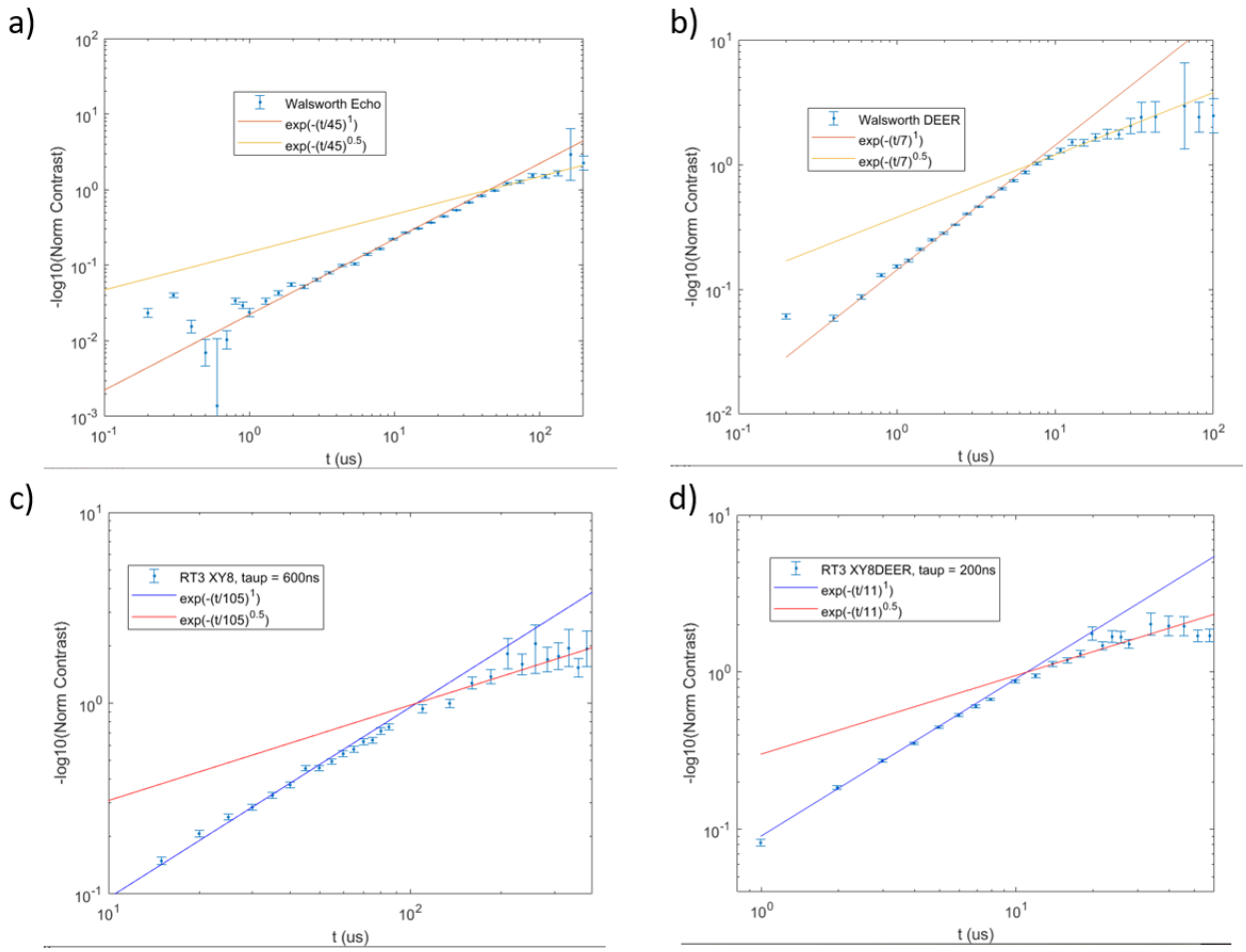

Figure 4.11: Crossovers verified in 3D sample for different measurements. a) Spin Echo b) DEER c) XY8 d) XY8-DEER

The DEER and XY8-DEER measurements are expected to follow Ramsey trends and directly measure the P1 correlation time, since they intentionally target the NV-P1 interaction; however, one would not also expect Spin Echo and XY8 to exhibit trends reminiscent of Ramsey. We can understand this surprising Ramsey-type result by observing the overall behavior and the T_2 for Spin Echo and XY8. First, the very existence of a crossover in both Spin Echo and XY8 means that there is some kind of dense bath transitioning from correlated to uncorrelated dynamics. If they were dominated solely by bath decorrelation due to a very short τ_c, then both Spin Echo and XY8 would exhibit a 1/3 stretched power decay throughout the measurements, and if they were dominated solely by coherent interactions with correlated dynamics they would exhibit simple exponential decay. Since the P1 correlation times measured in DEER and XY8-DEER are much shorter than the correlation

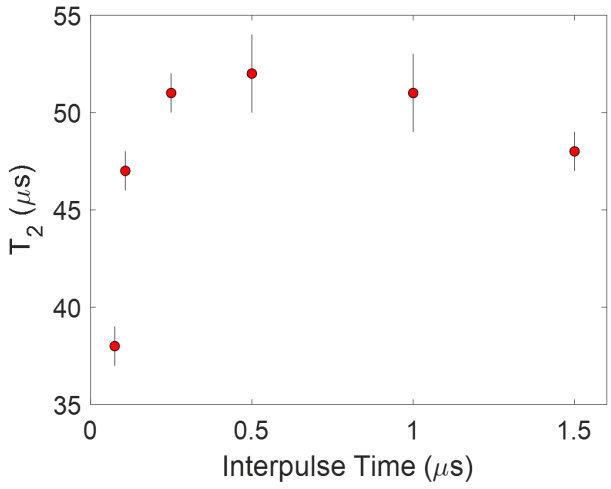

Figure 4.12: T_2^{XY8} vs τ_p. At short τ_p we observe a steep dropoff due to large pulse errors. At longer interpulse times, we observe a plateau. If the XY8 decay were due to a bath that could be filtered, we would expect monotonically decreasing T_2 with increasing τ_p as the bath becomes less filtered. The plateau suggests that there is a bath that is unaffected by the XY8 filter.

times measured in Spin Echo and XY8, we can surmise that they are suppressing the NV-P1 interactions effectively and are instead probing a different bath with a lower density. Second, T_2 does not increase dramatically between Spin Echo and XY8. XY8 should be much more effective at suppressing all interactions between the NV and P1 bath than Spin Echo, so if Spin Echo was decaying due to NV-P1 interactions (coherent and incoherent), we would expect the XY8 T_2 to be much larger than the Spin Echo T_2. The fact that it is not suggests that XY8 is not efficiently filtering the interactions with whatever bath is dominating the measurements. Third, when we decrease the inter-pulse time τ_p of XY8, we observe a plateau of the overall T_2 before it drops off at very short τ_p (Fig. **??**). The drop-off at short τ_p is an effect due to the accumulation of pulse error (many more pulses are applied when the inter-pulse time is short). The plateau strongly indicates that XY8 is not only inefficient at filtering the bath in question, it is incapable of doing so.

Taken together, we have a dense bath that is not composed of P1s, is sparser than the P1 bath, and cannot be filtered by Spin Echo and XY8. The only particles in the system that meet these criteria are the NVs themselves. We conclude then that Spin Echo and XY8 effectively measure NV-NV Ramsey and the NV bath correlation time. The P1 correlation crossover still exists within these measurements, but is too suppressed to be observed. With this consistent explanation of the qualitative decay behavior of two separate diamond samples, we have not only verified the predictive theory, but also the dimensionality of the q2D sample.

4.5 Conclusion and Outlook

This chapter reviewed work on the observation of 2D dynamics in a spin defect system. All efforts employed the local coherence dynamics of the high-density NV-P1 system to verify the q2D nature of a delta-doped diamond sample. Two experiments were proposed and attempted: one probing the scaling of local interactions with bath density, and another performing magnetic tomography of the geometric dependence of the dipolar interaction in 2D. Both measurements met with complications that halted their progress, the most crucial impediment arising out of the shape of the stretched exponential decay profile. This hindrance became a boon. Developing an analytical derivation of the stretched exponential decay first provided us with the understanding we needed to predict the existence of a crossover between correlated and uncorrelated bath dynamics. We then observed the transition in experiments for two diamond samples.This research lays the groundwork for the study of exotic driven phases of matter using dipolar spins in lower dimensions, such as the quasiperiodic prethermal time crystals [44]. Furthermore, it provides a more accurate and precise understanding of the coherence decay dynamics of any-dimensional spin ensemble system dominated by Gaussian statistics.

Equipped with a solid understanding of the diamond sample, we are prepared for exploring some of the exotic 2D physics it offers. Of the compelling phenomena are 2D many-body localization, 2D diffusion and hydrodynamics, and quasiperiodic time crystals, but also this platform positions our group to distinctly answer numerically- and analytically-intractable questions, such as what the nature of 2D groundstate of disorderd dipoles is. Future samples could offer better properties for simulation or sensing, but will always need to consider the influence of the local dynamics studied in this chapter.

Chapter 5

A Trial in TMDS

With the advent of graphene, next-generation nano-electronic devices are being designed around 2D materials whose favorable characteristics are distinct from their bulk counterparts [116, 94]. Whereas graphene is the quintessential 2D conductor, group-VI Transition Metal Dichalcogenides (TMDs) are the semiconductor analogs. When they are multilayered, TMDs are indirect bandgap semiconductors, but they become direct gap semiconductors as monolayer. Monolayer TMDs garnered attention for spin-valley properties suggesting applications in opto-electronics [139], transistors [125] and spin- and valley-tronics [111, 60].

This chapter recounts a project attempted as part of the Yao group's first experimental thrust—the study of 2D TMDs using NVs. We performed the work in collaboration with the research group of prof. Feng Wang. The idea was to use shallow (~ 5 nm) NVs to turn the TMD dynamics into the local dynamics of the NV as a means to boost the NV's sensitivity. We had chosen to work with low enough densities that we could resolve individual shallow NVs with the hope that we could work towards nano-NMR of defects in the TMDs. The project was eventually dropped due to shifting interests, but served as a launchpad for the lab's experimental trajectory, and its understanding of the NV environment.

The physics used to describe TMDs is very much solid state physics, but the general scheme for deriving its properties is similar to that found in the atomic physics of Section 1.3. Since this is an atomic physics thesis, I will try to conform the discussion of TMDs as much to our familiar atomic language as I can.

5.1 Introduction to TMDs

Group-VI TMDs are composed of a single transition metal atom connected to two chalcogenide atoms, with a stoichometric formula MX_2 for M = [Mo, W] and X = [S, Se]. The monolayer physics is essentially the same for any combination of atomic species, each combination having its own energy splittings. Looking from above, the atoms in the monolayer layer form a hexagonal lattice alternating M and X (Fig. 5.1b). Looking from the side, we can see that there are actually two layers of X atoms, one above and one below the M

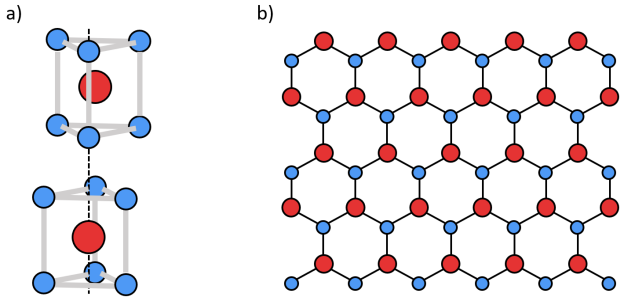

Figure 5.1: a) MX_2 from the side, exhibiting H-stacking. 6 X atoms form a trigonal prism centered around each M atom. b) Top-view of MX_2 hexagonal lattice.

atoms, with every 6 X atoms forming a trigonal prism centered around an M atom (Fig. 5.1a).

Multilayer and bulk TMDs are stacks of the 2D layers, which are strongly-bonded but weakly coupled via Van der Waals interaction. The stacking order is $2H$ (Fig. 5.1a) with a symmetry group D^4_{6h} that contains inversion symmetry. From the stacking diagram, we can see now why the TMD physics changes so drastically from bulk to monolayer (or to thin films with an odd number of layers): a monolayer breaks inversion symmetry and adds reflection symmetry, as the layer's symmetry group reduces to a D^1_{3h} crystal point group plus a reflection through the horizontal plane intersecting the M atoms.

To construct the energy diagram (band structure[1]) of the monolayer, we will briefly highlight a representation theoretic derivation highly reminiscent of the one from Section 1.3. We will start with a basis of atomic orbitals (d-orbitals of the M atom), and then apply symmetry constraints from from the symmetry group of the unit cell to find the irreducible representations. Any additional perturbations must comply with the symmetry group, e.g. constraining the polarization of the optical dipole transitions to circular.

The d-orbitals of the M atom are are projected onto three irreducible representations of the D^1_{3h} group: $A_1(d_{z^2}), E(d_{xy}, d_{x^2-y^2})$, and $E'(d_{zz}, d_{yz})$. The additional reflection symmetry serves to hybridize the the A_1 and E orbitals, which creates splitting between their energies—a 'bandgap' at particular locations with high symmetry in momentum space called 'K' and '$-K$' points [105]. The K and $-K$ points are valleys in the energy potential landscape that are time-reversals of each other (i.e. time-reversed momentum). With the symmetries at

[1]Electrons in a solid are free to travel throughout the solid, as opposed to being constrained to a small volume around an atom or molecule (i.e. NV center). Since electrons are waves whose wavelength depends on its momentum, the direction of the electron's velocity determines the periodic pattern of the crystal lattice potential that it encounters and the speed determines the resolution (from wavelength) with which it samples that lattice. As a result, the potential energy landscape (and linear combination of atomic orbitals) of the electron changes with momentum. This is what band structures represent. We will be focusing on a small enough portion of this landscape (the $\pm K$ points), that we can treat the band diagram as an atomic level diagram for our purposes.

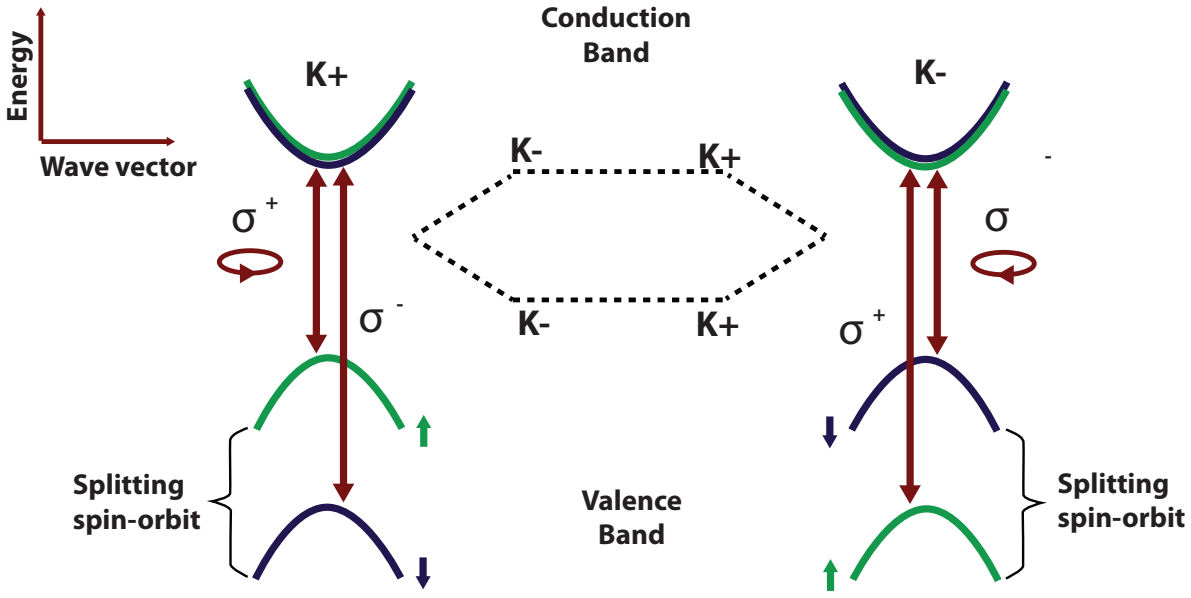

Figure 5.2: Energy level diagram of TMD. This is a zoom-in on the points of the band structure. Optical polarization selection rules are labelled.

these points we now have the basis functions

$$|\phi_c\rangle = |d_{z^2}\rangle, |\phi_v^\tau\rangle = \frac{1}{\sqrt{2}}\left(|d_{x^2-y^2}\rangle + i\tau\,|d_{xy}\rangle\right) \tag{5.1}$$

for $\tau = \pm 1$ being the valley index, and $c(v)$ indicate conduction (valence) bands.

With the wavevector basis near these points, we can now form the associated Hamiltonian and obtain the energy level diagram (Fig. 5.2). The Hamiltonian at these points in momentum space is $k \cdot p$, which is exactly what describes monolayer graphene with staggered sublattice potential [162], but in addition, the M's d-orbitals adds a strong spin-orbit coupling (SOC) $L \cdot S$

$$\hat{H} = k \cdot p + L \cdot S \approx at(\tau k_x \hat{\sigma}_x + k_y \hat{\sigma}_y) + \frac{\Delta}{2}\hat{\sigma}_z - \lambda\tau\frac{\hat{\sigma}_z - 1}{2}\hat{s}_z \tag{5.2}$$

where $\hat{\sigma}$ are the Pauli matrices for two basis fucntions, a is the lattice constant, t is the effective hopping integral, Δ is the energy gap, 2λ is the energy splitting due to SOC, and $\hat{\sigma}_z$ is the Pauli spin-z matrix. We see from this Hamiltonian that the spin and momenta are completely decoupled, so s_z is a good quantum number. Also, the time-reversal symmetry between the valleys intuitively flips the orientation of the spins in each valley. Finally, since the conduction band wavevector is made of d_{z^2}, which has $\mathbb{Z}_2$ symmetry, it is spin-degenerate [163].

The Hamiltonian permits calculating the coupling strength of of optical transitions. It is found that the conduction and valence bands are coupled exclusively by circular polarization σ^+ (σ^-) in the K ($-K$) valley [163]. Just like with the NV, optical fields couple only to the orbital portion of the wave function so spin is conserved in these transitions. Because of the time-reversed spin orientations of the valleys, the valleys' optical selection rules become spin selection rules, and each frequency drives transitions of opposite spins in each valley. In the end, there are four distinct selective excitations of spin and valley indices, which can be exploited for many of the aforementioned applications.

5.1.1 Van der Waals Glue

The van der Waals force typically is a weak attractive interaction that exists between all atoms and molecules at short distances [69]. It originates from the multipoles that two atoms or molecules mutually-induce in each other when they are ~ 0.5 nm apart: the polarization of the electron clouds around each nucleus becomes correlated in the two particles in an attractive way. When the particles become even closer (< 0.4 nm), the force becomes repulsive due to the pauli exclusion of their electron clouds. The force is relevant over short enough distances such that it is generally considered only between nearest neighbors. For this reason, it is additive without saturation when two atomically thin sheets come into contact—serving as strong adhesion. The van der Waals force is the main reason 2D materials can be stacked into structurally-sound 'heterostructure devices' or can be exfoliated onto the surface of a diamond for study with nearby NVs.

5.1.2 Resident Electron Spin Polarization

The dynamics in TMDs are typically orders of magnitude faster than in NVs ($\sim$ fs or ps versus $\sim$ ns or μs) [168, 67, 23, 165]. However, the lifetime of electrons or holes respectively above or below the Fermi level within a valence band, so called 'resident carriers,' are expected to be $\sim$ ns [167, 166]. While these lifetimes are still short relative to NV dynamics, since they are much longer than other TMD excitations or polarizations, resident carriers could feasibly produce a detectable magnetic field if the TMD is continuously driven. This section will outline our understanding of the process for polarizing the spin of resident carriers in one of the valleys to produce a magnetic field.

When circularly-polarized light is applied on an intravalley resonance, it creates an exciton, an electron-hole bound pair with one charge in the conduction band and the other in the valence band. Most of the time, excitons decay in $\sim$ ps, or scatter into other valleys as a bound pair while flipping its spin ≈ 300 fs [165, 23, 168]. Any field produced by excitons either decays or inverts so quickly that it averages to zero on NV timescales. Fortunately, there exists experimental evidence of an intervalley scattering process that unbinds the excitons, leaving a hole in the initial valley and an electron in the opposing valley [167, 166]. Under this process, the imbalance of resident electrons between the valleys and their long lifetimes could produce long-lived fields [67].

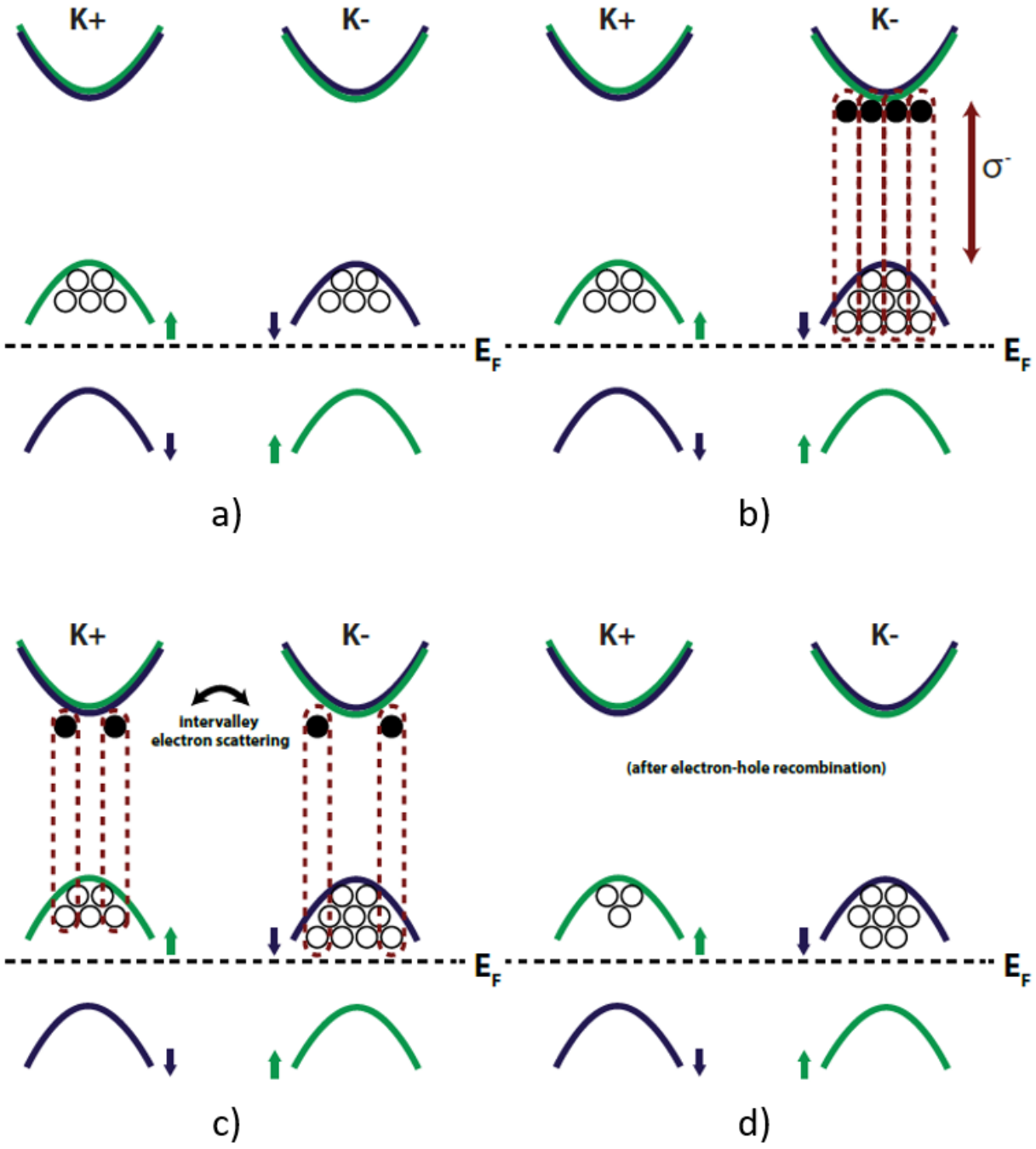

Figure 5.3: Proposed polarization process. a) The Fermi level is doped below between the two levels of the valence band, so holes occupy the upper SOC levels. b) Circularly-polarized light creates excitons in one K point. Some fraction of them quickly unbond into separate resident electrons and resident holes. c) The electrons scatter randomly and redistribute between the two K points. d) Finally, the electrons decay, filling the holes in both valence band.

The process is as follows. In a hole-doped TMD, the Fermi level can be tuned to sit between the two valence bands, above the lower band and under the upper band (Fig. 5.3). Circularly polarized light on resonance with the upper valence band excites some number of excitons. Given the scattering and decay processes described above, most of the excitons decay without issue, but the few whose electrons and holes are unbound have much longer ns lifetimes. The resident electrons are redistributed between the two K points, whereas the resident holes are left in their initial valley. Finally, the electrons decay back to the valence band and recombines with the holes, leaving an imbalance in the number of holes between the two K points. Since the K points have opposite spin orientations, this imbalance generates a net magnetization that lasts for the lifetime of the resident carriers $\sim$ ns. While ns is long for TMDs, since it is short for NV sensing times, the field generated would be detected as a noise source that broadens the NV's natural linewidth or shortens its T_2^*.

5.2 Proposed Experiments

There were two experiments our lab designed and seriously considered performing, detailed below.

5.2.1 Absolute Spin Density

By polarizing the spin of the resident carriers to produce a magnetic field which NVs could detect, we could potentially measure a value indicating the absolute density of resident carriers σ. This is opposed to Kerr measurements [167] that can only provide the relative change in spin density.

To see this, we estimate the size of the magnetic field produced by a monolayer TMD. Exciting the layer with a laser focused to a spot of radius R, we assume the resident electrons are generated instantaneously to form a uniform spin bath polarized along the out-of-plane direction $\hat{z}$ within a 2D disk of radius R (Fig. 5.4). Our NV sits a distance d below the 2D plane and detects the magnetic field from the disk. The magnetic scalar potential of a magnetic dipole is

$$\psi(\vec{r}) = \frac{\vec{m} \cdot \hat{r}}{4\pi|\vec{r}|^2} \tag{5.3}$$

where $\vec{m}$ is the magnetic moment and $\vec{r}$ is the displacement vector from the dipole. We can integrate eq. 5.3 over the disk to get a formula for the potential at the NV

$$\psi_{disk} = \frac{\sigma}{2}\left(1 - \frac{d}{(d^2 + R^2)^{1/2}}\right) \tag{5.4}$$

where the resident carrier density σ is the magnetic moment per unit area. The field at the NV is then

$$\vec{H} = -\nabla\psi = \frac{\sigma R^2}{2(d^2 + R^2)^{3/2}}\sin\theta\hat{z} \tag{5.5}$$

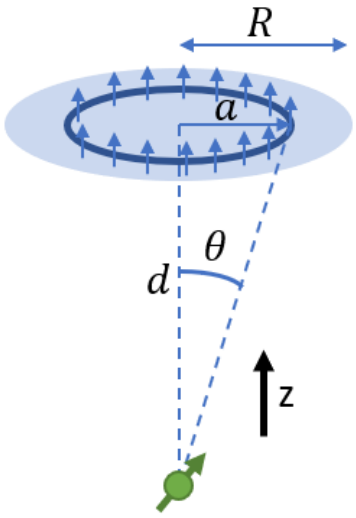

Figure 5.4: The NV can detect the magnetic field from a disk of resident electrons excited by a laser. To solve for the field of the disk, one must integrate over the radius a of rings. Since the depth $d \sim 10$ nm of the NV is much smaller than the diffraction-limit of the laser in z, both the NV and the TMD can be in focus simultaneously.

where θ is the angle the NV makes with the $\hat{z}$ axis ($\theta \approx 36^\circ$ for a [100] cut diamond). We see that the magnetic field on the NV is composed entirely of predetermined geometric factors d, R, and θ and the spin density σ. Consequently, a measurement of the field for a known geometry is a direct measurement of the absolute spin density.

Both the disk radius and NV depth are controlled by choice of experimental tools and for this experiment would be $R \sim 500$ nm and $d \sim 5 - 30$ nm. The magnetization density σ depends on the TMD chosen, but could be estimated by a simple calculation

$$\sigma = I\tau_k e_\sigma \left(\frac{hc}{\lambda}\right)^{-1} \mu_B \tag{5.6}$$

where I is the laser intensity ($\sim 1\mu\text{W}/\mu\text{m}^2$, τ_K is the lifetime of the resident electrons ('Kerr lifetime' of the local magnetic field), e_σ is the photon-to-carrier conversion efficiency ($\sim 0.05 - 5\%$ for MoS_2 and WSe_2), λ is the wavelength of the exciton resonance, and μ_B is the Bohr magneton. The Kerr lifetime depends on temperature, believed to be ~ 10 ns at 77 K and ~ 1 μs at 4 K for MoS_2 and WSe_2.

One issue that immediately arises is that the spin density could vary drastically for the ranges of Kerr lifetime and conversion efficiency. We estimated the possible spin densities for a variety of conversion efficiencies, Kerr lifetimes, and temperatures in WSe_2 heterostructures and monolayers (Fig. 5.5). In the worst case, only tens of resident electrons would be generated spread over a relatively immense area, producing a tiny signal. From the figure,

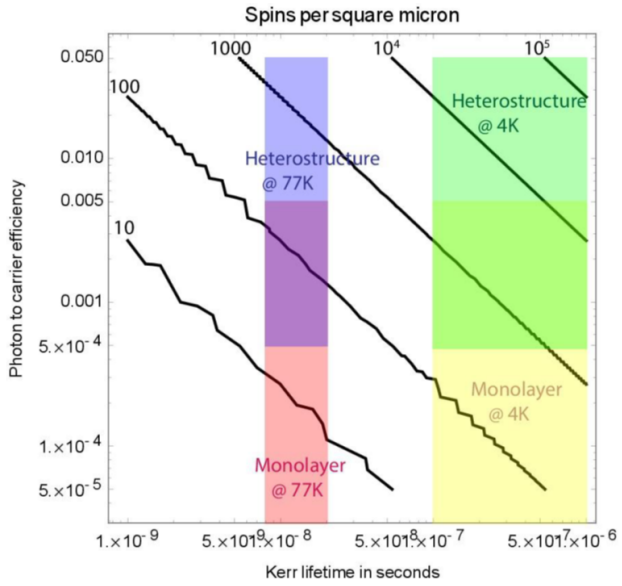

Figure 5.5: Number of spins per micron for given photon-to-carrier efficiency and Kerr lifetimes. We can compare this to expectations for the monolayer and heterostructures at different temperatures to determine which experiments are plausible.

we suspect we would need to study either heterostructures of TMD at 4 or 77 K or monolayers at 4 K to ensure a large enough signal.

5.2.2 FRET for TMD Transition Dipole Moment

Förster Resonance Energy Transfer (FRET)[2] is a transfer of an excitation from an excited particle ('donor') to an unexcited particle ('acceptor') via a non-radiative evanescent wave. Fundamentally, it is the same as one excited atom radiatively decaying and another atom absorbing the radiation. Both are mediated by electric dipolar interactions. The difference is that FRET occurs when the particles are too close for the donor to emit a photon to transfer its energy to the acceptor.

The efficiency of energy transfer through FRET E is expressed simply as

$$E = \frac{1}{1 + (r/R_0)^6} \tag{5.7}$$

with r being the separation between the two particles and R_0 being the Förster distance, the separation at which the efficiency drops to 50% [50]. The Förster distance encodes a ton of physics, most notably the overlap integral between the donor's emission spectrum

[2]Also called Fluorescence Resonance Energy Transfer by those who don't want to type 'ö'

and acceptor's absorption spectrum as well as the relative orientation of the two dipoles and their dipole moments. Typically for optical FRET $R_0 \sim 1 - 10$ nm.

Most often, FRET is used in biological studies to transfer energy between fluorophores and chromaphores as part of marking schemes [18]. In our case, we propose using FRET for two purposes. First, we would use it to determine the transition dipole moment of the TMD excitons μ_{TMD}. Since the transition dipole moment of NVs μ_{NV} is well-known [27], we can measure the FRET efficiency of a set of NVs at a pre-measured separations from and orientation to a TMD monolayer with a known absoprtion spectrum. The efficiency for transfer from a sole dipole to a sheet can be calculated [147]

$$E = \frac{\Gamma_{NV/TMD}}{\Gamma_{NV}} = \frac{m^*}{64\pi\epsilon^2\hbar^2 r^4}\mu_{TMD}^2\mu_{NV}^2(\sin^2\theta + 2\cos^2\theta) \tag{5.8}$$

where $\Gamma_{NV/TMD,NV}$ is the NV's fluorescence rate respectively with and without the TMD present, m^* is the effective mass of the exciton (half the electron mass), ϵ is the permittivity of diamond ($\approx 5.5\epsilon_0$), and θ is the angle the NV makes with $\hat{z}$. Knowing the relevant absorption/emission spectra and the relative orientation, the only unknown parameter is the transition dipole moment of the TMD.

Before investing in the experiment, we would like to estimate μ_{TMD} to ensure it is a feasible quantity to measure. We can do so by noting that it is the proportional to the overlap integral of the conduction and valence bands, which should place it around the size of the unit cell $\sim 3 - 5$ angstroms for any TMD. With this quantity, we can also estimate the Föster distance to be about 5 nm, meaning that we need NVs very close to the diamond surface in order to see the TMD quench the NV's fluorescence.

The second purpose of FRET measurements is much simpler in comparison to the first. Once μ_{TMD} is determined, the TMD monolayer can be easily used to calibrate the depth of shallow NVs below the surface of diamond using the FRET rate.

5.3 Experimental Efforts

Before shifting focus to other projects, we built the lab's first microscopy apparatus and performed two main sets of measurements on this experimental thrust, detailed in this section.

5.3.1 Experimental Apparatus

The apparatus we used for the following measurements is the most basic form of what was discussed in Section 1.4.3. We used a stripline to deliver microwaves to the NVs and applied magnetic fields with a permanent magnet on adjustable posts.

For the proposed measurements using the NV as a quantum sensor to study TMDs, we would need to exfoliate a flake of TMD or heterostucture onto the diamond surface. The NVs in the diamond need to be very shallow $\sim 1 - 10$ nm below the surface. Finally, the TMD/diamond sample needs to be cooled to liquid nitrogen (77 K) or liquid helium (4

K) temperatures. At the time of these measurements, we did not own a cryostat, but it would be required eventually. A crysostate would limit us to using air-based objective lenses which have a diffraction limit around 1 μm (we took this into account for our spin density estimates).

5.3.2 Shallow NV Depth Calibration

The first step to either the spin density or FRET measurements is to determine the precise depths of a set of NVs below the diamond surface. This depth becomes the separation d between the NV and the TMD that we would input into eqns 5.5 and 5.8. In addition, the NVs' bare fluorescence rates, saturation curves, and lifetimes must be characterized. Once the TMD is placed on the surface, we would extract information about the TMD based on how each of these changes.

We need a diamond sample with ~ 100 pm flatness to undergo implantation of nitrogen with low enough energy and density that the resultant single NV centers are distributed within $\sim 1-10$ nm. Fortunately, techniques for generating such shallow NV samples are well-developed [7, 81, 164]. We can thank our collaborators for walking us through the fabrication process and creating a sample. Starting with an electronic-grade Type IIa diamond, the surface is etched first with Ar and Cl_2 and then with O_2 to a flatness ~ 100 pm. Nitrogen ions were implanted with an energy of 2 KeV, which should create an average NV depth around 5 nm. Finally, the diamond was annealed in an O_2 environment at 800 C to both generate NVs and to terminate the diamond's surface dangling bonds. Terminating the surface prevents charge and magnetic impurities from bonding to the surface, increasing the rate of photobleaching and reducing the coherence times [164].

To calibrate the depths of the NVs, we followed a procedure that isolates the strength of the noise from a known proton bath [124]. The immersion oil we use to increase the refraction index of our objective lens and optimize the optical resolution is full of free-floating protons. An external field applied to the system causes the protons to Larmor precess at a frequency determined by the strength of the field (Fig. 5.6a). Seeing as they are in a viscous room-temperature medium, the amplitude and phase of the proton's Larmor precession varies over short timescales such that the net magnetization of the oil is negligible, but the variance in the magnetization is non-zero and proportional to the spin density.

For fields > 150 G, the precession frequency is in a range for NV spectroscopy methods relying on T_2 decoherence. The magnetization variance can then be directly measured via the decoherence in an XY8 decoupling sequence (Section 1.5.11). By varying the inter-pulse time, XY8 sweeps through the noise spectrum of the environment. At the Larmor frequency of the protons, the XY8 noise spectrum should exhibit a dip with contrast and width determined by the density of the proton bath and the distance the NV is away from the bath [124]. As long as we know the density of the proton bath and the magnetic field strength, the only free parameter is the NV depth (Fig. 5.6b). As the NV depth increases, the contrast of the noise Larmor precession decoherence signal decreases. Increasing the

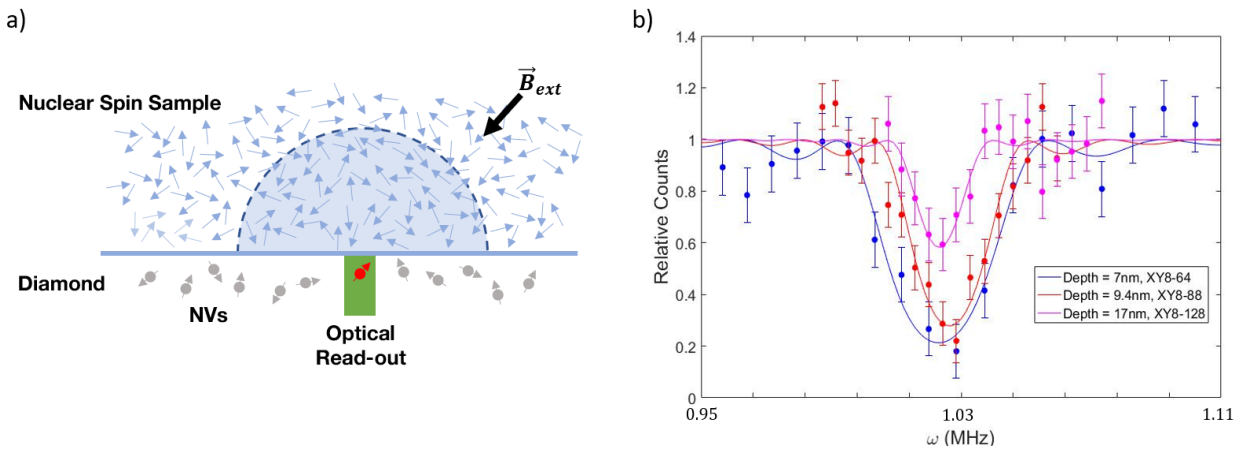

Figure 5.6: a) Schematic of NV depth calibration. With an applied external magnetic field, a free-floating proton bath in the oil creates a magnetic field that is zero on average, but has a non-zero variance due to the Larmor precession. b) In frequency space, the strength and width of the proton signal is determined by its depth. We measure the signal with the XY8 sequence.

number of pulses in the XY8 sequence permits the NV to decohere longer, boosting the contrast of the signal for deeper NVs.

We measured the proton density in the immersion oil at the Berkeley NMR facility. We then applied XY8 sequences on a set of NVs with a 200 G applied field, sweeping inter-pulse time to obtain noise spectra. The NV exhibited decoherence due to a single consistent Larmor frequency (within daily variance in external field). Fitting to the noise dips, we obtained a range of NV depths between 7nm and 20 nm (FIGURE). However, we never measured NVs shallower than 7 nm.

The question as to why we did not find NVs shallower than 7 nm was not answered before our experimental interests shifted. There were a set of NVs we found whose ODMR spectra displayed no NV resonances, which suggests exceptionally low T_2^* for these NVs and/or a high conversion rate to the NV^0 charged state. For all other NVs, we measured $T_2^* \sim 0.5\mu$s and $T_2^{SE} \sim 30\mu$s for this set of NVs, which is similar to the lifetimes in comparable samples [52, 106, 57]. It seemed then that the surface O_2 termination had succeeded in reducing magnetic noise, but was not adequately protecting the charge state of the shallowest NVs. We planned to redo surface cleaning and possibly the termination, but our experimental interests shifted before we proceeded further.

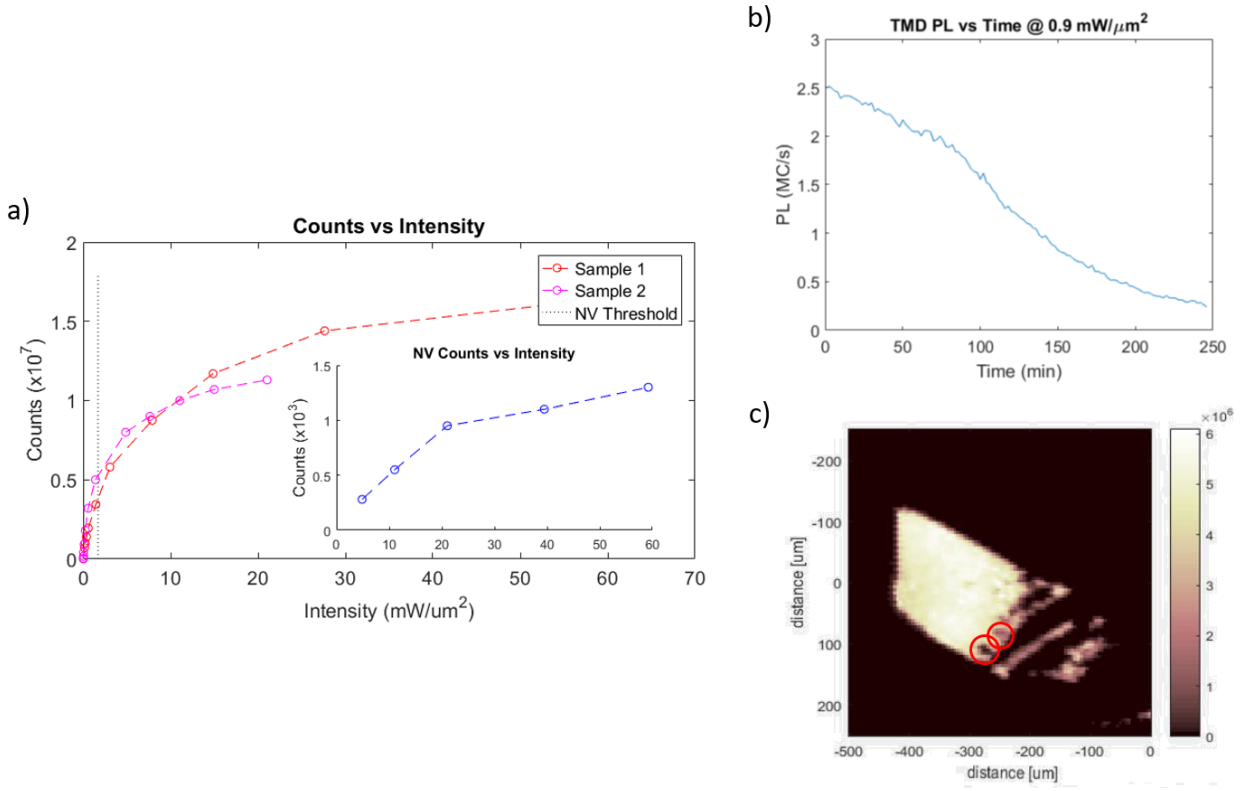

Figure 5.7: a) Saturation curves for two WSe_2 flakes and a shallow single NV. The flakes are two orders of magnitude brighter than the NV. b) The fluorescence rate of a spot on a WSe_2 flake versus time, exhibiting photobleaching. c) Confocal image with 532 nm laser light. Colorbar indicates photon counts. The red circled areas are locations that photobleached.

5.3.3 Burning TMDs

To test the feasibility of using the NVs and a monolayer TMD together, we wanted to probe for unexpected experimental issues. Our collaborators exfoliated a few flakes of monolayer WSe_2 onto the surface of a clean diamond with a low natural abundance of NVs (Type IIa). WSe_2 was chosen because its absorption and emission spectra are peaked at around 740 nm [9, 153], so it should exhibit a large FRET quenching of the NV and its emissions could feasibly be filtered away from the NV fluorescence.

We measured how the WSe_2 fluorescence saturated with increasing 532 nm laser intensity using an air objective to avoid contaminating the flake with oil (Fig. 5.7a). From saturation curves of two flakes we could make two conclusions. First, we found that using diamond as a substrate did not diminish the optical properties of the TMD. The fluorescence rate was comparable to what was expected given the photon collection efficiency of our setup. Second, by comparing the TMD's saturation curve to one of our shallow NVs, the WSe_2 is too bright

to be used as is with the single shallow NVs. The fluorescence rate of individual NVs is two orders of magnitude smaller than the rate of the monolayer at all laser intensities. Because the fluorescence of the TMD is a shot noise background that covers our NV's signal, the sensing SNR is reduced by more than a factor of 10, increasing all measurement times by a factor of 100. Even more crucially, small variations in this brightness completely obfuscates the location of the individual NVs. We would not be able to find and track individual NVs just a few nanometers below the WSe_2 layer if they appear as 1% variations in brightness under a layer with $> 10\%$ variations in brightness intrinsically measured.

The large disparity in brightness could naively be overcome by using a filter to cut out both NV and WSe_2 fluorescence above 740 nm; however, the TMD's emission does not simply cut off below 740nm. There is a phonon sideband that extends to lower wavelengths. We feared that there would still remain enough background fluorescence to stifle the experiment at room temperature. The natural solution then is to reduce the temperature of the sample to minimize the phonon sideband. Alternatively, our collaborators could stack heterostructures with a shifted emission spectrum. Before testing any of these solutions, a more pressing problem confronted us.

Continuously shining a laser on the WSe_2 flake under ambient conditions photobleached the flake irreversibly similar to how shallow NVs photobleach (Section 1.4.2). Over the course of a few minutes or hours, the photoluminescence diminished by a factor of 10 (Fig. 5.7b). In subsequent image scans of the flake under 532 nm illumination, we could observe holes seemingly burned into the flake (Fig. 5.7c). White light images revealed that the dim portions of the flake were still there, suggesting that they were photobleached, rather than truly burned away. The reduction in brightness occurred within hours even at laser intensities lower than what is feasible for using NVs. Unfortunately, this photobleaching was observed by our collaborators even at cryogenic temperatures when the laser intensity was at levels useful for NVs.

For a while we were not sure how to surmount the problem reasonably. We could reduce the duty cycle with which we apply the laser pulse to the sample. The TMD fluorescence lifetime did increase with lower duty cycle, but the integration times of our experiments would drastically increase. Eventually, we became privy to a solution with growing popularity in the 2D materials community: capping with hexagonal Boron Nitride (hBN). hBN is a 2D semiconductor that is found to be inert, so it does not alter the properties of other 2D layers in its heterostructure nor is it reactive to air and dust under ambient conditions. It is also transparent, permitting the study of optical properties of materials underneath it. The best solution then is to exfoliate the TMD flake onto the diamond, then protect the TMD against any chemical reactions on its surface that photobleach it by sealing its surface under a layer of hBN. Before implementing any of these solutions discussed, our experimental trajectory shifted, and projects on sensing properties of TMDs were put on hold. The Yao group did eventually return to sensing TMD heterostructures and exotic 2D materials, but using ensembles of shallow NVs instead (see the works of Satcher Hsieh and Jordan Hines).

5.4 Conclusions and Outlook

The work in this chapter attempted to turn the dynamics of an external TMD monolayer into the local dynamics of shallow NV centers by using FRET. In principle, such measurements would extract the transition dipole moment of the TMD. An additional experiment we considered was the measurement of the absolute spin density of an excited TMD. Before performing either experiment, the work was hindered by the local charge dynamics of the NV that shifted the defects to the neutral charged state, followed by the shifting of the lab's experimental trajectory.

Most crucially, this work led the Yao group to reflect deeply on the choice between single and ensemble NV experiments, and the limitations of the diamond sample we used. At first glance, shallow single NVs seem to hold many advantages over ensembles, such as a lower MW pulse error and precise depth calibration. Certainly these alluring traits are what swayed our group to this choice of sample, but in hindsight, they do not seem necessary to perform the desired experiments. Particularly, the measurement of the absolute spin density would likely be much easier using a delta-doped NV ensemble ~ 50 nm below the diamond surface, so that it is protected from deleterious surface effects. The field of a 2D magnetic disk 1 μm in diameter only drops by 5% over a 100 nm depth, leaving a strong signal with a small gradient across the layer, so even with a significant layer thickness (determined by SIMS measurements to 8 nm precision), the measurement with the layer would still produce fairly small errorbars on the absolute spin density. Finally, the ensemble would benefit from Heisenberg scaling sensitivity and a two or more orders of magnitude increase in brightness, putting it on par with the TMD brightness.

While an ensemble may have been less suited for a FRET measurement[3], many others were considered infeasible because we limited ourselves to the shallow single NV sample. Of note, an experiment we were considering after the ones in this chapter involved studying defects in TMDs. The primary obstacle to using single NVs for this purpose is the alignment of the defect to the NV—almost impossible. On the contrary, alignment is no issue for ensembles, and for many types of extended defects (line, and domains) an ensemble could image the entire target without issue[4]. Considerations involving a more thorough analysis of the expected field and the limitations of multiple types of samples are what led the group to choose ensembles in many subsequent sensing experiments, some of which are described in preceding chapters.

[3]FRET applies equally well to ensembles of NVs and has been used to calibrate an ensemble less than 4 nm from the diamond surface [7]. One could conceive of another diamond sample with a shallow ensemble of NVs grown via delta doping [117]; however, since the FRET distance is on the order of the layer thickness, the ultimate calculation of the TMD's transition dipole moment would have large errorbars.

[4]For point defects the story changes slightly. Neither type of plate diamond sample would necessarily be the competitive choice. Instead, a nanodiamond on an AFM would be the clear winner by miles [170]

Bibliography

[1] Kobrin et al., in preparation (2018).

[2] V M Acosta et al. "Broadband magnetometry by infrared-absorption detection of nitrogen-vacancy ensembles in diamond". In: *Applied Physics Letters* 97.17 (Oct. 2010), p. 174104.

[3] V M Acosta et al. "Diamonds with a high density of nitrogen-vacancy centers for magnetometry applications". In: *Physical Review B* 80.11 (Sept. 2009), p. 115202.

[4] V. M. Acosta et al. "Temperature Dependence of the Nitrogen-Vacancy Magnetic Resonance in Diamond". In: *Phys. Rev. Lett.* 104 (7 Feb. 2010), p. 070801. DOI: 10.1103/PhysRevLett.104.070801. URL: https://link.aps.org/doi/10.1103/PhysRevLett.104.0708012.

[5] Igor Aharonovich, Dirk Englund, and Milos Toth. "Solid-state single-photon emitters". In: *Nature Photonics* 10.10 (Oct. 2016), pp. 631–641.

[6] Ashok Ajoy and Paola Cappellaro. "Stable three-axis nuclear-spin gyroscope in diamond". In: *Physical Review A* 86.6 (Dec. 2012), p. 062104.

[7] Fahad Alghannam and Philip Hemmer. "Engineering of Shallow Layers of Nitrogen Vacancy Colour Centres in Diamond Using Plasma Immersion Ion Implantation". In: *Scientific Reports* 9.1 (Apr. 2019), p. 5870. ISSN: 2045-2322. DOI: 10.1038/s41598-019-42323-6. URL: https://doi.org/10.1038/s41598-019-42323-6.

[8] Mustafa Ahmed Ali Ahmed, Gonzalo A. Álvarez, and Dieter Suter. "Robustness of dynamical decoupling sequences". In: *Phys. Rev. A* 87 (4 Apr. 2013), p. 042309. DOI: 10.1103/PhysRevA.87.042309. URL: https://link.aps.org/doi/10.1103/PhysRevA.87.042309.

[9] Ozgur Burak Aslan, Minda Deng, and Tony Heinz. "Strain tuning of excitons in monolayer WSe2". In: *Physical Review B* 98 (Sept. 2018), p. 115308. DOI: 10.1103/PhysRevB.98.115308.

[10] M. Atatüre et al. In: *Nat. Rev. Mater* 3 (2018).

[11] N Bar-Gill et al. "Solid-state electronic spin coherence time approaching one second". In: *Nature Communications* 4.1 (Apr. 2013), p. 1743.

[12] John F. Barry et al. "Sensitivity optimization for NV-diamond magnetometry". In: *Rev. Mod. Phys.* 92 (1 Mar. 2020), p. 015004. DOI: 10.1103/RevModPhys.92.015004. URL: https://link.aps.org/doi/10.1103/RevModPhys.92.015004.

[13] John F. Barry et al. "Sensitivity optimization for NV-diamond magnetometry". In: *Rev. Mod. Phys.* 92 (1 Mar. 2020), p. 015004. DOI: 10.1103/RevModPhys.92.015004. URL: https://link.aps.org/doi/10.1103/RevModPhys.92.015004.

[14] Michael S J Barson et al. "Nanomechanical Sensing Using Spins in Diamond". In: *Nano Letters* 17.3 (Feb. 2017), pp. 1496–1503.

[15] Hannes Bernien et al. "Heralded entanglement between solid-state qubits separated by three metres". In: *Nature* 497.7447 (2013), p. 86.

[16] M. Block et al. *Optically Enhanced Electric Field Sensing using Nitrogen-Vacancy Ensembles*. 2020. arXiv: 2004.02886 [quant-ph].

[17] E Bourgeois et al. "Photoelectric detection of electron spin resonance of nitrogen-vacancy centres in diamond". In: *Nature Communications* 6.1 (Oct. 2015), p. 8577.

[18] C. R. Cantor and P. R. Schimmel. *Biophysical Chemistry Part-II*. Freeman, San Francisco, 1980.

[19] Paola Cappellaro and Mikhail D Lukin. "Quantum correlation in disordered spin systems: Applications to magnetic sensing". In: *Physical Review A* 80.3 (2009), p. 032311.

[20] F. Casola, T. van der Sar, and A. Yacoby. In: *Nat. Rev. Mater* 3 (2018).

[21] S. Chatterjee, J. F. Rodriguez-Nieva, and E. Demler. In: *Phys. Rev. B* 99 (2019).

[22] Edward H. Chen et al. "High-sensitivity spin-based electrometry with an ensemble of nitrogen-vacancy centers in diamond". In: *Phys. Rev. A* 95 (5 May 2017), p. 053417. DOI: 10.1103/PhysRevA.95.053417. URL: https://link.aps.org/doi/10.1103/PhysRevA.95.053417.

[23] Xi Chen et al. "Optical Control of Spin Polarization in Monolayer Transition Metal Dichalcogenides". In: *ACS Nano* 11.2 (2017). PMID: 28061025, pp. 1581–1587. DOI: 10.1021/acsnano.6b07061. eprint: https://doi.org/10.1021/acsnano.6b07061. URL: https://doi.org/10.1021/acsnano.6b07061.

[24] Joonhee Choi et al. "Robust Dynamic Hamiltonian Engineering of Many-Body Spin Systems". In: *Phys. Rev. X* 10 (3 July 2020), p. 031002. DOI: 10.1103/PhysRevX.10.031002. URL: https://link.aps.org/doi/10.1103/PhysRevX.10.031002.

[25] S. Choi, N. Y. Yao, and M. D. Lukin. "Quantum metrology based on strongly correlated matter". In: *ArXiv e-prints* (Dec. 2018). arXiv: 1801.00042 [quant-ph].

[26] S. Choi et al. "Observation of discrete time-crystalline order in a disordered dipolar many-body system". In: *Nature* 543.7644 (Mar. 2017), pp. 221–225.

[27] Yiwen Chu and Mikhail D. Lukin. *Quantum optics with nitrogen-vacancy centers in diamond*. 2015. arXiv: 1504.05990 [quant-ph].

[28] Y Chu et al. "Coherent Optical Transitions in Implanted Nitrogen Vacancy Centers". In: *Nano Letters* 14.4 (Mar. 2014), pp. 1982–1986.

[29] Wikimedia Commons. *NV Absorption*. File: `NVple.JPG`. 2008. URL: `https://commons.wikimedia.org/wiki/File:NVple.JPG`.

[30] A. L. Stevens D. B. McWhan. In: *Phys. Rev.* 139 (A682 1965).

[31] G. Davies and M. F. Hamer. "Optical Studies of the 1.945 eV Vibronic Band in Diamond". In: *Proceedings of the Royal Society of London. Series A, Mathematical and Physical Sciences* 348.1653 (1976), pp. 285–298. ISSN: 00804630. URL: `http://www.jstor.org/stable/79142`.

[32] Gordon Davies. "Charge states of the vacancy in diamond". In: *Nature* 269.5628 (Oct. 1977), pp. 498–500.

[33] A. Dewaele, P. Loubeyre, and M. Mezouar. In: *Phys. Rev. B* 70 (2004).

[34] M. W. Doherty. "et al". In: *Physics Reports* 528 (2013), p. 1.

[35] Marcus W Doherty et al. "Electronic properties and metrology applications of the diamond NV- center under pressure". In: *Physical review letters* 112.4 (2014), p. 047601.

[36] Florian Dolde et al. "Nanoscale Detection of a Single Fundamental Charge in Ambient Conditions Using the NV- Center in Diamond". In: *Physical Review Letters* 112.9 (Mar. 2014), p. 097603.

[37] F Dolde et al. "Electric-field sensing using single diamond spins". In: *Nature Physics* 7.6 (Apr. 2011), pp. 459–463.

[38] Y. Dovzhenko. "et al". In: *Nat. Commm* 9 (2018), p. 2712.

[39] Yuliya Dovzhenko et al. "Imaging the spin texture of a skyrmion under ambient conditions using an atomic-sized sensor". In: *arXiv preprint arXiv:1611.00673* (2016).

[40] A. Dréau et al. "Avoiding power broadening in optically detected magnetic resonance of single NV defects for enhanced dc magnetic field sensitivity". In: *Phys. Rev. B* 84 (19 Nov. 2011), p. 195204. DOI: `10.1103/PhysRevB.84.195204`. URL: `https://link.aps.org/doi/10.1103/PhysRevB.84.195204`.

[41] A. P. Drozdov et al. In: *Nature* 525 (2015).

[42] Chunhui Du et al. "Control and local measurement of the spin chemical potential in a magnetic insulator". In: *Science* 357.6347 (2017), pp. 195–198.

[43] Tim R. Eichhorn, Claire A. McLellan, and Ania C. Bleszynski Jayich. "Optimizing the formation of depth-confined nitrogen vacancy center spin ensembles in diamond for quantum sensing". In: *Phys. Rev. Materials* 3 (11 Nov. 2019), p. 113802. DOI: `10.1103/PhysRevMaterials.3.113802`. URL: `https://link.aps.org/doi/10.1103/PhysRevMaterials.3.113802`.

[44] Dominic V. Else, Wen Wei Ho, and Philipp T. Dumitrescu. "Long-Lived Interacting Phases of Matter Protected by Multiple Time-Translation Symmetries in Quasiperiodically Driven Systems". In: *Phys. Rev. X* 10 (2 May 2020), p. 021032. DOI: 10.1103/PhysRevX.10.021032. URL: https://link.aps.org/doi/10.1103/PhysRevX.10.021032.

[45] RJ Epstein et al. "Anisotropic interactions of a single spin and dark-spin spectroscopy in diamond". In: *Nature physics* 1.2 (2005), p. 94.

[46] G. Falkovich. *Fluid Mechanics*. second edn: Cambridge University Press, 2018.

[47] S. Felton et al. "Hyperfine interaction in the ground state of the negatively charged nitrogen vacancy center in diamond". In: *Phys. Rev. B* 79 (7 Feb. 2009), p. 075203. DOI: 10.1103/PhysRevB.79.075203. URL: https://link.aps.org/doi/10.1103/PhysRevB.79.075203.

[48] B. Feng, V. I. Levitas, and R. J. Hemley. In: *Int. J. Plasticity* 84 (2016).

[49] J. Forneris et al. "Mapping the local spatial charge in defective diamond by means of NV sensors - A "self-diagnostic" concept". In: *ArXiv e-prints* (June 2017). arXiv: 1706.07935 [cond-mat.mtrl-sci].

[50] Th. Főrster. "10th Spiers Memorial Lecture. Transfer mechanisms of electronic excitation". In: *Discuss. Faraday Soc.* 27 (0 1959), pp. 7–17. DOI: 10.1039/DF9592700007. URL: http://dx.doi.org/10.1039/DF9592700007.

[51] T. Gaebel et al. "Photochromism in single nitrogen-vacancy defect in diamond". In: *Applied Physics B* 82.2 (Feb. 2006), pp. 243–246. ISSN: 1432-0649. DOI: 10.1007/s00340-005-2056-2. URL: https://doi.org/10.1007/s00340-005-2056-2.

[52] Torsten Gaebel et al. "Room-temperature coherent coupling of single spins in diamond". In: *Nature Physics* 2.6 (June 2006), pp. 408–413. ISSN: 1745-2481. DOI: 10.1038/nphys318. URL: https://doi.org/10.1038/nphys318.

[53] Adam Gali, Maria Fyta, and Efthimios Kaxiras. "Ab initio supercell calculations on nitrogen-vacancy center in diamond: Electronic structure and hyperfine tensors". In: *Phys. Rev. B* 77 (15 Apr. 2008), p. 155206. DOI: 10.1103/PhysRevB.77.155206. URL: https://link.aps.org/doi/10.1103/PhysRevB.77.155206.

[54] E. Gilioli and L. Ehm. In: *IUCrJ* 1 (2014), pp. 590–603.

[55] D. R. Glenn. "et al". In: *Geochem. Geophys* 18 (2017), p. 3254.

[56] J. P. Goss et al. "The Twelve-Line 1.682 eV Luminescence Center in Diamond and the Vacancy-Silicon Complex". In: *Phys. Rev. Lett.* 77 (14 Sept. 1996), pp. 3041–3044. DOI: 10.1103/PhysRevLett.77.3041. URL: https://link.aps.org/doi/10.1103/PhysRevLett.77.3041.

[57] M. S. Grinolds et al. "Quantum control of proximal spins using nanoscale magnetic resonance imaging". In: *Nature Physics* 7.9 (Sept. 2011), pp. 687–692. ISSN: 1745-2481. DOI: 10.1038/nphys1999. URL: https://doi.org/10.1038/nphys1999.

[58] Isabell Gross et al. "Real-space imaging of non-collinear antiferromagnetic order with a single-spin magnetometer". In: *Nature* 549.7671 (2017), p. 252.

[59] A Gruber et al. "Scanning Confocal Optical Microscopy and Magnetic Resonance on Single Defect Centers". In: *Science* 276.5321 (June 1997), pp. 2012–2014.

[60] O. Gunawan et al. "Valley Susceptibility of an Interacting Two-Dimensional Electron System". In: *Phys. Rev. Lett.* 97 (18 Nov. 2006), p. 186404. DOI: 10.1103/PhysRevLett.97.186404. URL: https://link.aps.org/doi/10.1103/PhysRevLett.97.186404.

[61] H.-k. In: *Mao, X.-J* 90 (2018).

[62] E. L. Hahn. "Spin Echoes". In: *Phys. Rev.* 80 (4 Nov. 1950), pp. 580–594. DOI: 10.1103/PhysRev.80.580. URL: https://link.aps.org/doi/10.1103/PhysRev.80.580.

[63] P. Hargraves et al. In: *Phys. Rev. B* 38 (1988).

[64] B Hensen et al. "Loophole-free Bell inequality violation using electron spins separated by 1.3 kilometres". In: *Nature* 526.7575 (Oct. 2015), pp. 682–686.

[65] H. Horii and S. Nemat-Nasser. In: *Philos. Trans. Royal Soc. A* 319 (1986).

[66] S. Hsieh et al. "Imaging stress and magnetism at high pressures using a nanoscale quantum sensor". In: *Science* 366.6471 (2019), pp. 1349–1354. ISSN: 0036-8075. DOI: 10.1126/science.aaw4352. eprint: https://science.sciencemag.org/content/366/6471/1349.full.pdf. URL: https://science.sciencemag.org/content/366/6471/1349.

[67] Wei-Ting Hsu et al. "Optically initialized robust valley-polarized holes in monolayer WSe2". In: *Nature Communications* 6.1 (Nov. 2015), p. 8963. ISSN: 2041-1723. DOI: 10.1038/ncomms9963. URL: https://doi.org/10.1038/ncomms9963.

[68] Ryuji Igarashi et al. "Real-Time Background-Free Selective Imaging of Fluorescent Nanodiamonds in Vivo". In: *Nano Letters* 12.11 (Nov. 2012), pp. 5726–5732.

[69] A. C. Ipsen and K. Splittorff. "The van der Waals interaction in one, two, and three dimensions". In: *American Journal of Physics* 83.2 (2015), pp. 150–155. DOI: 10.1119/1.4896248. eprint: https://doi.org/10.1119/1.4896248. URL: https://doi.org/10.1119/1.4896248.

[70] Viktor Ivády et al. "Pressure and temperature dependence of the zero-field splitting in the ground state of NV centers in diamond: A first-principles study". In: *Phys. Rev. B* 90 (23 Dec. 2014), p. 235205. DOI: 10.1103/PhysRevB.90.235205. URL: https://link.aps.org/doi/10.1103/PhysRevB.90.235205.

[71] A. P. Jephcoat J. Akella G. S. Smith. In: *J. Phys. Chem. Solids* 49 (573 1988).

[72] Tzach Jaffe et al. "Novel Ultra Localized and Dense Nitrogen Delta-Doping in Diamond for Advanced Quantum Sensing". In: *Nano Letters* 20.5 (2020). PMID: 32356992, pp. 3192–3198. DOI: 10.1021/acs.nanolett.9b05243. eprint: https://doi.org/10.1021/acs.nanolett.9b05243. URL: https://doi.org/10.1021/acs.nanolett.9b05243.

[73] P. Jamonneau et al. "Competition between electric field and magnetic field noise in the decoherence of a single spin in diamond". In: *Phys. Rev. B* 93 (2 Jan. 2016), p. 024305. DOI: 10.1103/PhysRevB.93.024305. URL: https://link.aps.org/doi/10.1103/PhysRevB.93.024305.

[74] A. Jarmola et al. "Temperature- and Magnetic-Field-Dependent Longitudinal Spin Relaxation in Nitrogen-Vacancy Ensembles in Diamond". In: *Phys. Rev. Lett.* 108 (19 May 2012), p. 197601. DOI: 10.1103/PhysRevLett.108.197601. URL: https://link.aps.org/doi/10.1103/PhysRevLett.108.197601.

[75] A Jarmola et al. "Longitudinal spin-relaxation in nitrogen-vacancy centers in electron irradiated diamond". In: *Applied Physics Letters* 107.24 (Dec. 2015), p. 242403.

[76] A. Jayaraman. In: *Rev. Mod. Phys* 55 (1983).

[77] A. Jayaraman. *Metals*. Vol. 1. pp. 707 – 747: Elsevier of Handbook on the Physics and Chemistry of Rare Earths, 1978.

[78] F Jelezko et al. "Single spin states in a defect center resolved by optical spectroscopy". In: *Applied Physics Letters* 81.12 (Sept. 2002), pp. 2160–2162.

[79] K. Jensen et al. "Light narrowing of magnetic resonances in ensembles of nitrogen-vacancy centers in diamond". In: *Phys. Rev. B* 87 (1 Jan. 2013), p. 014115. DOI: 10.1103/PhysRevB.87.014115. URL: https://link.aps.org/doi/10.1103/PhysRevB.87.014115.

[80] Jonathan A Jones et al. "Magnetic field sensing beyond the standard quantum limit using 10-spin NOON states". In: *Science* 324.5931 (2009), pp. 1166–1168.

[81] Sora Kawai et al. "Nitrogen-Terminated Diamond Surface for Nanoscale NMR by Shallow Nitrogen-Vacancy Centers". In: *The Journal of Physical Chemistry C* 123.6 (2019), pp. 3594–3604. DOI: 10.1021/acs.jpcc.8b11274. eprint: https://doi.org/10.1021/acs.jpcc.8b11274. URL: https://doi.org/10.1021/acs.jpcc.8b11274.

[82] P. Kehayias. "et al". In: *Nat. Commm* 8 (2017), p. 188.

[83] Donggyu Kim et al. "A CMOS-integrated quantum sensor based on nitrogen–vacancy centres". In: *Nature Electronics* 2.7 (July 2019), pp. 284–289. ISSN: 2520-1131. DOI: 10.1038/s41928-019-0275-5. URL: https://doi.org/10.1038/s41928-019-0275-5.

[84] S. Klotz et al. In: *J Phys D Appl Phys* 42 (2009).

[85] S. Kolkowitz. "et al". In: *Science* 347 (2015), p. 1129.

[86] Y Kubo et al. "Strong Coupling of a Spin Ensemble to a Superconducting Resonator". In: *Physical Review Letters* 105.14 (Sept. 2010), p. 140502.

[87] G. Kucsko. "et al". In: *Nature* 500 (2013).

[88] G. Kucsko et al. "Critical Thermalization of a Disordered Dipolar Spin System in Diamond". In: *Phys. Rev. Lett.* 121 (2 July 2018), p. 023601. DOI: 10.1103/PhysRevLett.121.023601. URL: https://link.aps.org/doi/10.1103/PhysRevLett.121.023601.

[89] G Kucsko et al. "Nanometre-scale thermometry in a living cell". In: *Nature* 500.7460 (Aug. 2013), pp. 54–58.

[90] Ngoc Diep Lai et al. "Influence of a static magnetic field on the photoluminescence of an ensemble of nitrogen-vacancy color centers in a diamond single-crystal". In: *Applied Physics Letters* 95.13 (2009), p. 133101. DOI: 10.1063/1.3238467. eprint: https://doi.org/10.1063/1.3238467. URL: https://doi.org/10.1063/1.3238467.

[91] Abdelghani Laraoui et al. "Imaging thermal conductivity with nanoscale resolution using a scanning spin probe". In: *Nature Communications* 6.1 (Nov. 2015), p. 8954.

[92] D Le Sage et al. "Optical magnetic imaging of living cells". In: *Nature* 496.7446 (2013), p. 486.

[93] M P Ledbetter et al. "Gyroscopes based on nitrogen-vacancy centers in diamond". In: *Physical Review A* 86.5 (Nov. 2012), p. 052116.

[94] C. Lee et al. "Frictional characteristics of atomically thin sheets". In: *Science* 328.5974 (Apr. 2010), pp. 76–80.

[95] A. Lenef and S. C. Rand. "Electronic structure of the N-V center in diamond: Theory". In: *Phys. Rev. B* 53 (20 May 1996), pp. 13441–13455. DOI: 10.1103/PhysRevB.53.13441. URL: https://link.aps.org/doi/10.1103/PhysRevB.53.13441.

[96] A. O. Levchenko et al. "Inhomogeneous broadening of optically detected magnetic resonance of the ensembles of nitrogen-vacancy centers in diamond by interstitial carbon atoms". In: *Applied Physics Letters* 106.10 (2015), p. 102402. DOI: 10.1063/1.4913428. eprint: https://doi.org/10.1063/1.4913428. URL: https://doi.org/10.1063/1.4913428.

[97] J H N Loubser and J A van Wyk. "Electron spin resonance in the study of diamond". In: *Reports on Progress in Physics* 41.8 (Aug. 1978), pp. 1201–1248. DOI: 10.1088/0034-4885/41/8/002. URL: https://doi.org/10.1088%2F0034-4885%2F41%2F8%2F002.

[98] I. Lovchinsky et al. "Nuclear magnetic resonance detection and spectroscopy of single proteins using quantum logic". In: *Science* (2016). ISSN: 0036-8075. DOI: 10.1126/science.aad8022. eprint: https://science.sciencemag.org/content/early/2016/02/03/science.aad8022.full.pdf. URL: https://science.sciencemag.org/content/early/2016/02/03/science.aad8022.

[99] BJ Maertz et al. "Vector magnetic field microscopy using nitrogen vacancy centers in diamond". In: *Applied Physics Letters* 96.9 (2010), p. 092504.

[100] HJ Mamin et al. "Nanoscale nuclear magnetic resonance with a nitrogen-vacancy spin sensor". In: *Science* 339.6119 (2013), pp. 557–560.

[101] N. B. Manson, J. P. Harrison, and M. J. Sellars. "Nitrogen-vacancy center in diamond: Model of the electronic structure and associated dynamics". In: *Phys. Rev. B* 74 (10 Sept. 2006), p. 104303. DOI: 10.1103/PhysRevB.74.104303. URL: https://link.aps.org/doi/10.1103/PhysRevB.74.104303.

[102] Neil B. Manson, Xing-Fei He, and Peter T. H. Fisk. "Raman heterodyne detected electron-nuclear-double-resonance measurements of the nitrogen-vacancy center in diamond". In: *Opt. Lett.* 15.19 (Oct. 1990), pp. 1094–1096. DOI: 10.1364/OL.15.001094. URL: http://ol.osa.org/abstract.cfm?URI=ol-15-19-1094.

[103] J.P.D. Martin. "Fine structure of excited 3E state in nitrogen-vacancy centre of diamond". In: *Journal of Luminescence* 81.4 (1999), pp. 237–247. ISSN: 0022-2313. DOI: https://doi.org/10.1016/S0022-2313(99)00013-7. URL: http://www.sciencedirect.com/science/article/pii/S0022231399000137.

[104] Y Matsuzaki et al. "Optically detected magnetic resonance of high-density ensemble of NV^- centers in diamond". In: *Journal of Physics: Condensed Matter* 28.27 (July 2016), p. 275302.

[105] L. F. Mattheiss. "Band Structures of Transition-Metal-Dichalcogenide Layer Compounds". In: *Phys. Rev. B* 8 (8 Oct. 1973), pp. 3719–3740. DOI: 10.1103/PhysRevB.8.3719. URL: https://link.aps.org/doi/10.1103/PhysRevB.8.3719.

[106] P. C. Maurer et al. "Far-field optical imaging and manipulation of individual spins with nanoscale resolution". In: *Nature Physics* 6.11 (Nov. 2010), pp. 912–918. ISSN: 1745-2481. DOI: 10.1038/nphys1774. URL: https://doi.org/10.1038/nphys1774.

[107] J R Maze et al. "Properties of nitrogen-vacancy centers in diamond: the group theoretic approach". In: *New Journal of Physics* 13.2 (Feb. 2011), p. 025025. DOI: 10.1088/1367-2630/13/2/025025.

[108] J. Maze. "et al". In: *Nature* 455 (2008), p. 644.

[109] L. P. McGuinness et al. "Quantum measurement and orientation tracking of fluorescent nanodiamonds inside living cells". In: *Nature Nanotechnology* 6 (May 2011), 358 EP -. URL: http://dx.doi.org/10.1038/nnano.2011.64.

[110] Claire A. McLellan et al. "Patterned Formation of Highly Coherent Nitrogen-Vacancy Centers Using a Focused Electron Irradiation Technique". In: *Nano Letters* 16.4 (2016). PMID: 27010642, pp. 2450–2454. DOI: 10.1021/acs.nanolett.5b05304. eprint: https://doi.org/10.1021/acs.nanolett.5b05304. URL: https://doi.org/10.1021/acs.nanolett.5b05304.

[111] Hongki Min et al. "Intrinsic and Rashba spin-orbit interactions in graphene sheets". In: *Phys. Rev. B* 74 (16 Oct. 2006), p. 165310. DOI: 10.1103/PhysRevB.74.165310. URL: https://link.aps.org/doi/10.1103/PhysRevB.74.165310.

[112] Yoshimi Mita. "Change of absorption spectra in type-Ib diamond with heavy neutron irradiation". In: *Phys. Rev. B* 53 (17 May 1996), pp. 11360–11364. DOI: 10.1103/PhysRevB.53.11360. URL: https://link.aps.org/doi/10.1103/PhysRevB.53.11360.

[113] T. Mittiga et al. "Imaging the Local Charge Environment of Nitrogen-Vacancy Centers in Diamond". In: *Phys. Rev. Lett.* 121 (24 Dec. 2018), p. 246402. DOI: 10.1103/PhysRevLett.121.246402. URL: https://link.aps.org/doi/10.1103/PhysRevLett.121.246402.

[114] B. A. Myers, A. Ariyaratne, and A. C. Bleszynski Jayich. "Double-Quantum Spin-Relaxation Limits to Coherence of Near-Surface Nitrogen-Vacancy Centers". In: *Phys. Rev. Lett.* 118 (19 May 2017), p. 197201. DOI: 10.1103/PhysRevLett.118.197201. URL: https://link.aps.org/doi/10.1103/PhysRevLett.118.197201.

[115] Boris Naydenov et al. "Increasing the coherence time of single electron spins in diamond by high temperature annealing". In: *Applied Physics Letters* 97.24 (2010), p. 242511. DOI: 10.1063/1.3527975. eprint: https://doi.org/10.1063/1.3527975. URL: https://doi.org/10.1063/1.3527975.

[116] K. S. Novoselov et al. "Two-dimensional atomic crystals". In: *Proceedings of the National Academy of Sciences* 102.30 (2005), pp. 10451–10453. ISSN: 0027-8424. DOI: 10.1073/pnas.0502848102. eprint: https://www.pnas.org/content/102/30/10451.full.pdf. URL: https://www.pnas.org/content/102/30/10451.

[117] Kenichi Ohno et al. "Engineering shallow spins in diamond with nitrogen delta-doping". In: *Applied Physics Letters* 101.8 (2012), p. 082413. DOI: 10.1063/1.4748280. eprint: https://doi.org/10.1063/1.4748280. URL: https://doi.org/10.1063/1.4748280.

[118] E van Oort, N B Manson, and M Glasbeek. "Optically detected spin coherence of the diamond N-V centre in its triplet ground state". In: *Journal of Physics C: Solid State Physics* 21.23 (Aug. 1988), pp. 4385–4391. DOI: 10.1088/0022-3719/21/23/020. URL: https://doi.org/10.1088%2F0022-3719%2F21%2F23%2F020.

[119] Eric Van Oort and Max Glasbeek. "Electric-field-induced modulation of spin echoes of N-V centers in diamond". In: *Chemical Physics Letters* 168.6 (1990), pp. 529–532. ISSN: 0009-2614. DOI: https://doi.org/10.1016/0009-2614(90)85665-Y. URL: http://www.sciencedirect.com/science/article/pii/000926149085665Y.

[120] L. Oroszlány et al. In: *Phys. Rev. Lett* 115 (2015).

[121] P. Ovartchaiyapong et al. In: *Nat. Commm* 5 (2014).

[122] Matthew Pelliccione et al. "Scanned probe imaging of nanoscale magnetism at cryogenic temperatures with a single-spin quantum sensor". In: *Nature nanotechnology* 11.8 (2016), p. 700.

[123] L M Pham et al. "Magnetic field imaging with nitrogen-vacancy ensembles". In: *New Journal of Physics* 13.4 (Apr. 2011), p. 045021.

[124] Linh M. Pham et al. "NMR technique for determining the depth of shallow nitrogen-vacancy centers in diamond". In: *Phys. Rev. B* 93 (4 Jan. 2016), p. 045425. DOI: 10.1103/PhysRevB.93.045425. URL: https://link.aps.org/doi/10.1103/PhysRevB.93.045425.

[125] B. Radisavljevic et al. "Single-layer MoS2 transistors". In: *Nat Nanotechnol* 6.3 (Mar. 2011), pp. 147–150.

[126] N.R.S. Reddy, N.B. Manson, and E.R. Krausz. "Two-laser spectral hole burning in a colour centre in diamond". In: *Journal of Luminescence* 38.1 (1987), pp. 46–47. ISSN: 0022-2313. DOI: https://doi.org/10.1016/0022-2313(87)90057-3. URL: http://www.sciencedirect.com/science/article/pii/0022231387900573.

[127] D. A. Redman et al. "Spin dynamics and electronic states of N-V centers in diamond by EPR and four-wave-mixing spectroscopy". In: *Phys. Rev. Lett.* 67 (24 Dec. 1991), pp. 3420–3423. DOI: 10.1103/PhysRevLett.67.3420. URL: https://link.aps.org/doi/10.1103/PhysRevLett.67.3420.

[128] Lucio Robledo et al. "Spin dynamics in the optical cycle of single nitrogen-vacancy centres in diamond". In: *New Journal of Physics* 13.2 (Feb. 2011), p. 025013. DOI: 10.1088/1367-2630/13/2/025013. URL: https://doi.org/10.1088%2F1367-2630%2F13%2F2%2F025013.

[129] L J Rogers et al. "Singlet levels of the NV-centre in diamond". In: *New Journal of Physics* 17.1 (Jan. 2015), p. 013048. DOI: 10.1088/1367-2630/17/1/013048.

[130] L Rondin et al. "Magnetometry with nitrogen-vacancy defects in diamond". In: *Reports on Progress in Physics* 77.5 (May 2014), p. 056503.

[131] G. K. Samudrala et al. In: *High Press. Res* 34 (2014).

[132] Romana Schirhagl et al. "Nitrogen-Vacancy Centers in Diamond: Nanoscale Sensors for Physics and Biology". In: *Annual Review of Physical Chemistry* 65.1 (2014). PMID: 24274702, pp. 83–105. DOI: 10.1146/annurev-physchem-040513-103659. eprint: https://doi.org/10.1146/annurev-physchem-040513-103659. URL: https://doi.org/10.1146/annurev-physchem-040513-103659.

[133] Marlan O. Scully and M. Suhail Zubairy. *Quantum Optics*. Cambridge University Press, 1997. DOI: 10.1017/CBO9780511813993.

[134] Maria Simanovskaia et al. "Sidebands in optically detected magnetic resonance signals of nitrogen vacancy centers in diamond". In: *Phys. Rev. B* 87 (22 June 2013), p. 224106. DOI: 10.1103/PhysRevB.87.224106. URL: https://link.aps.org/doi/10.1103/PhysRevB.87.224106.

[135] Stephanie Simmons et al. "Magnetic field sensors using 13-spin cat states". In: *Physical Review A* 82.2 (2010), p. 022330.

[136] T. J. Smart et al. "High-Pressure Nano-seismic Events in Serpentine as a Function of Shear Stresses". In: *AGU Fall Meeting Abstracts*. Vol. 2019. Dec. 2019, MR22A–02.

[137] Benjamin Smeltzer, Lilian Childress, and Adam Gali. "13C hyperfine interactions in the nitrogen-vacancy centre in diamond". In: *New Journal of Physics* 13.2 (Feb. 2011), p. 025021. DOI: 10.1088/1367-2630/13/2/025021. URL: https://doi.org/10.1088%2F1367-2630%2F13%2F2%2F025021.

[138] M. Somayazulu. "et al". In: *Phys. Rev. Lett* 122 (2019), p. 027001.

[139] Andrea Splendiani et al. "Emerging Photoluminescence in Monolayer MoS2". In: *Nano Letters* 10.4 (2010). PMID: 20229981, pp. 1271–1275. DOI: 10.1021/nl903868w. eprint: https://doi.org/10.1021/nl903868w. URL: https://doi.org/10.1021/nl903868w.

[140] P L Stanwix et al. "Coherence of nitrogen-vacancy electronic spin ensembles in diamond". In: *Physical Review B* 82.20 (Nov. 2010), p. 201201.

[141] P. L. Stanwix et al. "Coherence of nitrogen-vacancy electronic spin ensembles in diamond". In: *Phys. Rev. B* 82 (20 Nov. 2010), p. 201201. DOI: 10.1103/PhysRevB.82.201201. URL: https://link.aps.org/doi/10.1103/PhysRevB.82.201201.

[142] L G Steele et al. "Optically detected magnetic resonance of nitrogen vacancies in a diamond anvil cell using designer diamond anvils". In: *Applied Physics Letters* 111.22 (Nov. 2017), p. 221903.

[143] L. G. Steele. "et al". In: *Appl. Phys. Lett* 111 (2017), p. 221903.

[144] S Steinert et al. "High sensitivity magnetic imaging using an array of spins in diamond". In: *Review of Scientific Instruments* 81.4 (Apr. 2010), p. 043705.

[145] E. Sterer, M. P. Pasternak, and R. D. Taylor. In: *Rev. Sci. Instrum* 61 (1998).

[146] See Supplementary. Material for additional details.

[147] R. S. Swathi and K. L. Sebastian. "Distance dependence of fluorescence resonance energy transfer". In: *In: Proceedings of the Indian Academy of Sciences - Chemical Sciences* 121.5 (2009), pp. 777–787.

[148] H. Tang. "et al". In: *Phys. Rev. Lett* 71 (1993), p. 444.

[149] R. Taylor, M. Pasternak, and R. Jeanloz. In: *J. Appl. Phys* 69 (1991).

[150] J-P Tetienne et al. "Magnetic-field-dependent photodynamics of single NV defects in diamond: an application to qualitative all-optical magnetic imaging". In: *New Journal of Physics* 14.10 (Oct. 2012), p. 103033. DOI: 10.1088/1367-2630/14/10/103033. URL: https://doi.org/10.1088%2F1367-2630%2F14%2F10%2F103033.

[151] Ann M Thayer and Alexander Pines. "Zero-field NMR". In: *Accounts of Chemical Research* 20.2 (May 2002), pp. 47–53.

[152] L. Thiel. "et al". In: *Nat. Nanotechnol* 11 (2016), p. 677.

[153] Philipp Tonndorf et al. "Photoluminescence emission and Raman response of monolayer MoS2, MoSe2, and WSe2". In: *Opt. Express* 21.4 (Feb. 2013), pp. 4908–4916. DOI: 10.1364/OE.21.004908. URL: http://www.opticsexpress.org/abstract.cfm?URI=oe-21-4-4908.

[154] David M Toyli et al. "Fluorescence thermometry enhanced by the quantum coherence of single spins in diamond". In: *Proceedings of the National Academy of Sciences* 110.21 (2013), pp. 8417–8421.

[155] DM Toyli et al. "Measurement and control of single nitrogen-vacancy center spins above 600 K". In: *Physical Review X* 2.3 (2012), p. 031001.

[156] P. Udvarhelyi et al. In: *Phys. Rev. B* 98 (2018).

[157] G Waldherr et al. "Violation of a temporal Bell inequality for single spins in a diamond defect center". In: *Physical Review Letters* 107.9 (2011), p. 090401.

[158] Wojciech Wasilewski et al. "Quantum noise limited and entanglement-assisted magnetometry". In: *Physical Review Letters* 104.13 (2010), p. 133601.

[159] DP Weitekamp et al. "Zero-field nuclear magnetic resonance". In: *Physical review letters* 50.22 (1983), p. 1807.

[160] S Whitehead and W Hackett. "Measurement of the specific inductive capacity of diamonds by the method of mixtures". In: *Proceedings of the Physical Society* 51.1 (Jan. 1939), pp. 173–190.

[161] E. Wigner and H. Huntington. In: *J. Chem. Phys* 3 (1935).

[162] Di Xiao, Wang Yao, and Qian Niu. "Valley-Contrasting Physics in Graphene: Magnetic Moment and Topological Transport". In: *Phys. Rev. Lett.* 99 (23 Dec. 2007), p. 236809. DOI: 10.1103/PhysRevLett.99.236809. URL: https://link.aps.org/doi/10.1103/PhysRevLett.99.236809.

[163] Di Xiao et al. "Coupled Spin and Valley Physics in Monolayers of MoS_2 and Other Group-VI Dichalcogenides". In: *Phys. Rev. Lett.* 108 (19 May 2012), p. 196802. DOI: 10.1103/PhysRevLett.108.196802. URL: https://link.aps.org/doi/10.1103/PhysRevLett.108.196802.

[164] Hayate Yamano et al. "Charge state stabilization of shallow nitrogen vacancy centers in diamond by oxygen surface modification". English. In: *Japanese Journal of Applied Physics, Part 1: Regular Papers Short Notes* 56.4 (Apr. 2017). ISSN: 0021-4922. DOI: 10.7567/JJAP.56.04CK08.

[165] Tengfei Yan et al. "Valley depolarization in monolayer WSe2". In: *Scientific Reports* 5.1 (Oct. 2015), p. 15625. ISSN: 2045-2322. DOI: 10.1038/srep15625. URL: https://doi.org/10.1038/srep15625.

[166] Luyi Yang et al. "Long-lived nanosecond spin relaxation and spin coherence of electrons in monolayer MoS2 and WS2". In: *Nature Physics* 11.10 (Oct. 2015), pp. 830–834. ISSN: 1745-2481. DOI: 10.1038/nphys3419. URL: https://doi.org/10.1038/nphys3419.

[167] Luyi Yang et al. "Spin Coherence and Dephasing of Localized Electrons in Monolayer MoS2". In: *Nano Letters* 15.12 (Dec. 2015), pp. 8250–8254. ISSN: 1530-6984. DOI: 10.1021/acs.nanolett.5b03771. URL: https://doi.org/10.1021/acs.nanolett.5b03771.

[168] T. Yu and M. W. Wu. "Valley depolarization due to intervalley and intravalley electron-hole exchange interactions in monolayer MoS_2". In: *Phys. Rev. B* 89 (20 May 2014), p. 205303. DOI: 10.1103/PhysRevB.89.205303. URL: https://link.aps.org/doi/10.1103/PhysRevB.89.205303.

[169] Hengyun Zhou et al. "Quantum Metrology with Strongly Interacting Spin Systems". In: *Phys. Rev. X* 10 (3 July 2020), p. 031003. DOI: 10.1103/PhysRevX.10.031003. URL: https://link.aps.org/doi/10.1103/PhysRevX.10.031003.

[170] Tony X. Zhou, Rainer J. Stöhr, and Amir Yacoby. "Scanning diamond NV center probes compatible with conventional AFM technology". In: *Applied Physics Letters* 111.16 (2017), p. 163106. DOI: 10.1063/1.4995813. eprint: https://doi.org/10.1063/1.4995813. URL: https://doi.org/10.1063/1.4995813.

[171] Xiaobo Zhu et al. "Observation of dark states in a superconductor diamond quantum hybrid system". In: *Nature Communications* 5 (Apr. 2014), p. 3424.

Appendix A

Bloch Sphere

The transformation from one eigenstate into an arbitrary superposition lends itself to the 'Bloch sphere' picture, wherein a 'Bloch vector' pointing from the origin to the north (south) pole of the sphere corresponds to the $|0\rangle$ ($|-1\rangle$) eigenstate. MW pulses applied to the state rotate the vector to new locations on the sphere. Projections onto the z-axis of the sphere correspond to the NV's population difference (the sum of the modulus of the coefficients in the superposition).

Since global phases are negligible, the first MW pulse in the measurement protocol can be defined to rotate the Bloch vector around the x-axis. This subsequently defines the y-axis of the sphere as the transverse axis that lies in the plane formed by the z-axis and the Bloch vector after the application of the first the MW pulse (Fig. A.1a). Until the NV is re-polarized by a laser, this remains the y-axis. The angle the Bloch vector's transverse component makes with the y-axis of the sphere now encodes the relative phase between

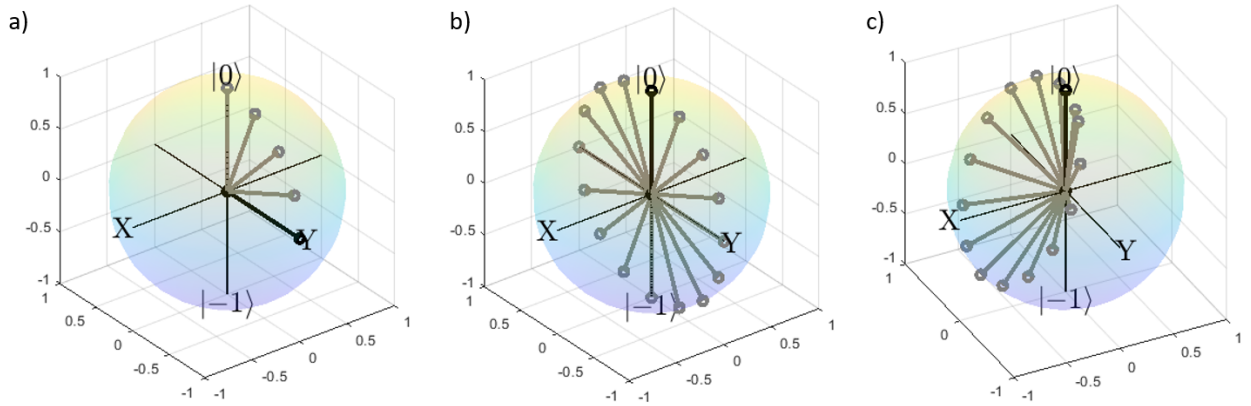

Figure A.1: The Bloch sphere places $|0\rangle$ at the north pole, $|-1\rangle$ at the south pole. a) The path of an $\pi/2$-pulse. Supposing it was the first pulse in the sequence, it is a rotation around the x-axis. b) The path of a Rabi oscillation. c) The path of a detuned Rabi oscillation.

the eigenstates. After the first MW pulse defines the y-axis, rotations around any axis of the sphere can be performed by shifting the phase of subsequent MW pulses. For example, rotations around the y-axis are performed by a MW pulse with a ± 90 degree phase shift relative to the first MW pulse applied. As an illustrative example, in the measurement of Rabi oscillations, the motion over the sphere is simply rotation around the x-axis, the projection onto the z axis following a perfect cosine pattern (Fig. A.1b). When driving an off-resonant transition, the detuning δ tilts the rotation axis away from the x-axis (it is effectively a B_z field). The resultant oscillation around the tilted axis cannot reach the south pole, but since it travels a shorter path, the Bloch vector completes its cycle faster (Fig. A.1c).